5-2015

Engineering the “Pluripotency” of Zr-based Bulk Metallic Glasses as Biomedical Materials

Lu Huang
University of Tennessee - Knoxville, lhuang11@utk.edu

Recommended Citation

Huang, Lu, "Engineering the “Pluripotency” of Zr-based Bulk Metallic Glasses as Biomedical Materials. " PhD diss., University of Tennessee, 2015.
https://trace.tennessee.edu/utk_graddiss/3306

To the Graduate Council:

I am submitting herewith a dissertation written by Lu Huang entitled "Engineering the “Pluripotency” of Zr-based Bulk Metallic Glasses as Biomedical Materials." I have examined the final electronic copy of this dissertation for form and content and recommend that it be accepted in partial fulfillment of the requirements for the degree of Doctor of Philosophy, with a major in Materials Science and Engineering.

Wei He, Major Professor

We have read this dissertation and recommend its acceptance:

Peter K. Liaw, Yanfei Gao, Roberto S. Benson, Elizabeth M. Fozo

Accepted for the Council:
Dixie L. Thompson

Vice Provost and Dean of the Graduate School

(Original signatures are on file with official student records.)

Engineering the "Pluripotency" of Zr-based Bulk Metallic Glasses as Biomedical Materials

A Dissertation Presented for the
Doctor of Philosophy
Degree
The University of Tennessee, Knoxville

Lu Huang
May 2015

DEDICATION

I would like to dedicate this thesis to my beloved husband, Dr. Wei Wu, for his relentless love, steadfast support, incredible patience, and unwavering trust; my parents, Xianming Huang and Weiping Liu, for giving their unconditional love and supporting all my dreams and endeavors; my sister and brother-in-law, Si Huang and Min Zheng, for their generous help whenever needed; and my niece, Zhiyan Zheng-Huang, for cheering me up and bringing so much laughter to my life; my farther-in-law and mother-in-law, Kun Wu and Jing Shi, for their encouragements; and the rest of my family and friends for their kind support.

ACKNOWLEDGEMENTS

I would like to express my deepest appreciation to my advisors Dr. Wei He and Dr. Peter K. Liaw. Their irreplaceable guidance and advice provided me such a great opportunity to learn, challenge, and explore my potentials in this exciting research area.

I am particularly grateful to Dr. Elizabeth Fozo for being a great mentor and offering me valuable directions and discussion on antimicrobial research. My special thanks go to Dr. Yanfei Gao for his generous help on finite element analyses. I sincerely acknowledge Dr. Roberto Benson for his constructive suggestions for my research. I also wish to express my gratitude to Dr. Tai-Gang Nieh for his guidance on nanoindentation, Dr. Gerd Duscher for his direction on transmission electron microscopy, and Dr. Deidra Mountain and Dr. Tim Sparer for their kindness in providing experimental materials and instructions.

I truly appreciate Dr. John Dunlap for providing tremendous help on microscopy. I am pleased to thank Dr. Paolo Vilmercati from Dr. Hanno Weitering's group for his help on surface chemistry measurements. My gratitude also goes to Dr. Patel Maulik from Dr. Kurt Sickafus's group for his help on diffraction technique. Many thanks to my labmates, collaborators and all those who help with my dissertation work: Dr. Yu Cao, Mr. Shuangcheng Tang, Ms. Emily Morin, Dr. Larissa Capeletti, Mr. Samuel Goddard, Mr. Joe Daniels-Mulholland, Mr. John Strange, and Mr. Lance Garret from Dr. He's group; Dr. Wei Wu, Dr. Gongyao Wang, Dr. Zhenke Teng, Dr. Andrew Chuang, Dr. Zhi Tang, Dr. Xie Xie, and Mr. Gian Song from Dr. Liaw's group; Ms. Bethany Miracle, Ms. Jia Wen, and Ms. Holly Saito from Dr. Fozo's lab; Mr. Mengkun Tian from Dr.

Duscher's lab; Mr. Richard Fisher and Ms. Stacy Kirkland from Dr. Mountain's lab; and Mr. Chao Pu from Dr. Gao's lab; Dr. Chao Zhu and Mr. Dong Wu from Dr. Nieh's lab. I am thankful for working in an inspiring and friendly research environment.

My gratitude is extended Ms. Carla Lawrence, Ms. Martha Gale, Ms. Tonya Brewer, Ms. Tracy Lee, Mr. Frank Holiway, Mr. Randy Stooksbury for their administrative support. I also want to thank Mr. Douglas Fielden, Mr. Larry Smith, and Mr. Danny Hackworth from machine shop, Mr. Stephen Stiner and Ms. Carol Winn from electronic shop, and Mr. Gregory Jones from the safety office for providing timely and constant technical support.

My final thanks go to National Science Foundation for the financial support under grant number of CMMI-1100080.

ABSTRACT

Bulk metallic glasses (BMGs) are a family of novel alloys with amorphous microstructures. The combination of their excellent mechanical properties, good chemical stability, high thermal formability, and general biocompatibility has brought up new opportunities for biomaterials. Research in this dissertation was focused on exploring multiple biomedical functionalities of Zr-based BMGs over a wide spectrum, combining materials and biological characterizations, through experimental and computational approaches. Four distinct yet interconnected tasks were endeavored, involving inflammation, hard-tissue implant, soft-tissue prosthesis, and pathogenic infection.

The inflammation that can be potentially triggered by Zr-based BMGs was investigated using macrophages. Lower level or comparable macrophage activations on were observed on Zr-based BMGs in comparison to commercial bio-alloys. The environmental stimuli can induce profound effects on macrophage activation in addition to substrate stimulation. Meanwhile, microstructure of the substrate was found to affect macrophage responses.

Ion implantation was employed to engineer the surface of a Zr-Al-Ni-Cu-Y BMG to enhance bone integration. Low energy Ca-ion implantations were adopted, which altered surface materials properties and introduced enhanced bone-forming cell adhesion. With higher fluence Ar-ion implantations, nano-sized Ar-bubbles were doped in the surface region of the Zr-based BMG, causing surface softening, which can be subsequently sensed by bone-forming cells. Cells exhibited less established adhesion and actin filament formation, whereas, higher rate of proliferation on surfaces with lower stiffness.

The potential of a Zr-Al-Fe-Cu BMG as a stent material was examined for the first time. The advantageous materials properties of the Zr-based BMG were revealed, including high strength, low elastic modulus, high elastic limit, and high biostability. Cell culture assays illustrated stronger adhesion and faster coverage of endothelial cells and slower growth of smooth muscle cells on the Zr-based BMG than on 316L stainless steel, which suggested promoted re-endothelialization and potentially lower risk of restenosis on the Zr-based BMG.

The capability to fight implant infections stacked additional biomedical benefits to Zr-based BMGs. The potency of Zr-Al-Ni-Cu(-Y) and Zr-Al-Co-Ag BMGs to inhibit bacterial growth were demonstrated against Gram positive *Staphylococcus aureus*. The biocidal effects of these Zr-based BMGs were related to the heavy-metal-ion release and microstructure.

TABLE OF CONTENTS

LIST OF TABLES

LIST OF FIGURES

CHAPTER I
INTRODUCTION AND GENERAL INFORMATION

Among the various classes of materials used medically, metals have enjoyed the longest record with examples dating back to 200 A.D. [1, 2]. Nowadays, metallic biomaterials have found widespread use not only as surgical tools, but also as implants to support tissue repair following injury or to replace failed tissue. The significance of metallic biomaterials as implants is underlined by their dominance in hard-tissue applications, such as bone implants (e.g., total hip joints, bone screws, etc.) and dental implants (e.g., crowns, bridges, dentures, etc.) [2]. Metals are also playing significant roles in implants interfacing with soft tissues, such as vascular stents, artificial heart valves, and neural electrodes [2]. Biomedical alloys that are commercially employed in medical procedures include noble metals and their alloys, stainless steels, Ti and its alloys, and Co alloys [2]. Despite their historical medical usage and great success in clinical practices, there remain areas of concern, such as stress shielding, particle disease, corrosion-fatigue failures, and foreign body inflammations [2-4]. These limitations of current biomedical alloys call for new materials as alternatives to conventional metallic biomaterials with enhanced mechanical and chemical properties, including: lower elastic modulus to avoid stress shielding, better wear resistance to minimize particle disease caused by toxic wear debris and severe metal leaching, higher fatigue endurance; and high corrosion resistance to withstand harsh *in vivo* working conditions (cyclic forces and corrosive environment); and improved biocompatibility to reduce immune rejection and promote integration to local tissues.

Under the vast demand of novel biomaterials, a revolutionary class of metallic materials, namely BMGs, has caught the attention of materials scientists. BMGs are new members to the materials society. Prior to their discovery, it was recognized that the constituent atoms in metals and alloys are arranged in a long-range atomic ordering fashion. The innovation with BMGs has revolutionized the perception of metallic materials, by presenting an amorphous structure for metals or alloys with constituent atoms randomly packed together, which forms an atomic structure with long-range disordering and short-range (within several nanometers) ordering [5-8]. Such an amorphous microstructure endows BMGs with a unique combination of mechanical, chemical, and physical properties [5-14]. The excellent mechanical properties, such as high strengths, low moduli, and high wear resistance [15, 16], together with their strong corrosion resistance [14], high thermal plastic formability [17, 18], and good biocompatibility [19, 20] are garnering interests for the biomedical applications of BMGs.

Ever since the first discovery of BMGs, great efforts have been made to design novel BMG compositions with attractive properties, to study the nature of these materials, and to promote their industrial applications. With the development of the alloy-fabrication techniques and alloy design, BMGs with large glass-forming ability have been achieved, allowing for the fabrication of BMGs with larger sample geometries up to centimeter scales [21-29]. This has furthered the opportunity for the scalable industrial applications of these amorphous alloys as structural or functional materials.

In addition to the favorable materials properties that influence the interactions between the implant materials and external mechanical (loading) or chemical (body fluid) environments, the implant devices will interact with the biological systems, which imposes further requirements on their biomedical functions. A successful implantation of a medical device requires an adequate inflammation and subsequent tissue integration following surgery. A series of biological events can be triggered upon insertion of a biomedical implant, which are briefly summarized in Figure 1.

Within seconds to hours after biomaterial implantation, proteins from body fluids or blood plasma first arrive at the implant surface [2]. In the following hours to days, inflammatory responses step in to clean up the necrotic tissues or defend the host tissue from the foreign materials. Inflammatory cells can reach the material surface and secrete a plethora of signaling molecules, which regulate downstream cell/tissue responses [30, 31]. Hard-tissue prostheses are exemplified by bone implants in Figure 1. During effective bone integration, elevated proliferation and extracellular matrix deposition of fibroblasts are undesirable, which can lead to fibrous encapsulation and the isolation of the device [32, 33]. Instead, osteoblasts can be recruited to the implant surface by proper pro-healing inflammation. The proliferation and differentiate of bone-forming cells to form woven bones, followed by bone remodeling, are desired to repair injured bone tissue or achieve bone regeneration [34]. Vascular stents are used as examples for soft tissue prostheses. The insertion of a stent into the blood vessel can stimulate the proliferation of smooth muscle cells resulting in restenosis to renarrow the lumen [35, 36]. On the other hand, the growth and coverage of endothelial cells on the stent surface can limit tissue scarring as well as blood-clot formation, ensuring stent integration [37, 38]. In addition to local cells and tissue, the implant material may also host the activities of

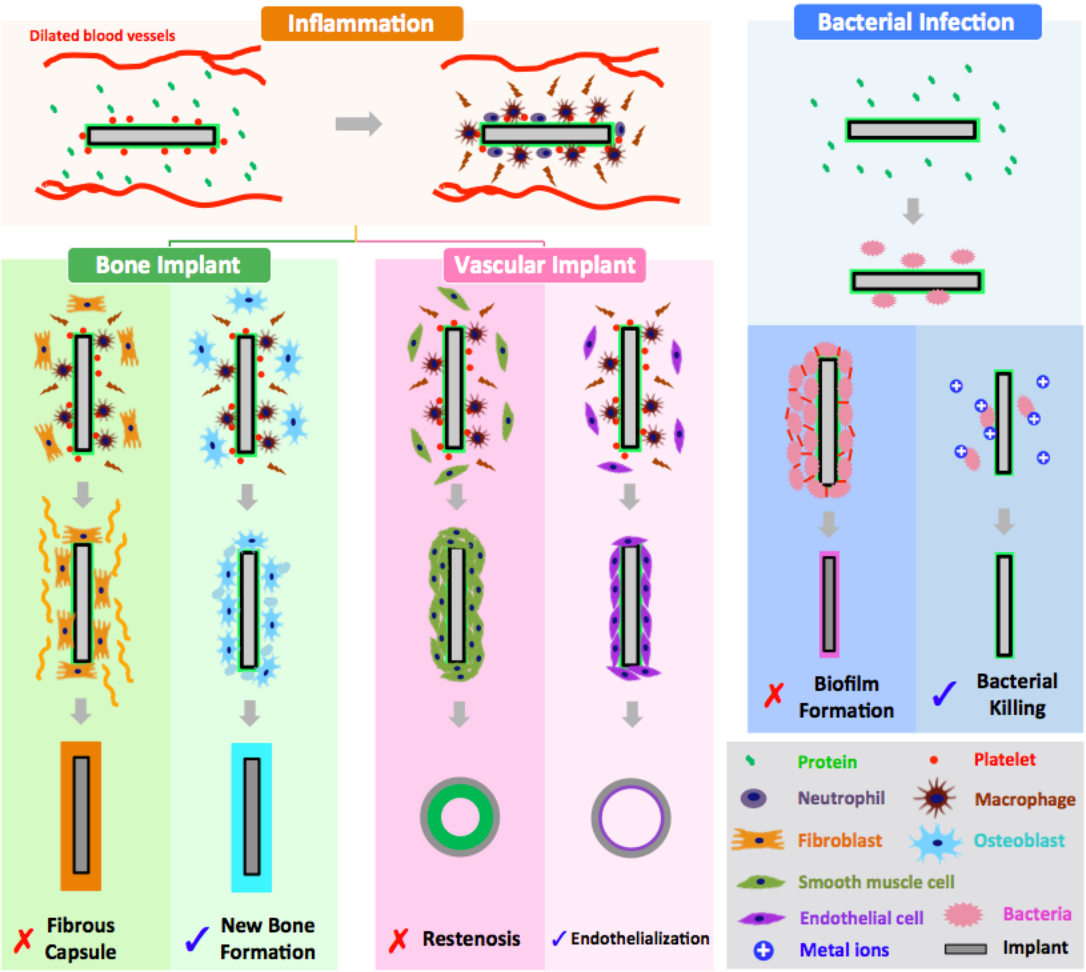

Figure 1 A schematic demonstration on the interactions between implant and cells or bacteria.

bacteria [39, 40]. The use of biomaterials with intrinsic antimicrobial properties can combat the colonization of pathogenic bacteria and greatly reduce the occurrence of peri-implantitis. Therefore, regardless of their specific purposes, the universal principles to design and investigate novel biomedical BMGs are summarized as: (1) to allow pro-healing inflammation, (2) to support activities of repairing or regenerative cells, and (3) preferably to prevent bacterial infection.

From the above discussion, it is concluded that an ideal biomedical BMG needs to fulfill the requirements on both favorable materials properties and biocompatibility to promote constructive cell/tissue responses. Amongst different BMG alloys, Zr-based BMGs are considered the most developed and investigated glass-forming systems. Zr-based alloys with high glass-forming abilities were developed with critical diameters larger than 1 cm [41, 42]. Moreover, a number of Zr-based glass-forming compositions were specifically designed for biomedical applications, owing to the high biocompatibility of the base element Zr [43-45]. Therefore, research in this thesis was focused specifically on exploring the biomedical potential of Zr-based BMGs. Systematic studies related to inflammation, wound healing, tissue regeneration, and pathology were exploited for the biomedical applications of Zr-based BMGs over a wide spectrum. Four distinct tasks combining materials characterizations, computer simulations, and biological characterizations were conducted, as demonstrated in Figure 2. The specific objectives of this dissertation were to engineer and characterize Zr-based BMGs, aiming at the multiple medical purposes:

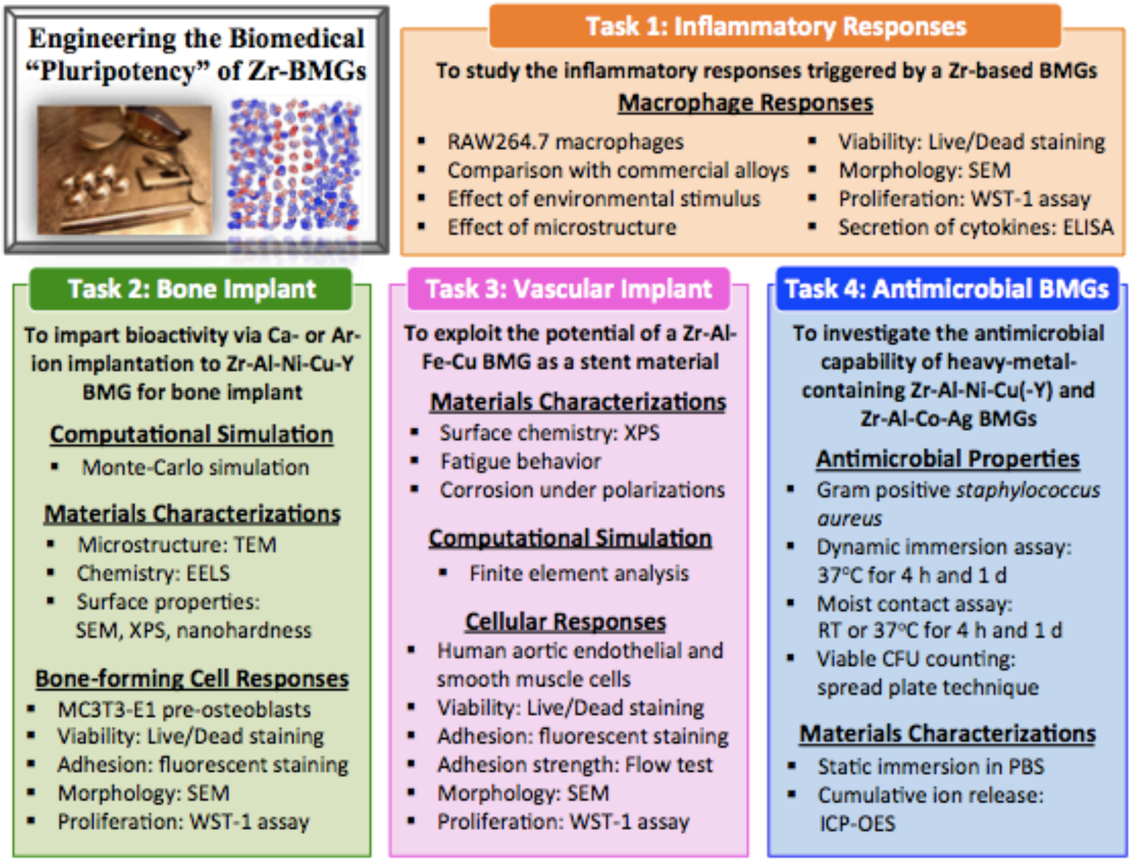

Engineering the Biomedical "Pluripotency" of Zr-BMGs

Task 1: Inflammatory Responses

To study the inflammatory responses triggered by a Zr-based BMGs

Macrophage Responses

- RAW264.7 macrophages
- Comparison with commercial alloys
- Effect of environmental stimulus
- Effect of microstructure
- Viability: Live/Dead staining
- Morphology: SEM
- Proliferation: WST-1 assay
- Secretion of cytokines: ELISA

Task 2: Bone Implant

To impart bioactivity via Ca- or Ar-ion implantation to Zr-Al-Ni-Cu-Y BMG for bone implant

Computational Simulation

- Monte-Carlo simulation

Materials Characterizations

- Microstructure: TEM
- Chemistry: EELS
- Surface properties: SEM, XPS, nanohardness

Bone-forming Cell Responses

- MC3T3-E1 pre-osteoblasts
- Viability: Live/Dead staining
- Adhesion: fluorescent staining
- Morphology: SEM
- Proliferation: WST-1 assay

Task 3: Vascular Implant

To exploit the potential of a Zr-Al-Fe-Cu BMG as a stent material

Materials Characterizations

- Surface chemistry: XPS
- Fatigue behavior
- Corrosion under polarizations

Computational Simulation

- Finite element analysis

Cellular Responses

- Human aortic endothelial and smooth muscle cells
- Viability: Live/Dead staining
- Adhesion: fluorescent staining
- Adhesion strength: Flow test
- Morphology: SEM
- Proliferation: WST-1 assay

Task 4: Antimicrobial BMGs

To investigate the antimicrobial capability of heavy-metal-containing Zr-Al-Ni-Cu(-Y) and Zr-Al-Co-Ag BMGs

Antimicrobial Properties

- Gram positive *staphylococcus aureus*
- Dynamic immersion assay: 37°C for 4 h and 1 d
- Moist contact assay: RT or 37°C for 4 h and 1 d
- Viable CFU counting: spread plate technique

Materials Characterizations

- Static immersion in PBS
- Cumulative ion release: ICP-OES

Figure 2 Schematic presentation of the objectives and tasks of the present thesis research.

(1) *Inflammatory responses*: Aiming at general implant applications, *in vitro* macrophage responses were conducted to understand the inflammation that can be potentially triggered by Zr-based BMGs. Other contributing factors including environmental stimulation and materials microstructural were also investigated.

(2) *Surface engineering towards bone implant applications*: Ion implantation technique was employed to engineer the surface chemistry or mechanical properties of a Zr-based BMG, in order to understand the effect of surface modification on materials properties and bone-forming cell behaviors.

(3) *Vascular implant applications*: Characterizations and simulations on material properties of a Zr-based BMG, along with application specific cell responses that determine the fate of stent integration were studied, in order to demonstrate the potential of a Zr-based BMG as a stent material for the first time.

(4) *Antimicrobial potency*: The capability of heavy-metal-containing Zr-based BMGs to inhibit bacterial growth was inspected and mechanistically analyzed to reveal their capability of fighting implant infections.

The principal outcome of this research will not only improve our understanding of the fundamentals underlying the interactions between Zr-based BMGs and their mechanical, chemical, and tissue environments through *in vitro* characterizations, but also greatly advance the research and development of Zr-based BMGs into the next-generation medical implant materials.

CHAPTER II
LITERATURE REVIEW

The unique characteristics of BMGs determined by their amorphous microstructures endorsed them as promising candidate biomedical materials. The first article that reported the characterizations of BMGs particularly regarding their biomedical applications was published in 1999, which described the corrosion behavior of a Pd-based BMG in artificial body fluid [46]. In later years, growing efforts have been made to study corrosion of BMGs in physiologically relevant environments [46-50]. The effects of external loading coupled with the simulated body environment on the material responses of BMGs were also investigated [51-54]. In 2003, researchers began their exploration in the cytotoxicity of BMGs using *in vitro* cell cultures [55-63]. More recently, the biocompatibility studies have advanced into *in vivo* animal experiments [19, 20, 60-63].

Over the past decade, there has been a continuous revolution in research concerning the medical potentials of BMGs. A number of novel BMG compositions (i.e., compositions with biocompatible elements) and surface engineering approaches were designed and developed, aiming at their medical practices [64-70]. With the ever increasing demand of new medical materials to satisfy the needs of the growing aging population, it will further propel the research to advance the development of biomedically applicable BMGs. In this chapter, a literature review on research progress gearing toward biomedical applications of BMGs will be presented, with an emphasis on the research related to Zr-based BMGs for long-term applications. With the word “biomaterial” implying the importance of both the material aspect and the biological aspect, Zr-based

BMGs must satisfy both in order to be considered a worthy family of new biomaterials. Hence, research efforts on the biomedical applications of Zr-based BMGs have been performed on both fronts. First, materials properties of Zr-based BMGs favorable for medical implantation usages are reviewed, including mechanical properties, stability in physiologically relevant environments, and the interactions of Zr-based BMGs with biological entities, such as biomolecules, cells, tissues, and microbes. Subsequently, examples of advanced research to tailor Zr-based BMGs for biomedical applications will be presented.

2.1 Biomedically-Relevant Mechanical Properties of Zr-based BMGs

One of the greatest advantages for the biomedical applications of metallic materials in macroscale forms is their capability to bear external loadings [71]. For Zr-based BMGs, their biomedical relevance as load-bearing components is naturally prominent in hard-tissue related treatments [19], whereas their applications as soft-tissue prostheses are also considered a subject of interest [20].

The superior mechanical properties of Zr-based BMGs over traditional load-bearing crystalline biomedical alloys are first highlighted by their low Young's modulus and high hardness (Figure 2). Taking bone implant for example, it is important to match implant material modulus with surrounding bone tissue in order to avoid stress shielding, which is one of the leading complications associated with load-bearing bone implants [72]. According to Wolff's law [72], the higher Young's modulus of current crystalline metals for bone implants than that of bone tissue can cause reduction of physiologically needed mechanical stress on adjacent bone, which leads to osteoporosis or bone resorption and implant loosening [73, 74]. There has been active research aiming to reduce the risk of stress shielding by designing new materials (i.e., β-Ti alloys) to lower the modulus of the implant devices [75-78]. However, the reduction in Young's modulus is usually associated with decreased wear resistance [79, 80]. Wear resistance is another important mechanical property that plays an essential role in the proper function of metallic implants, especially for joint implant devices. Taking bone prostheses for instance, the wear products due to the abrasion of the bone implants can cause another common complication, namely particle disease, which leads to periprosthetic osteolysis [81]. High wear resistance of the biomedical alloys, which can usually be translated as high hardness [82], can mitigate the production of wear particles. Therefore, high wear resistance/hardness, together with the low elastic modulus discussed above are desired materials properties for biomedical alloys. This combination can be achieved in the Zr-based BMG systems.

The Zr-based BMGs are known to exhibit low Young's modulus, while maintaining high hardness. For example, $Zr_{57}Ti_5Cu_{20}Ni_8Al_{10}$ BMG possesses a Young's modulus of 82 GPa and Vickers hardness around 5.4 GPa [83], which contrasts the Ti-13Nb-13Zr alloy with similar Young's modulus (79 - 84 GPa) but much lower Vickers hardness of 2.4 GPa [79]. A more general comparison between BMGs and crystalline alloys on their Young's modulus and hardness data is summarized in Figure 3 [15, 84]. Data for crystalline alloys locate on the higher left part of the diagram. Co alloys and stainless steels possess high hardness but high Young's modulus. Ti alloys and Mg alloys can be made to exhibit medium to low Young's modulus at the expense of hardness. In

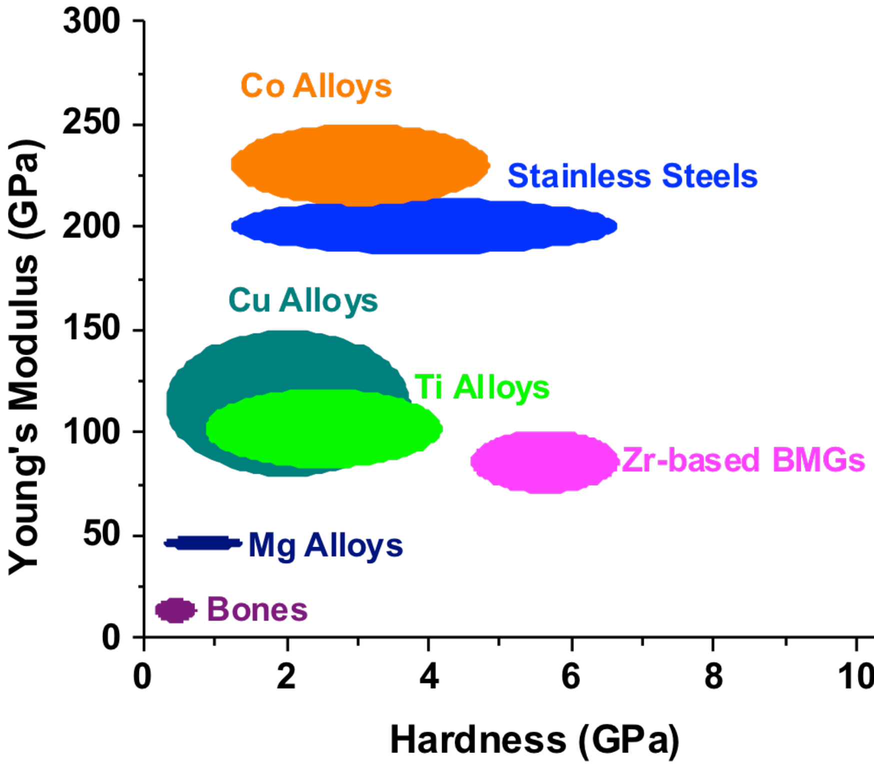

Figure 3 Vickers hardness versus Young's modulus data for different BMGs, traditional crystalline alloys, and polymers.

contrast, data for BMGs lie on the lower right part of the plot. The Young's moduli of Zr-based BMGs can reach as low as 80 - 100 GPa, with concurrently high hardness ranging from 5 - 9 GPa, making them competitive alternatives to medical steels and Ti- or Co-alloys.

The above discussion was focused on the mechanical responses of biomedical alloys to static loadings, whereas, fractures of biomedical implants are rarely caused by static loadings, but rather cyclic loadings. Implant materials, such as those used in total hip joints and artificial heart valves, undergo constant loading and unloading, which could lead to fatigue failures of medical devices at a stress level that is much lower than the yield strength. The investigations on the fatigue behavior of Zr-based BMGs are mainly conducted on Zr-based BMGs [85-92]. The fatigue endurance limits of BMGs and crystalline alloys are elucidated in Figure 4 [19, 92-94]. Some Zr-based BMGs exhibited ultrahigh fatigue endurance limits up to 1 GPa under uniaxial loadings [90, 91]. Nevertheless, it is worth noting that the data points are scattered when comparing results obtained from different testing methods [16]. Therefore, the choice of BMGs based on the available references regarding their fatigue properties needs a careful examination on the loading conditions and experimental setups. In general, the span of the fatigue endurance limit of BMGs mostly overlaps with that of crystalline alloys.

The other unique characteristic of BMGs is that they exhibit superplasticity within the supercooled liquid region, which is a temperature region between the glass transition temperature (T_g) and the onset temperature of crystallization (T_x). This superplastic

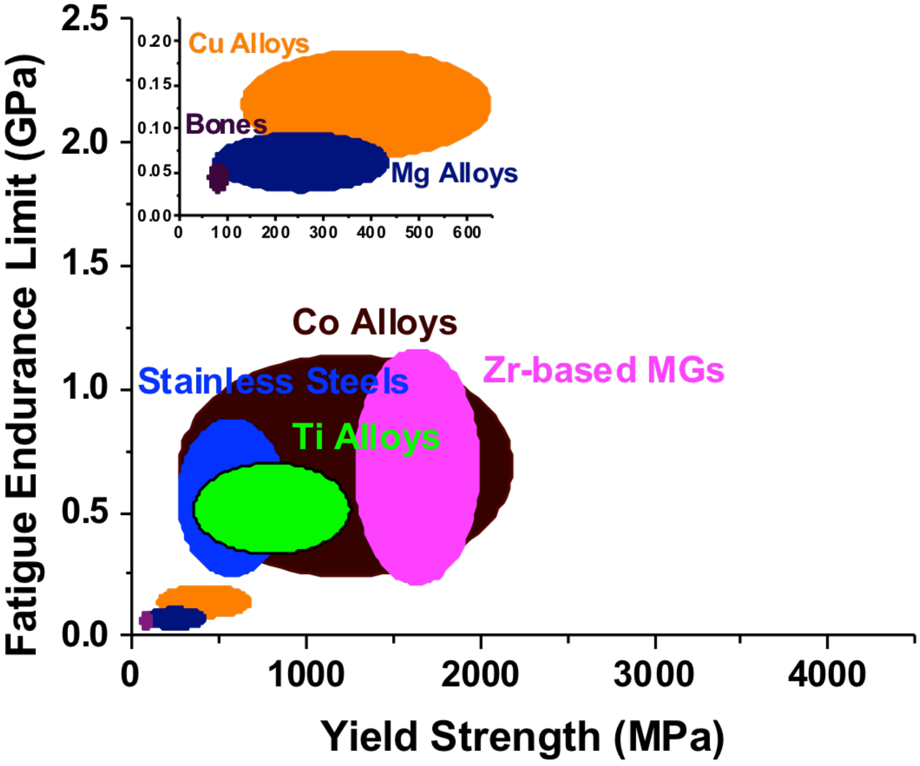

Figure 4 Fatigue endurance limit versus yield stress for different BMGs, traditional crystalline alloys, and polymers.

characteristic facilitates accurate three-dimensional thermal plastic formation [17, 18, 95, 96]. Within a temperature region between the T_g and T_x, which is typically around 30 - 150 K for Zr-based BMGs [7], severe and uniform deformation like plastics can be achieved. Using this unique feature, BMG articles, products, and devices with complex geometries and accurate surface patterns can be produced [18, 97-100]. The capability of BMGs to form accurate and complex geometries can simplify the processing and post-processing procedures, and eventually reduce the cost of implant devices.

2.2 Biostability of Zr-based BMGs

The human body presents an aggressive environment to any medical implants, with the presence of water, dissolved oxygen, a myriad of organic substances, and a wide variety of ions, as shown in Table 1 [14]. In addition, with pathological/physiological pH values ranging from 5.2 - 7.4 [101, 102], body temperature of around 37 °C, and dissolved oxygen being one fifth of that in air [103], it makes the environmental effect even more pronounced. Therefore, high corrosion resistance is required for the implants/devices to survive and retain desired function in the corrosive body fluids following implantation. Additionally, the high stability of biomaterials can prevent the occurrence of adverse tissue reactions to the corrosion products from uncontrolled breakdown of the implants.

Zr-based BMGs are usually considered to possess superior corrosion resistance to their crystalline counterparts. The underlying mechanisms for their expected high corrosion resistance of Zr-based BMGs are similar to those corrosion-resistant crystalline alloys, which involve either the formation of a protective oxide film (known as passive

Table 1 Compositions of different body fluids and phosphate buffered saline (unit: mM)

	Whole blood	Plasma	Phosphate buffered saline (PBS)
Bicarbonate	6.3-7.7	8-10	-
Chloride	77-86	100-110	139.7
Total phosphorus	0.25-0.37	0.31-0.58	9.6
Sulfate	0.1-0.2	0.35-0.75	-
Calcium	2.4	2-2.7	-
Magnesium	1.5-1.9	0.8-1.1	-
Potassium	40-60	4-5.6	4.2
Sodium	79-91	130-155	153

film) on the surface or the use of noble elements. Moreover, due to the uniform microstructure of BMGs, the passive films on the Zr-based BMG surfaces are expected to be more homogeneous. The absence of crystalline defects, such as dislocations, grain boundaries, and phase separation, further warrants the resistance of Zr-based BMGs to corrosion by eliminating the possibility of intergranular corrosion and galvanic corrosion.

Despite the high expectation of the corrosion resistance of Zr-based BMGs on the ground of their amorphous microstructure, early studies reported contradictory results, where pitting corrosion was observed at relatively low imposed potentials [50, 104-109]. The susceptibility to corrosion of Zr-based BMGs was later attributed to the presence of defects or artifacts [50, 109-111], which are recognized as higher energetic site to attract Cl^- adsorption and act as corrosion initiation sites [50, 108-112]. With the development of advanced fabrication technique and sample preparation, the presence of defects or artifacts can be diminished, however, the susceptibility to pitting of Zr-based BMGs was still observed. To understand the intrinsic pitting of Zr-based BMGs, another corrosion mechanism was proposed attributing the low corrosion resistance to the Cu-rich layer under the passive film, which was only applicable for Cu-bearing Zr-based BMGs [109].

Overall, the pitting resistance of Zr-based BMGs is governed by the susceptibility of passive films to the attack of Cl^- in the solutions. In order to improve the corrosion resistance of Zr-based BMGs, alloy design approaches were adopted to enhance surface properties of BMGs and produce more homogenous and stable passive films [106, 113, 114]. Minor addition of passivating elements is a strategy that has been commonly employed to improve the corrosion resistance of crystalline alloys [106, 113, 114]. This strategy was proved to be as efficient in BMGs as in crystalline alloys. The addition of elements exhibiting high affinity to oxygen, such as Nb [106, 113, 114], Ti [106, 115], and Y [50] were reported to significantly improve the pitting resistance. Alloying with noble elements has also been considered as an applicable method [116], although it may not be as efficient in some cases [104]. The corrosion resistance of Zr-based BMGs can also be advanced by increasing the Zr concentration to achieve high Zr content BMGs, which in principle tunes the surface composition to be more enriched with ZrO_2, resulting in an enhanced pitting resistance [45, 50, 117]. Increasing the Zr concentration may not only benefit the corrosion resistance of the Zr-based BMGs, but also improve their biocompatibility. Owing to the practices following the three routes discussed above, Zr-based BMGs with excellent corrosion resistance have been developed in recent years.

The polarization curves of Zr-based BMGs in various physiologically relevant solutions at 37 ^{o}C from selected reports in the literature were plotted in Figure 5, in comparison with traditional crystalline biomedical alloys [45, 50, 114-116, 118-120]. It can be observed in the polarization curves that Zr-based BMGs usually exhibit spontaneous passivation in physiologically relevant conditions due to passive film formation on the surface. The passive film prevents the underlying highly reactive amorphous alloy from being corroded by the solution. With the increase in imposed potential, passive films on the Zr-based BMGs usually break down at weak points leading to pitting corrosion, as indicated by the steep increase in current density at pitting potential. It is worth noting that not all Zr-based BMGs undergo passivation and pitting in simulated physiological environment. The Zr-based BMGs, which exhibit active dissolution, are not included in the current context of discussion [50, 104]. By comparing

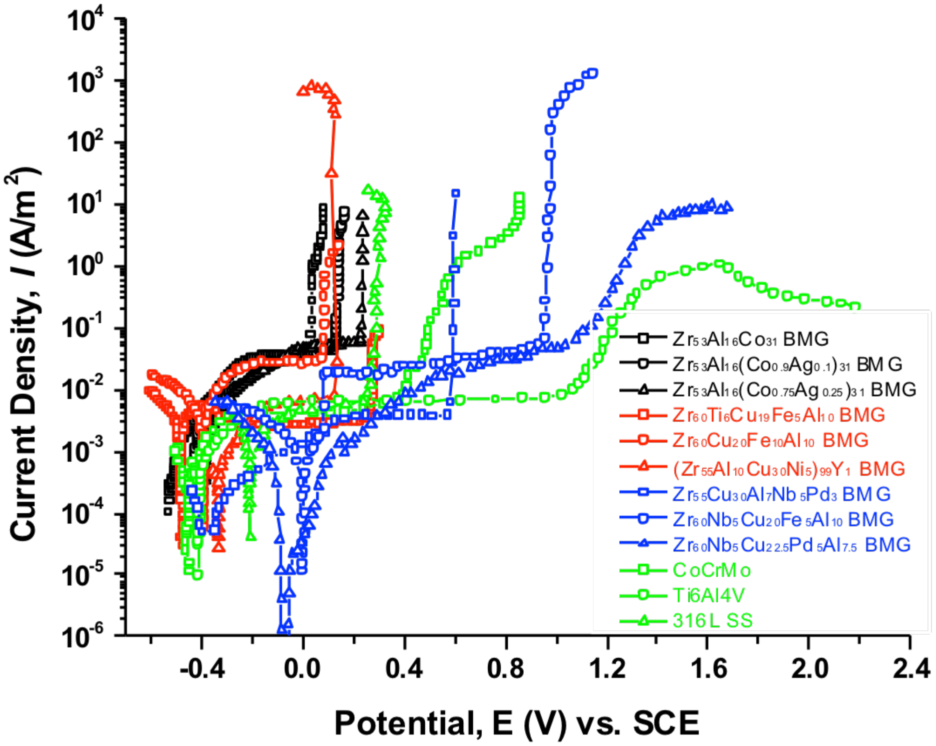

Figure 5 Summary plot of corrosion polarization curves of representative Zr-based BMGs in simulated physiological environments in comparison with crystalline biomedical alloys.

the polarization curves, it is concluded that the Zr-based BMGs with proper compositions can be comparably resistant to pitting corrosion with Ti-6Al-4V and Co-Cr alloys. For long-term applications, the use of these corrosion resistant Zr-based BMGs will be advantagous, since corrosion is considered an undesirable event.

2.3 Biological Functions of Zr-based BMGs

The biological responses to Zr-based BMGs have been explored via *in vitro* and *in vivo* investigations. A growing number of studies have been reported in recent years unveiling the promising perspective of the biomedical applications of Zr-based BMGs [19]. A variety of biomedical applications have been proposed and investigated mainly focused on their hard-tissue applications as bone [19, 68] and dental [59] implants; whereas their soft-tissue applications remain largely unexplored. Acknowledging the cell/tissue responses that can be involved in implant integration (Figure 1), *in vitro* responses and *in vivo* animal experiments were characterized with Zr-based BMGs. In addition to the biocompatibility studies, preliminary studies on the other biomedical functionalities were investigated, such as antimicrobial properties and bioactivity, which will undoubtedly impose additional advantages to the medical applications of these materials [121-123].

2.3.1 In vitro biocompatibility

As discussed in Chapter 1, protein adsorption is the very first event that occurred upon medical device implantation. It has been established that the nature, concentration, and conformation of the adsorbed proteins affect the subsequent cell/tissue responses to the implants [124, 125]. For example, fibronectin is usually considered to promote cell adhesion, while albumin is typically recognized to inhibit adhesion [126, 127]. Current research on protein adsorption on BMGs is very limited. It was initially demonstrated that higher amounts of both albumin [128] and fibronectin [129] were adsorbed on Zr-based BMGs than crystalline Ti. The generally higher amount of protein adsorption may possibly be related to enhanced cell adhesion and implant integration, whereas comprehensive studies on the competitive adsorption of different proteins and their conformations are necessary.

Responses of inflammatory cells to Zr-based BMGs were exploited in a few investigations mainly using macrophages in light of their critical role in chronic inflammation [130, 131]. The first report of macrophage responses on BMGs can be dated back to a 2003 *in vitro* cell culture study [55]. Cell viability, catalase activity, tumor necrosis factor-beta (TNF-β) cytokine release, and lactate dehydrogenase concentration of macrophages were found similar on a Zr-based BMG to those on pure Ti and polyethylene references [55]. The importance of inflammatory cell response to BMGs has been briefly revisited in two recent reports on Zr-based and Mg-based BMGs [45, 63]. Based on these pioneer studies, more systematic studies focused on foreign body responses are urged.

Fibroblasts were amongst those most commonly used cells to examine the biocompatibility of Zr-based BMGs in literature, in order to examine the cytotoxicity of the BMG substrates [20, 44, 45, 50, 55, 56, 61, 132]. Murine derived NIH3T3 and L929 fibroblast cell lines are two typical cell lines being used in the *in vitro* studies. A number of Zr-based BMGs were tested, which revealed general cytocompatibility Zr-based BMGs supporting either comparable or higher cell activities when comparing with crystalline biometals (i.e., Ti or Ti alloys). Study on fibroblasts that is more relevant to their functions in foreign body responses did not acquire enough efforts [64]. Future studies on fibrosis related fibroblast activities (i.e., morphological change, collagen production, gene expression, etc.) would be an interesting topic to exploit.

Aiming at bone implant applications, cells that are relevant to bone healing/regeneration were employed to study their activities on BMGs. Our group first employed mouse MC3T3-E1 pre-osteoblasts to investigate bone-forming cell responses on Zr-based BMGs [45, 57, 68]. Human MG63 osteoblast-like cells were also adopted in later biocompatibility studies [59, 120]. Similar to the cell studies with other cell types, studies on cell viability, adhesion, and proliferation were performed and the results were comparable to or slightly better than typical reference materials such as Ti-6Al-4V, pure Ti, or pure Zr. Differentiation and mineralization behaviors of bone forming cells are essential in new bone development [133]. Differentiation of the osteoblast-like cells was induced on the Zr-based BMG surfaces. Quantitative/qualitative analysis of alkaline phosphatase (ALP) activity and Ca deposition were conducted. The results indicated that Zr-based BMGs could support comparable bone-forming cell differentiation as Ti alloys did.

Endothelial cells are present in many processes after implantation. They are involved in wound healing to form neovascularization, and also compose the natural inner lining (endothelium) of blood vessels. To demonstrate the interaction of Zr-based BMGs and endothelial cells for the vascularization at dental implant site, human umbilical vein endothelial cells (HUVEC) were seeded on a Zr-Ti-Cu-Al BMGs, which showed higher proliferation rate after 7 d incubation and enhanced differentiation on the

Zr-based BMG than on cp-Ti [59, 60]. In terms of cell responses relevant to vascular device implantation, no findings have been reported.

Compared with those differentiated cells, stem cells are potent and capable of self-renewal and differentiation into various cell types, which showed their significance in tissue engineering [134]. Enhanced cell adhesion and faster proliferation of human mesenchymal stem cells (hMSCs) up to 2 days were reported on Zr-based BMGs as compared to Ti [128, 129]. The improved cell adhesion was partially attributed to the small amount of metal-ion release and improved protein adsorption, although a full understanding on the underlying mechanism demands further investigation [129].

2.3.2 In vivo characterizations

Based on the biosafety that has been established through *in vitro* cell culture studies, the research on the biocompatibility of Zr-based BMGs was further advanced to animal studies. *In vivo* characterizations have been reported using several small animal models in mouse, rat, hamster, or rabbit [20, 60, 61].

Animal studies on Zr-based BMGs mainly included subcutaneous implantation [20, 60, 61]. Zr-based BMGs of various compositions such as Zr-Ti-Cu-Ni-Be and Zr-Ti-Co-Be BMGs were implanted in mice or rabbits [20, 61]. The level of foreign body responses induced by implantation of Zr-based BMGs was comparable with that triggered by Ti alloys. *In vivo* test for dental implant application was carried out on Zr-Ti-Cu-Al BMG by oral mucosa irritation test, which showed similar biocompatibility of the Zr-based BMG to that of commercially pure Ti (cp-Ti) by histological analysis, after implantation into the cheek pouch of hamsters for weeks [60]. In general, these pioneer animal studies have revealed favorable biocompatibility of Zr-based BMGs with soft tissues in small animals. Efforts in hard-tissue implantation of Zr-based BMGs and the compatibility with large animals are desired in future studies.

2.3.3 Antimicrobial properties

Microbial infections of biomedical implants are not unusual cases, despite the stringent disinfection protocol and the use of laminar flow in the surgical sites [135, 136]. In order to achieve a higher success rate of device implantation, eliminate infection associated morbidity and mortality, and reduce financial burdens, researchers are actively developing antiseptic biomaterials, which possess intrinsic and long-lasting antimicrobial properties, in order to deter or inhibit bacterial adhesion, colonization, and biofilm formation [136-138]. Therefore, aiming at advancing the biomedical functions of BMGs, investigations on the impartment of antimicrobial properties to Zr-based BMGs and their efficiencies emerged in the past two years.

The first effort to investigate the antimicrobial potential of BMGs was made with Zr-based metallic glasses, however in the form of thin film on stainless steel substrate [139, 140]. The antimicrobial properties of the Zr-based metallic glass thin film were evaluated with five different Gram negative and Gram positive bacterial species (i.e., *Escherichia coli*, *Staphylococcus aureus*, *Pseudomonas aeruginosa*, *Acinetobacter baumannii*, and *Candida albicans*). Lower microbes to sample ratios were found on the Zr-based metallic glass than on bare stainless steels. Many possible mechanisms were proposed that were associated with material chemical ionization, crystallization with a redox reaction, material surface roughness, or amorphous covalent bonding [139]. In a later research on other BMGs (Cu-based, Ni-based, and Fe-based), the authors proposed that the antimicrobial properties of BMGs against *Escherichia coli* were rooted from the amorphous microstructure, since the biocidal capability of BMGs with significant different compositions was found similar to each other [121]. The above assumptions on the antimicrobial effects of BMGs need further experimental validations. These recent studies have opened up a new window of opportunity to exploit the additional biomedical benefit of BMGs to prevent bacterial infection of implants, which encourages more extensive and deeper investigations to guide future design.

2.4 Design and Surface Modification of Zr-based BMGs for Biomedical Applications

With the demonstration of general biosafety and versatile functions of Zr-based BMGs for potential biomedical applications, specific design of glass-forming compositions towards biomedical applications emerges to advance their biomedical applications. The basic idea for the design of biomedical Zr-based BMGs to simultaneously improve materials properties and biological interactions mainly follows two routes: tailoring the alloy composition and modifying surface properties.

There has been a continuous effort being made to the design of novel Zr-based BMGs ever since the first discovery of this amorphous material. With the deepened understanding in the fundamental science and materials properties of Zr-based BMGs, a major effort was directed toward the design of Zr-based BMGs to achieve specific properties to suit particular applications. Highly biocompatible Zr-based MGs can be designed that are low in or even free of “toxic” elements (i.e., Ni, Be, etc.) [19]. A large number of Zr-based BMGs were reported in the past years with specific emphasis on their biomedical applications [19, 43-45, 114, 120, 141, 142].

In addition to the compositional design of Zr-based BMGs, an alternative route was determined to modify their surface properties via surface engineering techniques, in order to further modulate cell behavior on the interfaces. Surface properties, including surface composition, topography, and mechanical characteristics, play crucial roles in tissue/material interactions [143-145]. Surface chemistry modifications to Zr-based BMGs were practiced using ion implantation [123] and surface oxidation [146] aiming at improving the bone integration of Zr-based BMGs by enhancing hydroxyapatite [HA, $Ca_{10}(PO_4)_6(OH)_2$] deposition, which is a common technique practiced with crystalline bone implant materials [147-158]. The introduction of surface features can alter both surface roughness and morphology to act as topographical cues for the downstream cellular activities. A previous study in our group indicated higher activity of alkaline phosphatase (ALP) of bone-forming cells on rough surfaces [68]. In addition, an exciting study was recently reported on the nanopatterning to Pt-based BMG produced by thermal plastic formation, which modulated responses of specific cell type(s) [64]. This technique can be applicable for Zr-based BMGs [18, 95], which can be an interesting research subject in the future. Surface mechanical modifications were also reported in Zr-based BMGs via ion implantation [159-162]. However, there is a lack of study on the relationship between surface mechanical properties and their biomedical functions. These previous studies verified the efficiency of surface modification and paved the ground of for further investigations to achieve an integration of desired properties.

CHAPTER III
MATERIALS AND METHODS

3.1 Materials

Zr-based BMGs with nominal compositions of $(Zr_{0.55}Al_{0.10}Ni_{0.05}Cu_{0.30})_{100-x}Y_x$ (x = 0 and 1), $Zr_{62.5}Al_{10}Fe_5Cu_{22.5}$, and $Zr_{53}Al_{16}(Co_{0.75}Ag_{0.25})_{31}$ (atomic percent, at.%) were fabricated using arc melting and copper mold casting technique. Pure metals of the constituent elements were melted and mixed in high purity argon atmosphere. The ingots were flipped over and re-melted for multiple times to assure homogeneity. Master ingots were shattered and heated up to molten state using induction heating in quartz tubes and injected into copper molds to form samples with different geometries. Plate samples with a geometry of 60 × 10 × 2 mm^3 were prepared for $(Zr_{0.55}Al_{0.10}Ni_{0.05}Cu_{0.30})_{100-x}Y_x$ (x = 0 and 1) and $Zr_{53}Al_{16}(Co_{0.75}Ag_{0.25})_{31}$ BMGs. Rod samples with a diameter of 6 mm were fabricated for $Zr_{62.5}Al_{10}Fe_5Cu_{22.5}$ BMG. Crystalline metals or alloys used as reference materials were commercially available. Ti-6Al-4V alloy (Grade 5) and 316L stainless steel were purchased from McMaster-Carr (USA). Pure copper (99.99 wt.%) and silver (99.9 wt.%) were obtained from Alfa Aesar (USA).

The $(Zr_{0.55}Al_{0.10}Ni_{0.05}Cu_{0.30})_{99}Y_1$ samples for the inflammatory response study (Task 1) were cut from as-cast plates using a diamond saw to a geometry of 5 × 5 × 2 mm^3, and manually ground with a lapping fixture (South bay tech, USA) using ascending grits of SiC sandpapers up to 600-grit. Ion implantation samples for bone implant study (Task 2) were machined to 5 × 5 × 2 mm^3 from the as-cast plates of $(Zr_{0.55}Al_{0.10}Ni_{0.05}Cu_{0.30})_{99}Y_1$ BMG, manually ground to 1200-grit surface finish using SiC sandpapers, and polished with 1-μm alumina slurry using a VibroMet vibratory polisher (Buehler, USA). Specimens in the vascular implant study (Task 3) were machined from $Zr_{62.5}Al_{10}Fe_5Cu_{22.5}$ BMG rods using a diamond saw. Mechanical test samples with an aspect ratio (length:diameter) of 2:1 were obtained with two end surfaces polished to 1200-grit surface finish, parallel to each other, and normal to the long axis. Corrosion test samples (10 mm long) were mount in epoxy resin, with exposed surfaces ground to 600-grit surface finish. Substrates for surface characterizations and cell culture studies were prepared as disc-shape (1.5 mm thick) with 600-grit surface finish. The geometry of samples for flow tests was manufactured to be $0.8 \times 3 \times 18$ mm^3. The square samples ($10 \times 10 \times 1$ mm^3) with 600-grit surface finish of $(Zr_{0.55}Al_{0.10}Ni_{0.05}Cu_{0.30})_{100-x}Y_x$ (x = 0 or 1) BMGs and $Zr_{53}Al_{16}(Co_{0.75}Ag_{0.25})_{31}$ alloys were used for antimicrobial studies (Task 4) and manually ground using SiC sandpapers up to 600-grit.

After sample preparation, all samples were ultrasonically cleaned in acetone, ethanol, and distilled water, respectively. Prior to biological assays, substrate materials were sterilized using 30-min ultraviolet light exposure [163]. The samples were positioned in the biosafety cabinet (Labconco purifier class II, Labcono, MO, USA) about 60 cm underneath the UV lamp, which generates a primary wavelength of light of 254 nm.

3.2 Materials Treatments

3.2.1 Ion implantation

Ion implantation to the polished $(Zr_{0.55}Al_{0.10}Ni_{0.05}Cu_{0.30})_{99}Y_1$ BMG substrates was conducted using an Eaton NV-200 implanter at the Alabama A&M University or the 400 kV ion implanter (National Electrostatics Corp., USA) in the Michigan Ion Beam Laboratory at the University of Michigan. Ar- or Ca-ions were implanted at different energies and fluences, as tabulated in Table 2. BMG specimens were attached to a heavy metal sample holder, which allowed heat dissipation during the implantation process and restricted the temperature rise of the specimens and crystallization [70].

3.2.2 Heat treatment

The $Zr_{53}Al_{16}(Co_{0.75}Ag_{0.25})_{31}$ BMG square samples were subjected to heat treatment to obtain crystalline counterparts. Samples were sealed in quartz tubes filled with pure argon. The heat treatment was performed at 853 K for 2 h at a heating rate of 30 K/min. Subsequently, the samples were cooled down to room temperature in the furnace.

3.3 Microstructures and Thermal Stability

The microstructure of as-cast or as-treated materials was examined using laboratory X-ray diffraction (XRD, Bruker D2, Germany) with Cu Kα radiation (λ = 1.5418 Å). Thermal stability of as-cast BMG samples was characterized using differential scanning calorimetry (DSC, Perkin-Elmer DSC7). Each DSC measurement was composed of two scans from 323 to 873 K in argon atmosphere at a heating rate of 20 K/min. The second scan was treated as the based line for background subtraction.

Surface microstructure of the $(Zr_{0.55}Al_{0.10}Ni_{0.05}Cu_{0.30})_{99}Y_1$ BMGs after 10 or 50 keV Ca- or Ar-ion implantation at 8×10^{15} ions/cm^2 was investigated using grazing incidence X-ray diffraction (GIXRD) using Empyrean diffractometer (PANalytical, Netherlands). Changes in atomic structure after ion irradiation was examined using X-ray

Table 2 Experimental parameters for ion implantation

Ion Species	Energy (keV)	Fluence (ions/cm^2)	Denotation	Implanter
Ca$^+$	10	8×10^{15}	Ca 10keV	Eaton NV-200 implanter
	50	8×10^{15}	Ca 50keV	
Ar$^+$	10	8×10^{15}	Ar 10keV	
	50	8×10^{15}	Ar 50keV	
	50	4×10^{16}	Zr-50L	National Electrostatics 400 kV ion implanter
	50	1×10^{17}	Zr-50H	
	100	1×10^{17}	Zr-100H	
	200	1×10^{17}	Zr-200H	

absorption spectroscopy (XAS) at Beamline 9-BM-B,C of the Advanced Photon Source at Argonne National Laboratory. The K-edge of Zr was measured by detecting total electron yield signals, which constrained the sampling depth and collected the structural information within the near-surface region.

Surface region of ion-implanted $(Zr_{0.55}Al_{0.10}Ni_{0.05}Cu_{0.30})_{99}Y_1$ BMG after 50, 100, or 200 keV Ar-ion implantation at 4×10^{16} or 1×10^{17} ions/cm^2 was sectioned out using Zeiss Auriga crossbeam focused ion beam (FIB; Zeiss, Germany) with Ga-ion beam. Characterizations of the BMGs were performed with a Zeiss Libra 200 MC transmission electron microscope (TEM; Zeiss, Germany) at an acceleration voltage of 200 kV. Selected area electron diffraction (SAD) patterns were collected from a round area with a diameter of 150 nm, which were used to determine the phase(s) of the samples. In addition, nano-beam electron diffraction (NBED) was achieved by converging the electron beam at an angle of 2.5 mrad unto a small area (around 0.5 nm in diameter). This technique allows for the detection of the structure of the BMG in the ultra-small area the same as the beam size. To high angle annular dark field (HAADF) images were recorded in the scanning transmission electron microscope (STEM) mode showing the microstructure of the images region with atomic number (Z) contrast. The advantage of high contrast in the Z-contrast images is derived from the large Z difference between the implanted Ar and the major element Zr in the BMG.

3.4 Mechanical Testing

Vickers hardness of the Zr-based BMGs and crystalline alloys were measured under 200-g load at room temperature with a microhardness indenter (Buehler, USA).

Uniaxial compression experiments were conducted using a MTS Materials Test System (MTS System Corporation, USA) servohydraulic machine at the strain rate of 10^{-4} s^{-1} at room temperature.

High-cycle compression-compression fatigue tests were conducted in air at room temperature. MTS machine was employed to apply load to the specimens at a frequency of 10 Hz (sinusoidal waveform) with an R ratio of 0.1 ($R = \sigma_{min} / \sigma_{max}$, σ_{min} and σ_{max} are the applied minimum and maximum stresses, respectively).

Fractography after static and cyclic compression test was observed using LEO 1525 scanning electron microscopy (SEM; Zeiss, Germany) at the acceleration energy of 20 keV. Secondary electron images were collected.

Nanoindentation experiments were performed at room temperature using a Hysitron Triboindenter (Hysitron, Inc., USA) to characterize surface nanohardness. For the indentations of 10 or 50 keV ion-implanted samples under a fluence of 8×10^{14} ions/cm^2, a Berkovich diamond tip was used with an effective tip radius of 233 nm. For each specimen, 15 indentations were carried out at 15 μm intervals. A loading function composed of a 5 s loading segment, 2 s holding segment with a maximum indentation depth of 250 nm, and 5 s unloading segment was applied with a peak load of 9 mN. For 50, 100, or 200 keV Ar-ion implanted samples under fluence of 4×10^{15} or 1×10^{16} ions/cm^2, a blunt Berkovich diamond tip was used with an effective tip radius of 759 nm. The indentation depth was so shallow that a sphere shape rather than three sided pyramid shape applies to the indenter tip. A maximum penetration depth of 35 nm was held for 1s after a 2 s loading segment, and then unloaded in 2 s. At least 12 indentations were executed at 10 μm intervals on each specimen. The stiffness, elastic modulus, and nanohardness of the samples were determined from the load-displacement curves obtained from the measurements. According to Oliver-Pharr method, [164] the elastic modulus is given by

$$E = (1-\nu^2)S/(2\gamma a)$$

Where S is the stiffness, *a* is the contact radius of the indentation, ν is the Poisson's ratio of the sample and it is about 0.362 for Zr-based BMG [165], γ is the correction factor [166].

3.5 Corrosion Resistance Characterizations

The corrosion test was performed using a three-electrode cell, consisting of a test specimen as the working electrode, a saturated calomel electrode (SCE, $E_{SCE} = 244$ mV) as the reference electrode, and a platinum foil as the counter electrode. Electrochemical experiments were performed at 37 °C in phosphate buffered saline (PBS) solution aerated with a 4 vol.% O_2/N_2 gas mixture to mimic physiological conditions. The composition of PBS solution was listed in Table 1. Prior to each polarization scan, the corrosion cell was immersed in the solution for 1 h to allow the open-circuit potential (OCP) to achieve a steady-state value. Potential-controlled cyclic-anodic-polarization experiments were conducted using the EG&G Princeton Applied Research 2263 potentiostat with the start potential of 20 mV below OCP, and a scan rate of 0.167 mV/s towards positive direction. The scans were reversed at pitting when the corrosion current density reached 10^4 mA/m^2. The potential was then decreased at the same scan rate until a potential of 50 mV below OCP was obtained.

The corrosion morphology after polarization was analyzed using SEM (Zeiss, USA). The chemical distributions of the constituent elements within a corroded area were mapped, using the energy-dispersive X-ray spectroscopy (EDX, Oxford, UK).

3.6 Surface Properties

Surface morphology of polished or ion-implanted Zr-based BMG samples was examined by SEM. Surface topography and roughness of each sample were measured using atomic force microscopy (AFM, Asylum Research, USA). Measurements were conducted under a non-contact mode. Both three-dimensional topography images and two-dimensional line profiles were recorded. Surface roughness data were obtained using Gwyddion image analysis software.

The surface chemistry of Zr-based BMGs was preliminarily examined using EDX. More accurate quantitative analyses of the surface chemistry were characterized using VersaProbe X-ray photoelectron spectroscopy (XPS; PHI, Japan). Measurements were performed employing an Al Kα monochromated X-ray source and the results were analyzed using XPSPEAK 4.1 data processing software. Shirley-type of background was used during data analysis.

Ar distributions in the near-surface regions of the implanted BMGs after ion implantation were further investigated by the monochromated electron energy-loss spectroscopy (EELS). The intensities of the Ar-$L_{2,3}$ ionization-edge were determined after background subtraction with a combination of a power law and a polynomial: $E^{-r} + aE^2 + bE + c$. Here, a, b, c, and r are fitting parameters, E is the energy [167, 168]. These intensities I of the Ar-$L_{2,3}$ ionization edge are directly related to the areal density N of Ar:

$I(\beta, \Delta) = N(\beta, \Delta) \times \sigma(\beta, \Delta) \times I_T$ [169]. Here, N is the absolute number of atoms per unit area, σ is the inelastic scattering cross-section, I_T is the total transmitted intensity, β and Δ represents the dependence of integration energy window and collection angle respectively. Since I_T, β, and Δ was kept constant in this experiment, the relative amount of Ar and Ar distribution could be directly obtained from EELS spectrum images.

Surface wettability of the samples was determined by the sessile-drop contact angle method with polar deionized water (DI water) and non-polar diiodomethane (DII) at room temperature, using a CAM-Plus contact angle goniometer (Cheminstruments, USA). Water droplets of 5 μl were placed on the samples, and contact angles were measured using the half-angle method (US Patent 5268733) at room temperature [170]. The surface free energy (SFE) for the tested samples was calculated based on the contact angle measurements following Owens-Wendt's equation [171].

$$1 + \cos\theta = 2(\gamma_s^d)^{1/2}[(\gamma_l^d)^{1/2}/\gamma_l] + 2(\gamma_s^p)^{1/2}[(\gamma_l^p)^{1/2}/\gamma_l]$$

where θ was the contact angle; γ_l was SFE of measured liquid; γ_s was SFE of tested sample; the superscripts d and p denoted dispersive and polar components of SFE. The SFE for each sample can be calculated with $\gamma_s = \gamma_s^d + \gamma_s^p$.

3.7 Ion Release Quantifications

Immersion tests of the $(Zr_{0.55}Al_{0.10}Ni_{0.05}Cu_{0.30})_{100-x}Y_x$ (x = 0 and 1) and $Zr_{53}Al_{16}(Co_{0.75}Ag_{0.25})_{31}$ BMGs, pure Cu, and pure Ag were performed at room temperature in the PBS solution to evaluate the release of Cu or Ag ions. Samples were immersed in 3 ml of PBS for different time periods. Immersion of Cu-containing samples was performed at room temperature. Ag-containing samples were kept at 37 °C during the immersion. Amounts of Cu or Ag ions dissolved into the PBS solution were quantified using an inductively-coupled plasma optical emission spectrometry (ICP-OES; Thermo Scientific, USA). The concentration of ion released from the substrates as a function of immersion time was quantified.

3.8 Computer Simulations

Simulations to describe the ion implantation process was performed using Stopping and Range of Ions in Solids (SRIM) package developed by Ziegler et al. [172]. The damages (i.e., displacement per atom, dpa) and ion distributions in the $(Zr_{0.55}Al_{0.10}Ni_{0.05}Cu_{0.30})_{99}Y_1$ BMG substrates were calculated employing the Monte-Carlo algorithms and a quantum mechanical treatment of ion-atom collisions [172]. In the full-cascade simulation, the displacement binding energy, surface binding energy, and lattice binding energy were set to be 40 eV, 2 eV, and 3 eV, respectively. The density of the Zr-based BMG applied in the simulation was experimentally measured to be 6.65 g/cm^3 following Archimedes' principle. The experimental fluences were plugged into the calculations to obtain the depth profiles of dpa and ion concentration.

Aiming at the potential stent application of the Zr-based BMGs, finite element analysis (FEA) was utilized to demonstrate the mechanical advantages of Zr-based BMGs with an actual stent configuration. The ABAQUS/Standard FEA package was employed to calculate the stress and strain fields of the stent under physiological loadings with systolic and diastolic pressure loads of 50 mmHg and 150 mmHg, according to American Society for Testing and Materials (ASTM) F2477 [173]. A 3D FEA model of

Table 3 Geometric parameters of the stent-vessel system for FEA

Part	Inner diameter (mm)	Outer diameter (mm)	Length (mm)
Stent	2.90	3.10	3.85
Vessel	3.00	3.40	5.00

stent-vessel system was constructed with the geometric parameters shown in Table 3. Considering that stent sliding in the vessel was more disastrous, the outer diameter was set to be 0.1 mm larger than vessel inner diameter to assure anchoring. Due to the symmetric condition in the axial direction and axisymmetry in tangential directions, a "30°" segment of half model was considered in the simulation. A 5-parameter third-order Mooney-Rivlin hyperelastic material was designated to simulate the arterial vessel wall with the constitutive model parameters that were reported in the literature [174]. The strain-energy density functions for hyperelastic model can be expressed as:

$$W = a_{10}(I_3 - 3) + a_{01}(I_2 - 3) + a_{20}(I_1 - 3)^2 + a_{11}(I_1 - 3)(I_2 - 3)+a_{30}(I_1 - 3)^3$$

where W was the strain energy density functions, a_{ij} were the constitutive model parameters, and I_1, I_2, and I_3 were the strain invariants.

The $Zr_{62.5}Al_{10}Fe_5Cu_{22.5}$ BMG (elastic modulus, E = 80 GPa; Poisson's ratio, ν = 0.38) and 316L stainless steel (E = 193 GPa, ν = 0.28) were treated as linear elastic materials. Based on the axisymmetric boundary condition, the tangential degree of freedom was constrained on the axial cross sections of stent and vessel segments to only allow radial expansion/compression. A general contact model with friction coefficient of 0.3 and non-penetrating normal condition was adopted to simulate the interfacial interactions between the two components at interface.

3.9 Cell Cultures and *In Vitro* Assays

3.9.1 Cell cultures

Murine derived RAW264.7 macrophages (kindly provided by Dr. Timothy Sparer at The University of Tennessee) were cultured in 15-mm Petri dishes. Cells were maintained at 37 ^{o}C in a 5 vol.% CO_2 balanced-air incubator in the growth medium composed of Dulbecco's modified eagle medium (DMEM) supplemented with 10% fetal bovine serum (FBS) and 1% antibiotics (Invitrogen, USA). Confluent cells were scraped off and resuspended in fresh medium for cell studies.

Murine derived bone-forming MC3T3-E1 pre-osteoblasts (ATCC, USA) maintained in T-25 flasks containing growth medium composed of alpha-minimum essential medium (α-MEM) supplemented with 10% FBS and 1% penicillin–streptomycin (Invitrogen, USA). Cells were harvested at confluency by detaching with 0.25% trypsin in ethylene diamine tetraacetic acid (EDTA, Invitrogen, USA) for cell culture studies.

Human aortic endothelial cells (HAECs) were received from Cascade Biologics, USA, and smooth muscle cells (HASMCs) were received from Lifeline Cell Technology, USA. Cells were maintained in basal culture medium supplemented with vasculife SMC lifefactors kit containing 0.1% recombinant human (rh) fibroblast growth factor (FGF) basic, 1% rh Insulin, 0.1% ascorbic acid, 5% L-glutamine, 0.1% rh epidermal growth factor (EGF), 5% FBS, and 1% antibiotics (Lifeline Cell Technology, USA). At confluency, cells were detached with 0.25% trypsin-EDTA and resuspended for cell studies.

3.9.2 Protein adsorption

Total protein adsorption on the $(Zr_{0.55}Al_{0.10}Ni_{0.05}Cu_{0.30})_{99}Y_1$ BMG and Ti-6Al-4V alloy was assessed by immersing the samples in macrophage cell growth medium (DMEM + 10 % FBS + 1 % antibiotics, Invitrogen, USA) at 37 ^{o}C for 30 min and 4 h, respectively. In order to minimize analytical errors, 9 samples were tested for each alloy. After incubation, samples were washed with PBS three times to remove residual medium. Adsorbed proteins were collected by immersing the samples in 250 μl of 5% sodium dodecyl sulfate (SDS, Sigma-Aldrich, USA) overnight on a plate shaker operated at 150 rpm. The amount of detached proteins was measured using a BCA protein assay (Pierce Biotechnology, USA) [30], according to manufacturer's instruction. An enhanced test protocol was applied using serial dilutions of bovine serum albumin (BSA) in the SDS solution as standards. Working reagent of 100 μl was added to 100 μl of sample or standard and mixed thoroughly on a shaker for 30 s. After 30 min incubation at 37 °C, the plate was cooled to room temperature and measured at 562 nm on a BioTek Synergy 2 Multi-Mode Microplate Reader (BioTek, USA).

3.9.3 Cell viability and adhesion

Initial cell attachment and viability at different incubation time points (4, 8 or 24 h) were studied with a LIVE/DEAD® Viability/Cytotoxicity Kit (Invitrogen, USA), which labeled live cells with calcein AM and dead cells with ethidium homodimer-1 (EthD-1). Samples were then rinsed with PBS and stained with the dye-containing PBS solution (2 μM calcein AM and 4 μM EthD-1) for 20 min at 37 ^{o}C. Fluorophore-labeled cells were viewed under a Zeiss Axio Observer A1 inverted fluorescent microscope (Zeiss, Germany) and fluorescent images were collected.

Cell adhesion and cytoskeleton formation on the substrates were further investigated by immunofluorescent staining of vinculin and F-actin. After different time periods of culture, cells were fixed in 4% paraformaldehyde for 20 min, permeabilized with 0.1% Triton X-100 (Sigma, USA) for 15 min, and blocked with 1% bovine serum albumin (Sigma, USA) for 20 min at room temperature. The intracellular vinculin was labeled through incubation with primary vinculin monoclonal antibody (diluted to 2 μg/ml; Chemicon, CA) for 1 h at RT, washed with PBS, and labeled with Alexa fluor 488 goat anti mouse IgG1 (γ1) (diluted to 10 μg/ml; Invitrogen, USA) for 1 h at RT. Simultaneously with Alexa fluor 488 staining, Alexa fluor 594 conjugated phalloidin (diluted to 40 μg/ml, Invitrogen, USA) was added to label the actin filaments of the cytoskeleton. The 4′, 6-diamidino-2-phenylindole (DAPI; Chemicon, CA) was used to label cell nuclei. Following PBS rinse, samples were mounted on a cover slip with fluoromount G (Southern Biotech, USA) antifade mounting solution. Fluorescent images were taken using the Zeiss fluorescent microscope.

3.9.4 Cell proliferation and morphological analyses

A water-soluble tetrazolium salt (WST-1, Roche applied science, USA) assay was used to assess cell proliferation behavior at different incubation periods. At each time point, samples were transferred to wells containing fresh growth medium and 10% WST-1 reagent. Subsequently, plate was incubated at 37 °C for 2 h. After mixing on a shaker for 1 min, supernatants were transferred to a 96-well plate. Quantification of formazan, which is a chromognic byproduct of mitochondrial dehydrogenation of terazolium salt, was realized by measuring the absorbance at 440 nm on the plate reader against a blank control. The intensity of measured light absorption is directly correlated to the metabolic activities and proportional to the number of cells.

The cell morphology was visualized using SEM. Cell layers were fixed and dried prior to imaging. Briefly, samples were washed with PBS and fixed with 3% glutaraldehyde (Electron Microscopy Sciences, USA) for 24 h at 4 ^{o}C. After rinsing with PBS 3 times, cells were dehydrated in ascending grades of ethanol baths (25%, 50%, 75%, and 100%). Dehydration in 100% ethanol was performed twice. Chemical drying with hexamethyldisilazane (HMDS) was conducted to warrant a thorough removal of water. Samples were soaked in the mixtures of 100% ethanol and HMDS at ratios of 2:1, 1:1, and 1:2, followed by 100% HMDS. Samples were then preserved in a vacuum desiccator to allow a complete evaporation of HMDS. Dried specimens were coated with gold using an SPI sputtering device for 20 s at 20 mA for SEM imaging. Secondary electron images were taken at accelerating voltages ranging from 3 to 5 kV.

3.9.5 Pro-inflammatory cytokine and nitric oxide assays

The production of pro-inflammatory tumor necrosis factor-alpha (TNF-α) from macrophages was measured using a BD OptEIA mouse TNF-α enzyme-linked immunosorbent assay (ELISA) kit (BD Biosciences, USA). According to the instruction, 50 μl of ELISA diluents were added to a 96-well plate pre-coated with anti-mouse TNF monoclonal antibody. Standards or samples (50 μl) were added to wells and incubated for 2 h at room temperature, allowing the binding of any existing TNF-α to the immobilized antibody. After washing and aspiration, 100 μl biotinylated polyclonal anti-mouse TNF antibody was added to each well and incubated at room temperature for 1 h, which produced an antibody-antigen-antibody sandwich. Following the second washing and aspiration, 100 µl streptavidin-horseradish peroxidase conjugate was added to each well and incubated for 30 min at room temperature. The wells were then thoroughly washed and aspirated, and 100 µl TMB one-step substrate reagent was added to each well. A blue color was developed after 30 min incubation at room temperature. The color intensity is directly proportional to the amount of TNF-α present. Stop solution (50 µl) was added to each well, followed by a plate reading at 450 nm.

The amounts of TNF-α secretion were normalized to the total protein contents obtained from the cell lysates in order to account for the difference in the number of adherent cells on different surfaces [175]. Cell layers were washed three times with PBS to displace any residual growth medium that could interfere with the quantification. Intracellular proteins were collected by transferring samples to microcentrifuge tubes containing 500 µl of 1× CyQUANT cell lysis buffer (Invitrogen, USA) and incubated for 5 min. After vortexing for 10 s, cell lysates were centrifuged at 12,000 rpm for 3 min at 4 °C. Total protein content in the supernatants was quantified using a Pierce Micro BCA Protein Assay Reagent Kit (Pierce, USA). Briefly, 25 µl sample was mixed with 200 µl of BCA working reagent for 30 s, and incubated for 30 min at 37 °C. The plate was cooled down and read at 562 nm using the plate reader.

The production of nitric oxide (NO) by macrophages that was accumulated in the culture medium was examined with Griess reagent (Promega, USA) following the manufacturer's instructions. The amount of nitrite, which was one of the primary stable and nonvolatile breakdown product of NO, was quantified. Briefly, 50 µL of 1%

sulfanilamide solution was added to 50 μL of each sample and incubated for 10 min at room temperature. Subsequently, 50 μL of the 0.1% N-1-napthylethylenediamine dihydrochloride solution was added and incubated for 10 min in dark at room termperature to terminate the reaction. The plate was measured immediately at 520 nm using the plate reader against blank culture medium. Nitrite standards with concentrations ranging from 0 to 100 μM in the macrophage culture medium were prepared to generate the standard curve.

3.9.6 Endothelial cell adhesion under a dynamic setting

Adhesion of HAECs on the substrates was further examined under a dynamic setting in a flow system. Flow tests were performed to the cell layers using the Bioptechs FSC3 system [176], as schematically presented in Figure 6. Substrates were mounted to a coverslip base using bees wax. Cells were seeded at a seeding density of 1×10^5 cells/cm^2 on the substrates and incubated at 37 °C for 20 h. After incubation the coverslips with adherent cells were assembled into the flow system, and cells were maintained in the micro-environmental chamber at 37 °C throughout the experiment. The cells were subjected to a shear stress of 4.05 dyns/cm^2 generated by the flow of the culture medium for 2 h. In parallel, reference groups of cells were statically cultured on the substrates. The flow direction was guided along the long axis of the specimen. Both groups of samples were fixed in paraformaldehyde and fluorescently stained to show the focal adhesion sites and cell nuclei, as described in Section 3.9.3.

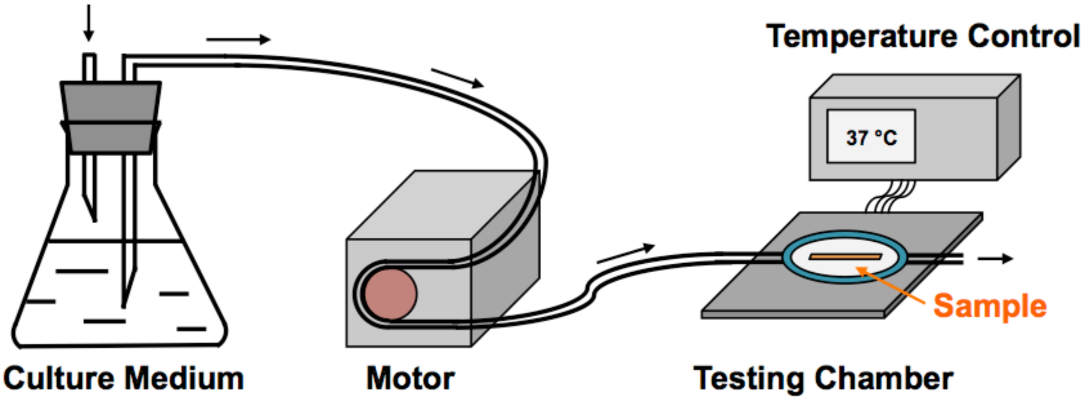

Figure 6 Schematic presentation of the flow test setup.

3.10 Bacterial Cultures and Assays

The *Staphylococcus aureus* (*S. aureus*) strain (ATCC6538, VA, USA) was statically cultivated in brain heart infusion (BHI, Fisher Scientific, USA) broth at 37 ^{o}C overnight. The overnight culture was diluted in tryptic soy broth (TSB, Fisher Scientific, USA) supplemented with 1 vol.% of glucose to an optical density ($OD_{600\ nm}$) of 0.01. Two different assays were performed including static contact and dynamic immersion. For static contact assay, the culture was then allowed to grow for 4 h at 37 ^{o}C to an $OD_{600\ nm}$ of about 0.3 (mid-log phase). Subsequently, 1 μl of the bacterial suspension was inoculated onto each specimen with an inoculation loop. Samples were statically incubated for 4 h at room temperature. For dynamic immersion assay, samples were placed in 3 ml of bacterial suspensions ($OD_{600\ nm} = 0.01$) in a 6-well plate at 37 ^{o}C for 24 h. After incubations, specimens were gently rinsed with PBS three times to remove non-adherent bacterial cells. For both assays, adherent bacteria were detached and re-suspended into 500 μl of PBS by a two-step vortexing procedure at 4 ^{o}C for 1 min for each step to avoid unnecessary cell deaths. Serial dilutions (10^{-2} and 10^{-3}) of the suspensions were plated on BHI agar plates and incubated overnight, followed by visual counting of colony forming units (CFUs).

3.11 Image Analyses

Cell parameters including number (density) of adherent cells, spread area, perimeter, circularity, and alignment were measured using ImageJ (NIH, USA) based on the SEM or fluorescent images.

3.12 Statistical Analyses

Results were statistically analyzed with JMP software (SAS Institute Inc., USA) using Student's *t*-test. Data were reported in the form of mean ± standard deviation (mean ± STDEV, $n \geq 3$). The significance level was defined as $p < 0.05$.

CHAPTER IV
INFLAMMATORY RESPONSE ON Zr-BASED BMGS

In terms of the research on the biomedical applications of Zr-based BMGs, little work was done to determine the inflammation that can be caused by BMGs [20, 55]. In light of the importance of inflammation during implantation induced foreign body response (discussed in Chapters 1 and 2), the present research was focused on the potential inflammatory responses that can be induced by Zr-based BMGs through *in vitro* studies. Macrophages play a very critical role among various types of cells that are involved in the foreign body response. Activated macrophages secrete a plethora of signaling molecules including cytokines (i.e., tumor necrosis factors, transforming growth factors, interleukin, prostaglandin, etc.), chemokines (i.e., monocyte chemoattractant proteins, macrophage inflammatory proteins, etc.), and other mediators (i.e., free radicals, nitric oxide, etc.) [30, 31]. The cytokine environment determines macrophage phenotypes, such as inflammatory, immunosuppressive, or healing, which tunes the behavior of immunocompetent cells and directs the downstream host responses [177]. Therefore, it is essential to study macrophage behavior toward new materials developed for potential biomedical implant applications.

In the present research, macrophage behavior on $(Zr_{0.55}Al_{0.10}Ni_{0.05}Cu_{0.30})_{99}Y_1$ BMG to gauge potential immune responses was studied via cell culture assays. Protein adsorption, macrophage adhesion, proliferation, and cytokine release were examined, in comparison with the commercial Ti-6Al-4V alloy. In addition, macrophage responses with and without external stimulations were investigated on a Ni-free $Zr_{62.5}Al_{10}Fe_5Cu_{22.5}$ BMG using 316L stainless steel as the reference material. Furthermore, the effects of the amorphous versus crystalline microstructures on the activations of the macrophages were probed in the $Zr_{53}Al_{16}(Co_{0.75}Ag_{0.25})_{31}$ glass-forming alloy system, using Ti-6Al-4V as the control material.

4.1 Macrophage Responses on a Zr-Al-Ni-Cu-Y BMG

Regarding the potential biomedical applications of Zr-based BMGs as implant materials, the mechanical, chemical, and biocompatibility of $(Zr_{0.55}Al_{0.10}Ni_{0.05}Cu_{0.30})_{99}Y_1$ BMG has been investigated using bone-forming cells in our previous research [54]. In particular, it was emphasized that the elastic moduli of $(Zr_{0.55}Al_{0.10}Ni_{0.05}Cu_{0.30})_{99}Y_1$ BMGs was measured to be about 85 GPa [68], which was significantly lower than 100-120 GPa of Ti alloys, 190-210 GPa of 316L stainless steels, and 210-250 GPa of Co-Cr alloys [82], benefiting the mechanical compatibility of the implants. In addition, the production of wear debris could activate macrophages and inflammatory responses, leading to aseptic loosening and osteolysis, which was considered to be the most prominent complication for total hip replacement. The microhardness of $(Zr_{0.55}Al_{0.10}Ni_{0.05}Cu_{0.30})_{99}Y_1$ BMG was almost 50% higher than that of Ti-6Al-4V alloy [68], implying a better wear resistance [178] and potentially smaller amounts of wear debris/particles. Moreover, surface properties that were considered to be key factors that influence protein adsorption and subsequent cellular behaviors on biomedical materials [126], were also investigated in a previous report from our group [68]. The Zr-based BMG demonstrated similar surface roughness and wettability/SFE to those of Ti-6Al-4V with the same sample preparation protocol. These previous findings set a solid foundation for the subsequent studies on macrophage response. Therefore, the present investigations were started with $(Zr_{0.55}Al_{0.10}Ni_{0.05}Cu_{0.30})_{99}Y_1$ BMG as a model Zr-based BMG system to demonstrate macrophage responses.

4.1.1 Initial Macrophage Attachment and Viability

The cellular behavior of macrophages was studied using murine derived macrophages, owing to the prevalent application of murine models in pre-clinical *in vivo* studies [179]. Specifically, the RAW264.7 cell line was employed, which was derived from the virus-induced tumor of BALB/c mice with a male genotype [30]. The motivation of selecting the most commonly used RAW264.7 cell line for the *in vitro* study of macrophage-biomaterial interactions was to enable comparisons of research findings in this study with existing reports on RAW264.7 macrophage interactions with various traditional medical alloys. However, direct comparison of results presented herein with those obtained from other types of macrophages (i.e., other immortalized cell lines or primarily-derived macrophages) should be carried out with caution because of phenotypic non-equivalence among these various types of macrophages [179].

The initial attachment and viability of RAW264.7 macrophages with and without the presence of serum were examined via Live/Dead staining (Figure 7). Live and dead cells were labeled with green and red fluorophores, respectively. A relatively early time point of 4 h was chosen to better distinguish the effect of protein conditioning. Very few dead/disrupted cells were observed on either Zr-based BMG or Ti alloy substrates, suggesting a high initial cellular viability. A large amount of adherent cells were disclosed on samples cultured with serum-containing medium, while a considerably lower number of cells were observed on samples in culture medium without serum

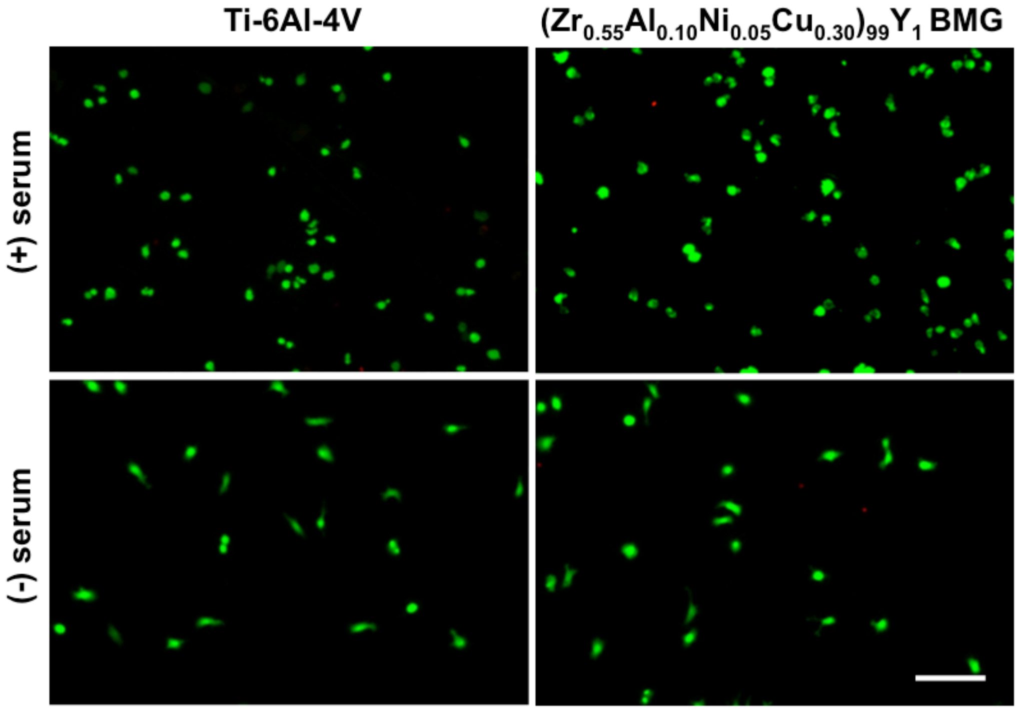

Figure 7 Live/Dead staining for RAW 264.7 macrophages on different substrates after 4 h growth with or without the presence of serum in the growth medium (green: live cells, red: dead/dying cells; scale bar: 100 μm).

supplementation. Semi-quantification on the number of adherent live cells on each substrate through image analysis can be found Figure 8, which showed a significant reduction in the number of adherent cells when the growth medium was deprived of serum proteins. Therefore, it was suggested that protein conditioning was essential in mediating macrophage cell adhesion to materials, which was primarily realized through the interaction of cell surface receptors and adsorbed proteins [124].

In light of the critical role of protein conditioning in mediating the initial cell adhesion, the gross protein adsorption on the $(Zr_{0.55}Al_{0.10}Ni_{0.05}Cu_{0.30})_{99}Y_1$ BMGs was evaluated in comparison with that on Ti-6Al-4V alloy [124, 125]. Instead of using a single component protein solution, serum-supplemented growth medium was selected to better mimic physiological conditions and gain an overview of total protein adsorption on the Zr-based BMG. The amount of total proteins adsorbed on each metallic substrate after immersion in the growth medium for 30 min or 4 h was quantified and presented in Figure 9. Generally, regardless of the test substrate, no significant differences were observed between the 30-min and the 4-h immersion groups, indicating that the major protein adsorption occurred within 30 min of immersion. The amount of total protein adsorption did not vary significantly between the Zr-based BMG and Ti-6Al-4V alloy at the given time points, which can be well correlated with the similar amount of cells found on the Zr-based BMG and Ti-6Al-4V alloys with serum conditioning.

The similar amounts of gross protein adsorption for Zr-based BMG and Ti-6Al-4V can be partially explained by the comparable surface hydrophilicity. Previous research suggested that various types of proteins in serum-supplemented culture medium

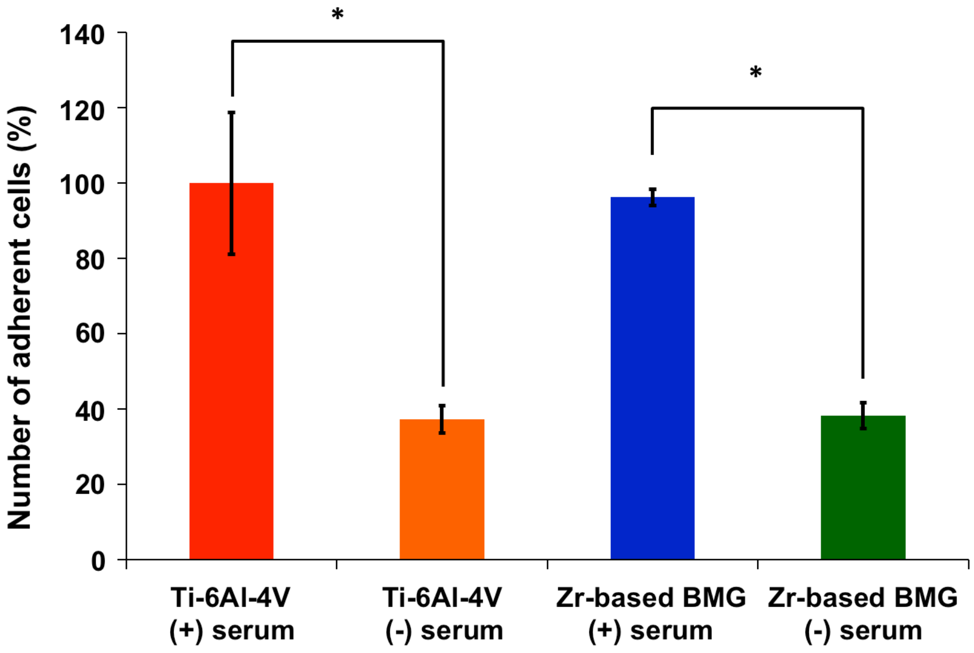

Figure 8 Semi-quantification on the number of adherent live RAW 264.7 macrophages after 4 h of growth on $(Zr_{0.55}Al_{0.10}Ni_{0.05}Cu_{0.30})_{99}Y_1$ BMG (denoted as Zr-based BMG) and Ti-6Al-4V alloy with or without the presence of serum (Mean ± STDEV, * denotes statistically significant differences at $p < 0.05$, data were presented as percentages of the number of adherent cells to that on Ti-6Al-4V with serum).

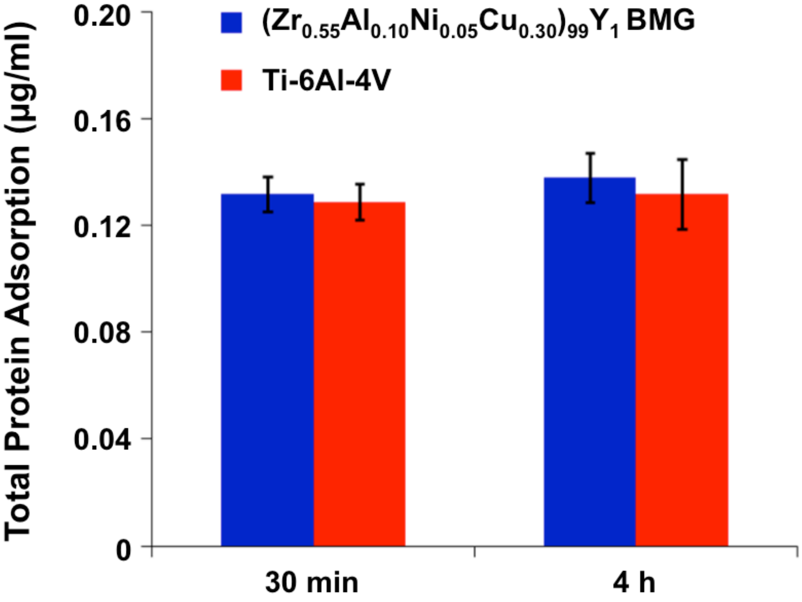

Figure 9 Total protein adsorption on Zr-based BMG and Ti-6Al-4V alloy after 30 min and 4 h immersion in serum supplemented growth medium (Mean ± STDEV).

could readily adsorb on Ti alloys. Among different types of proteins, albumin and fibronectin were typically studied [126, 127]. In particular, a higher amount of fibronectin, which was considered to promote cell adhesion, was found on Ti substrates after immersion in growth medium. In contrast, the adsorption of albumin, which was known to prohibit cell adhesion, was found in lesser amounts. Therefore, it is postulated that cell adhesion is closely related to the nature of the adsorbed protein on biomedical materials. Further analysis on the components and conformations of adsorbed proteins from the culture medium and investigation on the deposition of known types of proteins on the Zr-based BMG substrates are necessary to advance the understanding on the mediation effects of specific proteins.

4.1.2 Macrophage Proliferation and Cell Morphology

The proliferation behavior of macrophages was determined at day 1 through day 3 using a WST-1 assay, which correlated the number and metabolic activity of cells with absorbance. Figure 10 illustrated a growing number of cells with time on both alloy surfaces. The increase in WST-1 absorbance intensity with culture time suggested that cells were viable at longer time points. Both Zr-based BMG and Ti-6Al-4V substrates were capable of supporting macrophage proliferation. A slightly higher amount of cells was found on the Zr-based BMG substrate at day 2. The successful proliferation of cells assured that no adverse reactions of cell death would be induced by the metallic substrates. Such a general biosafety of Zr-based BMGs was consistent with our previous findings and many other studies using various types of mammalian cells including fibroblasts, osteoblast-like cells, etc. [20, 44, 45].

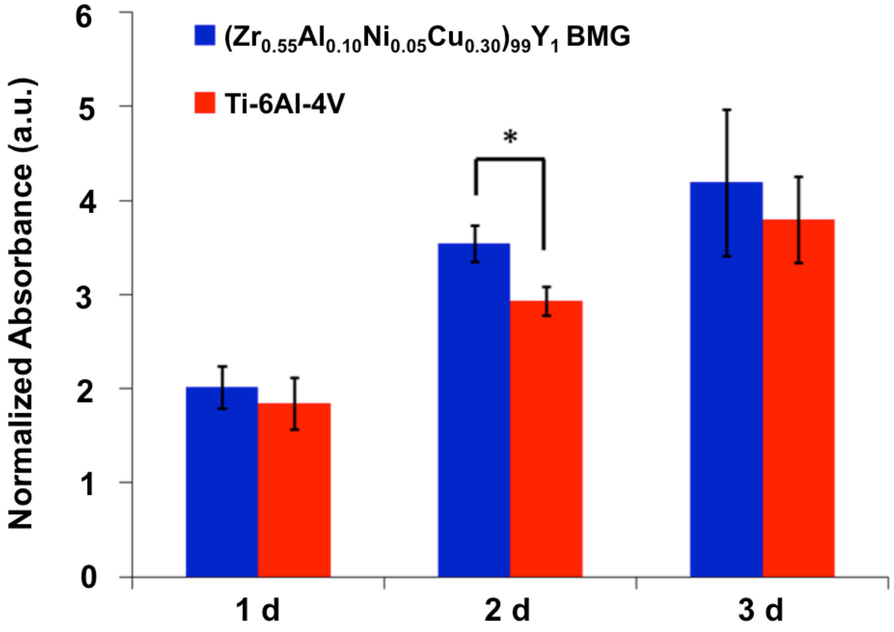

Figure 10 WST-1 assay results for RAW 264.7 cell proliferation activities after 1 - 3 d growth on $(Zr_{0.55}Al_{0.10}Ni_{0.05}Cu_{0.30})_{99}Y_1$ BMG and Ti-6Al-4V alloy (Mean ± STDEV, * denotes statistically significant differences at $p < 0.05$).

Figure 11 presented the SEM secondary electron images of macrophages at different time points. It was shown that cell numbers increased with increasing culture time, which agreed with the WST-1 assay results. To provide a close-up view of the cell morphology, representative images for individual cells on each alloy at day 1 were also shown in Figure 11. Generally, macrophages exhibited round morphology with the presence of surface ruffles and numerous extending pseudopodia at day 1.

Morphological criteria were typically used to determine the activation of macrophages, including the spreading, content of granules, extent of ruffling, and other finer details of cell surfaces [131, 180]. It was commonly acknowledged that morphological indicator of activated macrophages include the increases in cell size, number of granules, and ruffling of plasma membrane [131]. Qualitatively, the macrophages remained round-shaped on both substrates. Larger amounts of ruffling were observed for macrophages on Ti-6Al-4V alloy than on the Zr-based BMG. The average spread area, perimeter, and circularity of the cells were measured and quantified (Figure 12). The spread areas and cell perimeters of macrophages decreased consecutively with culture time, suggesting a reduction in macrophage activation over time [181, 182]. On both alloys, the circularity of the cells remained around 0.9 during the 3-day growth, indicating a mostly round morphology of the macrophages, which was in agreement with the direct observations of the SEM images. These observations suggested that both alloys were not highly stimulatory toward macrophages as compared with the morphologies of those stimulated macrophages reported in the literature [131, 183-185]. However, less cell spreading and smaller perimeters were found for those cells cultured on the Zr-based BMG substrates at days 1

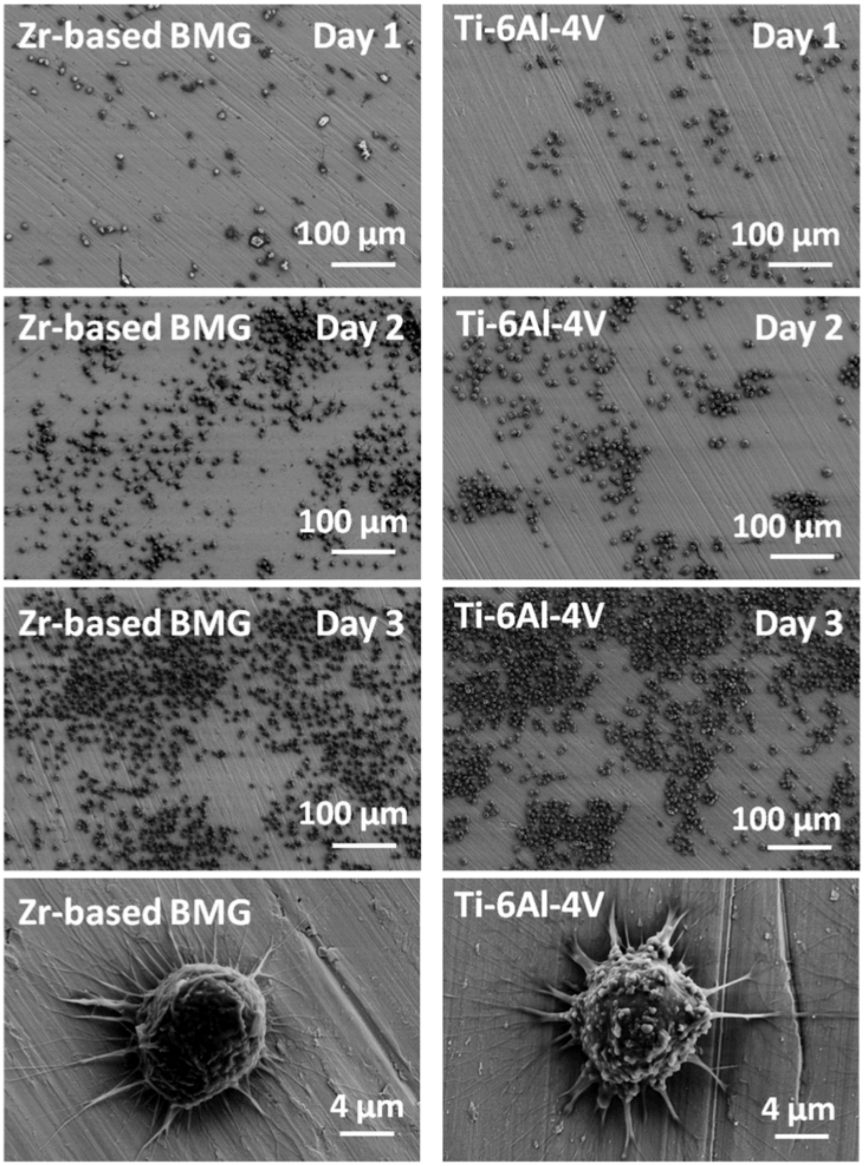

Figure 11 SEM images showing the morphological activations of RAW 264.7 macrophages on $(Zr_{0.55}Al_{0.10}Ni_{0.05}Cu_{0.30})_{99}Y_1$ BMG (denoted as Zr-based BMG) substrates (left column) and Ti-6Al-4V alloy substrates (right column) after 1 - 3 d of growth. Representative images of magnified view of individual cells on day 1 are also shown.

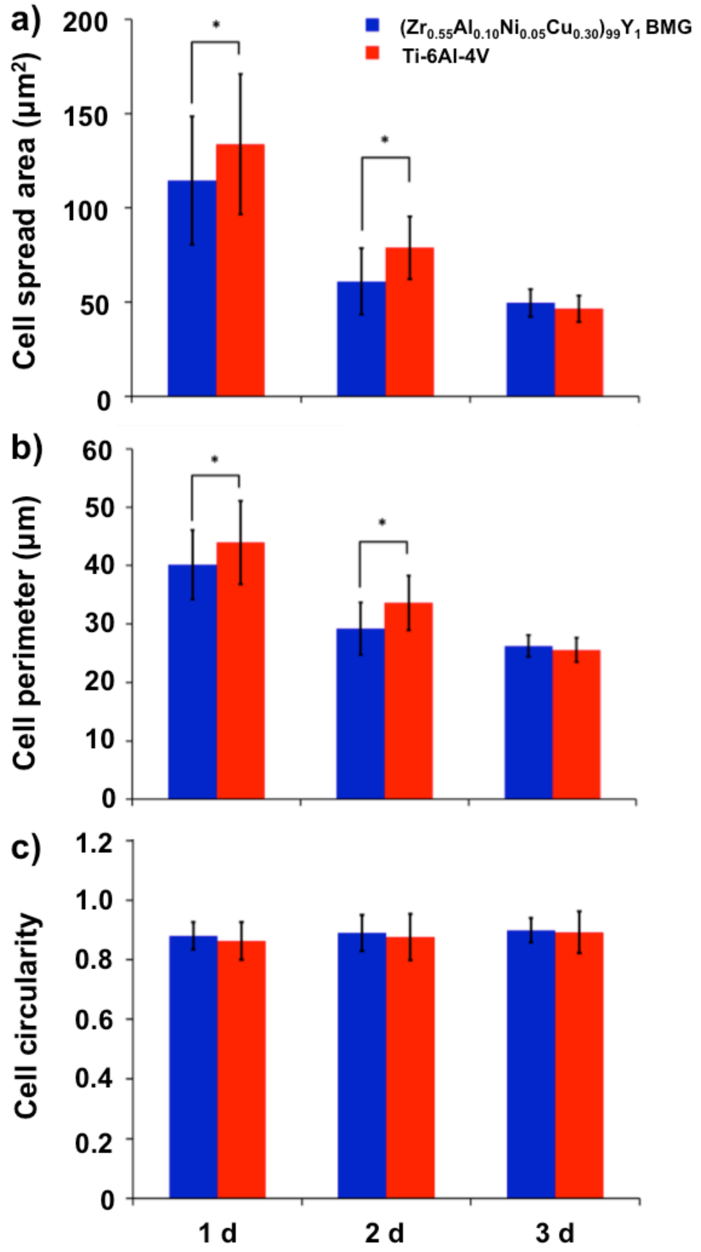

Figure 12 Statistical results of (a) average cell spread area, (b) perimeter, and (c) circularity of RAW 264.7 macrophages on different substrates on 1 - 3 d after seeding on $(Zr_{0.55}Al_{0.10}Ni_{0.05}Cu_{0.30})_{99}Y_1$ BMG and Ti-6Al-4V alloy (analyses were made on the SEM images presented in Figure 12; Mean ± STDEV, * denotes statistically significant differences at $p < 0.05$).

and 2. The smaller amount of ruffling and less extent of spreading initially indicated a lower level of stimulation to macrophages for the Zr-based BMGs.

4.1.3 Pro-inflammatory Cytokine Release

Complementary to the semi-quantitative evaluation from morphological observations, quantifications of cytokine secretions were used as markers of inflammation. Macrophages can produce various cytokines, including interleukin-1 (IL-1), IL-6, IL-10, transforming growth factor-beta 1 (TGF-β1), TNF-α, etc. These cytokines can be classified into pro-inflammation, anti-inflammation, pro-wound healing, and anti-wound healing [30]. TNF-α was found a pro-inflammatory and anti-wound healing cytokine. The degree of TNF-α secretion was pertinent to the level of inflammation. In addition to inflammation, TNF-family cytokines were found to affect bone formation and resorption [186]. They were known as osteolytic cytokines, together with other inflammatory cytokines (i.e., IL-6, IL-10, etc.), owing to their *in vivo* bone-resorbing effect [187].

The secretion profile of the pro-inflammatory cytokine TNF-α is depicted in Figure 13a. In order to account for any differences in the number of adherent cells, the amount of total intracellular protein was quantified, which was used to normalize the TNF- α concentration (Figure 13b). The amount of TNF-α accumulated from day 1 to 3, whereas, the secretion rate tended to slow down with time. At all three time points, macrophages cultured on the Zr-based BMG exhibited a lower level of TNF-α secretion compared to those on the control Ti-6Al-4V alloys. This finding correlated well with the aforementioned morphological observations.

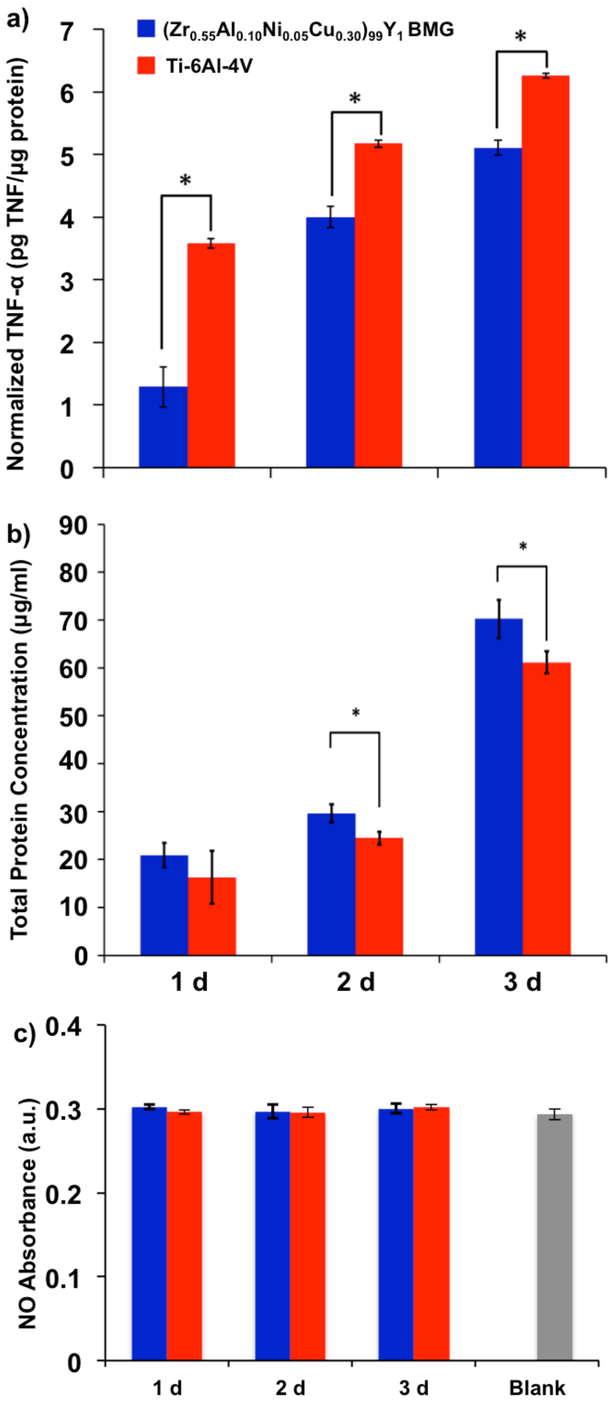

Figure 13 Production of mediators from RAW 264.7 macrophages after 1 - 3 d growth on $(Zr_{0.55}Al_{0.10}Ni_{0.05}Cu_{0.30})_{99}Y_1$ BMG and Ti-6Al-4V alloy: a) secretion profiles of normalized pro-inflammatory TNF-α; b) the amount of total intracellular proteins for normalization; and c) nitric oxide (NO) secretion profiles (Mean ± STDEV, * denotes statistically significant differences at $p < 0.05$).

Macrophage activation and cytokine secretion were established to be associated with different signaling pathways [188, 189]. A commonly acknowledged mechanism for TNF-α expression by macrophages when exposed to Ti-based alloys involved the activation of nuclear factor-kappa B (NF-κB) [190, 191]. Other transcription factors may also contribute to the expression of TNF-α, such as activated protein-1 (AP-1), cAMP-response element binding protein (CREB), etc. [192, 193]. It was postulated that the difference in TNF-α secretion by macrophages on the Zr-based BMG and Ti-6Al-4V alloy might be rooted from the regulation of these signaling pathways. Further studies are required to pinpoint the underlying mechanism for the lower pro-inflammatory cytokine production on the Zr-based BMG via the inhibition of different mediators of inflammatory signaling.

In addition to the TNF-α secretion, the production of nitric oxide (NO) by RAW 264.7 macrophages was also evaluated (Figure 13c). NO was identified to be a pro-inflammatory signal transduction molecule synthesized in cytotoxic activated macrophages, which was a key intracellular messenger for macrophage responses [194]. In the present study, it was found that no significant amount of NO was produced by the macrophages on any of the substrates without external stimulation. The absorbance read from the supernatant of each culture at each time point was found to be equivalent to the blank sample (blank culture medium). Further examinations on the production of NO, TNF-α, and other relevant cytokines are suggested for future studies.

4.2 Macrophage Responses on a Zr-Al-Fe-Cu BMG

To advance the understandings obtained in the Section 4.1, macrophage responses on a Zr-based BMG were further investigated with or without the external stimulation of lipopolysaccharide (LPS, 100 ng/ml). LPS is a major outer membrane component of Gram-negative bacteria, which is suggested to simulate the *in vivo* environmental stimuli during inflammation (i.e., bacterial infection) and induce the generation of pro-inflammatory cytokines [195-197]. Study in this subtask can help to combine the stimulating effects of the substrate materials from the environmental stimuli, which better simulates the *in vivo* conditions.

A newly-developed $Zr_{62.5}Al_{10}Fe_5Cu_{22.5}$ BMG [129] was selected as the substrate material for macrophage interaction, owing to the absence of potentially toxic elements (i.e., Ni, Be, etc.) that were used to facilitate BMG formation. This Ni-free Zr-based BMG will be discussed more extensively in Chapter 6 for its application as a candidate vascular stent material, in regards to its materials advantages and application-specific biocompatibility. In this section, the focus was set to evaluate the potential inflammation that could transpire before the interactions between the Zr-based BMG and vascular cells. In particular, cell proliferation, morphology, and cytokine secretion of the RAW264.7 macrophages cultured on the Zr-based BMG were qualitatively and quantitatively assessed. The 316L stainless steel was employed as the reference material, due to the longest history and dominant market share of stainless steels for stent applications [36]. For denotation purposes, the $Zr_{62.5}Al_{10}Fe_5Cu_{22.5}$ BMG and 316L stainless steel were abbreviated as ZrAlFeCu BMG and 316L SS.

4.2.1 Metabolic Activities of Macrophages and Cell Morphology

WST-1 assay was employed to evaluate the metabolic activities of the RAW264.7 macrophages at day 3 on the ZrAlFeCu BMG and 316L SS, as shown in Figure 14. The working mechanism of WST-1 assay relies on the reduction of WST-1 to formazan by cellular dehydrogenases. Therefore, results from this assay essentially quantify the overall metabolic activities of cells, which may also be used as implications for cell number or density. In Figure 14, it was demonstrated that both substrates were found to support certain levels of cell activities. In the culture with no external stimulation, higher macrophage metabolic activities were identified on the ZrAlFeCu BMG than on the 316L SS after 3-day of growth. The effect of LPS stimulation on the cell metabolic activities was also demonstrated in Figure 14. The LPS treatment did not introduce significant effects to the macrophage metabolism on the ZrAlFeCu BMG; whereas cell metabolic activities were reduced for those cultured on the 316L SS at day 3. The more active cell metabolism on the ZrAlFeCu BMG maybe related to the surface properties of the ZrAlFeCu BMG that encouraged cell adhesion, thus increased cell number, in general. The materials properties and adhesion of other mammalian cells of the ZrAlFeCu BMG in comparison with 316L SS will be discussed in greater details in Chapter 6. The higher number of adherent macrophages on the ZrAlFeCu BMG is not necessarily an adverse indication on its biocompatibility. It is the physiology of the macrophages that are essential in determining the characteristics of activation and the path of inflammation [197].

The SEM images in Figure 15 provided direct observations on cell numbers/densities after 3-day of growth on the substrates. In the LPS-free cultures, the

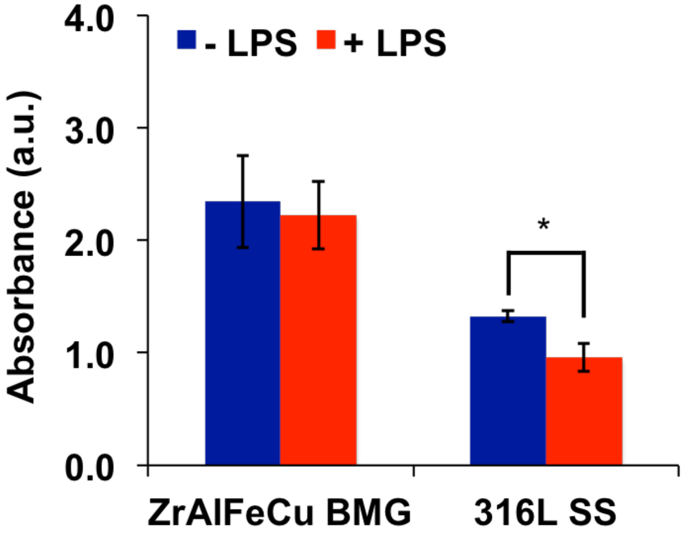

Figure 14 WST-1 assay results for the cell metabolic activities of RAW 264.7cells after 3 d growth on ZrAlFeCu BMG and 316L SS with or without LPS stimulation (Mean ± STDEV, * denotes statistically significant differences at $p < 0.05$).

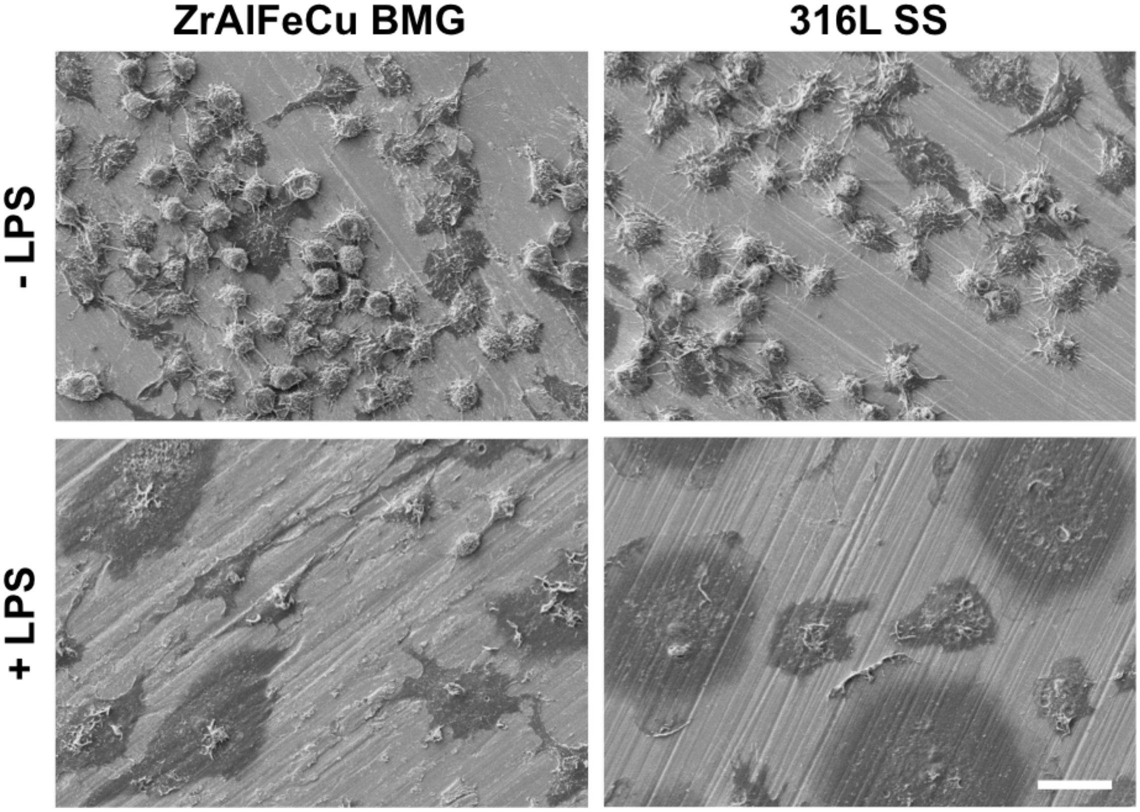

Figure 15 SEM images showing the morphological activations of RAW 264.7 macrophages on ZrAlFeCu BMG and 316L SS substrates after 3 d of growth with or without LPS stimulation (scale bar: 20 μm).

number of cells was qualitatively higher on the ZrAlFeCu BMG than on 316 L SS, which conformed with their high metabolic activities shown in Figure 14. With LPS treatment, the cell population densities were noticeably decreased on both substrates. Combining this observation with WST-1 results, it can be deduced that the metabolic activities of individual macrophages could have been boosted at the event of LPS stimulation.

Indications of morphological activations of the RAW264.7 macrophages after 3 day of growth were also delivered by the SEM observations (Figure 15). Without the stimulation of LPS, the macrophages exhibited small and round-shaped morphology on both ZrAlFeCu BMG and 316L SS substrates, demonstrating the low levels of stimulation of both materials to macrophages. A small portion of the cells was observed with larger spread areas, which indicated the activations for some of these cells. Therefore, the ZrAlFeCu BMG and 316L SS were found to be more stimulatory to the RAW264.7 macrophages, in comparison with the $(Zr_{0.55}Al_{0.10}Ni_{0.05}Cu_{0.30})_{99}Y_1$ BMG and Ti-6Al-4V alloy studied in the previous section. LPS treatment was found to impose a paramount stimulating effect on the macrophage activation, as evidenced by the significant increase in the cell spread area. Cells treated with LPS after 3-day culture became largely extended and flat on both materials, which are the typical morphological signs of macrophage activation [180]. The elevated activation may have contributed to the higher metabolic activities of the macrophages. Qualitatively, a small size of population of macrophages remained round and small on ZrAlFeCu BMG with LPS. In contrast, all of the cells on the 316L SS turned to be flat and extended. This suggested that the macrophages cultured on the ZrAlFeCu BMG may be less prone to environmental stimulation than those on the 316L SS.

4.2.2 Pro-inflammatory Cytokine Release

To provide quantitative evidences on the macrophage activations on ZrAlFeCu BMG and 316L SS, analyses on a biomolecular level to measure the secretion of the pro-inflammatory TNF-α were performed. The concentrations of TNF-α released into the culture media by the RAW264.7 macrophages were plotted in Figure 16a. The TNF- α concentration was normalized with the measured concentration of total intracellular protein to quantify the number of adherent cells (Figure 16b). The measurements on the amounts of total protein demonstrated similar results to those obtained from the WST-1 assay in Figure 14.

For the group of macrophage cultures without the stimulation of LPS, the secretions of pro-inflammatory TNF-α cytokine from cells on both materials were found to be maintained at relatively lower levels, although slightly higher than those found in the previous subtask for the $(Zr_{0.55}Al_{0.10}Ni_{0.05}Cu_{0.30})_{99}Y_1$ BMG and Ti-6Al-4V alloy. When comparing ZrAlFeCu BMG with the control material 316L SS, a marginally lower amount of TNF-α was detected for cells on ZrAlFeCu BMG. LPS treatment has dramatically elevated the TNF-α production. A more than 2-fold increase and a nearly 3-fold increase in TNF-α concentration were detected for ZrAlFeCu BMG and 316L SS, respectively, as the result of LPS stimulation. Similar to the morphological observation, the LPS stimulated activation of macrophages cultured on ZrAlFeCu BMG appeared to

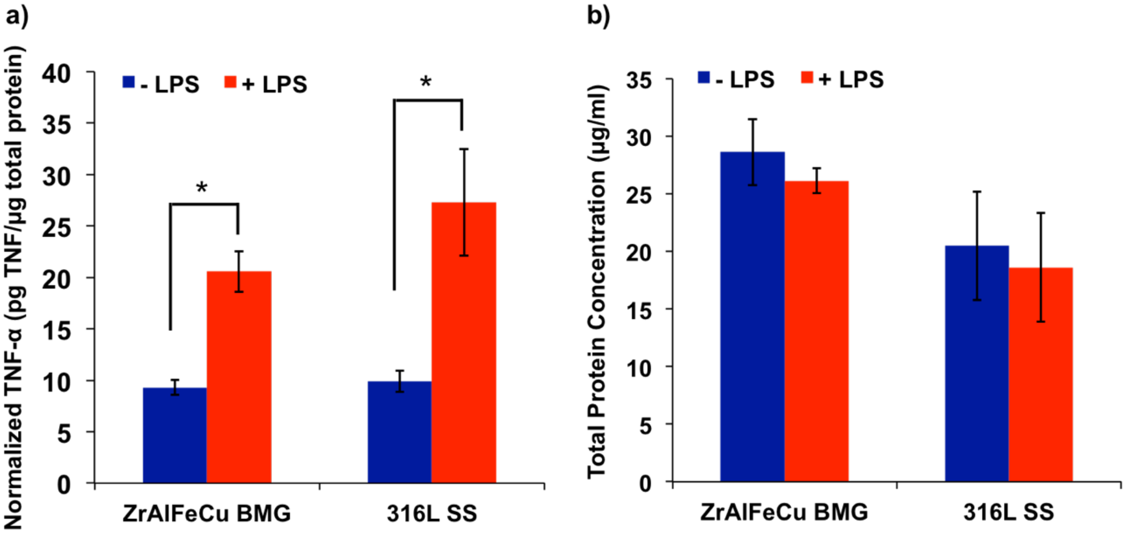

Figure 16 Production of pro-inflammatory TNF-α from RAW 264.7 macrophages after 3 d growth with or without LPS stimulation on ZrAlFeCu BMG and 316L SS substrates: a) secretion profiles of normalized pro-inflammatory TNF-α; b) the amount of total intracellular proteins for normalization (Mean ± STDEV, * denotes statistically significant differences at $p < 0.05$).

be less prominent than that on 316L SS, as substantiated by the lower level of cytokine secretion in Figure 15a. This lower sensitivity of macrophages to external stimulation may be related to the higher cell population and possibly other material or biological origins, necessitating future research to validate the postulations.

4.3 Macrophage Responses on Zr-Al-Co-Ag Alloys

In the first two sections of this chapter, the macrophage responses on Zr-Al-Ni-Cu-Y and Zr-Al-Fe-Cu BMGs were studied in comparison with commercial biomedical alloys. In addition, the effect of LPS stimulation was explored for macrophages on the Zr-Al-Fe-Cu BMG. Research in this section was expanded to examine the macrophage responses on a Zr-Al-Co-Ag BMG with or without the stimulation of LPS. Moreover, it was attempted in this study to initially understand the effects of microstructure by distinguishing the macrophage activities on the Zr-Al-Co-Ag alloys with amorphous and crystalline microstructures.

The $Zr_{53}Al_{16}(Co_{0.75}Ag_{0.25})_{31}$ BMG was selected in the present study based on its high glass-forming ability and well-documented materials properties. The biocompatibility of this Zr-based BMG was revealed in a previous joint research of our group, using bone-forming MC3T3-E1 cells to evaluate its potential as a bone-implant material [118]. In order to introduce crystallization, heat treatment to the as-cast Zr-Al-Co-Ag BMG was utilized to obtain its crystalline counterpart. The heat treatment induced changes in microstructure and materials properties will be discussed in detail in Chapter 7. The research in this section was directed towards the biocompatibility with the emphasis on material/macrophage interactions. For denotation purposes, the

$Zr_{53}Al_{16}(Co_{0.75}Ag_{0.25})_{31}$ BMG and the crystallized $Zr_{53}Al_{16}(Co_{0.75}Ag_{0.25})_{31}$ BMG after heat treatment were abbreviated as ZrAg-BMG and HT-ZrAg, respectively. Ti-6Al-4V alloy was employed as the reference material.

4.3.1 Metabolic Activities of Macrophages and Cell Morphology

The metabolic activities of macrophage on ZrAg-BMG, HT-ZrAg, and Ti-6Al-4V were assessed after 3-day incubation in cultures plus or minus LPS supplementation, depicted in the histogram in Figure 17 using WST-1 assay. In the cultures without LPS supplementation, it was shown that the overall cell metabolic activities on the ZrAg-BMG were comparable to those on the reference Ti-6Al-4V alloy. This was in agreement with the comparable bone-forming cell proliferation behaviors on ZrAg-BMG and Ti-6Al-4V reported previously [118]. In contrast, considerably higher metabolic activities of the adherent macrophages were found on the HT-ZrAg BMGs. In terms of the LPS effect, no statistically significant variations were introduced to the net macrophage metabolism by the presence of this external stimulus, which was similar to the finding for ZrAlFeCu BMG in Section 4.2.

The numbers of adherent macrophages were qualitatively assessed through SEM observations. In the LPS-free environment, the number of macrophages was found slightly higher on HT-ZrAg than on ZrAg-BMG. However, the difference was not as significant as that from the WST-1 assay, which indicated higher metabolism for individual cells on the HT-ZrAg sample. In general, the lager cell numbers and higher metabolic activities on the HT-ZrAg BMG could be related to the changes in surface properties (i.e., surface hydrophobicity, free energy, and chemistry) owing to the

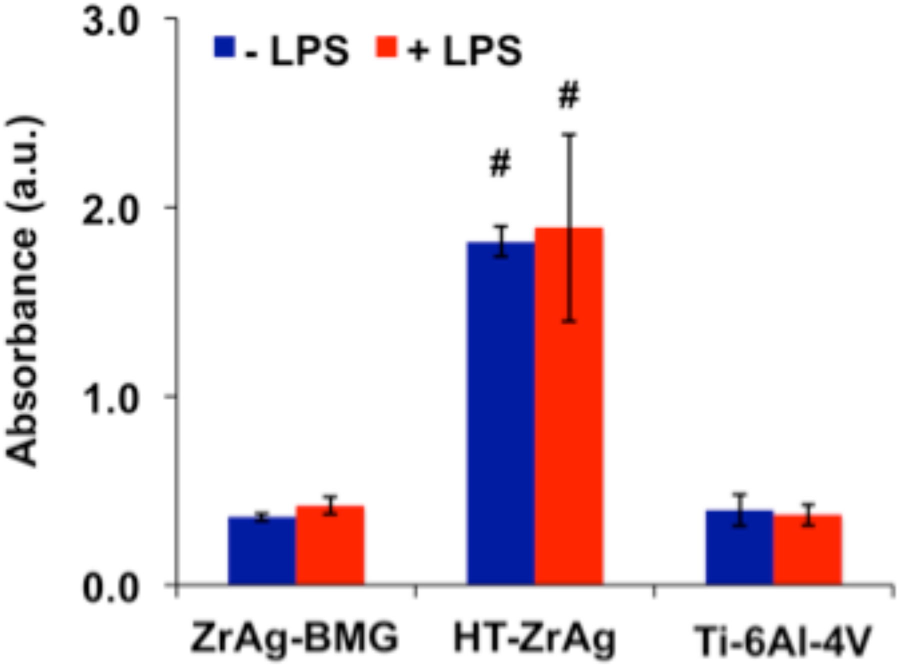

Figure 17 WST-1 assay results for metabolic activities of RAW264.7 macrophages after 3 d growth on ZrAg-BMG, HT-ZrAg, and Ti-6Al-4V substrates with or without LPS stimulation (Mean ± STDEV, # indicates statistically significant difference in comparison with the result for ZrAg-BMG under the same treatment condition at $p < 0.05$).

microstructural change. The enhanced hydrophobicity of the HT-ZrAg surface could be a contributing factor to promote protein adsorption, and hence, encourage cell adhesion. Characterizations on the surface properties of ZrAg-BMG and HT-ZrAg will be presented in Chapter 7. The treatment of LPS was found to decrease cell density and raise metabolism of macrophages on all substrates, as observed in Section 4.2.1.

Cell morphology after WST-1 assay was visualized using SEM images (Figure 18) to illustrate implications of macrophage activation. The geometry of cells was recognized to be spheroidal and small, which served as a general indication for the low levels of activations on all three substrates in the LPS-free cultures. In comparison with the macrophage morphology on Ti-6Al-4V alloy, the cells were spreading to relatively larger sizes on ZrAg-BMG and HT-ZrAg substrates with the absence of LPS stimulation. The tendency of the macrophages to extend their cell bodies on the ZrAg-BMG and HT-ZrAg implied higher levels of stimulations of the substrates. With the environmental stimulation of LPS, macrophages on all substrates were flattened and enlarged, in consistent with the macrophage behavior observed in Section 4.2. It was once again evident that the RAW264.7 macrophages were responsive to the LPS treatment, regardless of the testing metallic substrates in this study. Cells smaller in spread areas can be observed on HT-ZrAg BMGs, whereas these small-sized cells were absent on ZrAg-BMG and Ti-6Al-4V alloy.

4.3.2 Pro-inflammatory Cytokine Release

The evaluation on TNF-α release was used as a quantification approach to evaluate the synergistic stimulation of the substrate and the environmental stimulus to

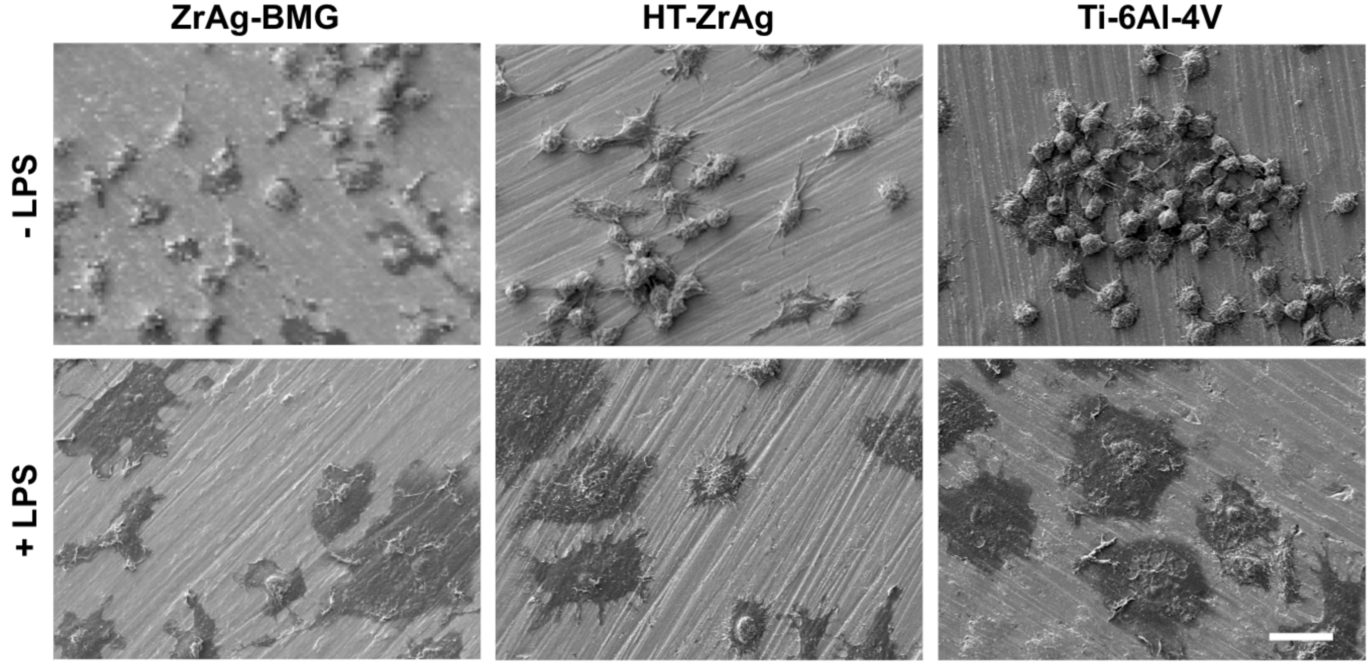

Figure 18 SEM images showing the morphological activations of RAW 264.7 macrophages on ZrAg-BMG, HT-ZrAg, and Ti-6Al-4V substrates after 3 d of growth with or without LPS stimulation (scale bar: 20 μm).

macrophages. The TNF-α concentrations are plotted in Figure 19a for each material group, using the amounts of total intracellular protein (Figure 19b) as the normalization scale to account for the differences in cell numbers. Although the differences amongst TNF-α secretions in the LPS-free cultures were not statistically significant for the three different material groups, the overall trend on the average TNF-α concentration was consistent with the SEM observation. The Ti-6Al-4V alloy appeared to be least stimulatory with the lowest production of TNF-α, followed by HT-Zr and ZrAg-BMG. When the external stimulation of LPS stepped in, significant increases in the contents of TNF-α were detected for all samples. Specifically, the LPS treatment upregulated the production of TNF-α by approximately 3-fold for ZrAg-BMG, 2-fold for HT-ZrAg, and 5.5-fold for Ti-6Al-4V. The TNF-α productions were comparable between the results for ZrAg-BMG and Ti-6Al-4V, indicating that the substrate effect was overwhelmed by the environmental stimulation. Nevertheless, TNF-α secretion under the stimulation of LPS from the macrophages grown on the HT-ZrAg sample was markedly lower than those on ZrAg-BMG and Ti-6Al-4V.

By combining the results in Figures 17 and 19b, it was concluded that higher number of cells and metabolism were associated with the macrophages on the HT-ZrAg sample than on ZrAg-BMG and Ti-6Al-4V. It was speculated that the higher cell population density on the HT-ZrAg surfaces can lead to the quorum sensing of these macrophages leading to the down regulation of cytokine release, which was proposed in a previous investigation on the macrophage responses to different Ti surfaces with LPS stimulation [185]. Moreover, a recent study unveiled that a preferred local proliferation,

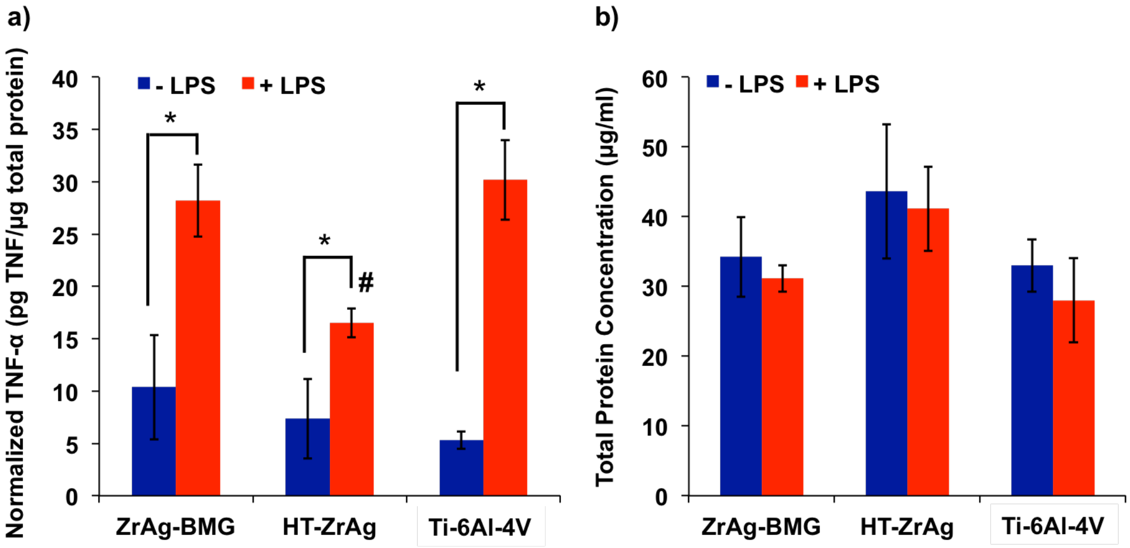

Figure 19 Production of pro-inflammatory TNF-α from RAW 264.7 macrophages after 3 d growth with or without LPS stimulation on ZrAg-BMG, HT-ZrAg, and Ti-6Al-4V substrates: a) secretion profiles of normalized pro-inflammatory TNF-α; b) the amount of total intracellular proteins for normalization (Mean ± STDEV, * denotes statistically significant differences at $p < 0.05$; # indicates statistically significant difference in comparison with the result for ZrAg-BMG under the same treatment condition at $p < 0.05$).

instead of recruitment, of macrophages was shown to be specific for the anti-inflammatory T helper 2 (TH2)-type inflammation [198]. Therefore, the promoted proliferation of macrophages on the HT-ZrAg surface possibly suggested that the subsequent inflammation path was altered due to the changes in microstructure and subsequent modifications in materials properties of the Zr-Al-Co-Ag BMG. Further investigations on the production of IL-4 and other mediators will be able to confirm or reject this hypothesis. In-depth research is also necessary to address additional questions that can be raised regarding the macrophage responses to the Zr-based BMGs and their crystalline counterparts in future studies. Critical issues include but not limited to: the macrophage responses to different degrees of crystallization; microstructure effect with different alloy compositions; the interconnection amongst microstructure, surface properties, and macrophage activities; the significance of substrate stimulation in comparison with environmental stimulations in the context of actual inflammation; etc. Lastly, it is noted that altering the microstructure of the glass-forming alloy can be deleterious to materials properties. A balance between materials properties and biocompatibility needs to be taken into consideration during the design of biomedical glass-forming materials.

4.4 Conclusions and Future Work

Research in this task presented the *in vitro* investigations on macrophage responses to Zr-based BMGs. In accordance with previous results, the Zr-based BMGs were found to support regular macrophage growth, indicating good cytocompatibility. Low levels of stimulations to RAW264.7 murine derived macrophages were found for the Zr-Al-Ni-Cu-Y, Zr-Al-Fe-Cu, and Zr-Al-Co-Ag BMGs. In particular, a lower degree of macrophage activation was suggested on the Zr-Al-Ni-Cu-Y BMG in comparison to the Ti-6Al-4V alloy, which was evidenced by both microscopic observation of cell morphology and biomolecular analysis. Macrophages cultured on both Zr-based BMGs and crystalline alloys were responsive to LPS stimulation, on top of the substrate stimulation. It was suggested that the cells on the Zr-Al-Fe-Cu BMG were less sensitive to LPS treatment than those on 316L stainless steel. In addition, the microstructure was revealed to influence macrophage activities in the Zr-Al-Co-Ag glass-forming alloy system, with the crystalline microstructure showing lesser stimulation.

To the author's best knowledge, studies in this chapter represented the first systematic investigation on the macrophage responses to BMGs within the context of inflammation, although an early study by Horton and coworkers has briefly described the behavior of macrophages and fibroblasts [55]. The results delivered in this study were complementary to those few animal studies in the literature [20, 61]. Normal foreign body response to Zr-based BMGs was reported by Schroers et al. in a mouse model [20] and by Liu et al. in a rabbit model [61]. It was noteworthy that the implantation of Pt-based BMG with the same shape resulted in a thinner collagenous capsule formation *in vivo*, indicating an even lower degree of foreign body response than that triggered by Zr-based BMG [20]. Thus, the inflammation induced by BMG implantation can be further reduced by proper selection of alloying elements.

The future research is recommended towards more comprehensive investigations on the *in vitro* activation of macrophages to Zr-based BMGs by studying the expression of multiple cytokines (i.e., TNF-β, IL-6, IL-10, IL-4, etc.) and NO, with or without the interference of external stimulations. It is also worth deepening the understandings on the effects of microstructure (i.e., relaxation of amorphous structure, partial crystallization, etc.) and chemical compositions of biomedically oriented Zr-based BMGs on macrophage-BMG interactions. Moreover, the exact molecular mechanism on the modulation of macrophage behaviors on Zr-based BMGs calls for further studies.

CHAPTER V
ION IMPLANTATION TO A Zr-Al-Ni-Cu-Y BMG FOR BONE IMPLANT APPLICATIONS

Research in this task was conducted to further modify $(Zr_{0.55}Al_{0.10}Ni_{0.05}Cu_{0.30})_{99}Y_1$ BMG, in order to enhance the materials properties and material-cell interactions for bone implant applications. As discussed in Section 2.4, surface engineering techniques were recognized as effective approaches to modulate the surface properties of Zr-based BMG, which conserve the bulk material composition and properties. The surface modification techniques that have been practiced in BMGs included physical [44, 111] and chemical [43, 68] treatments, surface patterning [64], laser treatment [199, 200], coating [201], and ion implantation [162, 202].

Ion implantation stands out from the variety of surface treatment methods as a promising technique, the competency of which to enhance the materials properties of Zr-based BMGs have been demonstrated in recent studies [162, 202-204]. Ion implantation alters the original surface of the substrate material, and the modified layer is intimately integrated into the substrate, providing a homogeneous and controllable doping of ions of interest [20, 205]. In addition, the flexibility of ion implantation technique allows for conveniently tuning surface characteristics. Such versatility has propelled ion implantation as the choice of surface modification in the present studies to tune the surface of the $(Zr_{0.55}Al_{0.10}Ni_{0.05}Cu_{0.30})_{99}Y_1$ BMG, the materials properties and biocompatibility of which have been readily discussed previously.

By adjusting impinging ion species and implantation parameters (i.e., ion-beam energy, fluence, and flux), both chemical and mechanical properties of the substrate surfaces can be altered on demand. In this study, the surface modifications to Zr-based BMG via ion implantation were studied aiming at two specific goals, including: 1) imparting bioactivity to the bioinert Zr-based BMG surface; and 2) generating surfaces with different mechanical properties to study cell rigidity sensing and regulate cell behaviors on the Zr-based BMG. Bone-forming MC3T3-E1 cells were employed throughout this task for cell culture studies, pertinent to the bone implant applications of the Zr-based BMG.

5.1 Ion Implantation of Zr-based BMGs towards Bioactivity

The surfaces of Zr-based BMGs, although biocompatible, are typically bioinert, which implies a lack of direct bonding between the tissue and the implant made from such materials. For applications such as orthopedic implants, it is highly beneficial to impart bioactivity into BMGs to facilitate biological bonding with bone tissues, so that the long-term performance and success of the implants can be warranted. Surface engineering techniques have been widely utilized to modulate surfaces of traditional biomedical alloys to endow bioactivity [143, 158, 205].

Bearing the similar concept, ion implantation of a Zr-Al-Cu-Ag BMG with Ca- and Ar-ions was investigated in a previous study of our group [70]. The choice of Ca-ions was inspired by the mineral phase of bone tissue, where the principal constituents are calcium, phosphate, carbonate, and hydroxyl ions [206]. Furthermore, the effectiveness of Ca-ion implantation has been demonstrated on traditional Ti alloys, which led to surface enrichment of Ca and consequently improved cell/material interaction on Ti surfaces, presumably due to the accelerated and increased precipitation of calcium phosphate that enhanced the bioactivity of Ti surface [143, 205]. As a reference group, Ar-ion implantation was performed. The use of Ar lied in the inertness and similarity in the atomic mass of Ar to that of Ca, which allowed us to differentiate the physical damage effect from chemically induced changes [70]. Additionally, Ar ion implantation has been reported to improve surface properties of BMGs and other metallic material, particularly surface hardness and corrosion resistance, which are advantageous for biomedical applications [205, 207].

In this subtask, the use of ion implantation for Zr-based BMG surface modification was extended to the $(Zr_{0.55}Al_{0.10}Ni_{0.05}Cu_{0.30})_{99}Y_1$ BMG substrate. The choice of this specific Zr-based BMG was based on its higher corrosion resistance than that of the Zr-Al-Cu-Ag BMG and the general biocompatibility, which are favorable for long-term implantation applications [50, 68]. The amorphous microstructure of Zr-based BMGs was considered key to their unique properties. Therefore, low acceleration energies (10 and 50 keV) of ions were employed in the current study in order to maintain the amorphous structure on the surface. The objective of this subtask was to understand the effects of low energy ion implantation with Ca- and Ar-ions on the Zr-based BMG. Material properties and responses of bone-forming cells on the ion-irradiated Zr-based BMG substrates were characterized, and the effects of ion implantation parameters including the type of ions and the acceleration energy were discussed.

5.1.1 SRIM simulations of Ca- or Ar-ion-implanted Zr-Al-Ni-Cu-Y BMG

Prior to the experiments, simulations on the ion implantation processes were performed in order to provide initial understanding and guidance for the experimental practices. The SRIM simulation results of the ion irradiation induced disorder and implanted ion concentration were plotted for Ar- and Ca-ion implantations in Figures 20a and b, respectively. The denotations of the samples were presented in Table 2. The calculated profiles for both types of ion implantations exhibited distorted bell shape, revealing the depths of the modified surface layer and the maxima of disorders and ion concentrations as a result of the ion bombardments. The thicknesses of the influenced region, which was characterized by the stopping ranges of the ions, were calculated to be around 25 nm and 80 nm for 10 keV and 50 keV ion-implanted samples, respectively, regardless of the type of ions used. Slight differences were noted in the distributions of disorders and implanted ions after Ar- and Ca-ion implantation. The resultant peak values of disorders created by 10 keV and 50 keV Ar-ion collisions were 17 dpa and 21 dpa at 5 nm and 17 nm. Peak concentrations of Ar were 11.0 at.% and 3.3 at.% located at 7.5 nm and 30 nm for 10 keV and 50 keV implantations, respectively. Similar, although slightly higher, damages were produced by Ca-ion irradiations, with the disorder maxima identified to be about 18 dpa for 10 keV ions and 23 dpa for 50 keV ions. In terms of implanted ion concentration in the matrix, the highest concentrations of Ca were 11.2 at.% and 3.5 at.% at about 7.5 nm and 27 nm from the surface for the 10 keV and 50 keV Ca-ion-implanted samples. For both types of ion irradiation, the distributions of implanted ions were much more dispersive for the 50 keV, as compared with the 10 keV implanted samples. With the increase of acceleration energy, ions were able to penetrate deeper and introduce more collision events to the substrate. Since the fluence of ions was fixed, higher acceleration energy created a broader distribution of the implanted ions with a consequent reduction in the corresponding peak concentration.

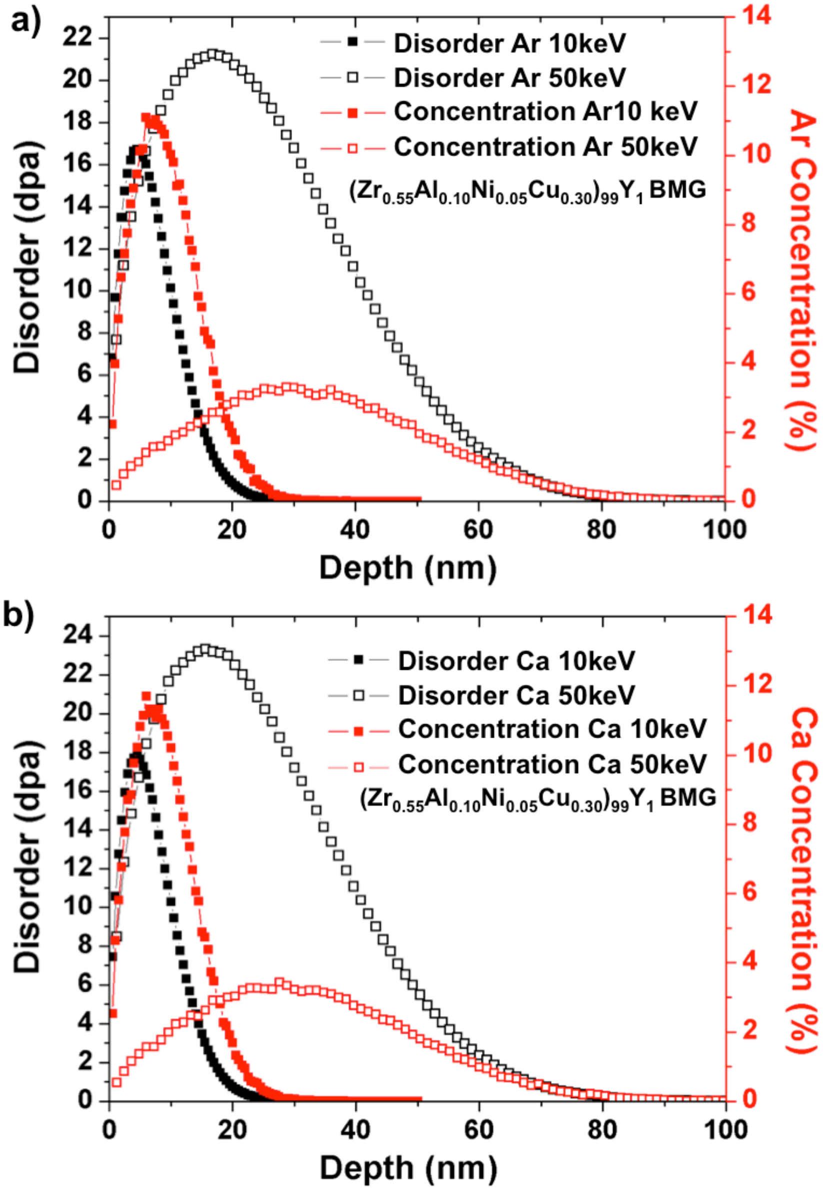

Figure 20 SRIM simulations for the distributions of disorders and ion concentrations after a) Ar-ion and b) Ca-ion implantation at 10 keV and 50 keV acceleration energies.

According to the simulation results, the maximum displacements per atom introduced by ion implantation were calculated to be smaller than 25 dpa. Such a low dpa was unlikely to introduce crystallization, which has been experimentally validated by GIXRD, using 50 keV Ar-ion-implanted Zr-based BMG as an example (Figure 21). The absence of crystalline peaks and the presence of the characteristic diffusive peak confirmed that the amorphous structure was maintained after ion implantations. This was in agreement with prior studies on Ar- or N-ion implantation to Zr- and Ti-based BMGs where the amorphous structure was observed after implantation using XRD and TEM [203, 208]. Although the long range atomic ordering was not introduced after ion implantation, the short-range ordering on the BMG surface could be altered due to the ion collision cascades.

5.1.2 Atomic structures of Ca- and Ar-ion-implanted Zr-Al-Ni-Cu-Y BMG

To probe the atomic structure changes due to the low energy ion irradiation suggested by SRIM simulation, nondestructive XAS technique was employed, which required no further sample preparation and prevented potential artificial damage to the sample. The detections were limited within the implanted surface regions by collecting total electron yield signals. The complete XAS spectra of the as-cast and ion-irradiated Zr-based BMG substrates were presented in Figure 22 as a function of X-ray energy. A crystalline Zr metal foil was also included in the XAS study as the standard reference material. The overall general shapes of the absorption edges for all Zr-based BMG samples were distinctly different from the reference metal foil. A further comparison of the XAS spectra between the ion-implanted and non-treated Zr-based BMG revealed a clear change in terms of peak position and width, shown in the enlarged view in inset of

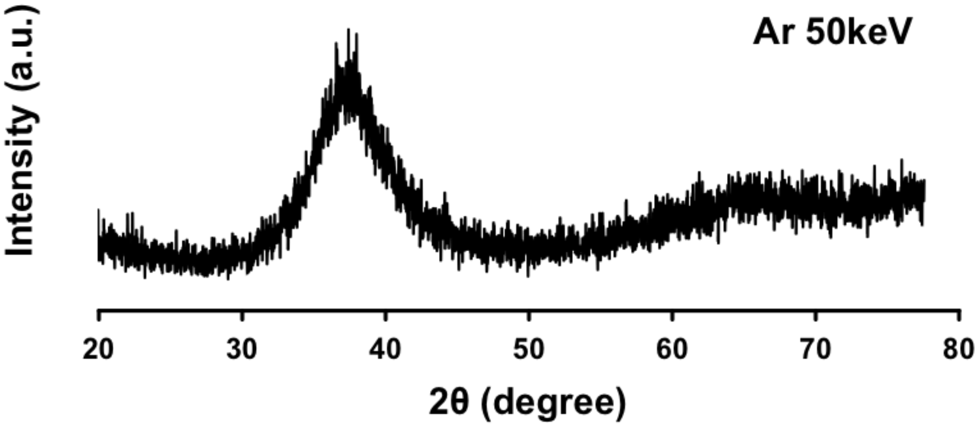

Figure 21 Grazing incidence X-ray diffraction pattern for the 50 keV Ar-ion-implanted $(Zr_{0.55}Al_{0.10}Ni_{0.05}Cu_{0.30})_{99}Y_1$ BMG

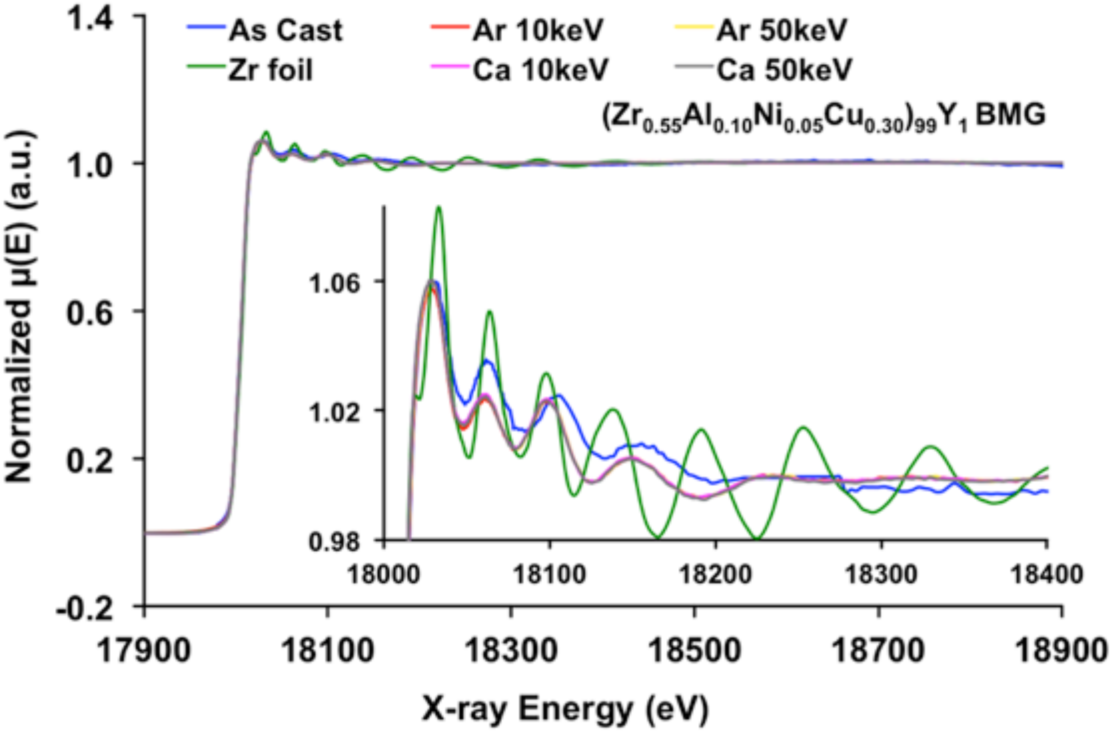

Figure 22 Normalized XAS spectra at Zr K-edge for $(Zr_{0.55}Al_{0.10}Ni_{0.05}Cu_{0.30})_{99}Y_1$ BMG before and after ion implantation and Zr foil. Inset shows the enlarged spectra at the Zr K-edge.

Figure 22. XAS results preliminarily revealed local changes in atomic structure after Ar- or Ca-ion implantation, which could cause structural relaxation or change in free volume as suggested in a previous report [70]. Nonetheless, the disparities in XAS spectra among the implanted BMGs were minute. Therefore, further detailed measurements and analyses to capture comprehensive information, such as radial distances and coordination numbers of the neighboring atoms, on the atomic structural changes induced by different implantation conditions are necessary in future studies.

5.1.3 Surface morphology and chemistry of Ca- or Ar-ion-implanted Zr-Al-Ni-Cu-Y BMG

Aside from the atomic structure modification, ion implantation to the Zr-based BMG may have introduced surface morphological and chemical modifications. The morphology before and after ion implantation was examined using AFM and SEM. Prior to any ion implantation process, the as-cast Zr-based BMG appeared mirror-like, typical of the polishing regime adopted in this study, as presented in Figure 23. The surfaces after ion implantation remained featureless as proved by the AFM images (Figure 23). Representative SEM secondary electron image collected for the surface of the Zr-based BMG after 50 keV Ca-ion implantation was presented in the inset of Figure 24a, confirming the featureless surface and no observable morphological changes. Moreover, EDX elemental analyses (Figure 24) of the average surface composition after ion implantation indicated that the surface composition was close to the alloy nominal composition. However, considering that the sampling depth of EDX was within a few microns [70], the compositional data obtained with this technique was inevitably

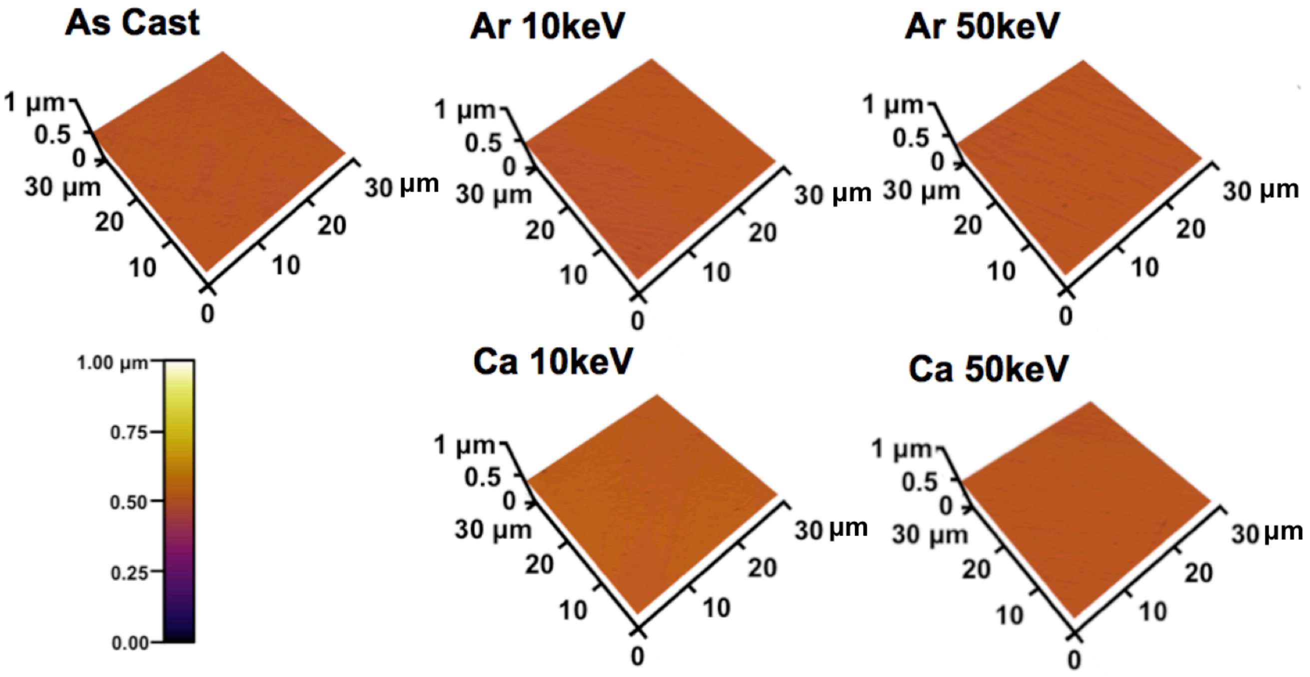

Figure 23 Representative AFM topography of the $(Zr_{0.55}Al_{0.10}Ni_{0.05}Cu_{0.30})_{99}Y_1$ BMG before and after ion irradiation under indicated conditions.

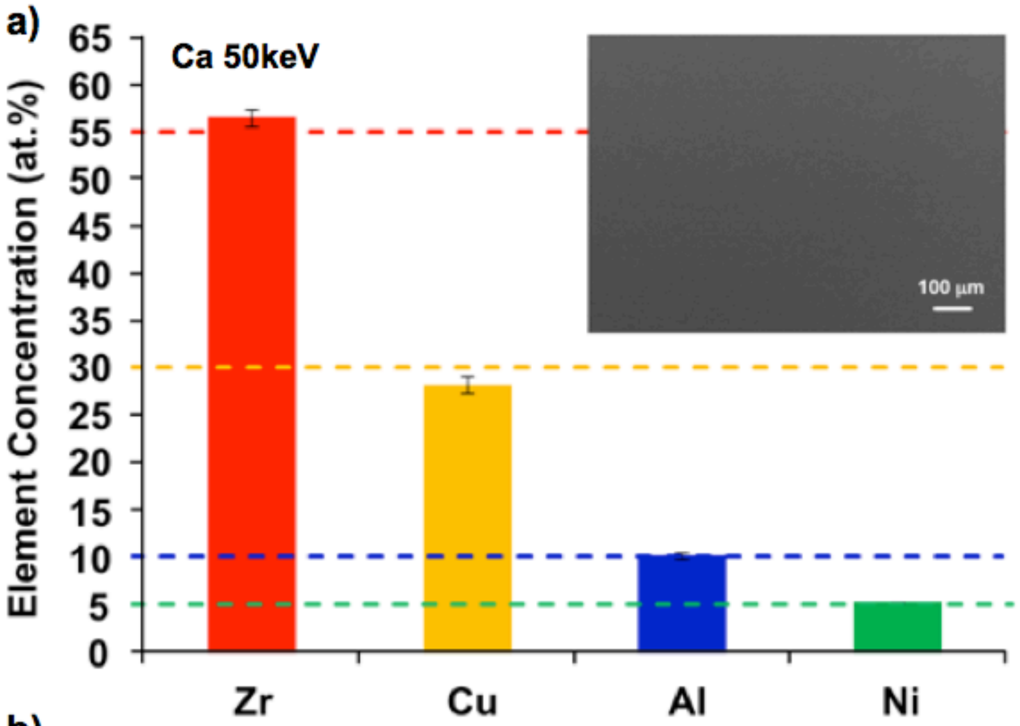

b)

Element	Nominal	As Cast	Ar 10keV	Ar 50keV	Ca 10keV	Ca 50keV
Zr	55	56.64± 0.74	57.17 ± 0.88	56.78 ± 0.48	56.48 ± 0.35	56.49 ± 0.89
Al	10	9.73 ± 0.46	9.41 ± 0.55	9.68 ± 0.76	9.68 ± 0.54	10.10 ± 0.34
Ni	5	4.98 ± 0.25	4.58 ± 0.54	4.83 ± 0.66	4.98 ± 0.10	5.17 ± 0.10
Cu	30	28.75 ± 0.62	28.84 ± 0.51	28.71 ± 0.57	28.86 ± 0.32	28.24 ± 0.87

Figure 24 EDX analyses on the surface compositions: a) bar graph for 50 keV Ca-ion implanted $(Zr_{0.55}Al_{0.10}Ni_{0.05}Cu_{0.30})_{99}Y_1$ BMGs (dashed lines indicate nominal alloy composition of the respective element; inset: SEM secondary electron image); b) summary of EDX elemental analyses of as-cast and ion-implanted substrates.

obscured by the non-treated region beneath the ion-implanted layer (less than 100 nm deep).

In order to focus solely on the ion-implanted region, XPS was employed to obtain a more surface sensitive chemical analysis. The sampling depth of XPS was related to the inelastic free mean path of the electrons, which ranges within a few nanometers [209]. XPS scans for the elements on the surface were recorded and the elemental quantifications were shown in Figure 25. Using the 50 keV Ca-ion-implanted Zr-based BMG sample as an example, the narrow scans in Figure 25a displayed the peaks for O1s, Zr3d, Al2s, Cu2p3, Y3d, Ni2p3, and Ca2p3. Quantifications of element concentrations for the as-cast and ion-implanted samples shown in the stacked bar graph (Figure 25b) manifested the dominance of O and Zr on the surface, which accounted for the major constituents of the surface oxide film. Oxygen was present in the forms of both metal oxide (marked as M_xO_y) and surface hydroxyl group (marked as OH). The largest amount of hydroxyl groups was found on the as-cast sample, and a significant decrease was observed after ion implantation. Similar to the as-cast surface characterized in a previous study from our group [68], the surface of ion-implanted Zr-Al-Ni-Cu-Y BMG was covered with a layer of passive film mainly composed of ZrO_2 together with small amounts of Al_2O_3 and Y_2O_3 (Figure 25). The concentration of Y_2O_3 was slightly increased, while Ni and Cu were mostly depleted on the surface after implantation (Figure 25b). After Ca-ion implantation, peaks for Ca could be explicitly distinguished in an energy range between 342 eV and 357 eV, which corresponded to the Ca2p3 peaks. The presence of Ca on the surfaces after Ca-ion irradiation was evidenced in the forms of

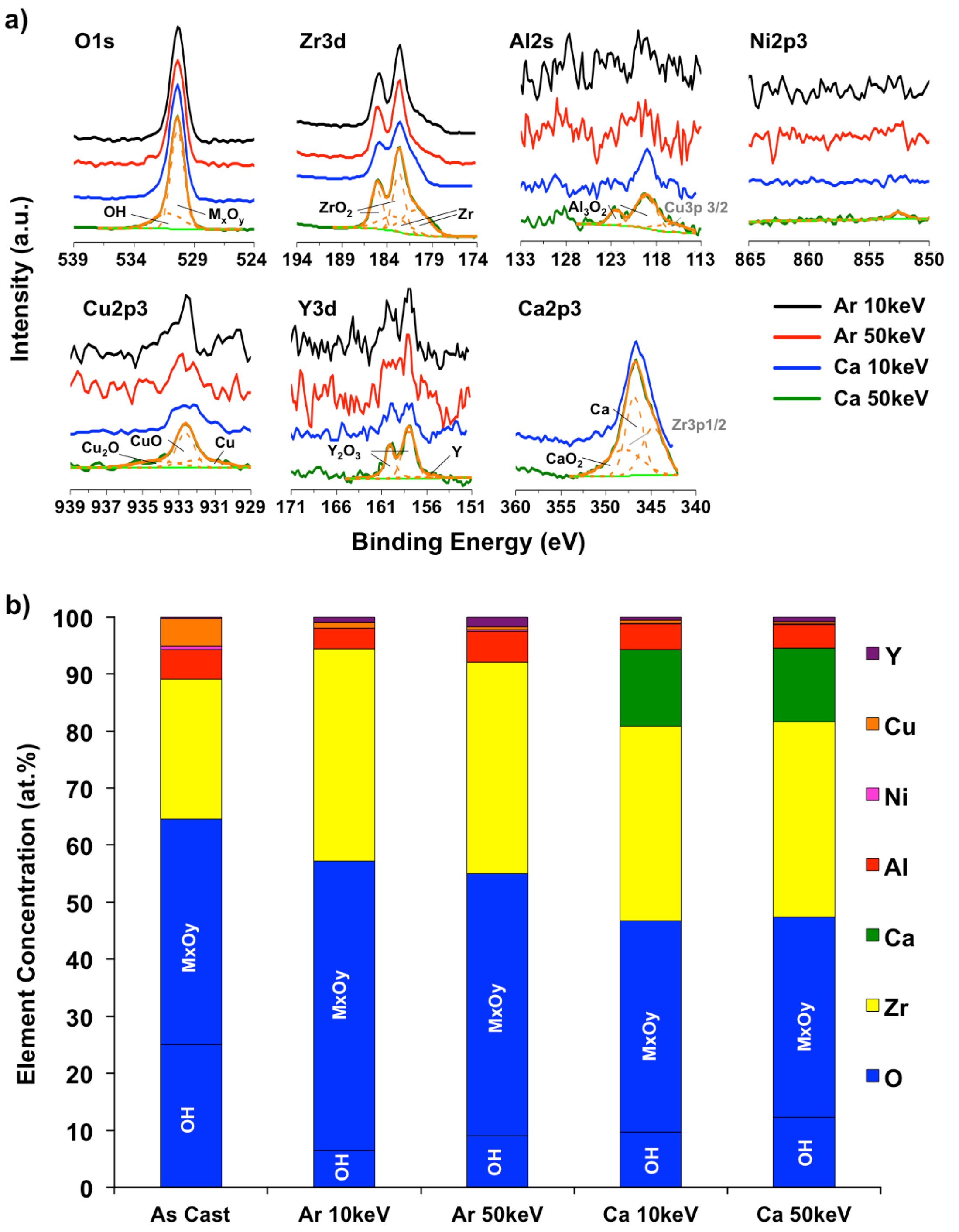

Figure 25 a) XPS narrow scans of O1s, Zr3d, Al2s, Cu2p, Y3d, and Ca2p3 for 50 keV Ca-ion implanted $(Zr_{0.55}Al_{0.10}Ni_{0.05}Cu_{0.30})_{99}Y_1$ BMGs; and b) quantifications of the element concentrations on the surface of the as cast and ion implanted Zr-based BMGs.

Ca and CaO, indicating that the bioactive element, Ca, has been successfully introduced to the bioinert Zr-based BMG surface through low energy Ca-ion implantation. The concentration of the Ca on the surface after 10 keV Ca-ion implantation (13.4 at.%) was slightly higher than that after 50 keV Ca-ion implantation (12.9 at.%).

Despite the inert nature of Ar ions, Ar-ion implantation modified the compositions of the surface layers on the Zr-based BMG by altering the fractions of the constituent components (i.e., metal oxides, and hydroxyl groups) of the ion-implanted surfaces, as compared with the as-cast surface (Figure 25b). Ca-ion implantation imparted more significant compositional alterations. According to the simulation, Ca ions were more concentrated on the surface after 10 keV implantation, in contrast to a relatively dispersive distribution of Ca over a broader region after 50 keV ion implantation. A similar trend to the simulation results was revealed by XPS analyses, showing a higher amount of Ca on 10 keV ion-implanted surface than on 50 keV implanted one, although the difference was not as significant as revealed by SRIM simulation. It is noted that SRIM simulations were performed with nominal alloy composition of the Zr-based BMG, whereas XPS measured the top surface covered by a layer of oxide film known as passive film [68] of the Zr-based BMG. The discrepancy between SRIM simulations and XPS measurements was mainly due to the fact that the surface composition usually diverges from the underlying compositions as the result of the formation of surface oxide film.

5.1.4 Surface nanohardness of Ca- or Ar-ion-implanted Zr-Al-Ni-Cu-Y BMG

The enhancement in surface hardness by ion implantation was observed in the present study. Surface nanohardness obtained from the indentation tests for each sample was summarized in Figure 26a. The nanohardness for the as-cast surface was around 6.45 GPa. After ion irradiation, the BMG surfaces were hardened, as shown by the increases in nanohardness. With an indentation depth larger than 250 nm, it was measured that 10 keV Ar ion implantation led to a 1.6% increase of surface nanohardness to 6.55 GPa, and 50 keV Ar ions gave rise to a 2.6% increase to 6.62 GPa in nanohardness. The surface nanohardness increased by 5.7% to 6.82 GPa after 10 keV Ca implantation and 7.3% to 6.92 GPa after 50 keV Ca-ion implantations, both in comparison with the as-cast sample.

When analyzing the nanohardness of ion-implanted samples, it was worth pointing out that the indentation depth was approximately 250 nm, as shown in Figure 26b, whereas the thickness of the modified layer was 25 or 80 nm according to the simulation results. Therefore, each measurement of hardness of the respective ion-implanted sample was a result of a composite structure composed of the ion-implanted layer and the substrate material. In general, the improvement in nanohardness after ion implantation may have been underestimated due to the relatively large indentation depth. However, the improvement in nanohardness was evident when comparing the Ar- and Ca-ion-implanted samples with the as-cast ones. Ion bombardment generated surface hardening found in this study was in accordance with those reported in previous research [70, 210]. The improvement in hardness could be attributed to the possible structural relaxation caused by irradiation, which was found to affect mechanical properties of BMGs [70, 211]. On the other hand, the surface hardening resulting from Ca-ion

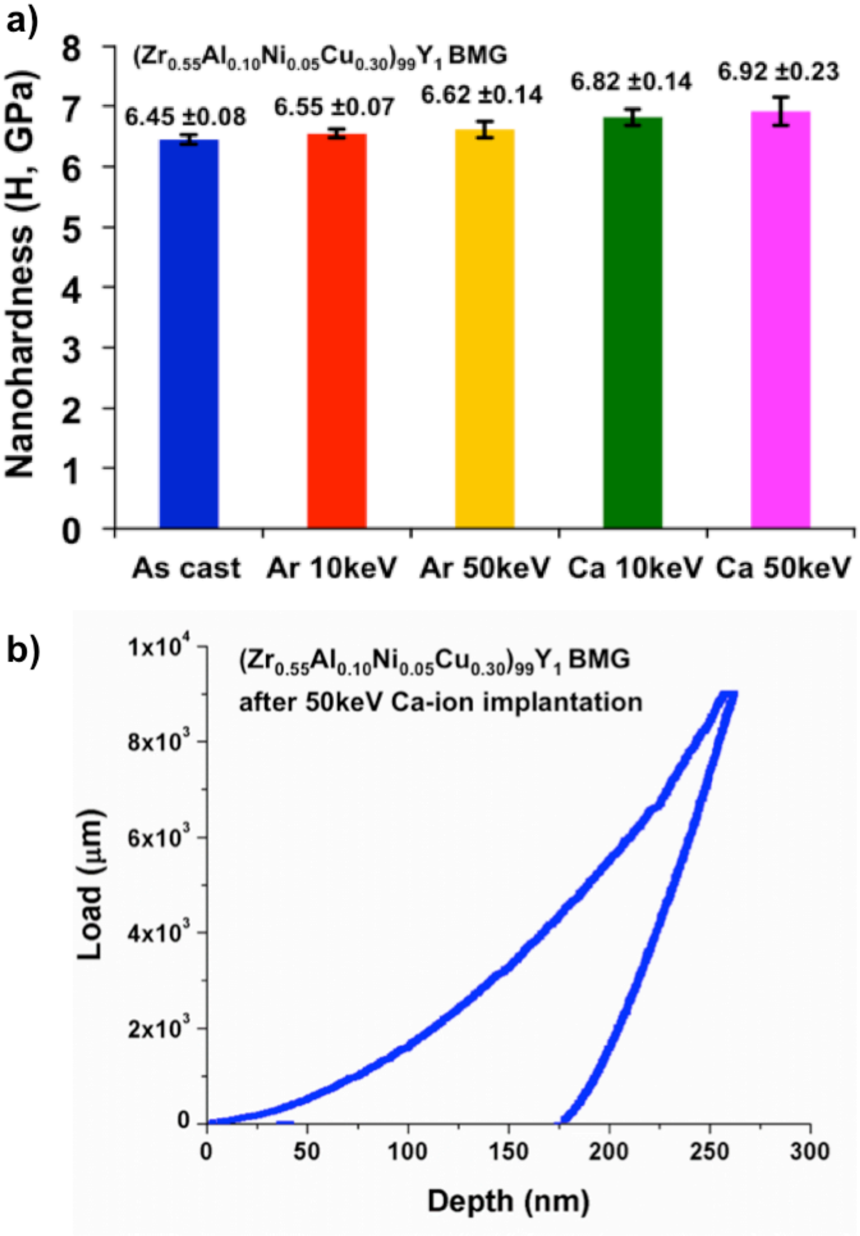

Figure 26 Nanoindentation of $(Zr_{0.55}Al_{0.10}Ni_{0.05}Cu_{0.30})_{99}Y_1$ BMG before and after 10 or 50 keV ion implantation: a) surface nanohardness; and b) representative load-depth curve of the sample after irradiation with Ca ions at 50 keV

implantation was found more considerable than from Ar-implantation at the same acceleration energy. The higher surface hardness resulting from Ca implantation could be attributed to substantial chemical change on the surface due to the formation of ceramic-like CaO on the surfaces and/or higher amount of metal oxides (i.e., ZrO_2 and Y_2O_3), as suggested by the XPS analyses (Figure 25). The improved nanohardness by ion implantation implied a higher wear resistance, which would be beneficial for bone implant materials, in terms of eliminating wear debris and subsequent particle disease.

5.1.5 Surface wettability of Ca- or Ar-ion-implanted Zr-Al-Ni-Cu-Y BMG

The surface hydrophilicity for the Zr-based BMG was varied after 10 or 50 keV ion implantation, which was demonstrated through water contact angle measurements using sessile drop method. The histogram in Figure 27 depicted a general increase in water contact angle after ion implantation, indicating that the surfaces were made less hydrophilic by ion implantation. A more significant increase in water contact angle was found on the Zr-based BMGs subjected to lower energy (10 keV) ion implantation, in comparison with those implanted with the same ion but higher energy (50 keV). In the meantime, under the same acceleration energy, the magnitude of surface wettability change was also dependent on the type of ion implantation, with Ar-ion-implanted Zr-based BMGs being even more hydrophobic than Ca-ion-implanted substrates. The insets in Figure 27 presented shadow images of the water droplets, which provided a qualitative view of the wettability change of the substrates as a result of ion implantation.

The hydrophobicity change of the tested specimens can be directly related to the amount of polar hydroxyl groups present on the surfaces, a higher amount of which

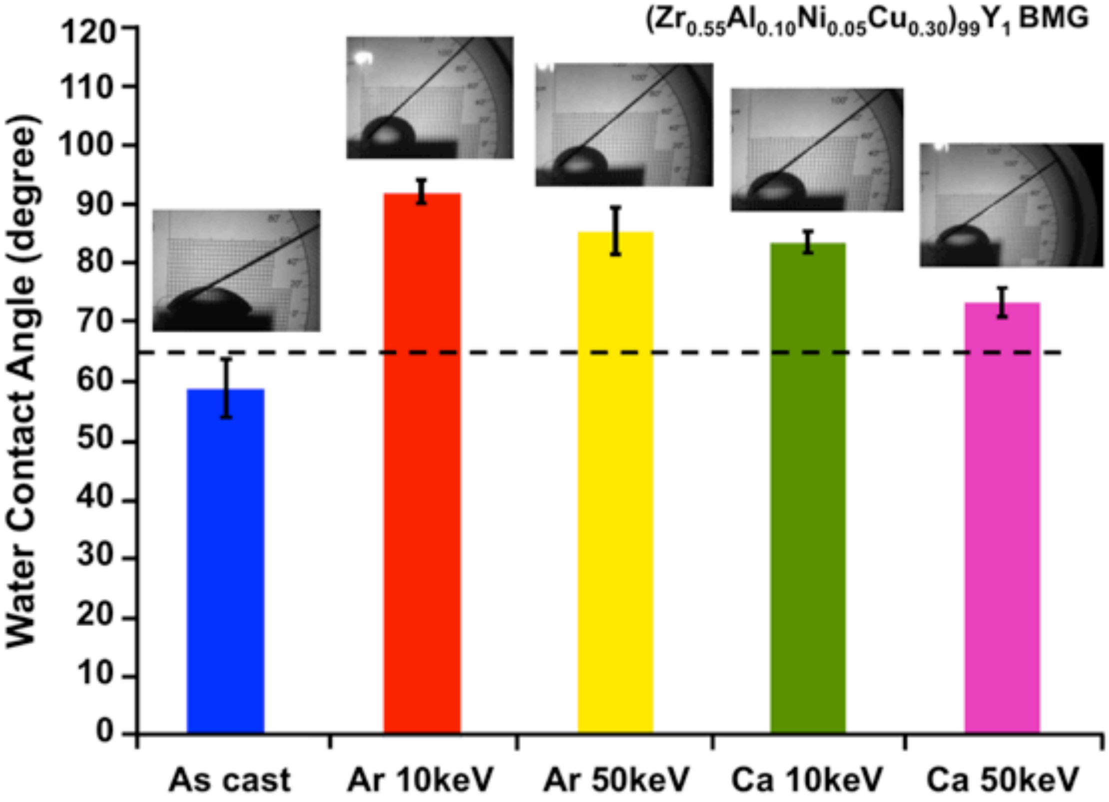

Figure 27 Water contact angles on as-cast or ion-implanted Zr-based BMG substrates (inset: shadow images of water droplets on corresponding substrates)

encouraged their interaction with polar liquid (water) and was found to improve surface hydrophilicity [212, 213]. The most hydrophilic as-cast surface was related to the highest amount of hydroxyl groups on the surface (Figure 25b). Among the surface treated samples, those after 10 keV Ar-ion implantation held the lowest amount of hydroxyl groups, hence the highest hydrophobicity; whilst a relatively larger amount of hydroxyl groups was observed on the less hydrophobic 50 keV Ca-ion-implanted samples.

Such increases in surface hydrophobicity following ion implantations could also affect corrosion resistance of the Zr-based BMG. It was reported in a ZrTiCuNiBe BMG system that a more hydrophobic surface could, to some extent, be related to higher corrosion resistance [214]. Therefore, the increased hydrophobicity of the Zr-based BMG after ion implantations observed in this study suggested a potential increase in corrosion resistance. In addition, the depletion or reduction of Ni and Cu on the alloy surface after implantation processes might also lead to improved corrosion resistance of the material [68]. The enhanced corrosion resistance of the Zr-based BMG after ion implantation was considered beneficial for long-term biomedical implants. A detailed investigation on the effect of ion implantation on corrosion resistance of BMGs would be topic of interest for future studies.

5.1.6 Cell adhesion on Ca- or Ar-ion-implanted Zr-Al-Ni-Cu-Y BMG

Bone-forming MC3T3-E1 cell line was used to study the cellular responses to the surface modification with low energy Ar- or Ca-ion implantation. Live/Dead staining images of the bone-forming MC3T3-E1 cells growing on the as-cast, Ar-ion-implanted, and Ca-ion-implanted samples were presented in Figure 28. Cells exhibited high viability

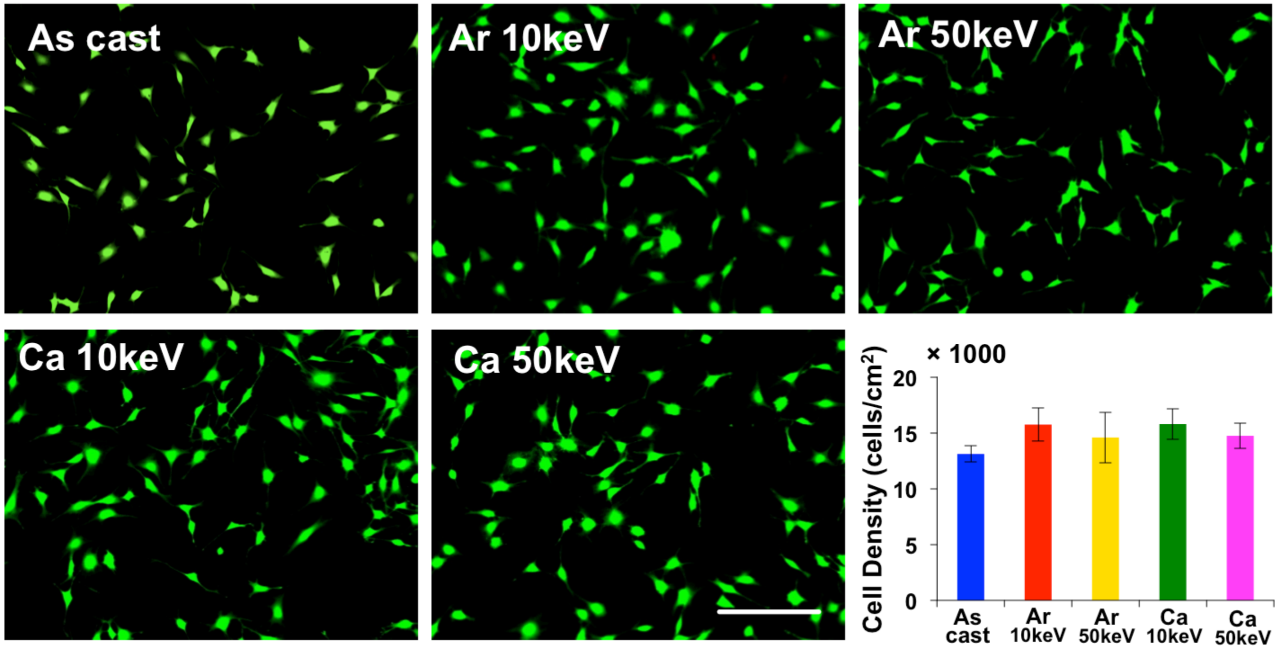

Figure 28 Live/Dead staining and density of adherent MC3T3-E1 cells on as-cast and ion-implanted $(Zr_{0.55}Al_{0.10}Ni_{0.05}Cu_{0.30})_{99}Y_1$ BMG substrates after 8 h culture (scale bar: 200 μm)

on all the samples, as shown by the strong green fluorescence for live cells and the absence of red signals for dead or membrane disrupted cells. The results indicated that, similar to their as-cast counterparts, the ion-implanted samples also supported initial cell attachment and exhibited no cytotoxicity to the cells. Furthermore, these images showed no distinct differences in adherent cell morphology among these various substrates. Quantification of the live cell density on each substrate following 8 h of culture was summarized in the bar graph in Figure 28. On average, higher adherent cell densities were found on ion-implanted samples, as compared with the cell density on the as-cast sample.

Cell adhesion was further accessed by fluorescent staining of vinculin (Figure 29). Overall, cells exhibited a polygonal morphology on all the substrates. The concentrated green fluorescent signals observed mainly on the periphery of the cytoplasm of adherent cells suggested the formation of focal adhesion plaques at the corresponding locations. Both as-cast and implanted samples were supportive of focal adhesion development. Qualitatively, the number of focal adhesion plaques displayed by cells attached on the ion-implanted substrates appeared to be higher than that on the as-cast sample.

It was well established that cell adhesion was directly affected by protein adsorption, which can be significantly influenced by surface hydrophobicity [126, 127, 215]. Ion implantation was shown to make the surface more hydrophobic, while a relatively more hydrophobic surface was considered to encourage protein adsorption [216]. Adsorption of proteins such as fibronectin from the culture medium promoted cell adhesion [127]. Therefore, higher numbers of adherent cells found on the ion-implanted

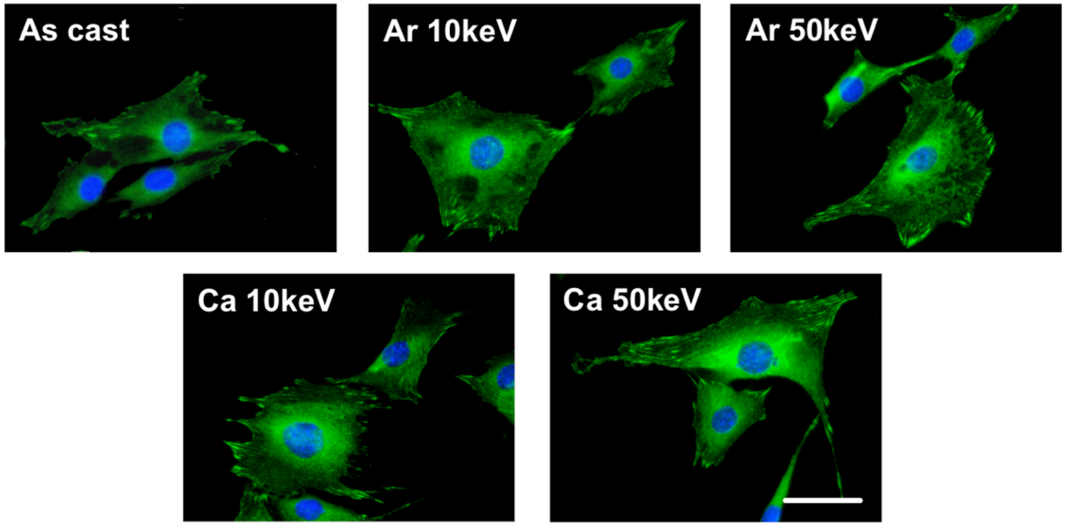

Figure 29 Green fluorescence staining of vinculin for MC3T3-E1 cells on as-cast and ion-implanted $(Zr_{0.55}Al_{0.10}Ni_{0.05}Cu_{0.30})_{99}Y_{1}$ BMG substrates after 8 h incubation showing focal adhesion plaques (scale bar: 50 μm). Blue staining illustrates cell nuclei

samples could be partially ascribed to the change of surface wettability. In the meantime, surface chemistry was considered an influencing factor to cell adhesion. Promoted cell adhesion with the presence of Ca on the surfaces in our study was in agreement with the higher cell adhesion and greater focal adhesion formation due to Ca-ion implantation to Ti surface [155]. The effects of wettability and chemistry changes led to an equivalent improvement of cell adhesion on Ca-ion-implanted samples to that on Ar-ion-implanted samples, although the hydrophobicity change by Ca-ion implantation was not as prominent as by Ar-ion implantation. In addition, the effect of chemical changes due to the presence of Ca was reflected by the increased number and improved formation of focal adhesion on Ca implanted samples. In fact, the mutual relationship among surface chemistry, hydrophobicity, and cell adhesion was extensively studied and established for biomedical alloys and polymers [155, 217, 218].

5.1.7 Summary

In the present study, low-energy Ca- or Ar-ions were implanted at 10 or 50 keV at a fluence of 8 × 10^{15} ions/cm^2 to $(Zr_{0.55}Al_{0.10}Ni_{0.05}Cu_{0.30})_{99}Y_1$ BMG, aiming at improving the biocompatibility and imparting bioactivity to the surface. The low energy ion implantation resulted in concurrent modifications in atomic structure, nanohardness, surface chemistry, hydrophobicity, and cell behavior on the surface of the Zr-based BMG, which were proposed to be mutually correlated with each other. The ion implantations were suggested to alter atomic structure on the surfaces according to SRIM simulation and XAS measurements. XPS revealed modified the surface chemistry and the introduction of Ca by Ca-ion implantation. The surface nanohardness was enhanced, with

Ca-ion implantation showing more prominent effect. The Zr-based BMG surfaces were altered to be more hydrophobic after ion implantation, which can be attributed to the reduced amount of hydroxyl groups on the implanted surfaces. Higher numbers of adherent cells were found on Ar- and Ca-ion-implanted samples, while more pronounced cell adhesion was observed on Ca-ion-implanted substrates.

5.2 Ion Implantation of the Zr-based BMG for Bone-Forming Cell Mechanical Sensing

Cell interactions with implantable materials are essential to the ultimate fates of the implants. Proper cell behaviors on biomaterial surface are desired in order to warrant successful implant integrations. To modulate cell behavior on the surface of a biomaterial, surface modifications in chemistry [217, 218] and topography [219-223] have been extensively researched and validated. In recent decades, regulating cell behavior with mechanical cues has emerged as a subject of great research interest [224-226]. An increasing number of studies have revealed that cells can sense the rigidity of their growth substrates, and transduce the effects of the mechanical microenvironment to change adhesion, proliferation, migration, and differentiation behaviors [227, 228]. In the majority of these studies on rigidity sensing, cells were interacting with "soft" polymeric materials, such as agarose and alginate hydrogels, polyacrylamide-based gels, poly(ethylene glycol)-based hydrogels, and polydimethylsiloxane, with relatively low elastic moduli ranging from tens of Pascal (Pa) to several megapascals [224-230]. Recently, Smith *et al.* used methacrylate-based networks to extend the moduli range to cover 60 to 850 MPa and studied cell responses [231]. Despite the progress, little has been reported to date on cell responses to substrate rigidity within the gigapascal range.

Considering hard tissues such as mineralized bone can exhibit high elastic modulus (~20 GPa) [232, 233] , and the prevalent use of rigid materials (i.e., metals and alloys) in orthopedic prostheses, it is of significant value to improve our understanding of the relationship between cell behavior and highly rigid materials. In this subtask, answers to the following two questions were sought: (1) will cells sense substrate rigidity change in the gigapascal range? (2) If so, what responses will cells exhibit? To address these questions, ion implantation was employed on BMGs to modulate substrate rigidity in the gigapascal range and investigated cell responses. This approach not only provides opportunities to fundamentally comprehend cell mechanosensing on rigid metallic surfaces, but also can be beneficial to guide the engineering of metallic implants for enhanced tissue integrations.

The rationale of selecting BMGs over common biomedical alloys as our test substrates to probe cell mechanosensing of high stiffness materials is because of the homogeneous microstructures of BMGs. Traditional crystalline biomedical alloys, such as Ti alloys, consist of different phases, grain boundaries, and segregations, all of which can exhibit distinctive mechanical properties. [234, 235] This inhomogeneity in the mechanical microenvironments could confound interpretation of cell responses to the overall mechanical variations among substrates. In contrast, the amorphous microstructure of BMGs overcomes the above issues, and thus allows cell mechanosensitivity studies conducted on surfaces exhibiting uniform mechanical properties. Although initially developed as a new family of engineering materials, BMGs have attracted great attentions from the biomaterials field because of their bulk mechanical properties, chemical stability, and polymer-like thermal processability [7, 10, 14, 18], which further makes BMG a relevant model material for the present work.

Among the many different types of BMGs available, the Zr-based $(Zr_{0.55}Al_{0.10}Ni_{0.05}Cu_{0.30})_{99}Y_1$ (at.%) BMG was used. Previous work has demonstrated that this Zr-based BMG is cytocompatible with MC3T3-E1 preosteoblasts, [57, 68] a cell line commonly used for bone-implant related studies, including in the context of mechanosensing, and is the subject of investigations herein.

To vary surface rigidity of the Zr-based BMG, the versatile yet facile ion implantation technique was employed. The effects of ion implantation of inert Ar ions to alter mechanical properties of Zr-based BMGs were previously reported [69, 123, 204, 208, 210]. By adjusting implantation parameters (i.e., ion-beam energy, fluence, and flux), it is feasible to fine-tune the surface mechanical properties of BMGs over a large span and allow subsequent study of cell response to such changes. In this study, low energy Ar-ion implantations were conducted at different implantation energies and fluences on $(Zr_{0.55}Al_{0.10}Ni_{0.05}Cu_{0.30})_{99}Y_1$ BMG substrate to confine the effects to the near-surface region.

For denotation purposes, samples were labelled as Zr-AC, Zr-50L, Zr-50H, Zr-100H, and Zr-200H for as-cast and various ion-implanted Zr-based BMG surfaces, as summarized in Table 2 in Chapter 3. Changes in material properties and bone-forming MC3T3-E1 cell responses as a result of ion implantation were discussed. Work presented in this subtask provided a paradigm to fundamentally understand cell mechanosensing on rigid metallic surfaces and assist the design of interfaces for enhanced cell-material interactions.

5.2.1 Surface mechanical properties of Ar-ion-implanted Zr-Al-Ni-Cu-Y BMG

Mechanical modifications to the Zr-based BMG as a result of Ar-ion implantations were characterized by nanoindentation. Representative load-displacement curves (Figure 30a) showed that, for all the ion-implanted samples, the maximum loads at the maximum indentation depth of 35 nm were lower than that of the Zr-AC sample. From these curves, elastic modulus (Em), stiffness, and hardness values of the respective sample were derived (Figures 30b-d). Generally, the Zr-based BMG surfaces after ion implantation were "softer" than the Zr-AC sample, and the extent of softening was dependent on the implantation energy and fluence. Specifically, the Em of the BMG surface decreased as the implantation energy decreased or the fluence increased. Collectively, these samples provide a modulus range spanning from 51 to 86 GPa. The effect of ion implantation on stiffness and nanohardness shared a similar trend as that for Em (Figures 30c and d). After ion implantation, surface stiffness variation of about 10 μN/nm from 24.23 to 35.31 μN/nm was achieved. Simultaneously, nanohardness ranging from 1.37 to 6.25 GPa was attained. Therefore, it was evident that ion implantation can be used to successfully adjust the mechanical properties of the Zr-based BMG surfaces.

5.2.2 Microstructure of Ar-ion-implanted regions of Zr-Al-Ni-Cu-Y BMG

In previous studies of the effect of room temperature Ar ion implantation on various Zr-based BMGs, both surface hardening [69, 123, 210] and softening [208] have been observed under different irradiation conditions. The underlying mechanism governing the ion implantation induced mechanical modifications was commonly suggested as the irradiation-induced microstructural alteration (i.e., structural relaxation or formation of nanocrystals) [69, 123, 208, 210].

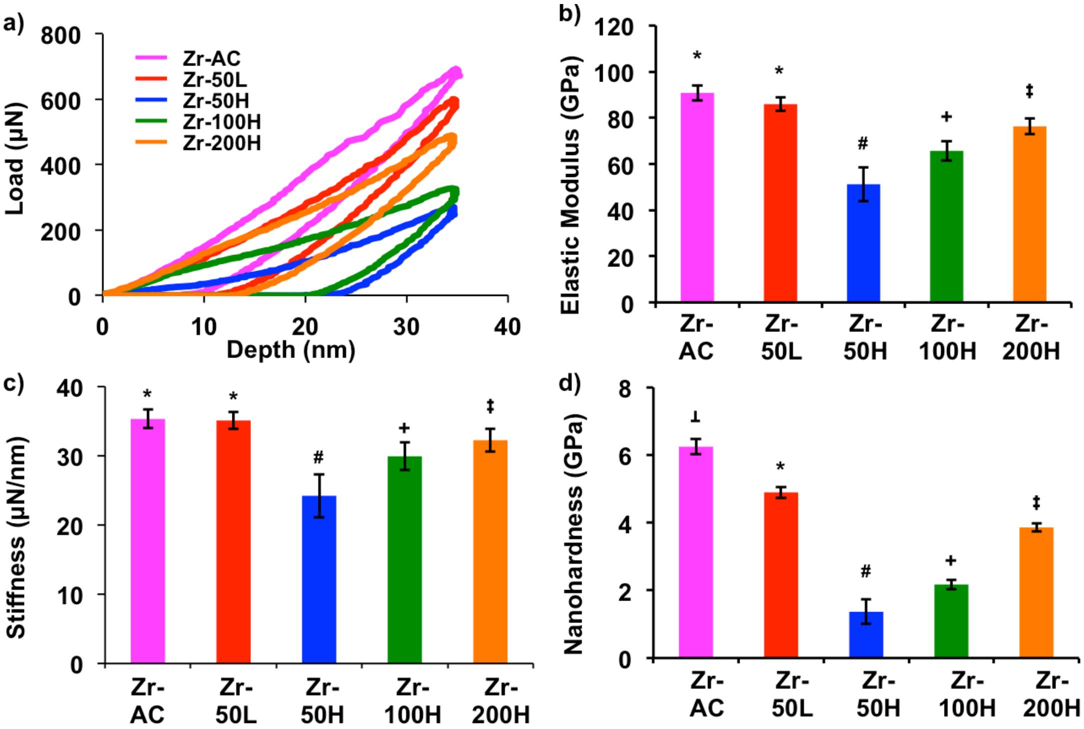

Figure 30 Surface mechanical properties of the ion-implanted surfaces of the $(Zr_{0.55}Al_{0.10}Ni_{0.05}Cu_{0.30})_{99}Y_1$ BMGs: a) representative load-displacement curves at a indentation depth of 35 nm, b) measured stiffness, c) reduced modulus, and d) nanohardness (Statistically different groups were separated by different symbols at significance level of $p < 0.05$)

To elucidate the specific softening mechanism associated with the Ar-ion implantation conditions used in this study, the microstructure of the surface regions on the Zr-based BMGs was analyzed using TEM. Cross-sectional TEM Z-contrast images for the near-surface regions (Figure 31) revealed the formation of nano-sized fine features after ion implantation. Depending on the implantation conditions, the size of such features and their depth profiles varied. For the Zr-50L and Zr-200H specimens, these nanofeatures were limited within ~55 nm-thick and ~250 nm-thick layer depths, respectively. The sizes of these nanofeatures were relatively small with diameters below 10 nm. In contrast, a drastically wider size distribution was noted for the other two implanted samples. For Zr-100H, larger features (40 - 80 nm in diameter) were seen distributed along the mid-section of the implanted zone, and were surrounded by much smaller nanofeatures. As for Zr-50H, features greater than 100 nm were formed when some of the round features merged to each other, resulting in protrusions or pockets on the surface.

The SAD patterns for the surface regions including the modified layer and for the bulk matrix region without ion implantation influences were acquired for all the ion-implanted samples, as shown in Figure 31. These diffraction patterns indicated the amorphous (or highly defective crystalline) microstructure of BMG throughout the surface region for each substrate. The two rings with sharp intensity represent the short-range atomic ordering of the BMG. The brightest ring of the diffraction pattern represented a lattice plane with d-spacing of approximately 0.5 nm, and the second

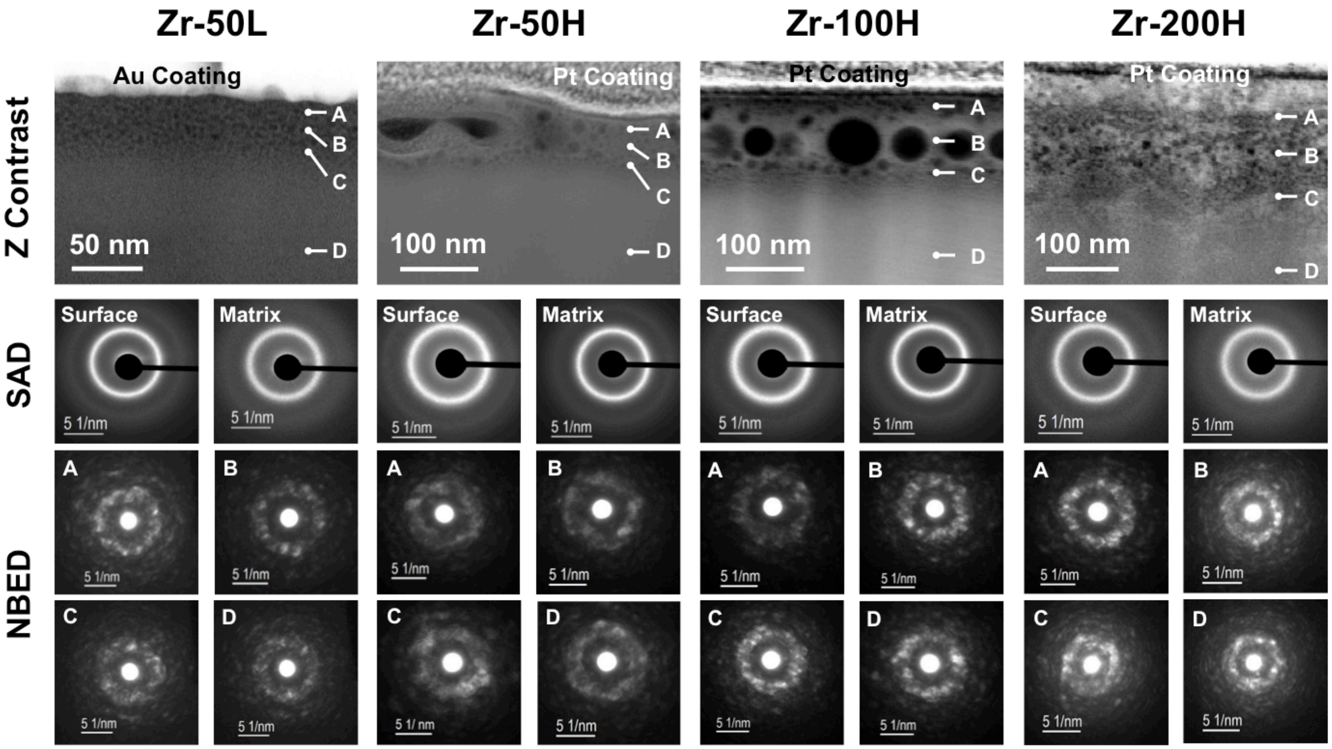

Figure 31 TEM observations on the surface cross-sections of the ion-implanted $(Zr_{0.55}Al_{0.10}Ni_{0.05}Cu_{0.30})_{99}Y_1$ BMGs. SAD images were taken from both surface and matrix regions. NBED patterns were taken at indicated spots as marked in the Z-contrast images.

intense ring represented d-spacing of approximately 0.3 nm. In the meantime, these two rings were significantly broadened, which originated from the lack of long-range atomic ordering or large distortion of lattice planes, giving rise to the deviation of d-spacing determinations. The SAD patterns for the surface and bulk matrix regions after implantation were virtually identical, suggesting that no distinct structural changes were introduced to the implanted surface region of the Zr-based BMG after Ar-ion irradiation.

NBED was used to further study the microstructure after implantation. Four different sites were inspected (Figure 31) including locations that were (A) near surface, (B) close to the middle of the implanted layer, (C) farther from surface but still within the implanted layer, and (D) away from the implanted layer. The d-spacing measured based on these nanobeam diffraction patterns confirmed the one measured from SAD patterns. The larger deviations of the d-spacing measurement from the NBED patterns were derived from the local distortion of the lattice plane due to the strain or the reflection disks in the convergent condition. The nanobeam diffraction patterns further validated that no significant structural changes were introduced to the implanted surface region of the Zr-based BMG after Ar-ion irradiation. It is confirmed that no distinctive differences were found between the diffraction from the modified layer and that from the bulk matrix of the substrate.

5.2.3 Ar-distributions in Ar-ion-implanted Zr-Al-Ni-Cu-Y BMG

To further determine whether these implantation-induced nanosized fine features are voids or Ar bubbles, chemical analyses were carried out. The results of EDS obtained from the implanted Zr-based BMG samples first confirmed the presence of Ar within the near-surface regions after implantation. The presence of Ar within the near-surface regions after ion implantation was detected (Figure 32). In addition to Ar maps, Ga and Au/Pt distributions were recorded in order to confirm that the FIB sectioning processes did not introduce significant disturbance to the ion-implanted surface layers, i.e. no Ga ions or Pt were implanted to the surface layers.

Spatially resolved (~0.5 nm) EELS was then used to reveal Ar distributions in the implanted layers by continuously recording spectra along the cross-section of the implanted samples. As shown in Figures 33, EELS-based Ar mappings clearly suggest the nature of those small nanofeatures (diameter < 20 nm) observed in the Z-contrast images being Ar bubbles formed by the segregation of implanted Ar ions. Despite the absence of Ar signals in the larger diameter features, it was rationalized that these apparent voids were originally filled with Ar, considering the TEM samples were prepared as thin lamella of less than 50 nm thick that inevitably led to the discharge of Ar gas from Ar bubbles with diameters above 50 nm.

Based on the EELS measurements, Ar depth profiles were also extracted (Figure 33b). The measured profiles exhibited distorted bell shapes, and the depth varied with the implantation energy, a higher value of which allowed deeper ion penetration. Peak concentrations of Ar were mostly located close to the midline of the implantation-modified layer, although disruptions occurred in the experimental measurements due to the artificial voids for Zr-50H and Zr-100H samples. The relative peak Ar concentrations determined by the highest numbers of Ar atoms were found dependent on both implantation energy and fluence.

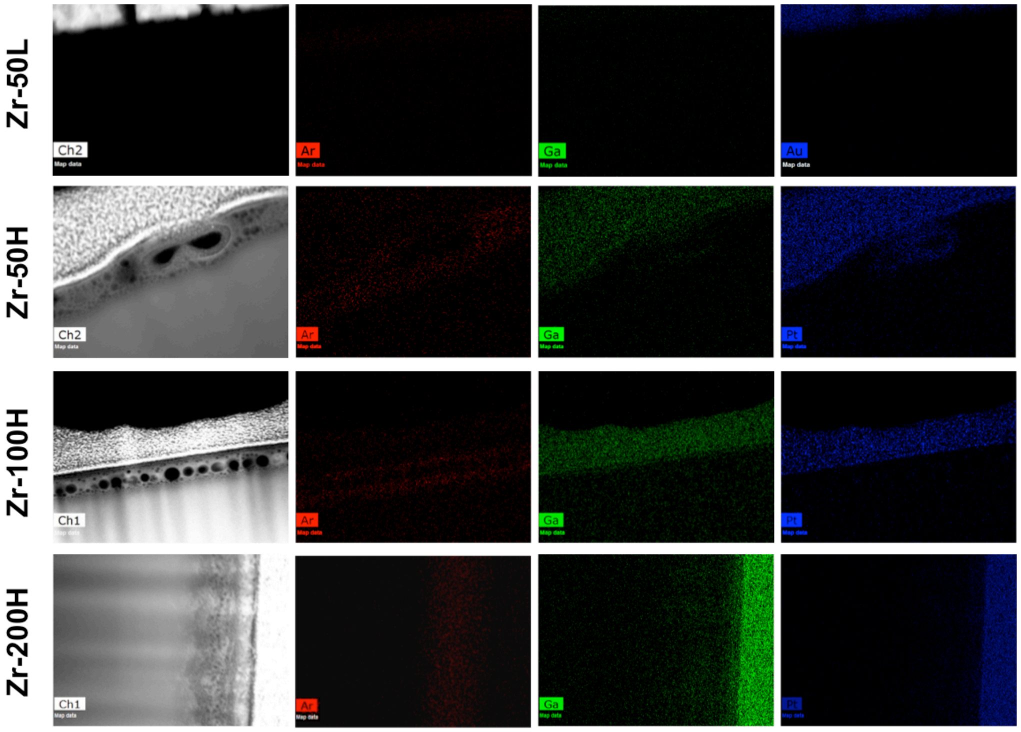

Figure 32 EDS mappings of Ar, Ga, and Au or Pt for the cross sections of the surface regions indicated in the Z contrast images for the Ar-ion implanted $(Zr_{0.55}Al_{0.10}Ni_{0.05}Cu_{0.30})_{99}Y_1$ BMG samples.

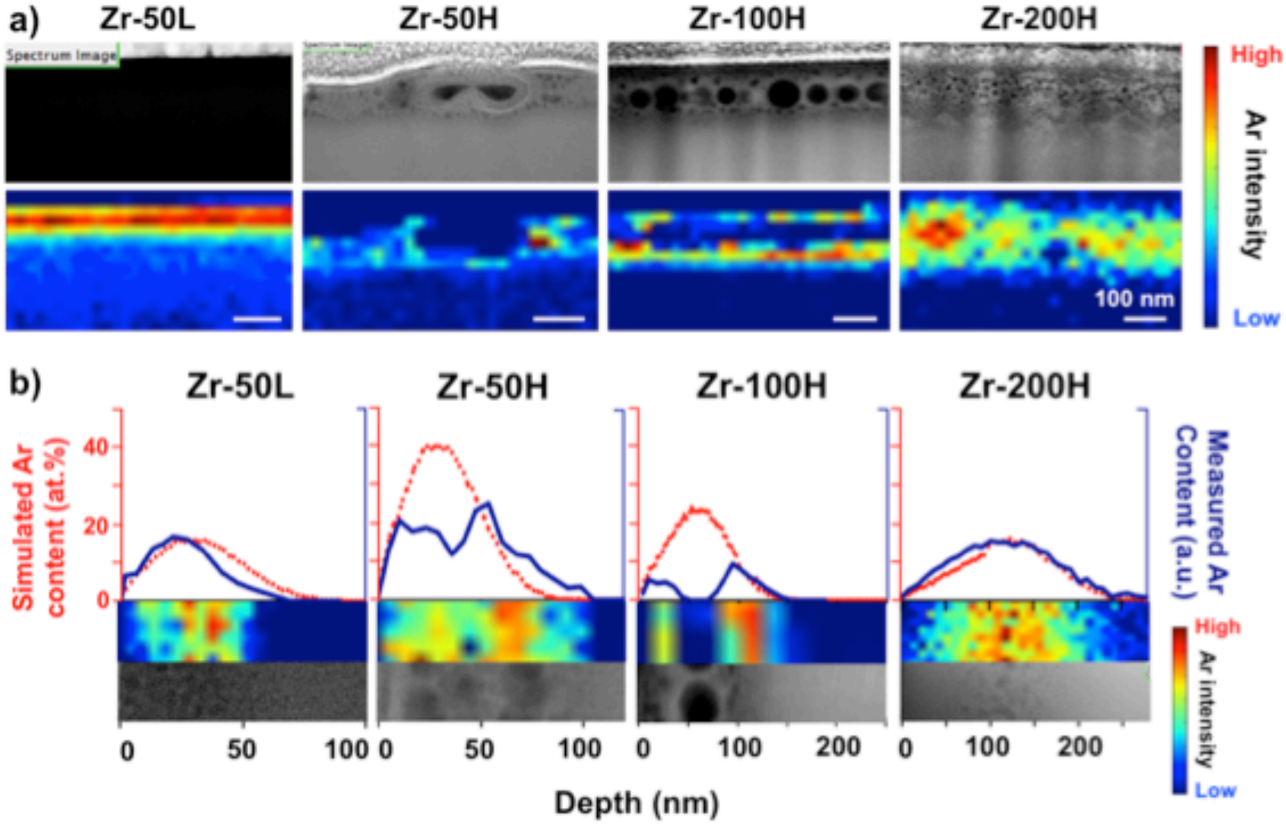

Figure 33 Ar distributions within the ion-implanted $(Zr_{0.55}Al_{0.10}Ni_{0.05}Cu_{0.30})_{99}Y_1$ BMG surfaces: a) EELS analyses together with TEM Z-contrast images for comparisons; and b) Comparisons between experimental analyses on Ar distributions by EELS and SRIM simulation results.

5.2.4 SRIM Simulation of Ar-ion-implanted Zr-Al-Ni-Cu-Y BMG

To complement the experimental observations, computational simulation SRIM software [172] was further employed to estimate the potential ion implantation effect on the Zr-based BMG substrates. The simulation results (Figure 33b) showed that the Ar profiles evolved with both implantation energy and fluence, which are consistent with the experimental findings. Both energy and fluence contributed to the damage and Ar concentration. At fixed energy of 50 keV, the dpa value and Ar concentration were directly proportional to the impinging fluence. The maxima of disorder and Ar concentration increased from 180 dpa and 18 at.% at the fluence of 4×10^{16} ions/cm^2 to 480 dpa and 42 at.% at the fluence of 1×10^{17} ions/cm^2. In the meantime, the dpa value and Ar concentration decreased with the increase in ion energy at the fixed fluence of 1×10^{17} ions/cm^2, since the fixed amount of ions can be dispersed into broader regions at higher acceleration energies.

In addition to the estimation of Ar-distribution, SRIM simulation can also be used to assess the implantation induced damages (i.e., displacement per atom, dpa), which were found proportional to the applied fluence and decreased with implantation energy (Figure 34). From the bell-shaped profiles, thickness of the influenced region and peak damage/concentration can be estimated for each implantation condition. The depth of modified region was mainly determined by the acceleration energy of the Ar-ions, which grew from 75 nm for 50 keV Ar ions to 150 nm and 250 nm for 100 and 200 keV ions, respectively. The peak damages generated by the collision cascades slightly descended from 480 to 400 dpa for 50, 100, and 200 keV Ar-ion implantations. Possible Ar concentration in the substrate decreased more dramatically with the increase in ion

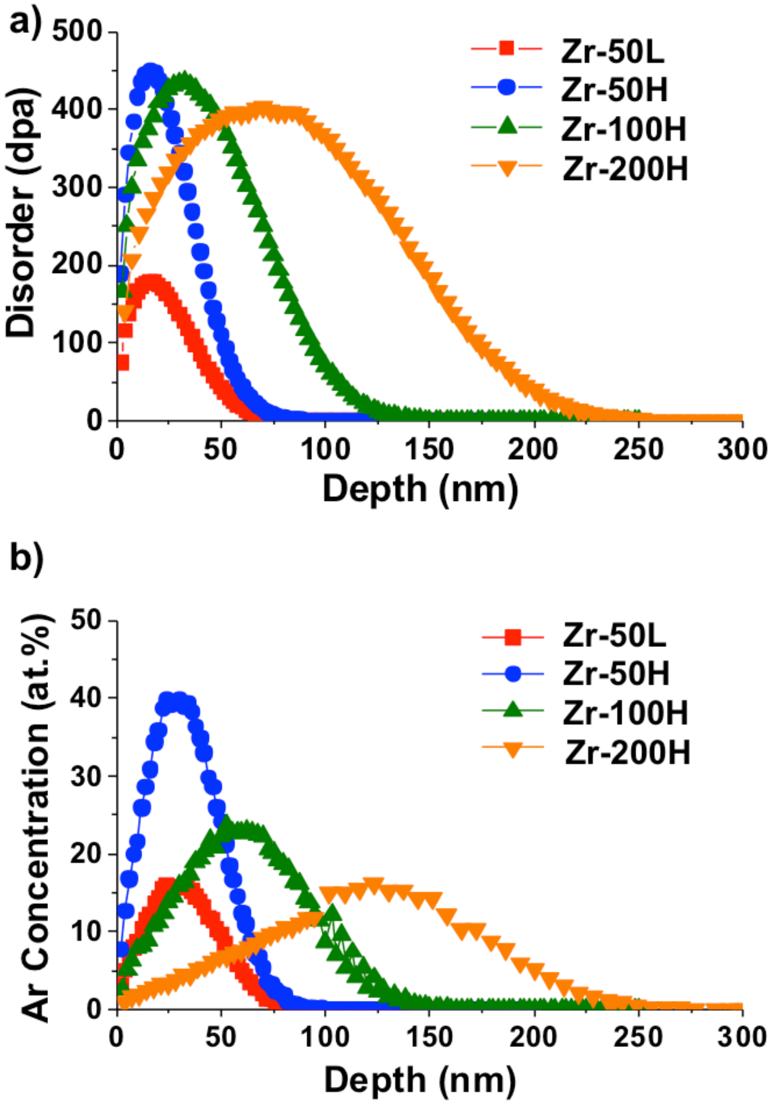

Figure 34 SRIM simulations on the distributions of disorders and Ar concentrations after Ar-ion implantations of $(Zr_{0.55}Al_{0.10}Ni_{0.05}Cu_{0.30})_{99}Y_1$ BMG at indicated conditions.

energy from 40 to 25 and 20 at.% for Ar-ion implantations at 50, 100, and 200 keV, respectively. The highest value of disorders was found to be close to 480 dpa. With such a high disorder, the microstructure of the Zr-based BMG can remain amorphous as shown in Figure 31.

5.2.5 Surface characterizations of Ar-ion-implanted Zr-Al-Ni-Cu-Y BMG

With the generation of Ar nanobubble doped layer on Zr-based BMG surfaces, mechanical variations at high rigidity levels (Em > 50 GPa) were readily achieved to study the mechanoresponses of bone-forming cells. Prior to the discussion on the cell responses to mechanical changes on the Zr-based BMG surfaces, it is necessary to take into consideration of potential contribution from other surface properties such as roughness and SFE that can affect cell behaviors.

Samples subjected to Ar-ion implantation were viewed under SEM and AFM to examine their surface morphological changes, as shown in Figure 35. Secondary electron images in Figure 35a were collected at 50,000 × magnification. Distinct features were observed for the Zr-50H sample. Large-sized Ar bubbles or pockets were found formed within the near-surface region of the Zr-50H sample, which were visible in the SEM image. These features were resulted from the protrusions caused by the Ar segregation or pockets due to the burst of the bubbles, which was consistent with the TEM observations in Figure 31. Representative AFM images for the indicated surfaces are presented in Figure 35b. The AFM observations were found in agreement with SEM observations, with roughest surface observed on the Zr-50H sample. The arithmetic averages of

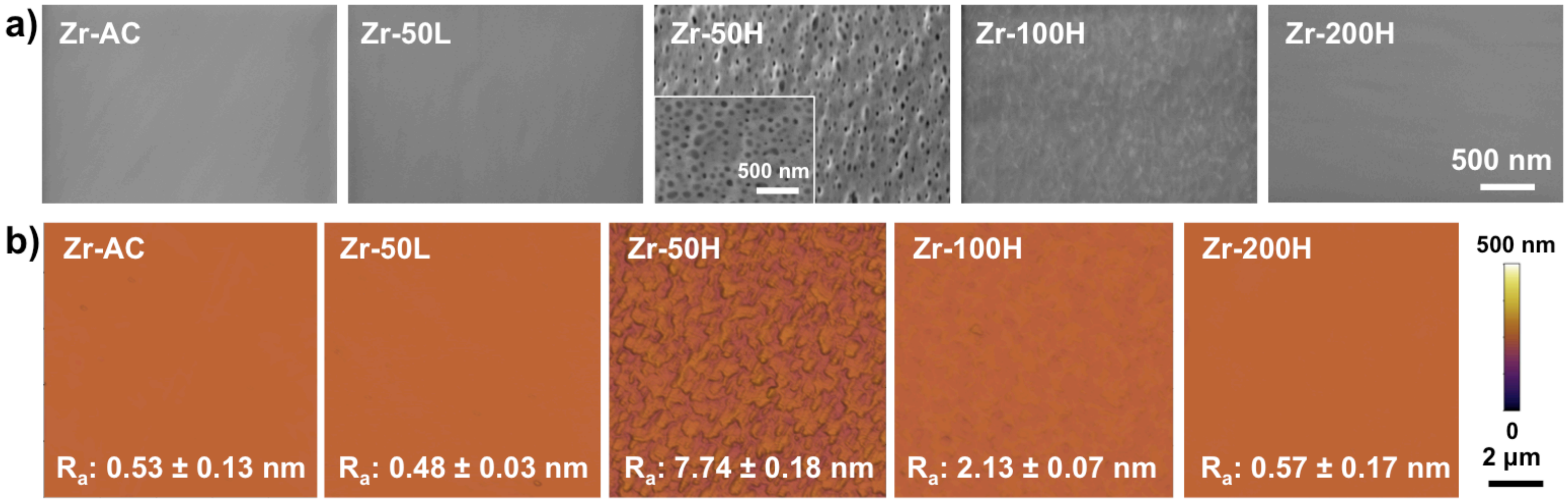

Figure 35 Morphological and topographical analyses of the $(Zr_{0.55}Al_{0.10}Ni_{0.05}Cu_{0.30})_{99}Y_1$ BMG surfaces before and after Ar-ion implantation using SEM (upper panel) and AFM (lower panel).

roughness (R_a) on the Zr-50H and Zr-100H samples were increased to 7.74 and 2.13 nm, as compared to those around 0.5 nm for Zr-AC, Zr-50L, and Zr-200H samples.

The calculated surface free energy (SFE) of each specimen was then used as a predicative index for potential influence on cell response [236]. As shown in Figure 36, although the SFE of the as-cast sample was significantly higher than any of the ion-implanted samples, no statistical differences in SFE were detected among the ion-implanted samples. Therefore, these ion-implanted samples allowed us to delineate the effect of variation of substrate rigidity in the gigapascal range on cell behaviors.

5.2.6 Cell adhesion on Ar-ion-implanted Zr-Al-Ni-Cu-Y BMG

As bone-forming cells are anchorage dependent, cell adhesion to substrates precedes any other cell functions and bears a significant role for cell growth. Therefore, adhesion of MC3T3-E1 cells on the Ar-ion implanted Zr-based BMG samples was first characterized. All the ion-implanted samples supported initial cell adhesion and maintained cell viability (Figure 37), which indicated that the Ar-ion implantation processes did not introduce any adverse effects to cells regarding their viability.

Adherent cell morphology was examined via fluorescent staining of focal adhesion (FA) plaques and cytoskeletal actin filaments. FAs are important in maintaining cell adhesion to the surface and serve as physical linkages connecting the cytoskeletal system and the microenvironment [237, 238]. Regardless of the rigidity of the ion-implanted BMG substrates, cells were able to develop great number of FAs, which are seen primarily concentrated at the periphery of the cells (Figure 38).

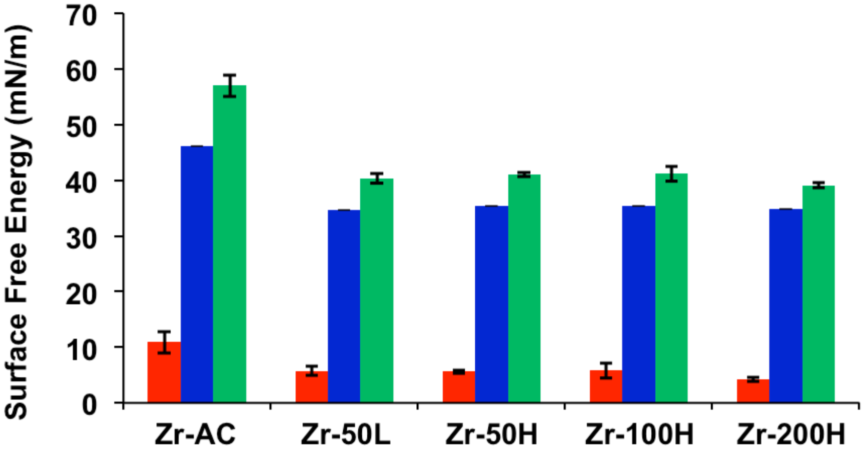

Figure 36 Surface free energies (red: dispersive part, blue: polar part; green: overall) of indicated substrates. The surface free energy and its components for each ion-implanted sample were found significantly different from those of Zr-AC sample at $p < 0.05$.

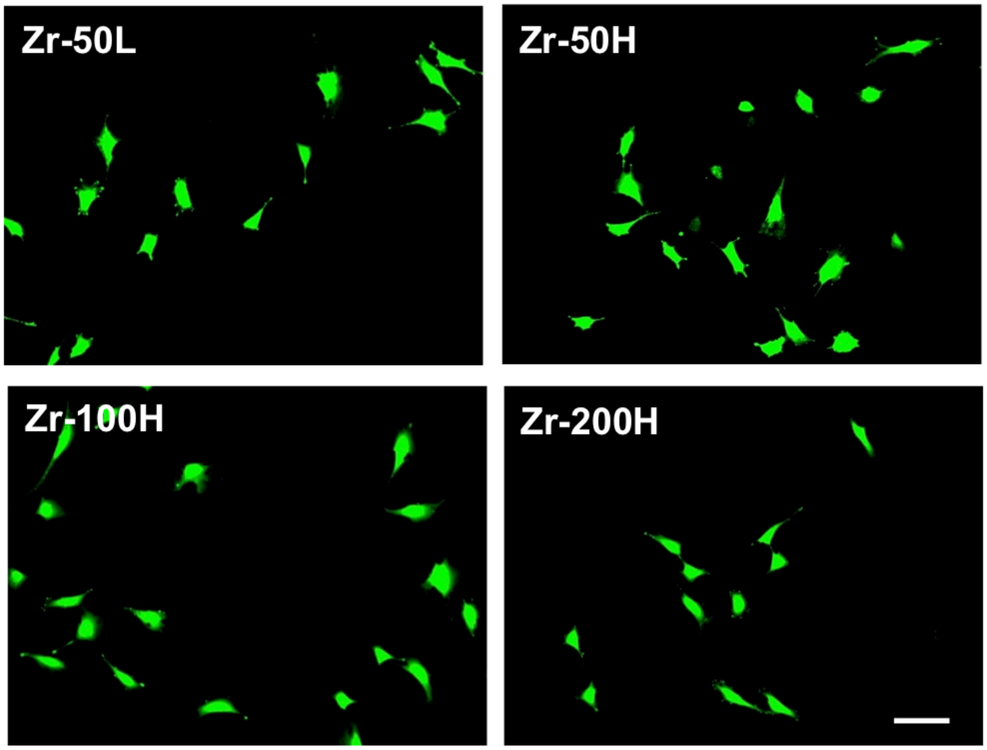

Figure 37 Live/Dead staining of MC3T3-E1 cells adherent on Ar-ion-implanted $(Zr_{0.55}Al_{0.10}Ni_{0.05}Cu_{0.30})_{99}Y_1$ BMG substrates after 24 h of incubation (scale bar: 100 μm).

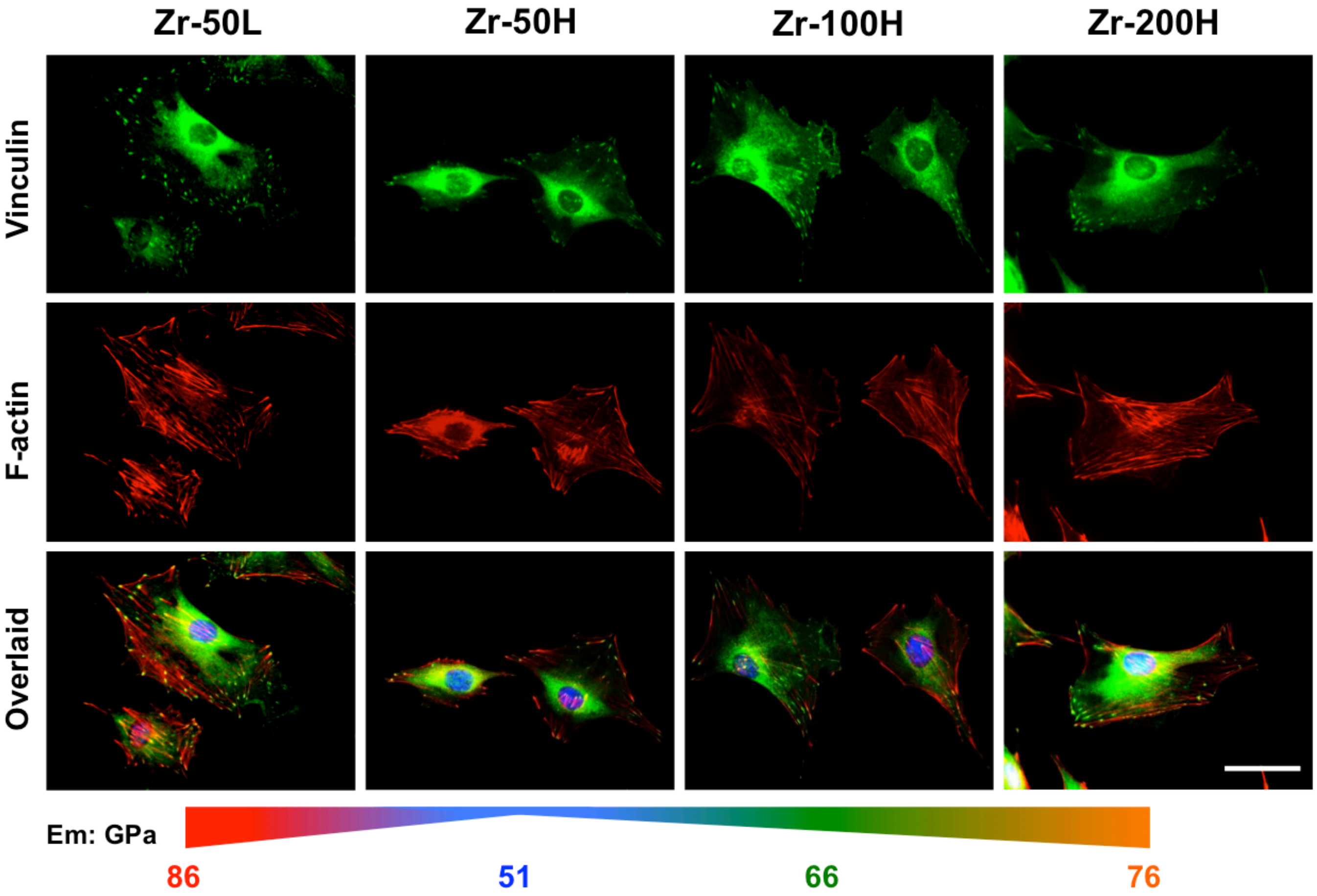

Figure 38 Fluorescent staining of MC3T3-E1 cells (green: vinculin; red: F-actin; blue: nuclei) on indicated $(Zr_{0.55}Al_{0.10}Ni_{0.05}Cu_{0.30})_{99}Y_1$ BMG substrates after 24 h culture (scale bar: 40 µm).

Quantitative analyses of FAs revealed that the average number of FAs per cell was dependent on substrate rigidity, with the least rigid Zr-50H surface (Em = 51 GPa) supporting the lowest amount of FA development (Figure 39a). Other cell parameters including perimeter, spread area, and circularity were also found to be affected by changes in substrate rigidity (Figures 39b-d). The spread area and perimeters of the cells on all substrates were found equivalent (Figures 39b and c). Circularity (roundness) of the cells on the surfaces ranged from 0.31 to 0.41 (Figure 39d). It was detected that cells tended to be less polarized on Zr-100H and Zr-200H, suggested by the larger values of circularity.

Staining of actin filaments revealed the formation of actin filament bundles running across the cell body and terminating at FAs (Figure 38). These bundles, also known as stress fibers, are crucial in the formation of cytoskeletal system and transduction of mechanical indications [239, 240]. Qualitatively speaking, the actin filament bundles were also affected by the substrate rigidity, where more pronounced stress fiber formation was observed for cells on Zr-50L (Em = 86 GPa) and Zr-200H (Em = 76 GPa) than those on Zr-50H (Em = 51 GPa) and Zr-100H (Em = 66 GPa).

These results of cell adhesion behavior study imply that, in spite of the elastic moduli of the BMG substrates being in the gigapascal range and much higher than physiologically attainable values, variations in substrate rigidity of gigapascal scale can be sensed by bone-forming cells and bring concomitant changes to cell functions. In comparison with previous findings obtained from MC3T3-E1 preosteoblast cells cultured on substrates with elastic moduli spanning kilopascal to megapascal rigidity, the general

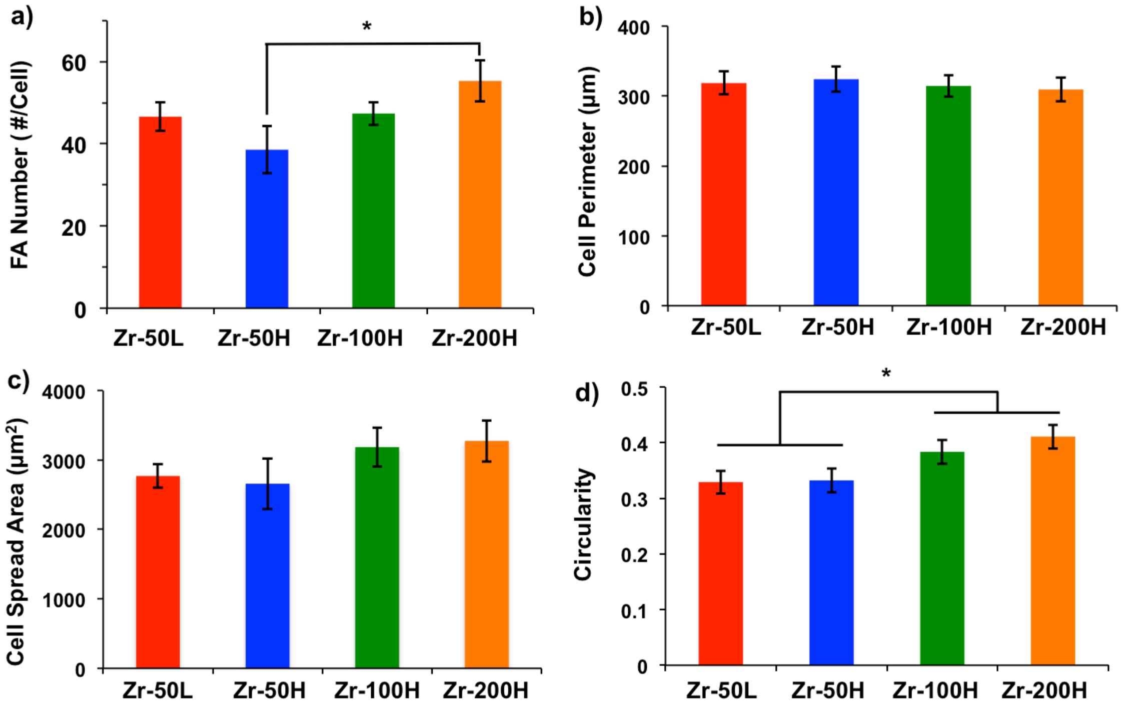

Figure 39 Statistical analysis on focal adhesion (FA) number and cell parameters based on fluorescent image analyses: (a) number of FA sites per cell density,(b) cell perimeter, (c) spread area, and (d) circularity (* denotes statistically significant differences at $p < 0.05$).

effect is similar, that is, cells respond to a stiffer surface by forming higher density of FAs and exhibiting more developed cytoskeletal structures [241-243].

5.2.7 Cell proliferation on Ar-ion-implanted Zr-Al-Ni-Cu-Y BMG

Proliferation of bone-forming cells into larger population prepares themselves for later biological activities (i.e., differentiation and mineralization). Proliferation of the MC3T3-E1 cells from days 1 to 5 on different surfaces was examined using WST-1 assay (Figure 40). Higher proliferation rates were detected on the less stiff Zr-50H, Zr-100H, and Zr-200H surfaces with elastic modulus lower than 77 GPa, in contrast to the Zr-50L surface with Em being the highest in the group.

Cell proliferation on indicated surfaces at each time point was also visualized using SEM (Figure 41). MC3T3-E1 cells grew from small to large populations on all surfaces after 5 d of growth. Cells were spaced and exhibited polygonal shapes at day 1, which confirmed the observations from the fluorescent images in Figure 3a. At day 3, the cells increased in number and more cell-cell interactions were observed. After 5 d growth, the cell layer reached near-confluency on the Zr-50L surface, while confluent cell layers were formed on Ar-implanted samples at the high fluence. SEM observations further confirmed the higher proliferation rates on high fluence Ar-ion implanted samples, which were in agreement with the WST-1 results.

Interestingly, our observation of higher proliferation rate of bone-forming cells on the less stiff surfaces is in disagreement with results reported by others using the same cell type. For example, Kong et al. found cell proliferation rate increased as the stiffness of the alginate hydrogel was raised from 20 to 60 and 110 kPa [242]. Khatiwala et al.

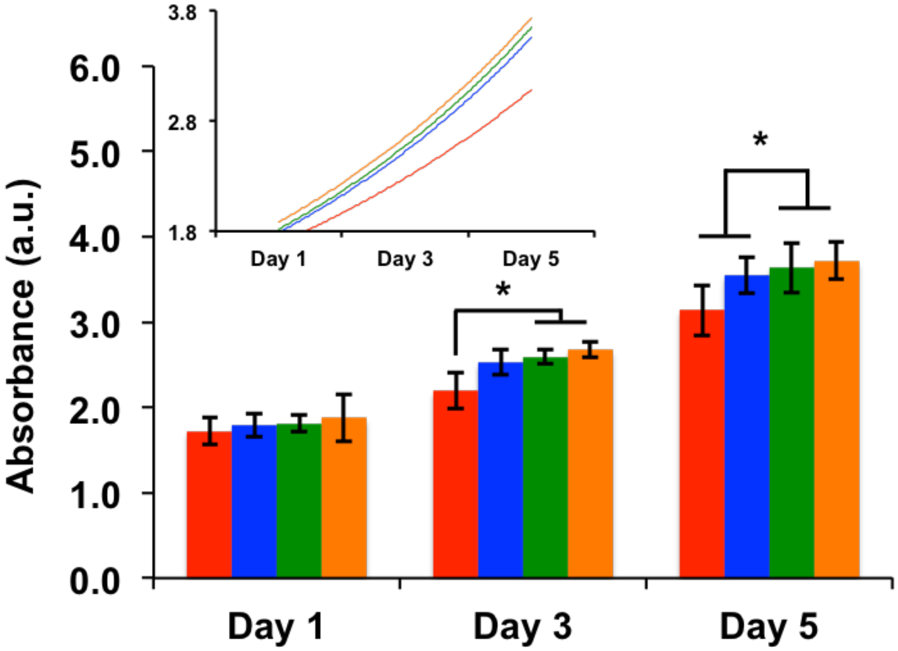

Figure 40 Proliferation of MC3T3-E1 bone-forming cells on as-cast or ion-implanted $(Zr_{0.55}Al_{0.10}Ni_{0.05}Cu_{0.30})_{99}Y_1$ BMGs from day 1 to 5 quantified with WST-1 assay (different letters denote results with statistically significant difference at $p < 0.05$)

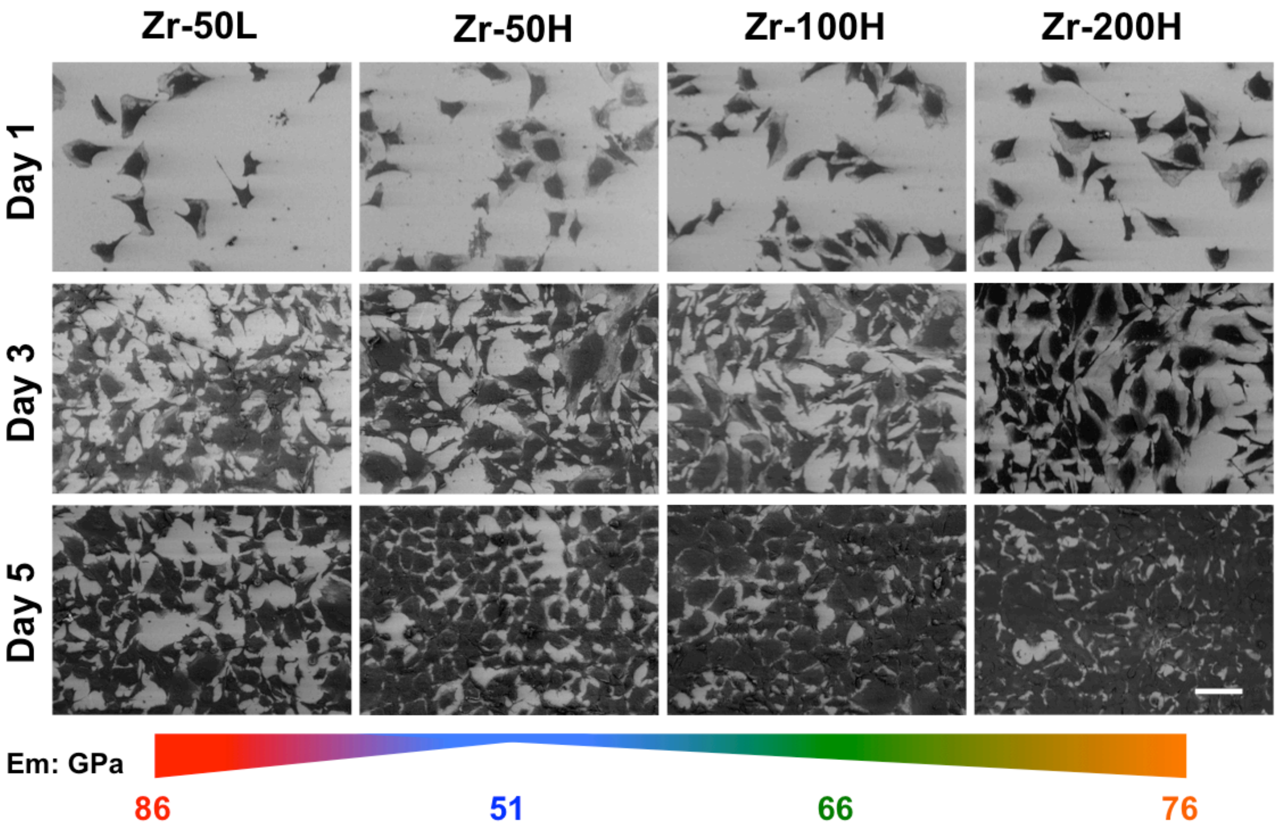

Figure 41 SEM images of MC3T3-E1 cell morphology on as-cast or ion-implanted $(Zr_{0.55}Al_{0.10}Ni_{0.05}Cu_{0.30})_{99}Y_1$ BMG after 1, 3, and 5 days of growth (scale bar: 100 µm)

compared the proliferative capacity of MC3T3-E1 cells on type II collagen functionalized polyacrylamide gels with stiffness of 11.78, 21.6, and 38.98 kPa, and noticed greater cell proliferation on stiffer gels [241]. The stiffness level of the investigated BMG substrates encompassed in the current work, being six orders of magnitude higher than those prior studies, may account for the different observations in the effect of substrate rigidity on cell proliferation. To shed light on such opposite effect on cell growth, future studies can focus on specific signaling pathways of different receptors or regulators, since the proliferation behavior of cells on different substrates has been found regulated by the signaling through cytoskeleton linkages and cell adhesion [237].

5.2.8 Summary

In conclusion, low energy Ar-ion implantation was utilized to modulate the surface rigidity of the Zr-based BMG substrate in the present study. The Zr-based BMG surfaces were softened due to the impartment of Ar nanobubbles into the amorphous matrix. By generating a nanobubble-doped transitional zone between the BMG substrate and bone-forming cells, it was shown for the first time that bone-forming cell adhesion could sense and react to mechanical cues of modulus changes at gigapascal level on BMG surfaces. Cell adhesion and actin filaments were found to be less established on less stiff surfaces, especially on the surface with an elastic modulus of 51 GPa, whereas faster growth was evidenced by the higher proliferation rate. Results in this study enriched our knowledge on the cell mechanosensing of the substrate rigidity on metallic materials with elastic moduli higher than 50 GPa. Furthermore, this study introduced a new platform for fundamental investigation of cell response to substrate rigidity previously unattainable with synthetic materials. The homogeneous amorphous microstructure of BMGs and the versatility of the ion implantation technique allows for the preparation of surfaces with tunable mechanical properties to enhance the interaction with cells. By advancing our understanding of bone cell mechanosensing in a broader range of substrate stiffness, it also makes surface mechano-engineering of metallic orthopedic implants a potential strategy to consider for promoting osseointegration.

5.3 Conclusions and Future Work

In this task, ion implantation was adopted as a versatile approach to successfully engineer the surface properties of the $(Zr_{0.55}Al_{0.10}Ni_{0.05}Cu_{0.30})_{99}Y_1$ BMG in order to modify surface chemistry for enhanced bioactivity and to modulate surface mechanical properties for cell rigidity sensing, respectively.

To impart bioactivity to the Zr-based BMG, low energy Ca-ion implantations were performed using Ar-ion implantation as reference. Modified materials properties were achieved including altered short-range atomic structure, tuned surface chemistry, enhanced surface nanohardness, and increased hydrophobicity. Improved cell adhesion after Ca-ion implantation was initially demonstrated, which suggested its potential to introduce bioactivity to the inert Zr-based BMG. Further investigations were suggested to focus on a comprehensive study of the Ca-ion irradiation with different parameters, and examination of long-term cell behavior on the ion-implanted BMG substrates.

Aiming at the study of bone-forming cell rigidity sensing on stiff metallic surfaces, a new materials platform, utilizing the amorphous microstructure of BMGs and the versatility of ion implantation, was developed for the fundamental investigation of cell responses to substrate rigidity variations in the gigapascal range, which was previously unattainable with polymeric materials. The surface rigidity of the Zr-Al-Ni-Cu-Y BMG was modulated with low energy Ar-ion implantation owing to the impartment of Ar nanobubbles into the amorphous matrix. Surface softening was achieved due to the formation of nanobubble-doped transitional zones in the Zr-based BMG substrate. This platform allowed for the investigations on the responses of bone-forming cells to the mechanical variations at the gigapascal level for the first time. Cell adhesion and actin filaments were found to be less established on less stiff surfaces, especially on the surface with an elastic modulus of 51 GPa, whereas faster growth was evidenced by the higher proliferation rate. Findings in this study broadened the understanding concerning the mechanosensing of bone cells on stiff substrates. It also suggests that surface mechano-engineering of metallic materials could be a potential strategy to promote osseointegration of such materials for bone implant applications. More comprehensive investigations with a library of ion-modified surfaces obtained via a combinatorial approach are necessary to further discern the relation between cell responses and mechanical properties of the BMG surfaces.

CHAPTER VI
Zr-Al-Fe-Cu BMG AS A VASCULAR-IMPLANT MATERIAL

Atherosclerosis is caused by plaque build-up in arteries, narrowing or clogging the blood vessel, and leading to insufficient oxygen and nutrient delivery to the end organs [244]. Adverse events of atherosclerotic disease include heart attack and stroke, both of which can be lethal to patients. Stent technology is employed as a typical treatment for atherosclerosis. Vascular stents are typically used to restore the lumen of a narrowed or clogged blood vessel in order to diminish the pressure difference within the vessel and to provide sufficient oxygen and nutrients to the end organs. Surgical interventions with stents have achieved great success to counteract atherosclerosis. Currently, materials used in US Food and Drug Administration (FDA) approved stents are mainly metallic materials including stainless steels, nitinol alloys, Co-alloys, Pt-Ir, etc. [36, 245]. Despite the prevalent uses of these alloys in current stent-assisted angioplasty, many issues persist during clinical practices. For example, mechanical failures to the stents can occur due to the pulsatile loading from the vessel wall [246]. The aggressive body environment can lead to corrosion and release of toxic metal ions of some constituent elements (i.e., Ni, Mo, etc.), raising questions regarding their long-term biocompatibility [247]. Moreover, the major difficulty that remains for current stent materials is the occurrence of thrombosis and restenosis. These post-surgical complications are caused by aggregation of platelets around the material and the dysfunctional proliferation of smooth muscle cells, both giving rise to re-narrowing of the lumen [248, 249]. The development of drug eluting stents to locally release anti-inflammatory therapeutics (i.e., heparin, paclitaxel, sirolimus, etc.) provides a short-term solution [35]; yet later-stage complications (i.e., late stent thrombosis or restenosis) have been reported [250, 251]. To intrinsically reduce stent failure caused by material incompatibility, there has been continuous research from a materials perspective to achieve stent materials with higher performance and biocompatibility [35]. In general, the desired properties of future stent materials were proposed as: 1) high elasticity to facilitate *in vivo* stent expansion from its collapsed form, 2) high strength and fatigue resistance to withstand the pulsatile pressure from the blood vessel wall, 3) radiopacity or magnetic resonance imaging (MRI) compatibility for *in vivo* imaging, 4) good biocompatibility to diminish thrombosis and restenosis, and 5) drug delivery capacity to further treat the implantation site if necessary [35, 36].

The emergence of BMGs provides new opportunities for the development of biomedical materials. A large number of studies were reported revealing the biocompatibility of BMGs and their perspective as hard-tissue prostheses [19, 20, 56, 68, 120]. However, limited data are available regarding their potential as soft-tissue implants [20]. By comparing the materials properties of BMGs with the aforementioned desired properties of stent materials, it is recognized that the properties of BMGs satisfy the requirements for stent applications to a great extent. BMGs satisfy the general requirements for stent applications. BMGs exhibit high elasticity with elastic strains as high as 2% [252], almost twice the value for crystalline alloys. High strength is a characteristic property of BMGs, which can reach up to 5 GPa [15, 16, 253]. Another feature of BMGs to highlight for stent applications is their high MRI compatibility. An earlier study has demonstrated that Zr-based BMGs exhibited a definitive shape as compared to the distorted configuration of a Cu-4Cr-2Nb crystalline alloy under MRI [55]. Moreover, BMGs are easily amenable for surface modification and functionalization [69, 254]. However, the capability and biocompatibility of BMGs in the context of potential stent materials remain unexplored.

To bridge the gap of knowledge, the newly-developed $Zr_{62.5}Al_{10}Fe_5Cu_{22.5}$ BMG [129] was identified as the model material. The initial cytocompatibility and inflammatory responses of this Ni-free Zr-based BMG and has been demonstrated in a previous study [129] and earlier in this dissertation. In this task, application-specific properties were characterized to study the Zr-based BMG as a candidate vascular stent material, including the mechanical properties, corrosion resistance, and surface characteristics. Biocompatibility of the Zr-based BMG was examined through *in vitro* assays using HAECs and HASMCs. The 316L stainless steel was employed as the reference material, due to the longest history and dominant market share of stainless steels as stent materials [36]. For denotation purposes, the $Zr_{62.5}Al_{10}Fe_5Cu_{22.5}$ BMG and 316L stainless steel were abbreviated as ZrAlFeCu BMG and 316L SS.

6.1 Mechanical Properties of the Zr-Al-Fe-Cu BMG

During service, vascular stents experience loadings from blood vessel walls, which pose requirements on their mechanical properties. The microhardness and compression behavior of ZrAlFeCu BMG were plotted in Figure 42. The microhardness of the ZrAlFeCu BMG was measured to be 4.5 GPa, in comparison with the 2.4 GPa of

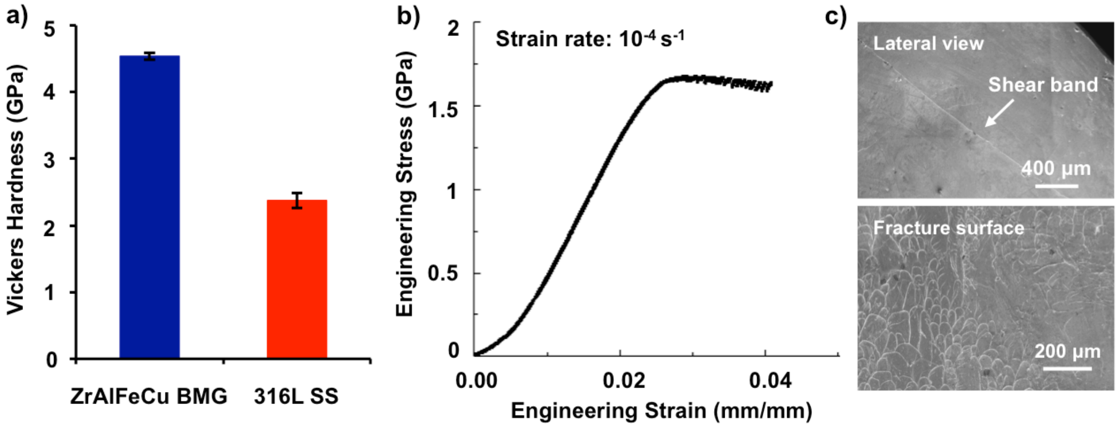

Figure 42 Quasi-static mechanical properties of the ZrAlFeCu BMG: a) Vickers hardness in comparison with 316L stainless steel; b) engineering stress-strain curve; and c) SEM observations of fractured sample.

316L SS (Figure 42a). Under quasi-static compression, the ZrAlFeCu BMG showed the yield strength of 1.7 GPa, the elastic limit of 2%, and the Young's modulus of 80 GPa, as revealed by the compressive stress-strain curve (Figure 42b). The high strength of the Zr-based BMG greatly enables the production of stents with thinner struts, which benefits its deliverability. In addition, it has been demonstrated that the use of thinner struts can reduce the rate of restenosis [35, 255, 256]. It is also worth mentioning that high elastic limit of about 2% and low Young's modulus indicated that the elastic deformation with external loading was facilitated. The fracture morphology of ZrAlFeCu BMG under compression was characterized by shear banding visible on the lateral surface and vein pattern on the fracture surface of the material, which are shown in Figure 42c.

In addition to the quasi-static mechanical testing, the ZrAlFeCu BMG was examined with cyclic loading in this study, as vascular stents usually endure cyclic pulsatile loading from the blood vessel wall after deployment. It is known that fatigue fracture can occur to materials after a certain number of cycles even when the imposed stresses are much lower than the yield strength. The applied stresses concentrate at defects, introducing accumulation of fatigue damage to the material and eventually resulting in catastrophic failure. For vascular stents, the typical requirement for their fatigue life is 10 years of equivalent use at 72 beats per minute or at least 380 million cycles [257]. To experimentally characterize the fatigue endurance of the ZrAlFeCu BMG, the fatigue process was accelerated by increasing the frequency of the cyclic loadings in practical measurements. Compression-compression fatigue behavior of ZrAlFeCu BMG was illustrated in Figure 43. It was manifested in Figure 43a that, below

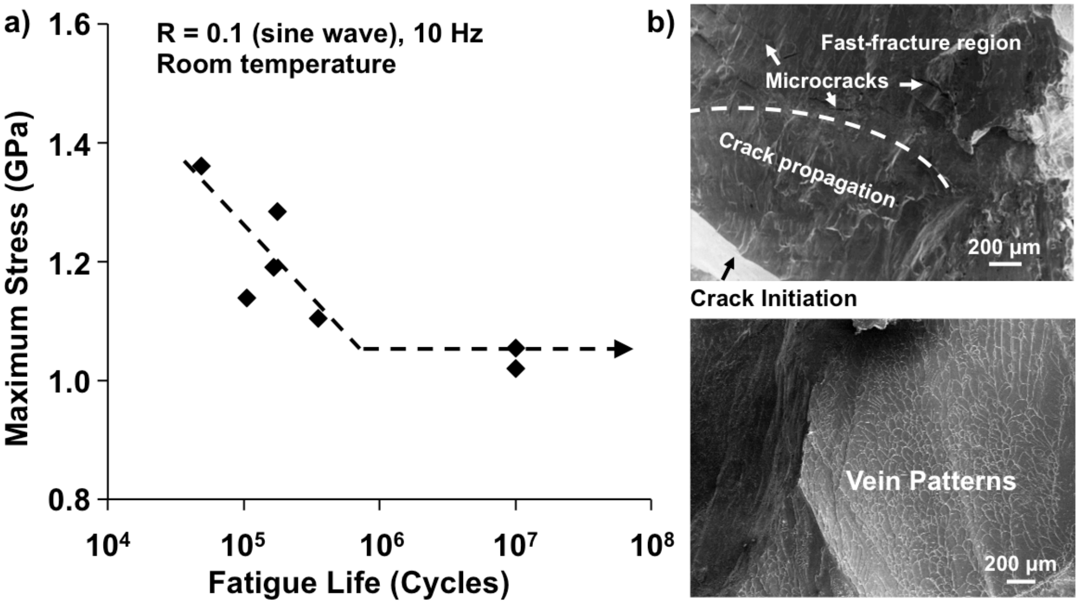

Figure 43 Fatigue behavior of ZrAlFeCu BMG: a) stress-fatigue life (S-N) curve under cyclic compression-compression loading; and b) fractography of specimen failed at a maximum applied stress of 1.36 GPa.

the maximum applied stress of 1.054 GPa, the ZrAlFeCu samples were able to survive 10^7 cycles of loading. The 10^7 cycles are commonly chosen to represent the fatigue life of a material at fatigue endurance limit [258]. At maximum applied stresses higher than 1.054 GPa, samples failed within 10^6 cycles. The fractography of a representative sample failed at the maximum applied stress of 1.360 GPa was analyzed (Figure 43b), featuring the crack initiation site on the surface of the sample, a small portion of crack propagation with relatively smooth morphology, and a rough fast-fracture region with typical vein patterns. In comparison with the fatigue strengths of 316L stainless steel typically lower than 500 MPa under different loading conditions [259, 260], the high endurance limit of ZrAlFeCu BMG (> 1 GPa) under cyclic loadings further qualified this material as a stent material in terms of its mechanical properties.

6.2 Finite Element Analyses of the Zr-Al-Fe-Cu BMG Stent

To gain insights into the mechanical behaviors of future stents made from Zr-based BMG under physiologically relevant loadings, FEA was employed to model the distributions of Von Mises stress and maximum principle strain over a fully expanded stent. A truss-like stent configuration shown in Figure 44 was employed for FEA analysis. The distributions of Von Mises stress and maximum principle strain were modeled over a fully expanded stent under applied pressure loads ranging from 50 - 150 mmHg to simulate the diastolic and systolic pressures from the vessel, according to ASTM F2477 [173]. The maximum Von Mises stress on the ZrAlFeCu BMG stent was found to be approximately 65 MPa under 150 mmHg pressure loading (Figures 44a and b), which was similar to the maximum stress of around 67 MPa for 316L SS (Figure 44c).

a) Von Mises stress distribution of the ZrAlFeCu stent (whole model)

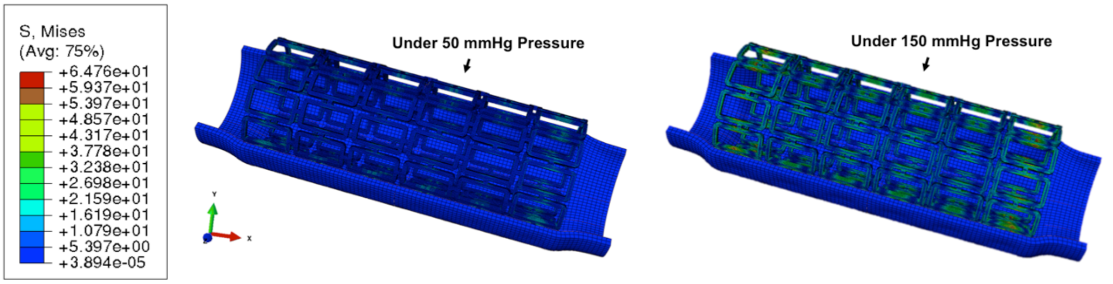

b) Von Mises stress distribution of the ZrAlFeCu stent

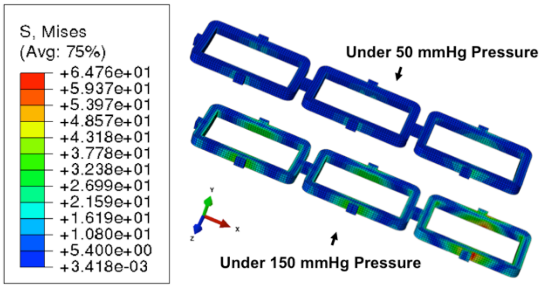

c) Von Mises stress distribution of the 316L SS stent

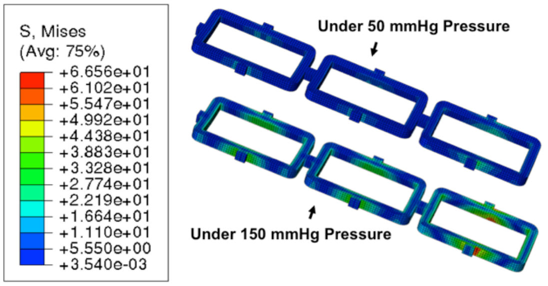

d) Maximum principle strain distribution of the ZrAlFeCu stent

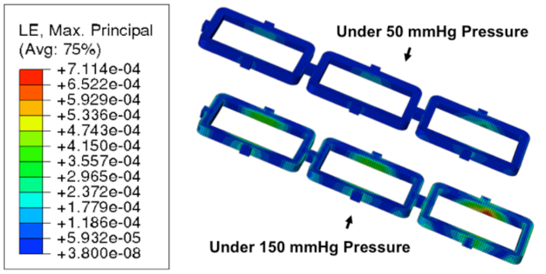

e) Maximum principle strain distribution of the 316L SS stent

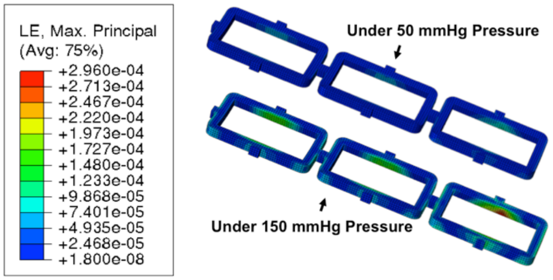

Figure 44 Finite element analyses on the Von Mises stress (a-c) and maximum principle strain (d, e) distributions of ZrAlFeCu BMG (a, b, d) or 316L SS (c, e) stent under 50 or 150 mmHg pressure load.

The maximum Von Mises stress on the ZrAlFeCu BMG-based stent was comparable to that on the 316L SS stent, and was significantly lower than the yield stress and fatigue endurance limit of the ZrAlFeCu BMG. The results indicate that such BMG-stent can sustain the physiological loadings, and it is possible to further reduce the strut thickness of the stent. The maximum strain on the ZrAlFeCu BMG stent, as shown in Figure 44d, was predicted to be 7.1×10^{-4}. In contrast, the maximum strain on a 316L SS stent was estimated to be near 3.0×10^{-4} (Figure 44e). The maximum principle strains on stents made of both materials were much smaller than their elastic limits, implying that the deformation of stent with the blood vessel would be constrained within elastic region. However, the strain for ZrAlFeCu BMG was found twice as large as that for 316L SS, which suggested that the stent made of ZrAlFeCu BMG could be more flexible and deformed more easily with the blood vessel during beats. This was owing to the lower Young's modulus of the ZrAlFeCu BMG, which made it a more compliant material for stent applications. The "compliance mismatch" between the native artery and the stent was reported to be correlated with intimal hyperplasia, particularly at the distal end of the stent [261]. The use of a more compliant material as the base material for stent fabrication, in addition to the design of different geometries for compliance matching stents, would be beneficial to improve stent biocompatibility [261, 262]. It should be noted that the present FEA study was based on one type of stent configuration in its deployed form to showcase the potential mechanical advantages of BMG-based stent over 316L SS-based stent. Future FEA studies should be carried out to aid the selection of stent design parameters most suitable for BMG materials and guide the development of BMG-based prototype stents with improved mechanical performance. Examples of such simulation studies include modeling Zr-based BMG stents using different configurations relevant to clinically used stents [263], their complex strain conditions in crimped forms, during expansion, and after deployment [264], and the mechanical impact of stenting to a pathogenic blood vessel [174].

6.3 Corrosion Behavior of the Zr-Al-Fe-Cu BMG

In order to maintain the mechanical integrity of the stent and hinder the production of metal ions and corrosion products that can be toxic to cells or tissues, requirements on the corrosion resistance have been imposed to indwelling stent materials. The corrosion behavior of the ZrAlFeCu BMG was characterized in comparison with 316L SS in PBS solution, which contained the major ions present in the blood plasma [265]. The corrosion behavior of the ZrAlFeCu BMG was summarized in Figure 45. Prior to polarization, the recorded OCP of ZrAlFeCu BMG was shown to increase with time (Figure 45a), indicating that the stability of the ZrAlFeCu BMG surface was enhanced after immersion in the PBS solution. The polarization curves for both alloys (Figure 45b) displayed spontaneous passivation, and the passive region observed for the ZrAlFeCu BMG was much wider than that for the 316L SS. However, the passive films were found susceptible to pitting at specific threshold potentials at which a steep increase of current density in the polarization curves occurred. Such threshold potential, commonly known as pitting potential (E_{pit}), along with other corrosion parameters, including corrosion potential (E_{corr}) and pitting overpotential (E_{pit} - E_{corr}), were derived from the polarization curves and presented in Figure 45c. The pitting overpotential is a gauge of pitting resistance, the higher value of which indicates higher pitting resistance.

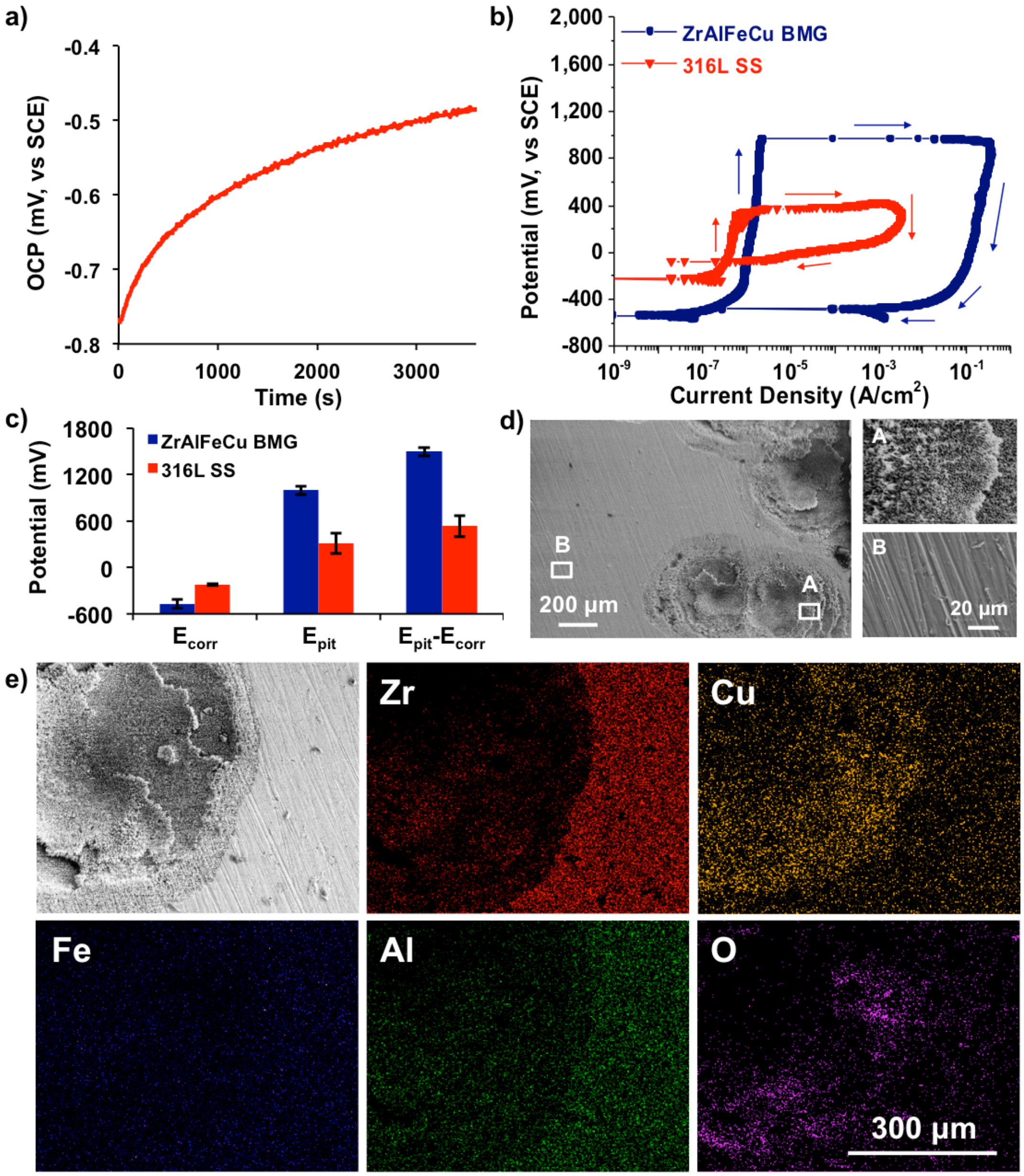

Figure 45 Corrosion characteristics of the ZrAlFeCu BMG: a) open circuit potential (OCP) with time; b) corrosion polarization curve and c) corrosion parameters in comparison with 316L stainless steel; d) SEM images showing corrosion morphology; and e) EDX maps of Zr, Cu, Fe, Al and O.

ZrAlFeCu BMG exhibited a pitting overpotential around 1500 mV, which was found more than twice that of 316L SS (~ 600 mV), proving the high corrosion resistance of the Zr-based BMG. It is worth noting that, during reversed scan (Figure 45b), the polarization curves of ZrAlFeCu BMG and 316L SS crossed the curves of their respective forward scans at E_{corr}, indicating that both materials possessed slight repassivation capability. Higher corrosion resistance of ZrAlFeCu BMG compared to that of 316L SS was demonstrated by polarization test, suggesting the improved stability and inertness of the alloy in the aggressive physiological environment. In addition, the large passive region of the ZrAlFeCu BMG indicated high stability of the passive film of this material.

As shown in Figure 45d, SEM examination of the corroded BMG sample revealed the formation of corrosion pits on the surface and the typical honeycomb structure within the pit, which was commonly observed in the corrosions of Cu-containing Zr-based BMGs [45, 50]. EDX mapping in Figure 45e showed enrichment of Cu in the pit and depletion of other alloying elements. The regional enrichment of O implied the formation of corrosion products in forms of oxides. The EDX measurements indicated that the corrosion process of the ZrAlFeCu BMG was similar to the one proposed in our previous studies, which involved the breakdown of passive film due to Cl^- attack, the preferential dissolution of alloying elements and the formation of metastable CuCl and subsequent CuO as a result of hydrolysis [45, 50].

6.4 Surface Characterizations of the Zr-Al-Fe-Cu BMG

The corrosion resistance of the ZrAlFeCu BMGs can be attributed to the formation of the passive films on the surface of the alloy, which is akin to the corrosion-resistant mechanism of other Zr-based BMGs [45]. The XPS spectra (Figure 46a), both survey and narrow scans, showed the presence of O, Zr, Al and Cu, and the absence of Fe on the surfaces of as-cast and PBS-immersed ZrAlFeCu BMG. C peaks were also detected due to the inevitable contamination. Moreover, the chemical states of each element were analyzed by deconvolutions of the narrow scan spectra (Figure 46b). O1s peaks were found composed of peaks for O^{2-} and OH, which were responsible for metal oxides (M_xO_y) and the hydroxyl groups (-OH) on the sample surface. Zr3d narrow scan spectrum was consisted of doublets of Zr 3d5/2 and 3d3/2, corresponding to the peaks of ZrO_2 (Zr^{4+}) and metal Zr (Zr^0). The peaks for Zr^0 tended to disappear on immersed sample. Similarly, peaks for Al2p were analyzed, showing the presence of Al_2O_3. Cu existed mainly in the form of metal, with formation of a small amount of oxides after immersion. The concentration of each element was quantified in Figures 46c and d. The compositions of passive films formed on both as-cast and immersed ZrAlFeCu BMG surfaces were mainly ZrO_2 with small amounts of Al_2O_3 and Cu/CuO_x. After immersion, Zr content increased and Al content decreased in the passive film. In addition, a higher amount of hydroxyl groups was found on the immersed surface.

The tendency of pitting, although at very high anodic potential, was also rooted from the susceptibility of ZrO_2 and Al_2O_3 to the attack of Cl^- in the solution. When comparing the surface chemistry of the Zr-based BMG before and after immersion in

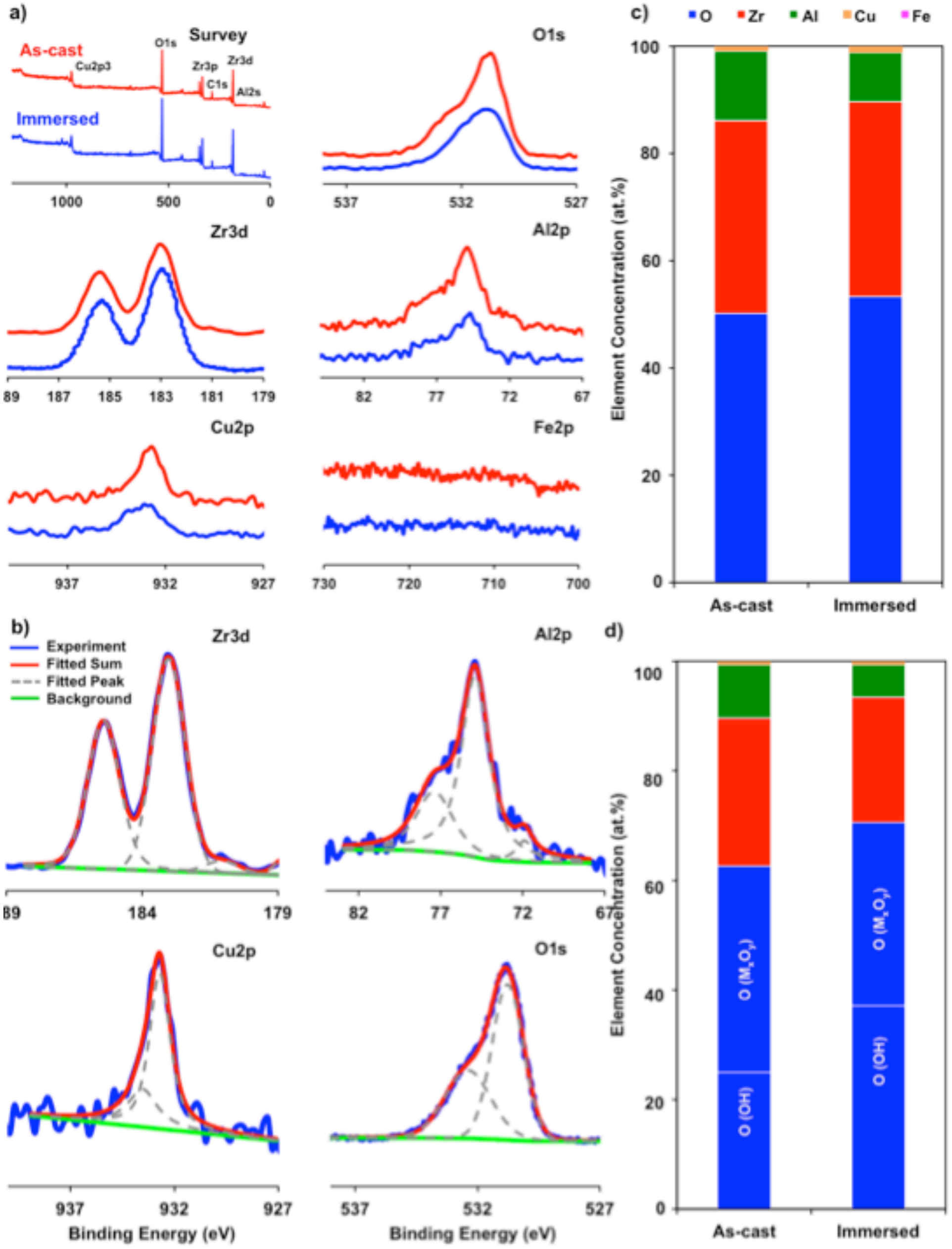

Figure 46 XPS surface chemical analyses of the ZrAlFeCu BMG: a) representative XPS survey spectra and narrow scans for O1s, Zr3d, Al2p, Cu2p, and Fe2p; b) deconvolution of narrow scan spectra for as-cast ZrAlFeCu BMG; c) quantifications on the concentrations of different elements excluding surface hydroxyl groups; and d) elemental quantifications of surface compositions including hydroxyl groups.

PBS, an increased Zr:Al ratio (ZrO_2:Al_2O_3) was observed in the passive film formed in PBS. It has been reported that ZrO_2 formed on pure Zr is nobler and more resistant to Cl^- induced pitting than Al_2O_3 on pure Al [266]. Therefore, this increase in Zr content suggested that the passive film formed in PBS solution is more stable than that formed in air, further proved by the experimental observation of increased OCP with time during immersion (Figure 45a). Overall, the corrosion resistance of ZrAlFeCu was considered sufficient to provide a stable substrate for the stent material to survive in and induce minimal chemical interruptions to its surrounding in *in vivo* environment.

Contact angles of DI water and DII on ZrAlFeCu BMG and 316L SS were presented in Figure 47a. The water contact angle on ZrAlFeCu BMG was measured to be around 50°, which was slightly lower than the 56° of 316L SS, indicating good surface hydrophilicity. Water-contact angles on both substrates were lower than the Berg limit ($\theta = 65°$) [27]. The average contact angles for the nonpolar DII liquid were read as 37° and 35° for ZrAlFeCu BMG and 316L SS, respectively. SFEs and its polar and dispersive components for both substrates were plotted in Figure 47b, as calculated using the contact-angle data. Considering hydrophobic surfaces are characterized by low SFE (up to 50 mN/m) [267, 268], the calculated SFEs of ZrAlFeCu BMG and 316L SS being higher than 50 mN/m further imply that both surfaces are hydrophilic. No statistically significant differences were found for the wettability and surface free energy between the two groups of materials.

Surface properties are not only directly related to the corrosion resistance of metallic materials, but also affect the thrombosis and neointimal hyperplasia [36]. It has

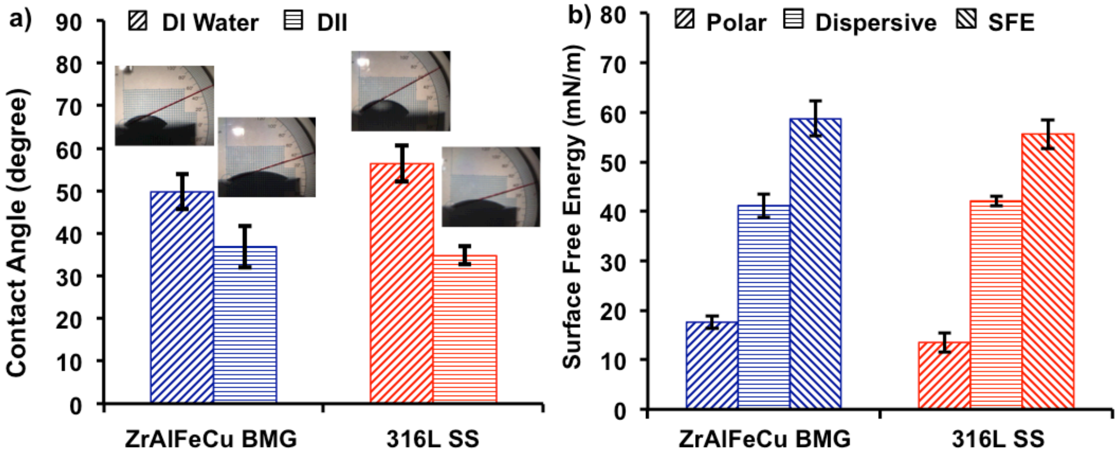

Figure 47 Surface wettability of ZrAlFeCu BMG and 316L stainless steel: a) deionized (DI) water and diiodomethane (DII) wetting behavior (insets: shadow images of droplets); and b) surface free energy (SFE) with its polar and dispersive components.

been reported that the stability of the oxide film determines the release of metal ions, which can induce activation of platelets and leukocytes [36]. Therefore, higher stability of the passive film would account for the biocompatibility of the material, which rationalizes the benefit of the highly-stable ZrAlFeCu BMG surface. In addition, surface wettability and SFE play a critical role in regulating biological response on biomaterial surfaces [2]. In the context of stent materials, SFEs directly influence hemocompatibility of biomaterials. For example, Kwok and co-workers reported that by doping diamond-like carbon (DLC) films with phosphorus, the SFE of DLC film increased from 42.9 to 72.4 mJ/cm^2 and an improvement in hemocompatibility of the DLC film was observed [50]. Recently, Shabalovskaya et al. evaluated wettability and surface energy of native Nitinol surfaces and their results suggest a positive correlation between the polar component of SFE and the hemocompatibility of Nitinol [51]. In fact, the significance of surface properties is evident from many of the surface modification-based strategies striving to improve vascular stent performances [2, 8, 52].

6.5 Endothelial and Smooth Muscle Cell Viability and Proliferation on the Zr-Al-Fe-Cu BMG

Vascular stents are in direct contact with the inner walls of blood vessels that are naturally lined with endothelium formed by endothelial cells. Research has shown that stent coverage with an endothelial cell layer can greatly reduce the risk of restenosis and thrombosis [38, 269]. However, in the event of excessive proliferation of smooth muscle cells triggered by acute inflammatory responses to stent placement, restenosis could occur and lead to implant failure [270, 271]. Therefore, appropriate cell behavior of vascular endothelial and smooth muscle cells to promote endothelial cell coverage and reduce restenosis are essential to stent integration, which justified our choices of HAECs and HASMCs for the cell culture studies.

Live/Dead staining revealed that adherent HAECs and HASMCs on both ZrAlFeCu BMG and 316L SS substrates are highly viable (Figure 48). It indicated that both substrates exhibited no cytotoxicity and supported the attachment of HAECs and HASMCs within a relatively short timeframe of 24 h. For both cell types, the number of adherent cells was qualitatively higher on the ZrAlFeCu BMG substrate than on the 316L SS substrate.

The proliferation behavior and metabolic activities of the HAECs and HASMCs over a longer time period were monitored from days 1 to 5 using WST-1 assay and SEM observation, as shown in Figure 49. The histograms for WST-1 results for HAECs in Figure 49a presented significantly higher cells metabolic activities on the ZrAlFeCu BMG, which was correlated to a higher number of cells, than on 316L SS at all three time points. From days 3 to 5, it was noticed that the metabolic activities of HAECs reached plateau on the ZrAlFeCu BMG, whereas continuous growth was observed on 316L SS. Nevertheless, the HAEC metabolic activities on 316L SS were still significantly lower than on the ZrAlFeCu BMG at day 5. The SEM images in Figure 49c illustrated the growth of HAECs into larger populations with incubation time, however, with different proliferation behaviors on the two different substrates. HAECs on ZrAlFeCu BMG started with a larger population at day 1, with cell-cell interactions readily observed. Cell interactions to a larger extent can be observed and cells tended to merge into a confluent layer on the ZrAlFeCu BMG at days 3 and 5. On 316L SS, a lower number of adherent

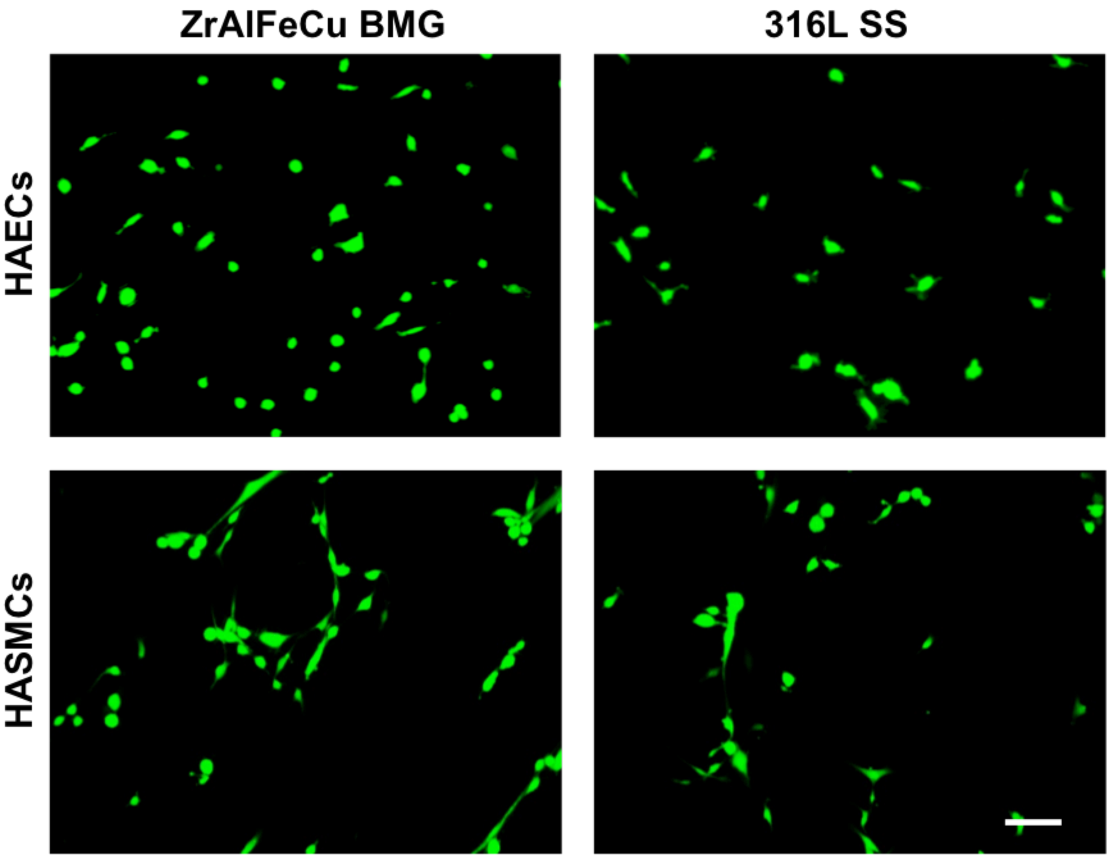

Figure 48 Live/Dead staining (green/red) showing cell viability of HAECs and HASMCs on indicated substrates after 24 h of culture (Scale: 100 μm).

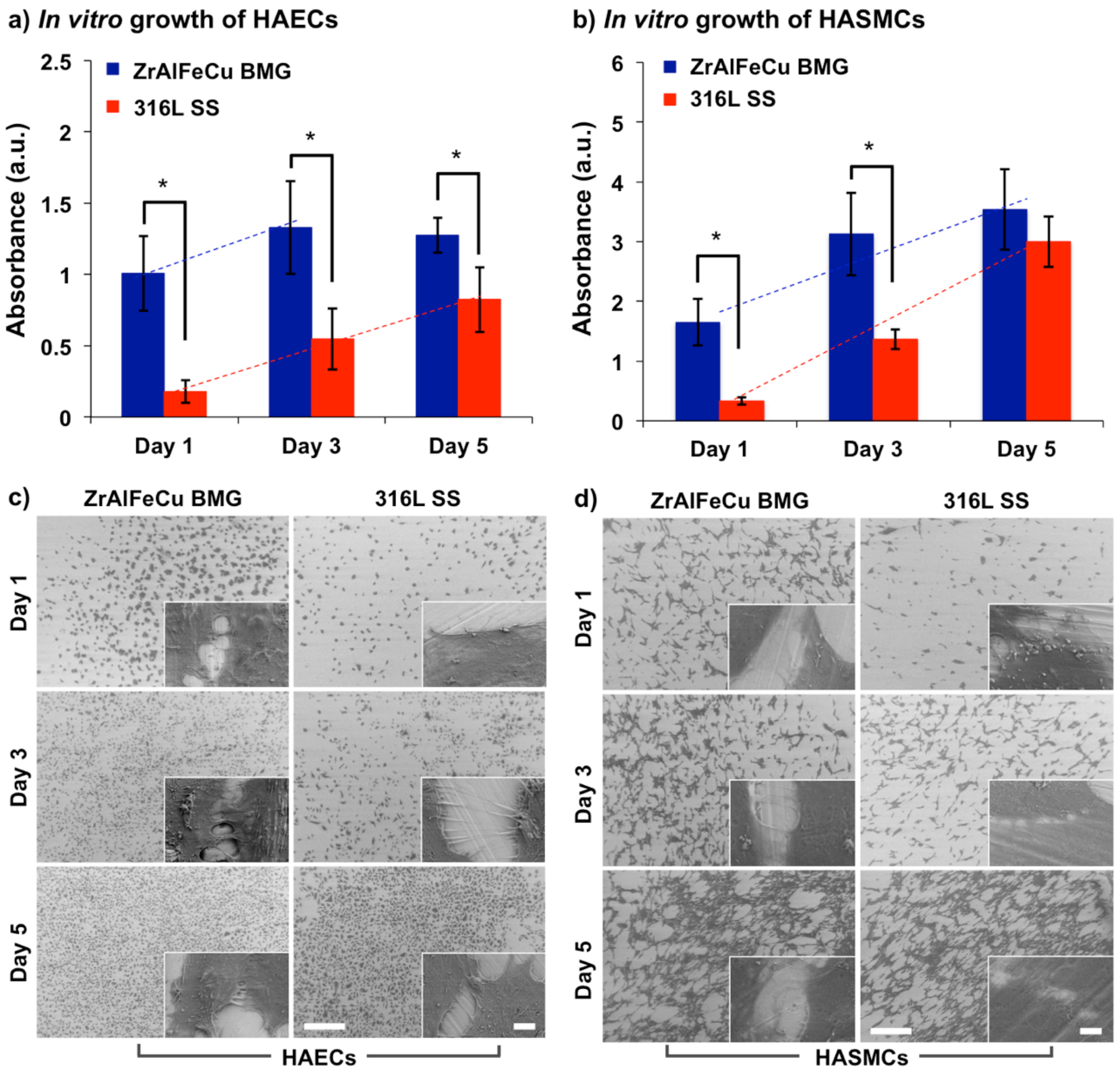

Figure 49 Proliferation studies of vascular cells HAECs (a, c) and HASMCs (b, d) on indicated substrates over a period of 5 days: a-b) Cell metabolic activity measured by the WST-1 assay (data presented as Mean ± STDEV; *denotes statistically significant differences at $p < 0.05$; n = 3); c-d) SEM images showing cell morphology (scale bars: 500 μm in large images and 5 μm in insets).

cells were observed with individual cells extending short filopodia. The cell-cell interactions can be observed on 316L SS at day 3, as they interacted through long and thin filopodia. This interaction was enhanced on day 5 and cells were approaching confluency. The SEM observations were in agreement with the WST-1 assay results.

Similarly, HASMC proliferation was examined and manifested in Figures 49b and d. HASMCs proliferated on both substrates during the investigated timeframe. At days 1 and 3, numbers of cells were significantly higher on ZrAlFeCu BMG than on the 316L SS. Cell reached near-confluency at day 5, with comparable metabolic activities of HASMCs on both substrates as demonstrated by WST-1 assay and direct visualization of the cultures under SEM. SEM images in Figure 49d also presented HASMC interactions with each other at each time point.

Comparing the proliferation behaviors of different types of cells on ZrAlFeCu BMG and 316L SS, the benefits of using the Zr-based BMG as a potential stent material were disclosed. Fast rate to reach confluency of HAECs was found on the ZrAlFeCu BMG, as concluded from the WST-1 assay. At day 5, the plateau in metabolic activities on ZrAlFeCu BMG can be explained by the contact inhibition of HAECs [272]. It has been established that sparse endothelial cells are in active growth mode, while confluent cells switch themselves to survival mode requiring lower energy [272] and, hence, lower metabolic activities. In fact, the SEM observations revealed an increase in the number of HAECs from days 3 to 5. Although the proliferation rate (slope of the dashed line in Figure 49a) of HAECs on ZrAlFeCu BMG was slightly higher than that on 316L SS, the greater number of initially adherent cells led to an earlier formation of confluent HAEC layer on the Zr-based BMG surface than on 316L SS. This suggested faster re-endothelialization on the Zr-based BMG and can be beneficial for successful implant integration. Research has shown that re-endothialization of the stent can greatly reduce the risk of restenosis and thrombosis, whereas lack of re-endothelialization is usually an indicator of stent failure [38]. Conversely, the proliferation rate (the slope of the dashed line in Figure 49b) of HASMCs was found lower on ZrAlFeCu BMG than on 316L SS. Despite the higher number of adherent cells on the BMG surface at day 1, HASMCs reached near-confluency at day 5 on both substrates. Combining the results of the two experiment sets, it was established that the ZrAlFeCu BMG supports faster HAEC coverage but slower HASMC growth, as compared to 316L SS, which suggested a lower risk of restenosis on the Zr-based BMG.

A number of factors were postulated to be responsible for the different cell behaviors on ZrAlFeCu BMG and 316L SS, including but not limited to surface chemistry, corrosion resistance, microstructure, and mechanical properties. The major constituents of the ZrAlFeCu BMG surface were ZrO_2 and Al_2O_3, which are also known as the biomedical ceramics, zirconia and alumina. In fact, zirconia and alumina have been successfully applied as coating materials to improve the corrosion resistance and biocompatibility of biomedical stainless steels [273-276]. This can be related to the higher biocompatibility of the ZrAlFeCu BMG over 316L SS in our study. Moreover, the apparent differences in microstructure and mechanical properties between the two materials could also contribute to the different cell responses, which need further investigation to fill the knowledge gap. The underlying mechanism governing the initial cell attachment and proliferation on the Zr-based BMGs in comparison with those on 316L SS would also be an interesting subject for future research.

6.6 Endothelial Cell Adhesion under a Dynamic Setting

Besides proliferation, the strength of HAEC adhesion on the two different substrates was studied. The cells or cell layer adherent on the stent surface suffer from the flow of blood, which creates shear force to potentially affect cell adhesion and proliferation after stent deployment [277, 278]. In the present work, the quality of cell adhesion to the substrate was indirectly evaluated by forcing a shear stress to the cell layer under flow of culture medium.

Representative fluorescent images (Figure 50a) elucidated the cell adhesion with and without the effect of shear stress. Semi-quantifications on cell parameters, including cell numbers, alignments, spread areas, perimeters, and circularities, were performed based on the fluorescent images. Denudation of endothelial cells from each substrate after the flow test was evidenced in Figure 50b. The remaining fractions of cells adherent on ZrAlFeCu BMG and 316L SS were found to be 87% and 75%, respectively. Therefore, the adhesion of HAECs was found stronger on the ZrAlFeCu BMG, as the fraction of remaining cells was higher than on 316L SS after flow test.

As shown in Figure 50c, the angle between the long axis of cell nuclei and flow direction was shifted to smaller angle ranges on both substrates, indicating that cells were realigned under the shear stress of the flow towards flow direction. The tendency of realignment is more prominent on 316L SS. The average angle between the long axis of cell and flow direction was reduced from 44° to 31° on ZrAlFeCu BMG and 25° on 316L

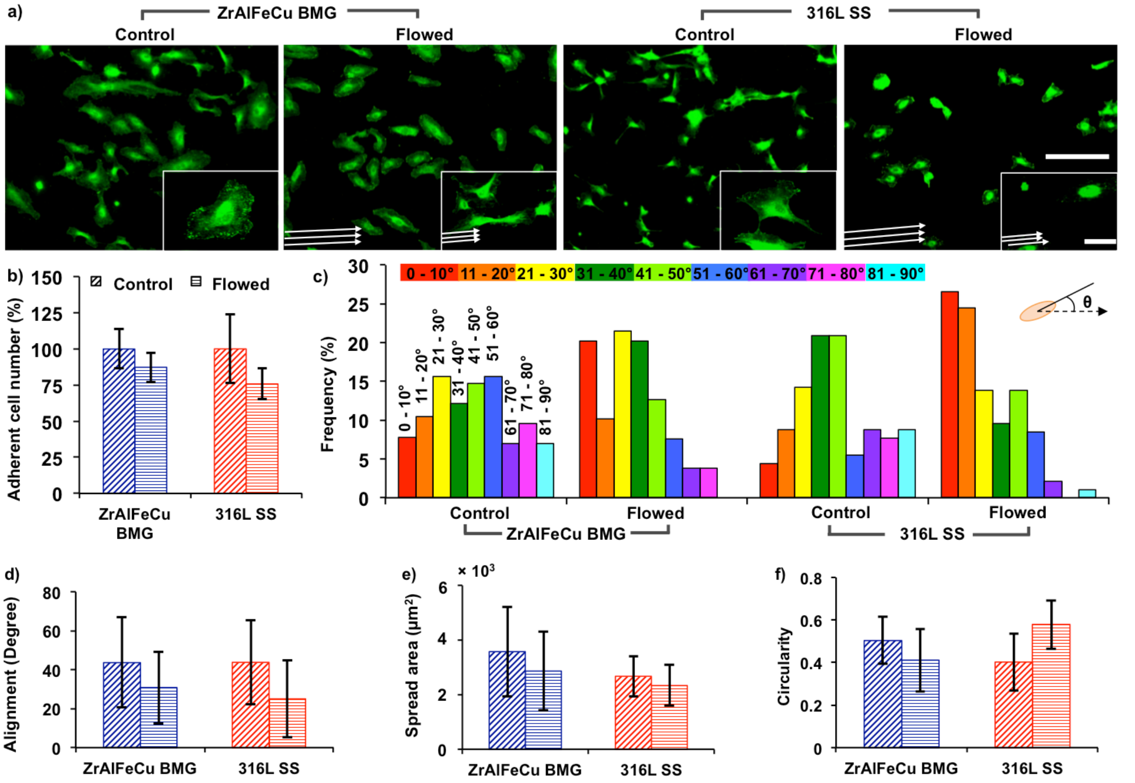

Figure 50 HAEC adhesion after 2 h flow test: a) immunostained focal adhesions of HAECs on indicated substrates (scale bars: 200 μm; white arrows indicate flow directions); b) number of adherent cells before and after flow test (Mean ± STDEV, results were normalized to those obtained on non-flowed control sample within each group); and c) histograms of the absolute cell orientation angle relative to the long axis of the specimen or the flow direction obtained from analysis of over 80 cells per group (inset: schematic presentation of the cell nuclei orientation angle measurement); d) cell alignment with respect to the flow direction; e) cell spread area; and f) circularity (data in d-f were presented in the form of Mean ± STDEV, n > 50).

SS, respectively (Figure 50d). The stronger tendency of cell realignment under the flow observed for the 316L SS substrate suggested that HAECs on 316L SS were more susceptible to the effect of flow than on ZrAlFeCu BMG, likely resulting from a weaker interaction between HAECs and 316L SS.

Furthermore, the fluidic flow induced morphological changes to the adherent HAECs. The HAECs exhibited a well-spread morphology on ZrAlFeCu BMG under static incubation as shown in Figure 50a. Under the effect of the shear stress, the average spread area was also reduced on both substrates (Figure 50e). These cells were also found more polarized after flow with a decrease in average circularity from 0.5 to 0.4 on ZrAlFeCu BMG, but more rounded up on 316L SS with an increase in average circularity from 0.4 to 0.6 (Figure 50f). The alteration in polarity of the cells was possibly owing to the loss of focal adhesion sites to a certain degree. The initially large spread area of HAECs on ZrAlFeCu BMG may contribute to the higher quality of adhesion. In contrast, the originally more polarized HAECs on 316L SS during static incubation (Figures 50a) were found to be smaller but more circular after flow. The flow induced morphological changes of HAECs may be associated with changes in other cell behaviors such as adhesion, division, metabolism, ion channel activation, protein expression, et al. [279], which require further examination on ZrAlFeCu BMG.

6.7 Conclusions and Future Work

In the present study, the potential of a Ni-free Zr-Al-Fe-Cu BMG to serve as vascular stent material was exploited for the first time. The mechanical property of the Zr-based BMG was featured by high strengths under both quasi-static and cyclic loadings, facilitating the design of stents with thinner struts to feasibly reduce the risk of restenosis. Complementary FEA results on a specific stent configuration further verified the mechanical advantages of the high-strength Zr-based BMG, and additionally revealed its compliance with the beat of the blood vessel wall, as compared with 316L stainless steel. Corrosion resistance of the Zr-based BMG was found significantly higher than that of medical 316L stainless steel, indicating its high stability in the *in vivo* environment, which was attributed to the formation of ZrO_2-rich surface oxide film. *In vitro* cell culture studies revealed the general cytocompatibility of the Zr-based BMG. More importantly, faster coverage of endothelial cells and slower growth of smooth muscle cells were observed on the Zr-based BMG than on 316L stainless steel, which suggests promoted re-endothelialization and lower risk of restenosis. In addition, the Zr-based supported stronger endothelial cell adhesion. While these promising findings unveil additional exciting biomedical prospect for the Zr-based BMG, further investigations, both *in vitro* and *in vivo*, are needed before BMG vascular stent becomes a reality. One such study that deserves immediate attention is the evaluation of hemocompatibility of the Zr-based BMG, which is vital for any blood-contacting device.

CHAPTER VII
Cu- OR Ag-BEARING Zr-BASED BMGS AS ANTIMICROBIAL MATERIALS

Antimicrobial properties provide considerable benefits for implant materials. Regardless of the stringent disinfection and surgical protocols, there are still a large number of infections associated with implant devices [39, 40]. Post-surgical infections are considered common complications in surgeries [135, 136]. For example, bacterial infection is among the most serious complications for total hip arthroplasty, which leads to revision procedures, difficulties in bone reconstruction, and high medical costs [135, 136, 280]. The use of antimicrobial materials to combat the growth of bacterial cells on biomedical alloys will reduce the occurrence of peri-implantitis, which can not only reduce the infection associated morbidity and mortality rates but also abate the medical costs. In an effort to achieve intrinsic and long-lasting antimicrobial materials, alloys containing heavy metal elements with toxicity to microorganisms (i.e., Cu, Ag, Zn, etc.) were developed [281, 282]. However, their large-scale utilization was difficult due to the high cost associated with the noble elements, poor mechanical properties, as well as their susceptibility to corrosion [283]. Surface engineering approaches have also been attempted to modify traditional alloys, such as stainless steels and Ti alloys [284], yet the high cost and the lack of durability of which needs to be taken into consideration for viable long-term applications. Hence, the design and development of novel alloys coupling properties for sustainable performance and antimicrobial abilities remain a highly active area of research for materials scientists.

The emergence of Zr-based BMGs offers a new opportunity to achieve materials with the aforementioned desirable traits. Their potential and favorable properties to serve as biomedical implant materials were elaborated in the previous sections. In addition, Zr-based BMGs can be potentially antimicrobial. A close examination of the compositions of Zr-based BMGs reported to date reveals the frequent inclusions of heavy metal elements to tune various materials properties. For example, Cu is commonly alloyed in Zr-based BMGs to attain good glass formers [42]. The addition of Ag was found to be a glass-formation enhancing element in Zr-based glass-forming systems [116]. The presence of these biocidal elements implies that there may be antimicrobial potential of BMGs.

The antimicrobial behavior of two groups of heavy-metal-containing Zr-based BMGs, including Cu-bearing $(Zr_{0.55}Al_{0.10}Ni_{0.05}Cu_{0.30})_{100-x}Y_x$ (x = 0 and 1) BMGs and the Ag-bearing $Zr_{53}Al_{16}(Co_{0.75}Ag_{0.25})_{31}$ BMG, were investigated in this task against the Gram positive bacterium *S. aureus*. *S. aureus* is frequently found on people and animals and recognized as one of the most common organisms affecting implants and causing surgical infections [285]. Therefore, it was rational to study the antimicrobial properties of Zr-based BMGs against *S. aureus*, aiming at their biomedical applications. To the author's best knowledge, the research in this task reported for the first time the antimicrobial behavior of BMGs against a Gram positive bacterium in the context of healthcare oriented applications.

7.1 Antimicrobial Properties of Cu-bearing Zr-based BMG

Cu has been known as a biocidal reagent since ancient times [286]. In this subtask, the $(Zr_{0.55}Al_{0.10}Ni_{0.05}Cu_{0.30})_{100-x}Y_x$ (x = 0 and 1) BMGs, which were a group of Zr-based BMGs well studied in previous research [50, 68], were selected as the model material system. The high concentration of Cu around 30 at.% was postulated to impose potential antimicrobial potency to the materials. The results were compared with commercial biomedical Ti-6Al-4V alloy and pure Cu, which served as negative and positive controls, respectively. For denotation purposes, the $Zr_{55}Al_{10}Ni_5Cu_{30}$ and the $(Zr_{0.55}Al_{0.10}Ni_{0.05}Cu_{0.30})_{99}Y_1$ BMGs were labelled as ZrCu-BMG and ZrCuY-BMG.

7.1.1 Substrate characterizations on the Cu-bearing Zr-based BMG

Surface properties of a substrate material affect the adhesion of bacterial cells. The surface properties of the $(Zr_{0.55}Al_{0.10}Ni_{0.05}Cu_{0.30})_{100-x}Y_x$ (x = 0 and 1) BMGs have been investigated in a previous research from our group [68]. The surface SFEs were found comparable amongst the Zr-based BMGs and the Ti-6Al-4V [68]. In this study, in order to achieve comparable surface finish and surface topography, all test samples were processed with the same polishing technique. The ridge-groove structure on all samples as a result of grinding can be observed in AFM topography images (Figure 51a). The spacing between neighboring valleys, which are the projection of ridges, was measured to be around 10 - 20 μm in the line profiles (Figure 51b). The average surface roughness ranged between 130 to 160 nm for the polished substrates.

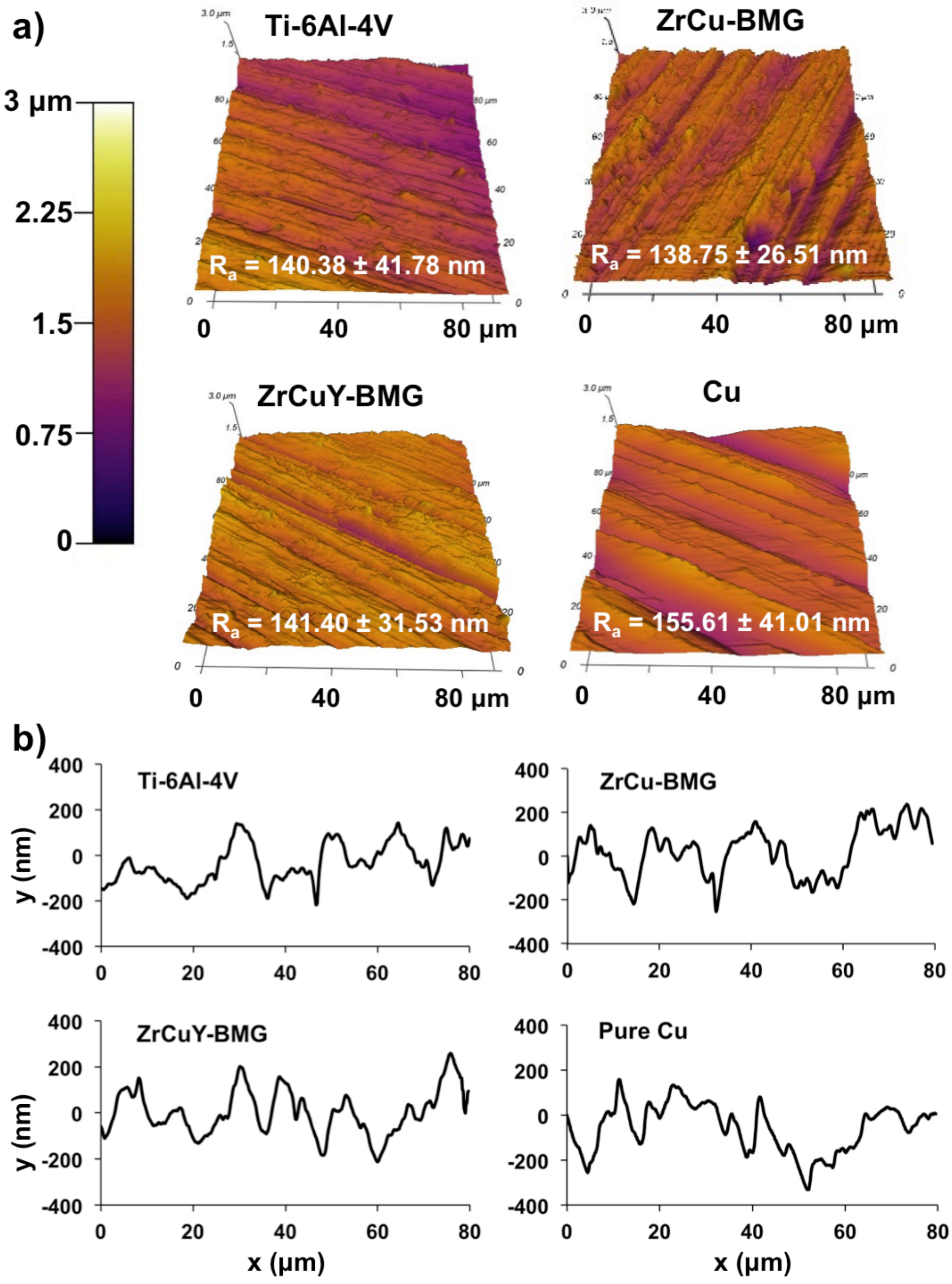

Figure 51 AFM measurements on a) 3D topography images and average surface roughness (R_a) values, and b) line profiles for the ZrCu- and ZrCuY-BMGs, Ti-6Al-4V alloy, and pure copper substrates.

7.1.2 Bacterial culture studies on the Cu-bearing Zr-based BMG

The antimicrobial effects of the Cu-bearing Zr-based BMGs were examined with ATCC 6538 *S. aureus* at room temperature under two experimental settings, including static moist contact and dynamic immersion. The results of bacterial killing after 4 h of moist contact were shown in Figure 52. Significantly lower numbers of CFUs were found on Zr-based BMGs, as compared to the negative control of Ti-6Al-4V alloy. Approximately one order of magnitude lower for the ZrCu-BMG and a half order of magnitude lower for the ZrCuY-BMG were observed than that found on Ti-6Al-4V substrate. The killing efficiency for pure Cu was potent as no viable cells were observed after 4 h of contact. It was noticeable that smaller population of bacteria survived on ZrCu-BMG than on ZrCuY-BMG, which suggested a higher killing ability for the ZrCu-BMG. Representative photos of the CFUs on agar plates were presented in Figure 52b, showing the variations in the CFU populations after contact with the metallic substrates. A direct comparison can be made based on the images, which was in agreement with the quantification results, which confirmed the antimicrobial activity of the Cu-bearing Zr-based BMGs after 4 h of contact.

The numbers of CFUs and representative photos of CFUs on agar plates after 24 h of dynamic immersion were presented in Figure 53. Results from the dynamic-immersion tests, revealed little Cu-induced bacterial killing effect for the Zr-based BMGs, despite the presence of Cu in the compositions. Comparable populations of CFUs were observed on the Zr-based BMGs and Ti-6Al-4V alloy. Biofilm formations of *S. aureus* were observed on all of the substrates after 1 day of immersion. Thus, bacteria were capable of

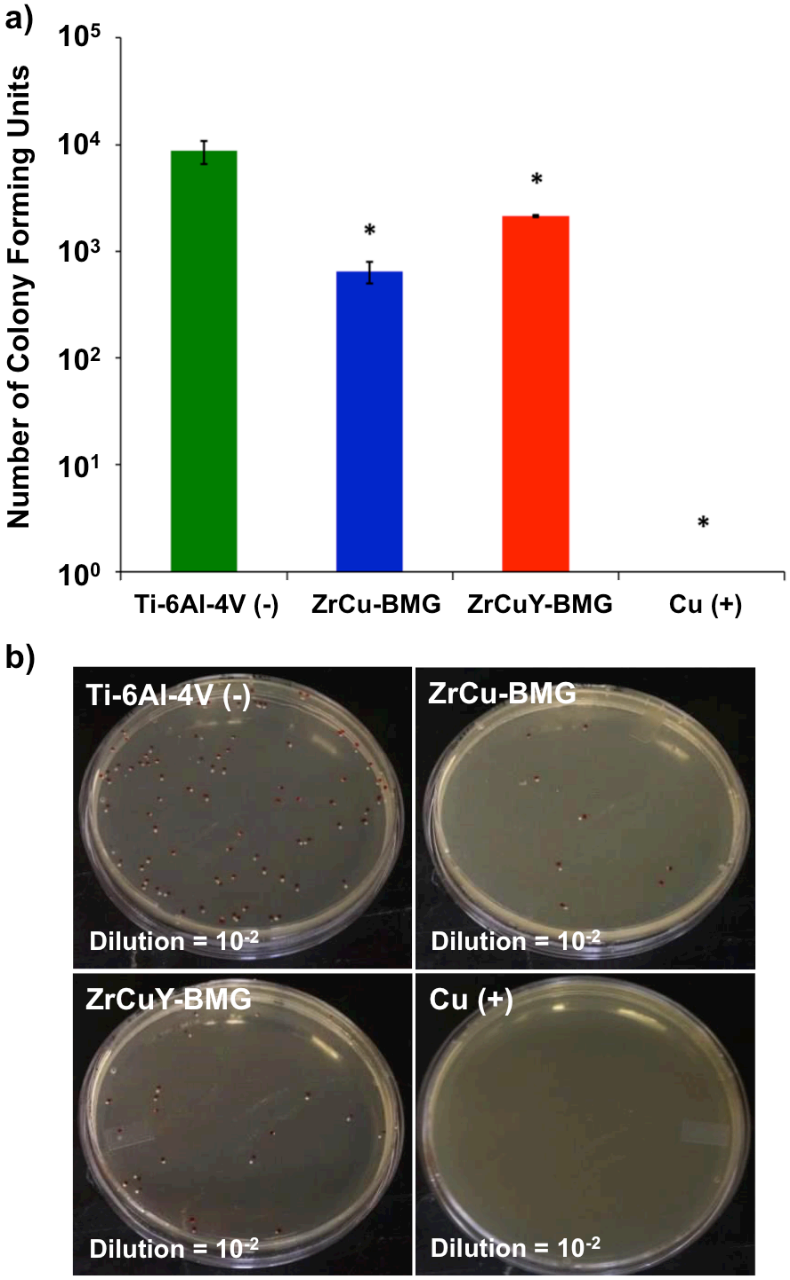

Figure 52 a) Number of colony forming units (CFUs) of *S. aureus* (Mean ± STDEV, * denotes statistically significant differences at $p < 0.05$, statistical analysis was performed with respect to the results for Ti-6Al-4V); and b) representative photos of CFUs on BHI agar plates (dilution = 10^{-2}) on indicated substrates after 4 h of contact at 25 °C.

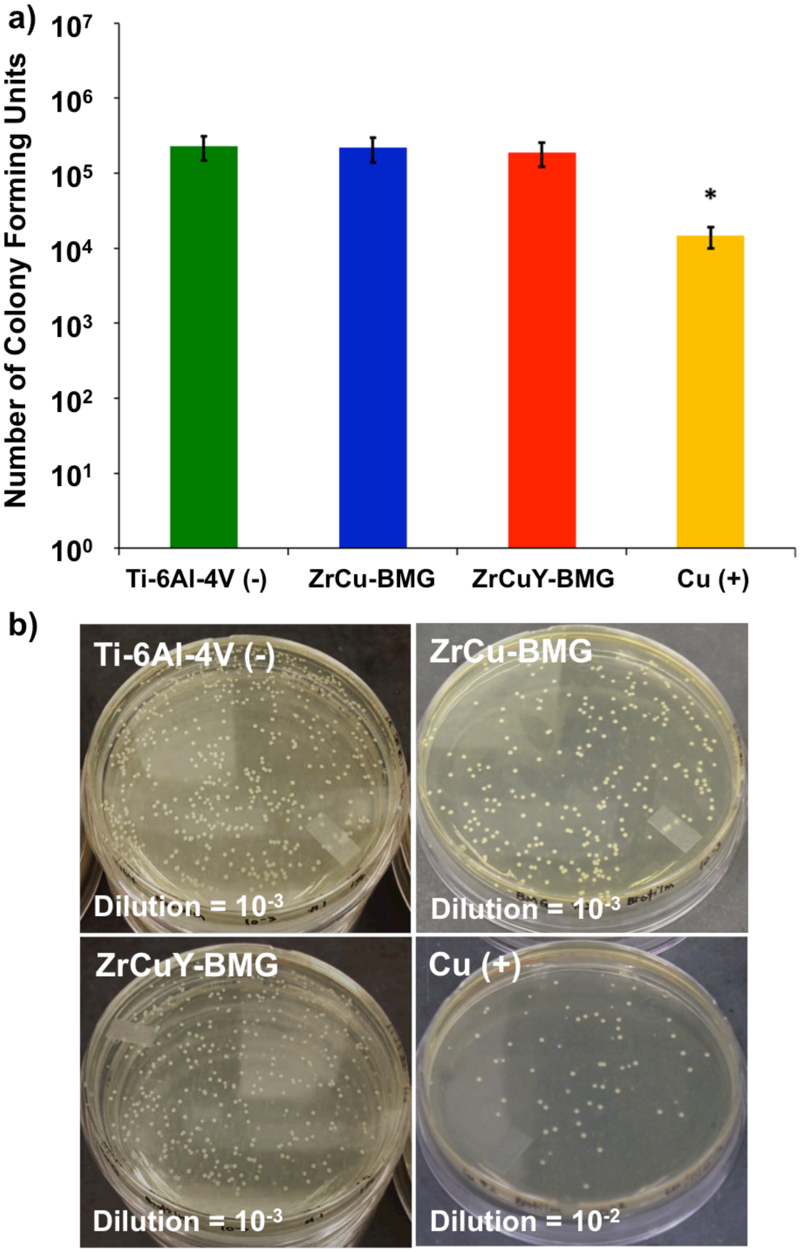

Figure 53 a) Number of colony forming units (CFUs) of *S. aureus* on indicated substrates (Mean ± STDEV, * denotes statistical significance at $p < 0.05$, statistical analysis was performed with respect to the results for Ti-6Al-4V), and b) representative photos of CFUs on BHI agar plates (dilution = 10^{-3} for BMGs and Ti64, dilution = 10^{-2} for Cu) after 24 h of dynamic immersion at 37 ^{o}C adhering to BMG surfaces. Reduction in the number of viable bacterial cells was only observed on pure Cu samples with a much smaller population of CFUs present on Cu surfaces after incubation. In this experimental setting, the bacteria-killing effect of the Zr-based BMGs was absent despite the presence of 30 at.% of Cu. Pure Cu exhibited killing effect after 24 h of dynamic immersion, with the number of CFUs decreased by more than one order of magnitude, as compared with Ti-6Al-4V and Zr-based BMGs. Since the dynamic immersion conditions used in the present study could be more severe than those usually encountered *in vivo*, the antimicrobial performance of Zr-based BMGs under a less aggressive condition may exhibit distinguishable killing effect.

7.1.3 Antimicrobial mechanism of the Cu-bearing Zr-based BMG

To further understand the killing mechanism of the Zr-based BMGs, the bactericidal efficiency was directly correlated with the concentration of Cu ions released into the surrounding environment. The profiles of Cu-ion release from the two Zr-based BMGs and pure Cu were recorded as a function of immersion time, as shown in Figure 54. The cumulative amounts of Cu ions increased in PBS for both pure Cu and Cu-containing BMGs over the time of immersion. The amounts of Cu ions dissociated into PBS from pure Cu were significantly greater than from both Zr-based BMGs at all three time points, which was consistent with the higher rate of cell death of *S. aureus* on pure Cu and the lack of antibacterial effect for the Zr-based BMGs after 1 day of dynamic immersion. The insufficient amount of Cu ions released by the Cu-bearing Zr-based BMGs in the solution was considered to be below the critical value to cause damage of *S. aureas*. Therefore, it was concluded that the increased amount of Cu ions was responsible

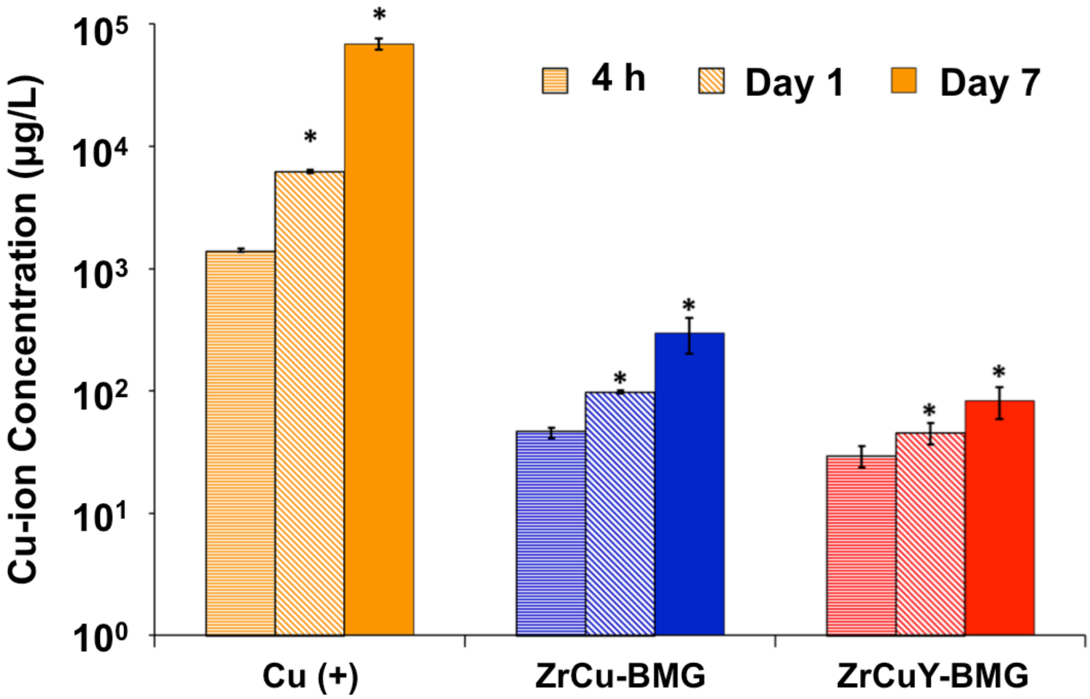

Figure 54 Amounts of Cu ions released from the Cu and Cu-containing Zr-based BMGs as a function of immersion time in PBS at room temperature (Mean ± STDEV, l denotes statistically significant differences at $p < 0.05$, statistical analysis was performed with respect to the results obtained at 4 h for each group).

for the effective bacterial killing by pure Cu in both moist contact and dynamic immersion assays. The cumulative Cu-ion concentrations dissolved from the Zr-based BMGs and pure Cu at 4 h were determined to be about 30 - 60 μg/L and 10^2 μg/L, respectively. At day 1, approximately 10^2 μg/L of Cu ions were detected for both Zr-based BMG samples, in contrast with the 10^4 μg/L for pure Cu. The difference was even greater (three orders of magnitude) after 7 days of immersion. When comparing the results between the two BMG samples, a statistically larger amount of released Cu ions was detected for ZrCu-BMG than ZrCuY-BMG, though the differences were less than one order of magnitude. This observation agreed with the previous findings that Zr-BMG exhibits a higher corrosion penetration rate than that of ZrCuY-BMG in PBS [50].

The main killing mechanisms of Cu ions were proposed for the biocidal effect of Cu [282, 287, 288], including: 1) the interference to the permeability of cell membrane, 2) the degradation of genomic and plasmid DNA, 3) oxidation or damage of sulfhydryl group (i.e. Fe-S cluster), and 4) the generation of reactive hydroxyl radicals through a Fenton-type redox reaction:

$$Cu^{+} + H_2O_2 \rightarrow Cu^{2+} + OH^{-} + OH^{\bullet}$$

These radicals can then cause oxidation of proteins and lipids. A schematic representation illustrating the antimicrobial mechanisms of Cu was presented in Figure 55. The use of Cu as antimicrobial agent is advantageous, since Cu ions disrupt bacterial cells in a general manner, instead of targeting particular enzymes or pathways. Such a generalized mode of action decreases the risk of bacterial resistance [282, 286, 287].

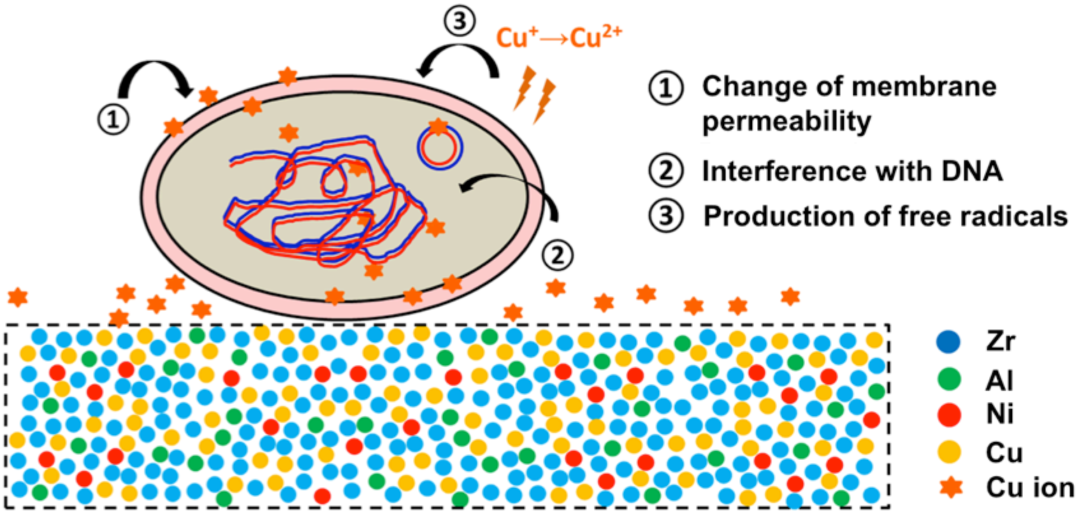

Figure 55 Schematic presentations (not to scale) for the possible antimicrobial mechanisms of Cu ions released from a Zr-based BMG substrate.

The dependence of *S. aureus* viability on the concentration of Cu^{2+} concentration has been previously reported [289]. A decrease in the number of viable bacteria was related to the increase in $CuSO_4$ concentration. It was noted that different experiment settings could also lead to significant variations in bacterial metabolism and death. For example, the viability of *S. aureus* in TSB was found to be much higher than that in defined medium at the same Cu-ion concentrations [289]. The critical Cu^{2+} concentration to induce cell death in TSB broth in their study was approximately 100 mg/L, whereas the effective concentration in our dynamic immersion assay was lower, indicating that the killing mechanism of Cu or Cu-containing alloys was more complicated than solely Cu^{2+} killing, and may include the contributions from Cu^{+}, free radical, etc., as discussed above, which requires further investigations.

It is worth mentioning that samples were completely dried after 4 h of incubation during the contact assay. Therefore, other killing mechanisms may have been involved at the later stage of contact, in addition to the initial Cu-ion killing on the wet surface. Research has shown that dry copper surfaces provide different antimicrobial properties than Cu ions [288, 290]. It was proposed that dry Cu surfaces could pose a killing capability to those bacteria with an increased level of resistance against Cu ions [288, 290]. Therefore, the double strikes from both ionic Cu and dry Cu surfaces may lead to a more effective biocidal approach. Meanwhile, it would be less likely for the bacteria to develop resistance to both killing mechanisms.

7.2 Antimicrobial Properties of Ag-bearing Zr-based BMGs

Ag has been shown to be much more efficient at inhibiting bacterial growth than Cu. Low concentrations of Ag ions as low as 0.1-0.5 ppb was reported to considerably deter bacterial growth [291]. Therefore, work in this subtask was extended to study Ag-bearing Zr-based BMG that may be more potent in regards to its antimicrobial property. Specifically, the $Zr_{53}Al_{16}(Co_{0.75}Ag_{0.25})_{31}$ BMG was selected due to its high glass-forming ability and well-documented mechanical, chemical, and biocompatible properties in a previous joint research of our group [118]. To further understand the antimicrobial mechanisms of the Ag-bearing, the crystalline counterpart of the $Zr_{53}Al_{16}(Co_{0.75}Ag_{0.25})_{31}$ BMG achieved by heat treatment, aiming at distinguishing the effect of the amorphous microstructure on the antimicrobial properties of the Ag-bearing Zr-based BMGs. Ti-6Al-4V alloys and 316 L stainless steels were employed as negative controls, while pure Ag was used as positive control. For denotation purposes, $Zr_{53}Al_{16}(Co_{0.75}Ag_{0.25})_{31}$ BMG, crystallized $Zr_{53}Al_{16}(Co_{0.75}Ag_{0.25})_{31}$ BMG after heat treatment, and 316L stainless steel were termed as ZrAg-BMG, HT-ZrAg, and 316L SS in the following context.

7.2.1 Materials characterizations on the Ag-bearing Zr-based BMG

The microstructures of ZrAg-BMG and HT-ZrAg were examined using XRD as shown in Figure 56. The amorphous microstructure of the as-cast ZrAg-BMG was verified by the characteristic diffusive peak located at a 2-theta of approximately 38°. However, the crystallization of the ZrAg-BMG after 2 h heat treatment was evidenced by the presence of the sharp Bragg peaks, each set of which represented a specific crystalline

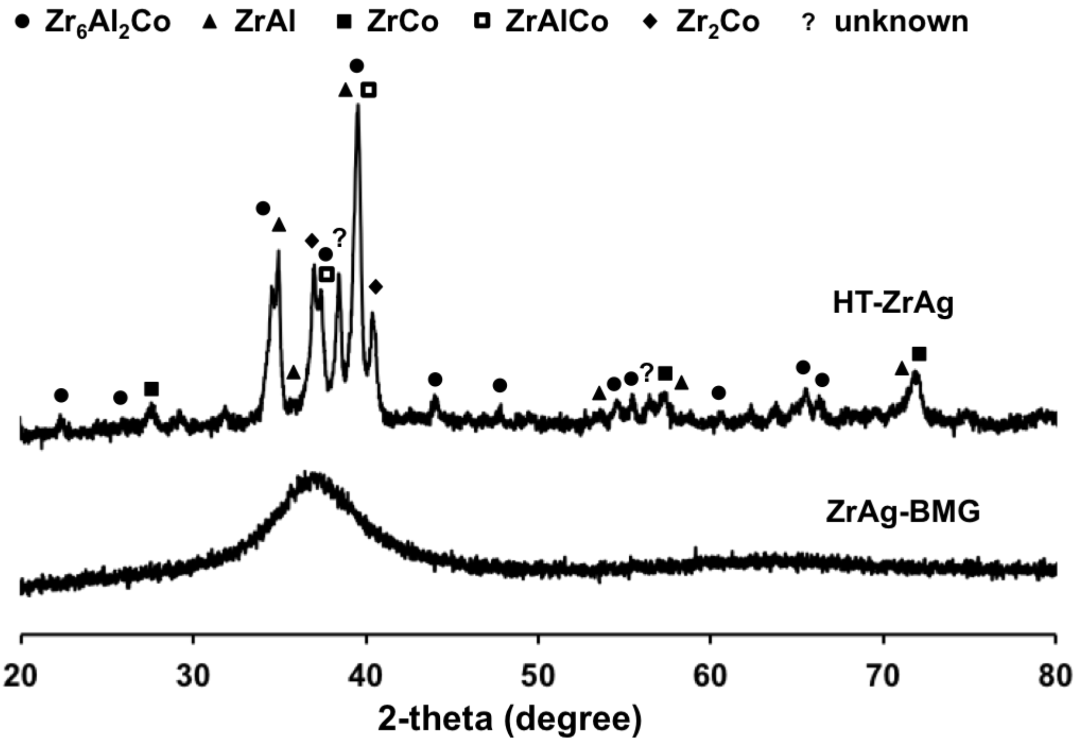

Figure 56 X-ray diffraction patterns for ZrAg-BMG and HT-ZrAg

phase. Formations of Zr_6Al_2Co, ZrAl, ZrCo, ZrAlCo, Zr_2Co, and a portion of unknown phases were identified.

Surface roughness and topography of the testing specimens were measured by AFM and presented in Figure 57a. A similar polishing protocol was employed to achieve the 600-grit surface finish for all substrates. The average roughness (R_a) of the substrates ranged from 100 to 225 nm. The pure Ag surface was found to be the roughest amongst all materials ($R_a = 223.7 \pm 16.5$ nm). The roughness values for the other four alloys were generally comparable to each other, which diminished the potential effect of surface roughness on the subsequent bacterial behavior.

Water wetting behavior and SFE of the alloys were presented in Figure 57b. From the water contact angle measurements, it was determined that all tested substrates were hydrophilic with water contact angles smaller than 60°. The average water contact angle on the ZrAg-BMG was at least 5° smaller than those of HT-ZrAg, Ti-6Al-4V, and 316L SS, indicating a more hydrophilic surface on the ZrAg-BMG. Accordingly, the SFE was higher on the ZrAg-BMG surface than on HT-ZrAg, Ti-6Al-4V, and 316L SS. The differences of the average SFEs were above 3.6 mN/m when comparing the results between ZrAg-BMG and other tested alloys.

The release profile of Ag ions as a function of exposure time from pure Ag or Ag-bearing Zr-based alloys in PBS solution was plotted in Figure 58. Overall, the amounts of Ag-ions released to the solution were increased cumulatively from 2 h to 7 d for all tested substrates, indicating that all three substrates were capable of releasing Ag ions to the

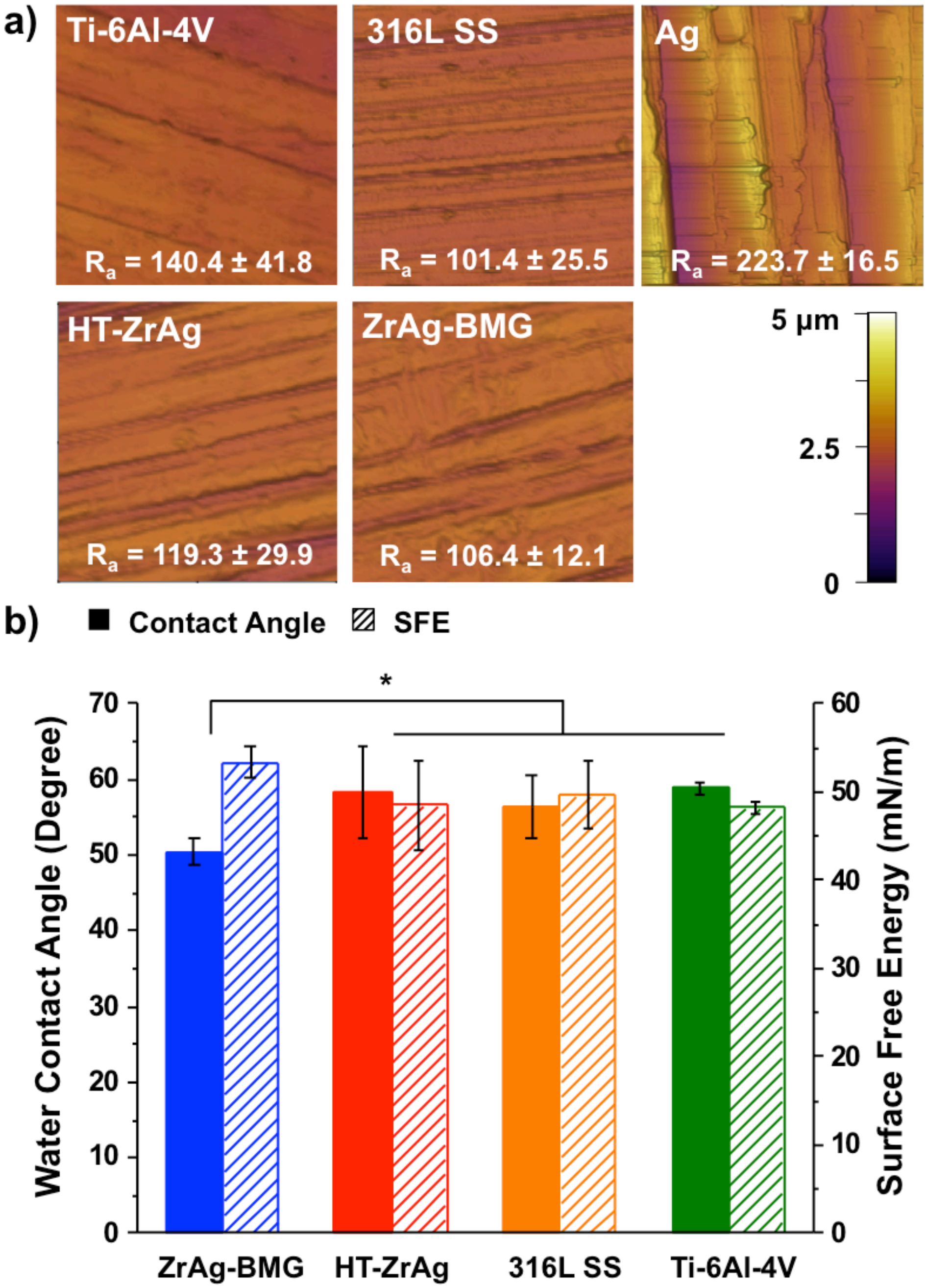

Figure 57 Surface characterizations of indicated substrates: a) AFM topography and surface average roughness (R_a); and b) water contact angle and surface free energy (SFE) (Mean ± STDEV, * denotes statistically significant differences at $p < 0.05$).

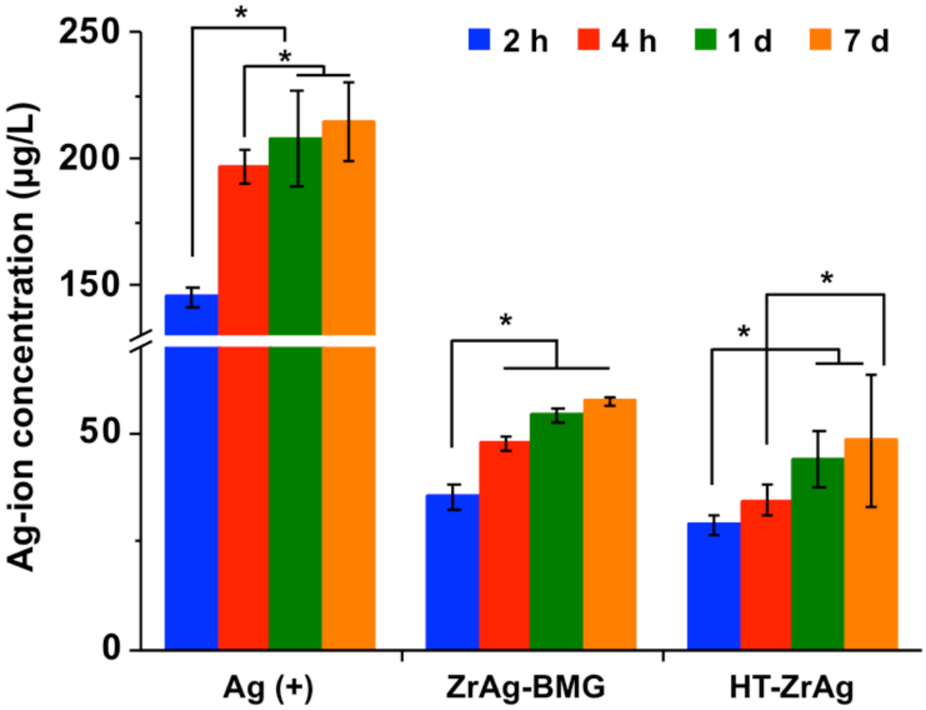

Figure 58 Ag-ion concentrations released from pure Ag and Ag-containing Zr-based alloys as a function of immersion time in PBS at 37°C (Mean ± STDEV, * denotes statistically significant differences at $p < 0.05$).

simulated physiological environment. It was apparent that much higher Ag-ion concentrations were detected for the pure Ag samples than the ZrAg alloys. When comparing the Ag-ion concentrations between solution samples with ZrAg-BMG and HT-ZrAg, the released amount of Ag ions was found constantly lower for HT-ZrAg samples than for ZrAg-BMG sample at shorter time periods up to 1 d. The Ag-ion release from these two ZrAg alloys eventually reached statistical equivalency at 7 d. Regarding the release rate of Ag ions, it was observed that majority amounts of Ag ions were rapidly discharged into the solution from pure Ag and ZrAg-BMG within 4 h of immersion, followed by marginal increases up to 7 d. In contrast, the Ag-ion release rate for HT-ZrAg was found to be much more gradual, with a constant increase from 2 h to 7 d. The different capabilities of the two Zr-Al-Co-Ag alloys to release Ag ions into the surrounding environment are proposed to be related to their surface chemical stability. Similar to the discussion in Section 7.1.3, the higher surface chemical stability, presented by the higher corrosion resistance, constrains the release of metal ions can sustaining the integrity of the material as a whole. A comparison on the corrosion behavior of ZrAg-BMG and HT-ZrAg is demanded to be directly correlated with the results on Ag-ion release.

7.2.2 Bacterial culture studies on the Ag-bearing Zr-based BMG

The antimicrobial effects of the ZrAg-BMG and its crystalline counterpart were examined with *S. aureus* ATCC 6538 at the physiological temperature of 37 °C using moist contact assay. The numbers of viable CFUs after 2 or 4 h incubations were presented in Figure 59a. After 2 h incubation, the number of CFUs on ZrAg-BMG was

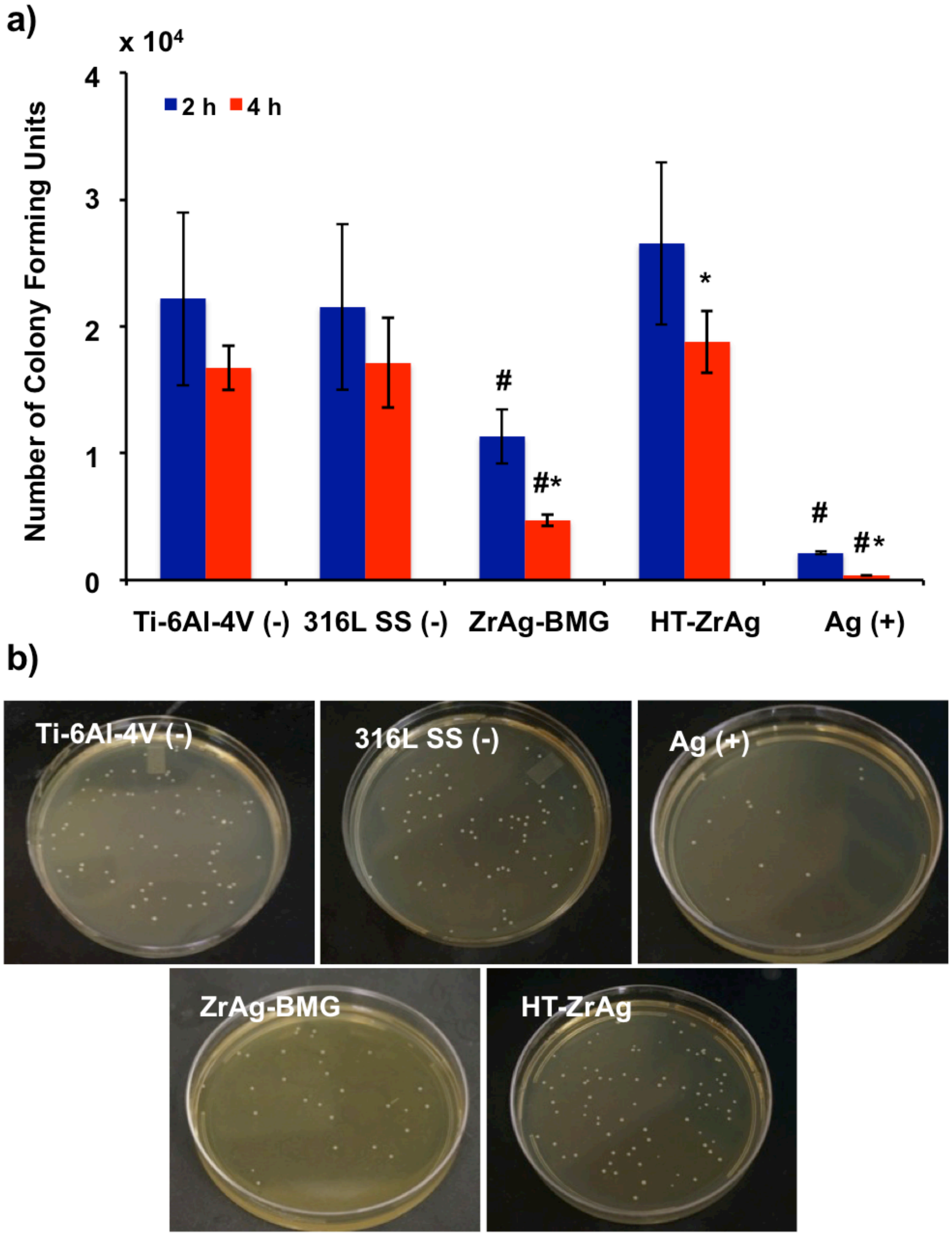

Figure 59 a) Number of colony forming units (CFUs) of *S. aureus* (Mean ± STDEV) on indicated substrates after 2 or 4 h contact; and b) representative photos of CFUs on BHI agar plates (dilution = 10^{-2}) on indicated substrates after 2 h of moist contact at 37°C (Mean ± STDEV, * denotes statistically significant differences in comparisons with corresponding 2 h results, # denotes statistically significant differences in comparison with corresponding results on Ti-6Al-4V, both at $p < 0.05$).

significantly reduced by approximately 50% (or half an order of magnitude), as compared to the negative controls, suggesting its high potency to reduce bacterial infections. On the contrary, bacterial viability on HT-ZrAg was found slightly higher than the negative controls, although not statistically significant. Pure Ag exerted the highest toxicity to *S. aureus* after 2 h incubation with the lowest number of viable CFUs present on the surface, which was 96% or almost two orders of magnitude lower than the negative controls.

With the increase of incubation time to 4 h, a decrease in bacterial viability was observed on all substrates as a result of desiccation. However, a steeper drop in the number of viable CFUs was observed on the ZrAg-BMG. The number of CFUs on ZrAg-BMG at 4 h was 80% or more than one order of magnitude lower than the negative controls at 2 h, and 70% or more than one order of magnitude lower than the negative controls at 4 h. When comparing within the group, the CFU numbers on the ZrAg-BMG at 4 h decreased by two-fold as compared to that at 2 h. A statistically significant decrease in the number of viable bacterial cells (> 30%) was also observed on HT-ZrAg at 4 h in comparison to its 2 h counterpart, which suggested its potential biocidal property, although the number of viable *S. aureus* on HT-ZrAg was still comparable to negative controls at 4 h. The killing efficacy of pure Ag was further enhanced after 4 h incubation, on which a high killing rate of around 99% was observed in comparisons with the negative controls.

Representative photos of the CFUs on agar plates after 2 h incubation on different substrates were presented in Figure 59b. The CFU populations varied after contacts with different materials after 2 h incubation. Overall, the qualitative analyses based on the direct observation of the images agreed with the quantification results of CFUs, which showed an increase in bacterial population and a decrease in antimicrobial efficacy in the following order: pure silver, ZrAg-BMG, HT-ZrAg, and the negative controls.

7.2.3 Antimicrobial mechanisms of the Ag-bearing Zr-based BMG

The most distinctive difference between ZrAg-BMG and HT-ZrAg was the microstructure. The amorphous microstructure may affect the antimicrobial properties of the alloys. An earlier study on the *E. coli* responses to multiple BMG compositions reported that the antimicrobial effects was independent from alloy compositions within their testing ranges, which might, to some extent, originate from their amorphous nature [121]. In our study, we have observed the significantly higher antimicrobial proficiency of the amorphous ZrAg-BMG than the crystalline HT-ZrAg at early time points, which also implied that amorphous microstructure could be a contributing factor to the antimicrobial efficacy. Furthermore, the different antimicrobial properties of ZrAg-BMG and HT-ZrAg may not be simply or solely attributed to the microstructure alterations but also to the concurrent alterations in surface properties (chemistry and hydrophobicity) introduced by vitrification or crystallization.

Surface hydrophobicity and free energy are critical factors influencing the thermodynamics of bacterial adhesion [292, 293]. A thermodynamic model of bacterial adhesion was developed by Absolom et al., which predicted that a linear decrease in the number of adherent bacteria with the increase of substrate SFE when the liquid surface tension was higher than bacterial surface tension [293]. This model was substantiated over a wide span of substrate SFEs ranging from 16.4 to 66.7 mN/m with different bacterial strains including *S. aureus*, *Staphylococcus epidermidis*, *Escherichia coli* (*E. Coli*), and *Listeria monocytogenes* [293]. In general, it was acknowledged that a relatively more hydrophilic material is more resistant to bacterial adhesion than a hydrophobic one [292]. A direct relationship between the numbers of adherent *S. aureus* in TSB and surface free energy of the substrates was reported in a previous study on Ti-6Al-4V alloys [294]. Through UV irradiation, the authors have altered the Ti alloy surface towards more hydrophilic, with an increase in SFE from 33.8 to 59.9 mN/m. Meanwhile, reduction in the adhesion of *S. aureus* was observed on the more hydrophilic surface [294]. Bearing the same concept, we postulate that the higher hydrophobicity and lower SFE of the HT-ZrAg (Figure 57) could be related to a higher number of adherent bacteria (Figure 59) on the surface as compared to those of the ZrAg-BMG. The potentially higher amount of adherent bacterial cells could subsequently lead to less perceptible antimicrobial properties at early time points. However, future research is necessitated to systematically establish and validate the relationship amongst microstructure, surface properties, bacterial adhesion, and the subsequent antimicrobial potency.

In addition to the possible contribution due to bacterial adhesion, the disturbance to the adherent bacteria induced by Ag ions was proposed as an additional antimicrobial mechanism for the ZrAg alloys and pure Ag. The bacterial killing mechanisms of Ag ions against *S. aureus* have been reported in a number of previous studies [291, 295-297]. Major disruptions to bacteria by Ag ions were reported as: the damage of cell membrane components, proteins, or enzymes containing nucleophilic sulfhydryl, hydroxyl, and amine functionalities that are capable of coordinating Ag ions; interference with DNA replication abilities; and displacement of metal ions (i.e., Zn^+ and Ca^{2+}) that are essential to bacterial cell survival [295, 296, 298]. The direct relationship between the killing efficiency of the material and capability to discharge Ag ions was also found applicable in the present research. With the highest amounts of Ag-ion released from pure Ag (Figure 58), the highest rate of bacterial killing was detected (Figure 59). Correspondingly, the slower release and smaller amounts of dissolved Ag ions from HT-ZrAg may partially contribute to its lower antimicrobial properties than that of the ZrAg-BMG. It is noted that comparable amounts of Ag-ion were found in the PBS solutions immersed with ZrAg BMG and HT-ZrAg after 7 days. Therefore, a higher killing rate might be observed for HT-ZrAg with prolonged incubation to allow for a sufficient release of Ag ions. This speculation requires to be verified with further investigations. Moreover, aiming at advancing the bacterial killing efficiency of Zr-based BMGs, compositional design to promote the release of Ag ions can be adopted. This can be realized by increasing the content of Ag in the alloy composition or alloying with nobler metal elements (i.e., Pt, Pd, etc.) to galvanically encourage the production of Ag ions [299]. Nevertheless, the design of biomedically-oriented Ag-containing Zr-based BMGs should take into consideration to counterpoise between the toxicity of Ag ions to microbes and the biosafety to mammalian cells or tissues [300, 301], in order to achieve optimal performance combining antimicrobial properties and biocompatibility. Meanwhile, compositional changes also affect other materials properties of the Zr-based BMGs (i.e., glass forming ability, mechanical properties, corrosion resistance, etc.) [302].

This challenges future alloy design to universally strengthen the material and biomedical advantages of the Zr-based BMG.

7.3 Conclusions and Future Work

The studies in this task revealed the initial antimicrobial effects of Cu-bearing and Ag-bearing Zr-based BMGs against the Gram positive bacterium *S. aureus*. Numbers of CFUs on these Zr-based BMGs were significantly reduced after 2 or 4 h of moist contact, as compared with the non-biocidal Ti-6Al-4V alloy or 316L stainless steel. The killing efficacy of the Zr-based BMGs was directly related to the release of heavy metal ions from the substrate materials, which provided references for the future design of antimicrobial BMGs. In addition, the amorphous microstructure was also found contributing to the antimicrobial properties of the Zr-based BMGs. Future studies will be directed to pinpoint optimal alloy compositions and microstructures aiming at integrating killing effects to bacteria yet maintaining desired materials properties and high biocompatibility to mammalian cells or tissues. More in-depth investigations on the killing mechanisms are also desired.

CHAPTER VIII
CONCLUSIONS AND RECOMMENDATIONS

The advancement in the fabrication techniques of the Zr-based BMGs and their suitable properties encourage their applications as candidate biomedical materials. The research conducted in this dissertation was directed to engineer and probe the properties of Zr-based BMGs to fulfill multiple biomedical functionalities. By coupling experimental approaches with computational simulations, and integrating materials characterizations with biological assays, Zr-based BMGs were investigated for specific biomedical applications as different implant materials, regarding their application-oriented materials properties, interface engineering of Zr-based BMGs through ion beams, and cell responses to these material surfaces.

The discussion of this dissertation was started with the investigation on the potential inflammation triggered by implantation of Zr-based BMGs. Further on, aiming at bone implant applications, ion implantation was employed to impart bioactive elements to the surface of bioinert Zr-based BMGs to enhance the interaction between the substrate material and bone-forming cells. The surface engineering with ion beams was further extended to modify surface rigidity of the Zr-based BMGs, which provided new information to understand rigidity sensing of bone-forming cells on rigid substrates and to regulate cell behaviors. In addition, the opportunity of a Zr-based BMG to serve as a stent material was explored for the first time. Last but not least, the capability of heavy-metal-containing Zr-based BMGs to combat bacterial infection was analyzed. Major conclusions achieved in this dissertation were listed as follows:

Inflammatory responses to Zr-based BMGs:

1. Low levels of macrophage activations were observed on the Zr-based BMGs. In particular, the Zr-Al-Ni-Cu-Y BMG was found to be less stimulatory than Ti-6Al-4V alloys, as evidenced by morphological and biomolecular signs.

2. The presence of environmental stimulus can induce macrophage activation to a greater extent, showing the synergistic effect of external and material stimulations on macrophage behaviors. Macrophages cultured on the Zr-Al-Fe-Cu BMG appeared to be less sensitive to LPS treatment than those on 316L stainless steel.

3. The microstructure of the substrate material can influence macrophage responses. The crystalline Zr-Al-Co-Ag alloy was found to be less stimulatory than the amorphous Zr-Al-Co-Ag BMG to macrophages under LPS treatment in this study.

Ca-ion implantation to induce bioactivity to a Zr-based BMG:

4. The surface atomic structure of Zr-based BMG can be altered by low energy Ca- or Ar-ion implantations, which was revealed by XAS measurements. The change in atomic structure can lead to concurrent modifications of materials properties.

5. Modification of the surface chemistry and the introduction of Ca were realized by Ca-ion implantation. The Zr-based BMG surfaces were altered to be more hydrophobic after irradiation, which was attributed to the reduced amount of hydroxyl groups on the implanted surfaces. Surface hardening, especially after Ca-ion implantation was observed, possibly due to surface structure relaxation.

6. Higher numbers of adherent cells and more pronounced cell adhesion were observed on Ca-ion-implanted substrates, which initially demonstrated the effectiveness of Ca-ion implantation to impart bioactivity to Zr-based BMGs.

Bone-forming cell rigidity sensing on nanobubble embedded Zr-based BMG surface generated by Ar-ion implantation:

7. Ar-ion implantations successfully produced “nanobubble cushions” with a graded distribution on the Zr-based BMG surface, which were composed of nanosized Ar-bubbles embedded in the amorphous matrix.

8. The presence of nanobubbles resulted in surface softening of the Zr-based BMG, as presented by the decreased stiffness, elastic modulus, and nanohardness. The degree of softening was directly related to the concentration and distribution of Ar nanobubbles.

9. Bone-forming cells could perceive and react to mechanical cues on Zr-based BMG surfaces. Less established cell adhesion and actin filament formation yet higher rate of proliferation were found on Zr-based BMG surfaces with lower stiffness.

10. A novel approach to fundamentally investigate cell rigidity sensing on rigid BMG surfaces was demonstrated, the experimental design of which can be guided with SRIM simulation.

Applications of a Zr-based BMG as a stent material:

11. The mechanical advantages of the Zr-based BMG were revealed by experiments and FEA. Its high strength allowed for the design of thinner stent struts with

a lower risk of restenosis. Its low elastic modulus and high elastic limit facilitated elastic deformation of the stent to compliantly deform with beats of blood vessel wall.

12. Due to the formation of the highly stable passive film, the corrosion resistance of the Zr-based BMG in simulated physiological environment was found significantly higher than that of medical 316L stainless steel, indicating its high biostability *in vivo*.

13. The faster coverage of endothelial cells and slower growth of smooth muscle cells were observed on the Zr-based BMG than on 316L stainless steel, which suggested promoted re-endothelialization and potentially lower risk of restenosis on the Zr-based BMG.

14. Under the shear stress generated by the flow of the culture medium, endothelial cell adhesion was found to be stronger on Zr-based BMG than on 316L stainless steel, suggesting that the cell layer on Zr-based BMG stent surface may undergo fewer disruptions from the blood flow.

Antimicrobial properties of heavy-metal-containing Zr-based BMGs:

15. The initial antimicrobial potency of heavy-metal-containing Zr-based BMGs was demonstrated via moist contact assays.

16. The killing efficacy of these Zr-based BMGs was directly related to the release of heavy metal ions from the substrate materials. In addition, the amorphous microstructure may contribute to the antimicrobial efficacy.

Based on the findings in this dissertation, directions for future work are recommended in order to further deepen the scientific understanding and broaden the scope for the biomedical functions of BMGs. From the perspective of materials engineering, metallurgical efforts to develop biomedical BMGs with a suite of favorable materials properties and biocompatibility/bioactivity will significantly advance the progress towards their practical applications. Combinatorial approaches are suggested to prepare, characterize, and correlate different microstructures, bulk properties, surface properties, and biocompatibility. Piecing together the findings from such studies, the relationship amongst the interconnected microstructure, materials properties, and biomedical performance could be essentially established, which will provide guidelines for the optimization of BMGs for specific biomedical applications.

From the biomedical point of view, more extensive and systematic *in vitro* studies and mechanistic understandings on the cellular behaviors associated with different biomedical functionalities of the materials will provide useful information to comprehend the BMG/cell interactions. More detailed propositions were itemized at the end of respective Chapters for the four distinct biomedical functionalities studied in this dissertation. Collectively, investigations on a wide range of application-specific cells and corresponding biomolecules are proposed. Work in this dissertation can also be expanded to examine cell activities at different time points to include both short- and long-term behaviors. In addition to the cell culture studies, *in vivo* investigations in various animal models will be the next rising subject to endeavor, with an increasing number of studies being reported in recent years.

LIST OF REFERENCES

[1] Crubzy E, Murail P, Girard L, Bernadou J-P. False teeth of the Roman world. Nature. 1998;391:29-30.

[2] Ratner BD. Biomaterials Science: An Introduction to Material in Medicine. San Diego, CA: Elsevier Academic Press; 2004.

[3] Yaszemsk MJ, Trantolo DJ, Lewandrowski K-U, Hasirci V, Altobelli DE, Wise DL. Biomaterials in orthopedics. New York, NY: Marcel Dekker, Inc.; 2004.

[4] Wise DL, Trantolo DJ, Altobelli DE, Yaszemsk MJ, Grasser JD. Human biomaterials application. Totowa, NJ: The Humana Press; 1996.

[5] Greer AL. Metallic Glasses. Science. 1995;267:1947-1953.

[6] Loffler JF. Bulk metallic glasses. Intermetallics. 2003;11:529-540.

[7] Wang WH, Dong C, Shek CH. Bulk metallic glasses. Materials Science and Engineering: R. 2004;44:45-89.

[8] Inoue A, Takeuchi A. Recent development and application products of bulk glassy alloys. Acta Materialia. 2011;59:2243-67.

[9] Inoue A, Wang XM, Zhang W. Developments and applications of bulk metallic glasses. Institue of Problems of Mechanical Engineering-Russian Acadamy Sciences. 2008;18:1-9.

[10] Ashby MF, Greer AL. Metallic glasses as structural materials. Scripta Materialia. 2006;54:321-326.

[11] Byrne CJ, Eldrup M. Materials science - Bulk metallic glasses. Science. 2008;321:502-503.

[12] Greer AL. Metallic glasses ... on the threshold. Materials Today. 2009;12:14-22.

[13] Wang WH. Bulk metallic glasses with functional physical properties. Advanced Materials. 2009;21:4524-4544.

[14] Scully JR, Gebert A, Payer JH. Corrosion and related mechanical properties of bulk metallic glasses. Journal of Materials Research. 2007;22:302-313.

[15] Trexler MM, Thadhani NN. Mechanical properties of bulk metallic glasses. Progress in Materials Science. 2010;55:759-839.

[16] Schuh CA, Hufnagel TC, Ramamurty U. Mechanical behavior of amorphous alloys. Acta Materialia. 2007;55:4067-4109.

[17] Schroers J. The superplastic forming of bulk metallic glasses. JOM. 2005;57:35-39.

[18] Schroers J. Processing of bulk metallic glass. Advanced Materials. 2010;22:1566-1597.

[19] Demetriou MD, Wiest A, Hofmann DC, Johnson WL, Han B, Wolfson N, et al. Amorphous metals for hard-tissue prosthesis. JOM. 2010;62:83-91.

[20] Schroers J, Kumar G, Hodges TM, Chan S, Kyriakides TR. Bulk metallic glasses for biomedical applications. JOM. 2009;61:21-29.

[21] Peker A, Johnson WL. A highly processable metallic-glass - $Zr_{41.2}Ti_{13.8}Cu_{12.5}Ni_{10.0}Be_{22.5}$. Applied Physics Letters. 1993;63:2342.

[22] Zhang T, Inoue A. New bulk glassy Ni-based alloys with high strength of 3000 MPa. Materials Transactions. 2002;43:708-711.

[23] Park ES, Kim DH. Effect of atomic configuration and liquid stability on the glass-forming ability of Ca-based metallic glasses. Applied Physics Letters. 2005;86:201912.

[24] Inoue A, Nishiyama N, Amiya K, Zhang T, Masumoto T. Ti-based amorphous alloys with a wide supercooled liquid region. Materials Letters. 2007;61:2851-2854.

[25] Zheng Q, Ma H, Ma E, Xu J. Mg-Cu-(Y,Nd) pseudo-ternary bulk metallic glasses: The effects of Nd on glass-forming ability and plasticity. Scripta Materialia. 2006;55:541-544.

[26] Dai CL, Guo H, Shen Y, Li Y, Ma E, Xu J. A new centimeter-diameter Cu-based bulk metallic glass. Scripta Materialia. 2006;54:1403-1408.

[27] Ponnambalam V, Poon SJ, Shiflet GJ. Fe-based bulk metallic glasses with diameter thickness larger than one centimeter. Journal of Materials Research. 2004;19:1320-1323.

[28] Schroers J, Johnson WL. Highly processable bulk metallic glass-forming alloys in the Pt-Co-Ni-Cu-P system. Applied Physics Letters. 2004;84:3666-3668.

[29] Inoue A, Nishiyama N, Matsuda T. Preparation of bulk glassy Pd40Ni10Cu30P20 alloy of 40 mm in diameter by water quenching. Materials Transactions. 1996;37:181-184.

[30] Van den Beucken J, Walboomers XF, Vos MRJ, Sommerdijk N, Nolte RJM, Jansen JA. Macrophage behavior on multilayered DNA-coatings in vitro. Journal of Biomedical Materials Research Part A. 2007;80A:612-620.

[31] Sethi RK, Neavyn MJ, Rubash HE, Shanbhag AS. Macrophage response to cross-linked and conventional UHMWPE. Biomaterials. 2003;24:2561-2573.

[32] Maniatopoulos C, Pilliar RM, Smith DC. Threaded versus porous-surfaced designs for implant stabilization in bone-endodontic implant model. Journal of Biomedical Materials Research. 1986;20:1309-1333.

[33] Ratner BD. Reducing capsular thickness and enhancing angiogenesis around implant drug release systems. Journal of Controlled Release. 2002;78:211-218.

[34] Roberts WE, Smith RK, Zilberman Y, Mozsary PG, Smith RS. Osseous adaptation to continuous loading of rigid endosseous implants. American Journal of Orthodontics. 1984;86:95-111.

[35] O'Brien B, Carroll W. The evolution of cardiovascular stent materials and surfaces in response to clinical drivers: A review. Acta Biomaterialia. 2009;5:945-58.

[36] Mani G, Feldman MD, Patel D, Agrawal CM. Coronary stents: A materials perspective. Biomaterials. 2007;28:1689-1710.

[37] de Prado AP, Pérez-Martínez C, Cuellas-Ramon C, Gonzalo-Orden JM, Regueiro-Purrinos M, Martínez B, et al. Time course of reendothelialization of stents in a normal coronary swine model characterization and quantification. Veterinary Pathology Online. 2011;48:1109-1117.

[38] Kipshidze N, Dangas G, Tsapenko M, Moses J, Leon MB, Kutryk M, et al. Role of the endothelium in modulating neointimal formation - Vasculoprotective approaches to attenuate restenosis after percutaneous coronary interventions. Journal of the American College Cardiology. 2004;44:733-739.

[39] Smyth ETM, McIlvenny G, Enstone JE, Emmerson AM, Humphreys H, Fitzpatrick F, et al. Four country healthcare associated infection prevalence

survey 2006: Overview of the results. Journal of Hospital Infection. 2008;69:230-248.

[40] Alicia I. Hidron MD, Jonathan R. Edwards MS, Jean Patel P, Teresa C. Horan MPH, Dawn M. Sievert P, Daniel A. Pollock MD, et al. NHSN Annual Update: Antimicrobial-Resistant Pathogens Associated With Healthcare-Associated Infections: Annual Summary of Data Reported to the National Healthcare Safety Network at the Centers for Disease Control and Prevention, 2006–2007. Infect Control Hosp Epidemiol. 2008;29:996-1011.

[41] Luo J, Duan HP, Ma CL, Pang SJ, Zhang T. Effects of yttrium and erbium additions on glass-forming ability and mechanical properties of bulk glassy Zr-Al-Ni-Cu alloys. Materials Transactions. 2006;47:450-453.

[42] Jin K, Loffler JF. Bulk metallic glass formation in Zr-Cu-Fe-Al alloys. Applied Physics Letters. 2005;86:241909.

[43] Wada T, Qin FX, Wang XM, Yoshimura M, Inoue A, Sugiyama N, et al. Formation and bioactivation of Zr-Al-Co bulk metallic glasses. Journal of Materials Research. 2009;24:2941-2948.

[44] Qiu CL, Chen Q, Liu L, Chan KC, Zhou JX, Chen PP, et al. A novel Ni-free Zr-based bulk metallic glass with enhanced plasticity and good biocompatibility. Scripta Materialia. 2006;55:605-608.

[45] Huang L, Yokoyama Y, Wu W, Liaw PK, Pang SJ, Inoue A, et al. Ni-free Zr-Cu-Al-Nb-Pd bulk metallic glasses with different Zr/Cu ratios for biomedical applications. Journal of Biomedical Materials Research Part B. 2012;100B:1472-1482.

[46] Hiromoto S, Numata H, Tsai AP, Nakazawa K, Hanawa T, Sumita M. Polarization behavior of Pd78Si16Cu6-xCrx amorphous alloys in an artificial body fluid. Journal of the Japan Institute Metals. 1999;63:352-360.

[47] Kwokal A, Metikos-Hukovic M, Radic N, Poljak-Guberina R, Catovic A. Amorphous alloys resistant to corrosion in artificial saliva solution. Journal of Materials Science: Materials in Medicine. 2003;14:605-610.

[48] Morrison ML, Buchanan RA, Leon RV, Liu CT, Green BA, Liaw PK, et al. The electrochemical evaluation of a Zr-based bulk metallic glass in a phosphate-buffered saline electrolyte. Journal of Biomedical Materials Research Part A. 2005;74A:430-438.

[49] Liu L, Qiu CL, Chen Q, Zhang SM. Corrosion behavior of Zr-based bulk metallic glasses in different artificial body fluids. Journal of Alloys and Compounds. 2006;425:268-273.

[50] Huang L, Qiao D, Green BA, Liaw PK, Wang J, Pang S, et al. Bio-corrosion study on zirconium-based bulk-metallic glasses. Intermetallics. 2009;17:195-199.

[51] Maruyama N, Nakazawa K, Hanawa T. Fatigue properties of Zr-based bulk amorphous alloy in phosphate buffered saline solution. Materials Transactions. 2002;43:3118-3121.

[52] Wang Y, Shi L-L, Duan D-L, Li S, Xu J. Tribological properties of Zr61Ti2Cu25Al12 bulk metallic glass under simulated physiological conditions. Materials Science And Engineering: C. 2014;37:292-304.

[53] Morrison ML, Buchanan RA, Liaw PK, Green BA, Wang GY, Liu CT, et al. Corrosion-fatigue studies of the Zr-based Vitreloy 105 bulk metallic glass. Materials Science And Engineering: A. 2007;467:198-206.

[54] Huang L, Wang GY, Qiao DC, Liaw PK, Pang SJ, Wang JF, et al. Corrosion-fatigue study of a Zr-based bulk-metallic glass in a physiologically relevant environment. Journal of Alloys and Compounds. 2010;504:S159-162.

[55] Horton JA, Parsell DE. Biomedical potential of a zirconium-based bulk metallic glass. MRS Proceedings. 2002;754;179-184.

[56] Buzzi S, Jin K, Uggowitzer PJ, Tosatti S, Gerber I, Löffler JF. Cytotoxicity of Zr-based bulk metallic glasses. Intermetallics. 2006;14:729-734.

[57] He W, Chuang A, Cao Z, Liaw PK. Biocompatibility study of zirconium-based bulk metallic glasses for orthopedic applications. Metallurgical and Materials Transactions: A. 2010;41A:1726-1734.

[58] Gu XN, Xie XH, Li N, Zheng YF, Qin L. In vitro and in vivo studies on a Mg–Sr binary alloy system developed as a new kind of biodegradable metal. Acta Biomaterialia. 2012;8:2360-2374.

[59] Li J, Shi L-L, Zhu Z-d, He Q, Ai H-J, Xu J. $Zr_{61}Ti_2Cu_{25}Al_{12}$ metallic glass for potential use in dental implants: Biocompatibility assessment by in vitro cellular responses. Materials Science and Engineering: C. 2013;33:2113-2121.

[60] Li J, Ai H-J. The responses of endothelial cells to $Zr_{61}Ti_2Cu_{25}Al_{12}$ metallic glass in vitro and in vivo. Materials Science and Engineering: C. 2014;40:189-196.

[61] Liu L, Qiu CL, Huang CY, Yu Y, Huang H, Zhang SM. Biocompatibility of Ni-free Zr-based bulk metallic glasses. Intermetallics. 2009;17:235-240.

[62] Zberg B, Uggowitzer PJ, Loffler JF. MgZnCa glasses without clinically observable hydrogen evolution for biodegradable implants. Nature Materials. 2009;8:887-891.

[63] Wang YB, Xie XH, Li HF, Wang XL, Zhao MZ, Zhang EW, et al. Biodegradable CaMgZn bulk metallic glass for potential skeletal application. Acta Biomaterialia. 2011;7:3196-3208.

[64] Padmanabhan J, Kinser ER, Stalter MA, Duncan-Lewis C, Balestrini JL, Sawyer AJ, et al. Engineering cellular response using nanopatterned bulk metallic glass. ACS nano. 2014;8:4366-4375.

[65] Liu FJ, Yang QW, Pang SJ, Ma CL, Zhang T. Ductile Fe-based BMGs with high glass forming ability and high strength. Materials Transactions. 2008;49:231-234.

[66] Qin FX, Wang XM, Wada T, Xie GQ, Asami K, Inoue A. Formation of hydroxyapatite on Ti-coated Ti-Zr-Cu-Pd bulk metallic glass. Materials Transactions. 2009;50:605-609.

[67] Li HF, Wang YB, Cheng Y, Zheng YF. Surface modification of $Ca_{60}Mg_{15}Zn_{25}$ bulk metallic glass for slowing down its biodegradation rate in water solution. Materials Letters. 2010;64:1462-1464.

[68] Huang L, Cao Z, Meyer HM, Liaw PK, Garlea E, Dunlap JR, et al. Responses of bone-forming cells on pre-immersed Zr-based bulk metallic glasses: Effects of composition and roughness. Acta Biomaterialia. 2011;7:395-405.

[69] Huang L, Zhu C, Muntele CI, Zhang T, Liaw PK, He W. Surface engineering of a Zr-based bulk metallic glass with low energy Ar- or Ca-ion implantation. Materials Science and Engineering: C. 2015;47:248-255.
[70] Wang J, Huang L, Zhu S, Li Q, Guan S, Zhang T. Glass-forming ability, fragility parameter, and mechanical properties of Co–Ir–Ta–B amorphous alloys. Journal of Alloys and Compounds. 2013;576:375-359.
[71] Pilliar RM. Metallic biomaterials. Biomed Mater: Springer; 2009. p. 41-81.
[72] Wolff J, Maquet P, Furlong R. The law of bone remodelling: Springer-Verlag Berlin; 1986.
[73] Harris WH. Will stress shielding limit the longevity of cemented femoral components of total hip replacement? Clinical Orthopaedics Related Research. 1992;274:120-123.
[74] Engh Jr CA, Young AM, Engh Sr CA, Hopper Jr RH. Clinical consequences of stress shielding after porous-coated total hip arthroplasty. Clinical Orthopaedics Related Research. 2003;417:157-163.
[75] Ryan G, Pandit A, Apatsidis DP. Fabrication methods of porous metals for use in orthopaedic applications. Biomaterials. 2006;27:2651-2670.
[76] Niinomi M, Nakai M. Titanium-based biomaterials for preventing stress shielding between implant devices and bone. International Journal of Biomaterials. 2011;2011:836587.
[77] Niinomi M. Mechanical biocompatibilities of titanium alloys for biomedical applications. Journal of the Mechanical Behavior of Biomedical Materials. 2008;1:30-42.
[78] Niinomi M, Nakai M, Hieda J. Development of new metallic alloys for biomedical applications. Acta Biomaterialia. 2012;8:3888-3903.
[79] Niinomi M. Mechanical properties of biomedical titanium alloys. Materials Science and Engineering: A. 1998;243:231-236.
[80] Chen Y, Xu Z, Smith C, Sankar J. Recent advances on the development of magnesium alloys for biodegradable implants. Acta Biomaterialia. 2014;10:4561-4573.
[81] Harris WH. Osteolysis and particle disease in hip replacement: A review. Acta Orthopaedica. 1994;65:113-123.
[82] Khruscho M. Principles of abrasive wear. wear. 1974;28:69-88.
[83] Wang WH. Correlations between elastic moduli and properties in bulk metallic glasses. Joural of Applied Physics. 2006;99:093506.
[84] Zhang Y, Zhao DQ, Pan MX, Wang WH. Glass forming properties of Zr-based bulk metallic alloys. Journal of Non-Crystalline Solids. 2003;315:206-210.
[85] Gilbert C, Ritchie R, Johnson W. Fracture toughness and fatigue-crack propagation in a Zr–Ti–Ni–Cu–Be bulk metallic glass. Applied Physics Letters. 1997;71:476-478.
[86] Wang GY, Liaw PK, Smyth A, Denda M, Peker A, Freels M, et al. Fatigue characteristics of a Zr-based bulk metallic glass. Reviews on Advanced Materials Science; 2008;18;18-22.

[87] Peter WH, Liaw PK, Buchanan RA, Liu CT, Brooks CR, Horton JA, et al. Fatigue behavior of $Zr_{52.5}Al_{10}Ti_5Cu_{17.9}Ni_{14.6}$ bulk metallic glass. Intermetallics. 2002;10:1125-1129.

[88] Menzel BC, Dauskardt RH. Stress-life fatigue behavior of a Zr-based bulk metallic glass. Acta Materialia. 2006;54:935-943.

[89] Launey ME, Busch R, Kruzic JJ. Effects of free volume changes and residual stresses on the fatigue and fracture behavior of a Zr-Ti-Ni-Cu-Be bulk metallic glass. Acta Materialia. 2008;56:500-510.

[90] Qiao DC, Wang GY, Jiang WH, Yokoyama Y, Liaw PK, Choo H. Compression-compression fatigue and fracture behaviors of Zr50Al10Cu37Pd3 bulk-metallic glass. Materials Transactions. 2007;48:1828-1833.

[91] Hess PA, Menzel BC, Dauskardt RH. Fatigue damage in bulk metallic glass II: Experiments. Scripta Materialia. 2006;54:355-361.

[92] Wang GY, Liaw PK, Morrison ML. Progress in studying the fatigue behavior of Zr-based bulk-metallic glasses and their composites. Intermetallics. 2009;17:579-590.

[93] Qiao DC, Wang GY, Liaw PK, Ponnambalam V, Poon SJ, Shiflet GJ. Fatigue behavior of an $Fe_{48}Cr_{15}Mo_{14}Er_2C_{15}B_6$ amorphous steel. Journal of Materials Research. 2007;22:544-550.

[94] Watanabe LY, Roberts SN, Baca N, Wiest A, Garrett SJ, Conner RD. Fatigue and corrosion of a Pd-based bulk metallic glass in various environments. Materials Science and Engineering: C. 2013;33:4021-4025.

[95] Duan G, Wiest A, Lind ML, Li J, Rhim WK, Johnson WL. Bulk metallic glass with benchmark thermoplastic processability. Advanced Materials. 2007;19:4272-4275.

[96] Zhang B, Zhao DQ, Pan MX, Wang WH, Greer AL. Amorphous metallic plastic. Physical Review Letters. 2005;94:4.

[97] Hofmann DC. Bulk metallic glasses and their composites: A brief history of diverging fields. Journal of Materials. 2013;2013:517904.

[98] Schroers J, Pham Q, Peker A, Paton N, Curtis RV. Blow molding of bulk metallic glass. Scripta Materialia. 2007;57:341-344.

[99] Kumar G, Tang HX, Schroers J. Nanomoulding with amorphous metals. Nature. 2009;457:868-872.

[100] Schroers J, Nguyen T, O'Keeffe S, Desai A. Thermoplastic forming of bulk metallic glass--Applications for MEMS and microstructure fabrication. Materials Science and Engineering: A. 2007;449-451:898-902.

[101] Lardner A. The effects of extracellular pH on immune function. Journal of leukocyte biology. 2001;69:522-530.

[102] Hiromoto S, Tsai AP, Sumita M, Hanawa T. Effect of pH on the polarization behavior of Zr65Al7.5Ni10Cu17.5 amorphous alloy in a phosphate-buffered solution. Corrosion Science. 2000;42:2193-2200.

[103] Hiromoto S, Tsai AP, Sumita M, Hanawa T. Corrosion behavior of $Zr_{65}Al_{7.5}Ni_{10}Cu_{17.5}$ amorphous alloy for biomedical use. Materials Transactions. 2001;42:656-659.

[104] Green BA, Meyer HM, Benson RS, Yokoyama Y, Liaw PK, Liu CT. A study of the corrosion behaviour of $Zr_{50}Cu_{(40-x)}Al_{10}Pd_x$ bulk metallic glasses with scanning Auger microanalysis. Corrosion Science. 2008;50:1825-1832.

[105] Pang SJ, Zhang T, Kimura H, Asami K, Inoue A. Corrosion behavior of Zr-(Nb-)Al-Ni-Cu glassy alloys. Materials Transactions. 2000;41:1490-1494.

[106] Raju VR, Kuhn U, Wolff U, Schneider F, Eckert J, Reiche R, et al. Corrosion behaviour of Zr-based bulk glass-forming alloys containing Nb or Ti. Materials Letters. 2002;57:173-177.

[107] Hiromoto S, Tsai AP, Sumita M, Hanawa T. Polarization behavior of bulk Zr-base amorphous alloy immersed in cell culture medium. Materials Transactions. 2002;43:3112-3117.

[108] Gebert A, Mummert K, Eckert J, Schultz L, Inoue A. Electrochemical investigations on the bulk glass forming $Zr_{55}Cu_{30}Al_{10}Ni_5$ alloy. Materials and Corrosion. 1997;48:293-297.

[109] Mudali UK, Baunack S, Eckert J, Schultz L, Gebert A. Pitting corrosion of bulk glass-forming zirconium-based alloys. Journal of Alloys and Compounds. 2004;377:290-297.

[110] Gebert A, Buchholz K, Leonhard A, Mummert K, Eckert J, Schultz L. Investigations on the electrochemical behaviour of Zr-based bulk metallic glasses. Materials Science and Engineering: A. 1999;267:294-300.

[111] Gebert A, Concustell A, Greer AL, Schultz L, Eckert J. Effect of shot-peening on the corrosion resistance of a Zr-based bulk metallic glass. Script Materialia. 2010;62:635-638.

[112] Gebert A, Gostin PF, Schultz L. Effect of surface finishing of a Zr-based bulk metallic glass on its corrosion behaviour. Corrosion Science. 2010;52:1711-1720.

[113] Qiu CL, Liu L, Sun M, Zhang SM. The effect of Nb addition on mechanical properties, corrosion behavior, and metal-ion release of ZrAlCuNi bulk metallic glasses in artificial body fluid. Journal of Biomedical Materials Research Part A. 2005;75A:950-956.

[114] Zhang T, Liu FJ, Pang SJ, Li R. Ductile Fe-based bulk metallic glass with good soft-magnetic properties. Materials Transactions; 2007;48:1157-1160.

[115] Monfared A, Vali H, Faghihi S. Biocorrosion and biocompatibility of Zr-Cu-Fe-Al bulk metallic glasses. Surface and Interface Analysis. 2013;45:1714-1720.

[116] Hua NB, Pang SJ, Li Y, Wang JF, Li R, Georgarakis K, et al. Ni- and Cu-free Zr-Al-Co-Ag bulk metallic glasses with superior glass-forming ability. Journal of Materials Research. 2011;26:539-546.

[117] Dhawan A, Roychowdhury S, De PK, Sharma SK. Potentiodynamic polarization studies on bulk amorphous alloys and $Zr_{46.75}Ti_{8.25}Cu_{7.5}Ni_{10}Be_{27.5}$ and $Zr_{65}Cu_{17.5}Ni_{10}Al_{7.5}$. J Non-Crystalline Solids. 2005;351:951-955.

[118] Hua N, Huang L, Wang J, Cao Y, He W, Pang S, et al. Corrosion behavior and in vitro biocompatibility of Zr–Al–Co–Ag bulk metallic glasses: An experimental case study. Journal of Non-Crystalline Solids. 2012;358:1599-604.

[119] Wang YB, Zheng YF, Wei SC, Li M. In vitro study on Zr-based bulk metallic glasses as potential biomaterials. Journal of Biomedical Materials Research Part B. 2011;96B:34-46.

[120] Liu Y, Wang YM, Pang HF, Zhao Q, Liu L. A Ni-free ZrCuFeAlAg bulk metallic glass with potential for biomedical applications. Acta Biomaterialia. 2013;9:7043-7053.

[121] Lin B, Mu R, Yang LF, Bian XF. Antibacterial effect of metallic glasses. Chinese Science Bulletin. 2012;57:1069-1072.

[122] Qin FX, Wang XM, Inoue A. Observation of bone-like apatite on Ti-coated $Zr_{55}Al_{10}Ni_5Cu_{30}$ bulk metallic glass after alkali treatment. Intermetallics. 2008;16:917-922.

[123] Jia H, Muntele CI, Huang L, Li X, Li G, Zhang T, et al. A study on the surface structures and properties of Ni-free Zr-based bulk metallic glasses after Ar and Ca ion implantation. Intermetallics. 2013;41:35-43.

[124] Kao WJ, Hubbell JA, Anderson JM. Protein-mediated macrophage adhesion and activation on biomaterials: a model for modulating cell behavior. Journal of Materials Science: Materials in Medicine. 1999;10:601-605.

[125] Shen MC, Horbett TA. The effects of surface chemistry and adsorbed proteins on monocyte/macrophage adhesion to chemically modified polystyrene surfaces. Journal of Biomedical Materials Research. 2001;57:336-345.

[126] Deligianni DD, Katsala N, Ladas S, Sotiropoulou D, Amedee J, Missirlis YF. Effect of surface roughness of the titanium alloy Ti-6Al-4V on human bone marrow cell response and on protein adsorption. Biomaterials. 2001;22:1241-1251.

[127] Yang YZ, Cavin R, Ong JL. Protein adsorption on titanium surfaces and their effect on osteoblast attachment. Journal of Biomedical Materials Research Part A. 2003;67A:344-349.

[128] Huang H-H, Sun Y-S, Wu C-P, Liu C-F, Liaw PK, Kai W. Corrosion resistance and biocompatibility of Ni-free Zr-based bulk metallic glass for biomedical applications. Intermetallics. 2012;30:139-143.

[129] Sun Y-S, Zhang W, Kai W, Liaw PK, Huang H-H. Evaluation of Ni-free Zr–Cu–Fe–Al bulk metallic glass for biomedical implant applications. Journal of Alloys and Compounds. 2014;586:S539-543.

[130] Valles G, Gonzalez-Melendi P, Gonzalez-Carrasco JL, Saldana L, Sanchez-Sabate E, Munuera L, et al. Differential inflammatory macrophage response to rutile and titanium particles. Biomaterials. 2006;27:5199-5211.

[131] Anderson JM, Miller KM. Biomaterial biocompatibility and the macrophage. Biomaterials. 1984;5:5-10.

[132] Jiang QK, Wang XD, Nie XP, Zhang GQ, Ma H, Fecht HJ, et al. Zr-(Cu,Ag)-Al Bulk Metallic Glasses. Acta Materialia. 2008;56:1785-1196.

[133] Dimitriou R, Jones E, McGonagle D, Giannoudis PV. Bone regeneration: Current concepts and future directions. BMC Medicine. 2011;9:66.

[134] Bianco P, Robey PG. Stem cells in tissue engineering. Nature. 2001;414:118-121.

[135] Gristina AG. Biomaterial-centered infection: microbial adhesion versus tissue integration. Science. 1987;237:1588-1595.

[136] Hendriks JGE, van Horn JR, van der Mei HC, Busscher HJ. Backgrounds of antibiotic-loaded bone cement and prosthesis-related infection. Biomaterials. 2004;25:545-556.

[137] Zhao LZ, Wang HR, Huo KF, Cui LY, Zhang WR, Ni HW, et al. Antibacterial nano-structured titania coating incorporated with silver nanoparticles. Biomaterials. 2011;32:5706-5716.

[138] Chen W, Liu Y, Courtney HS, Bettenga M, Agrawal CM, Bumgardner JD, et al. In vitro anti-bacterial and biological properties of magnetron co-sputtered silver-containing hydroxyapatite coating. Biomaterials. 2006;27:5512-5517.

[139] Chiang PT, Chen GJ, Jian SR, Shih YH, Jang JSC, Lai CH. Surface antimicrobial effects of Zr61Al7.5Ni10Cu17.5Si4 thin film metallic glasses on escherichia coli, staphylococcus aureus, pseudomonas aeruginosa, acinetobacter baumannii and candida albicans. Fooyin Journal of Health Sciences. 2010;2:12-20.

[140] Chiang PT, Chen GJ, Jian SR, Shih YH. Effects of buffer layers on adhesion and antimicrobial properties of amorphous ZrAlNiCuSi films. Materials Technology. 2012;27:107-109.

[141] Liu L, Chan KC, Qiu CL, Chen Q. Formation and biocompatibility of Ni-free Zr60Nb5Cu20Fe5Al10 bulk metallic glass. Materials Transactions. 2007;48:1879-1882.

[142] Liu Z, Chan KC, Liu L. Development of Ni- and Cu-free Zr-based bulk metallic glasses for biomedical applications. Materials Transactions. 2011;52:61-67.

[143] Hanawa T. In vivo metallic biomaterials and surface modification. Materials Science and Engineering: A. 1999;267:260-6.

[144] Chrzanowski W, Neel EAA, Armitage DA, Knowles JC. Effect of surface treatment on the bioactivity of nickel-titanium. Acta Biomaterialia. 2008;4:1969-1984.

[145] Keogh MB, O’Brien FJ, Daly JS. Substrate stiffness and contractile behaviour modulate the functional maturation of osteoblasts on a collagen–GAG scaffold. Acta Biomaterialia. 2010;6:4305-4313.

[146] Liu L, Chan KC, Yu Y, Chen Q. Bio-activation of Ni-free Zr-based bulk metallic glass by surface modification. Intermetallics. 2010;18:1978-1982.

[147] Pham MT, Reuther H, Matz W, Mueller R, Steiner G, Oswald S, et al. Surface induced reactivity for titanium by ion implantation. Journal of Materials Science: Materials in Medicine. 2000;11:383-391.

[148] Krupa D, Baszkiewicz J, Kozubowski JA, Barcz A, Sobczak JW, Bilinski A, et al. Effect of phosphorus-ion implantation on the corrosion resistance and biocompatibility of titanium. Biomaterials. 2002;23:3329-40.

[149] Krupa D, Baszkiewicz J, Kozubowski JA, Barcz A, Sobczak JW, Bilinski A, et al. Effect of calcium-ion implantation on the corrosion resistance and biocompatibility of titanium. Biomaterials. 2001;22:2139-2151.

[150] Pham MT, Matz W, Reuther H, Richter E, Steiner G, Oswald S. Interface-mediated synthesis of hydroxyapatite. Journal of Biomedical Materials Research. 2002;59:254-258.

[151] Tsyganov I, Wieser E, Matz W, Reuther H, Richter E. Modification of the Ti-6Al-4V alloy by ion implantation of calcium and/or phosphorus. Surface and Coating Technology. 2002;158:318-23.

[152] Nayab S, Shinawi L, Hobkirk J, Tate TJ, Olsen I, Jones FH. Adhesion of bone cells to ion-implanted titanium. Journal of Materials Science: Materials in Medicine. 2003;14:991-997.

[153] Nayab SN, Jones FH, Olsen I. Human alveolar bone cell adhesion and growth on ion-implanted titanium. Journal of Biomedical Materials Research Part A. 2004;69A:651-657.

[154] Krupa D, Baszkiewicz J, Kozubowski JA, Barcz A, Sobczak JW, Bilinski A, et al. Effect of dual ion implantation of calcium and phosphorus on the properties of titanium. Biomaterials. 2005;26:2847-2856.

[155] Nayab SN, Jones FH, Olsen I. Effects of calcium ion implantation on human bone cell interaction with titanium. Biomaterials. 2005;26:4717-4727.

[156] Nayab SN, Jones FH, Olsen I. Effects of calcium ion-implantation of titanium on bone cell function in vitro. Journal of Biomedical Materials Research Part A. 2007;83A:296-302.

[157] Hanawa T, Kamiura Y, Yamamoto S, Kohgo T, Amemiya A, Ukai H, et al. Early bone formation around calcium-ion-implanted titanium inserted into rat tibia. Journal of Biomedical Materials Research. 1997;36:131-136.

[158] Yang Y, Kim KH, Ong JL. A review on calcium phosphate coatings produced using a sputtering process—an alternative to plasma spraying. Biomaterials. 2005;26:327-37.

[159] Hu Z, Zhao ZQ, Wu YD, Lu T, Xing JS, Wei BC. Surface features of Zr-based and Ti-based metallic glasses by ion irradiation. Vacuum. 2013;89:142-146.

[160] Nagata S, Sasase M, Takahiro K, Tsuchiya B, Inouye A, Yamamoto S, et al. Ion induced structural modification and nano-crystalline formation of Zr-Al-Ni-Cu metallic glasses. Nuclear Instruments and Methods in Physics Research Section B: Beam Interactions with Materials and Atoms. 2009;267:1514-1517.

[161] Iqbal M, Qayyum A, Akhter JI. Surface modification of Zr-based bulk amorphous alloys by using ion irradiation. Journal of Alloys and Compounds. 2011;509:2780-2783.

[162] Yang YZ, Tao PJ, Li GQ, Mu ZX, Ru Q, Xie ZW, et al. Effects of ion implantation on surface structures and properties for bulk metallic glass. Intermetallics. 2009;17:722-726.

[163] Kowalski W. Ultraviolet germicidal irradiation handbook: UVGI for air and surface disinfection. Springer. 2009.

[164] Oliver WC, Pharr GM. Measurement of hardness and elastic modulus by instrumented indentation: Advances in understanding and refinements to methodology. Journal of Materials Research. 2004;19:3-20.

[165] Lewandowski J, Wang W, Greer A. Intrinsic plasticity or brittleness of metallic glasses. Philosophical Magazine Letters. 2005;85:77-87.

[166] Hay J, Wolff P. Small correction required when applying the Hertzian contact model to instrumented indentation data. Journal of Materials Research. 2001;16:1280-1286.

[167] Egerton R, Malac M. Improved background-fitting algorithms for ionization edges in electron energy-loss spectra. Ultramicroscopy. 2002;92:47-56.

[168] Su D, Zeitler E. Background problem in electron-energy-loss spectroscopy. Physical Review B. 1993;47:14734.
[169] Brown PD. Transmission Electron Microscopy—A Textbook for Materials Science. Cambridge Univ Press. 1999.
[170] Paital SR, Dahotre NB. Wettability and kinetics of hydroxyapatite precipitation on a laser-textured Ca-P bioceramic coating. Acta Biomaterialia. 2009;5:2763-2772.
[171] Owens DK, Wendt RC. Estimation of surface free energy of polymers. Journal of Applied Polymer Science. 1969;13:1741-1747.
[172] Ziegler JF, Biersack JP, Littmark U. The stopping and Range of Ions in Solids. New York: Pergamon Press. 1985.
[173] ASTM-F2477-07. Standard test methods for in vitro pulsatile durability testing of vascular stents. Philadelphia PASfTaM.Lally C, Dolan F, Prendergast PJ. Cardiovascular stent design and vessel stresses: A finite element analysis. Journal of Biomechanics. 2005;38:1574-1581.
[174] Lally C, Dolan F, Prendergast PJ. Cardiovascular stent design and vessel stresses: a finite element analysis. Journal of Biomechanics. 2005;38:1574-1581.
[175] Popat KC, Leoni L, Grimes CA, Desai TA. Influence of engineered titania nanotubular surfaces on bone cells. Biomaterials. 2007;28:3188-3197.
[176] http://www.bioptechs.com/Products/FCS3/fcs3.html.
[177] Anderson JM, Rodriguez A, Chang DT. Foreign body reaction to biomaterials. Seminars in Immunology. 2008;20:86-100.
[178] Khruscho.Mm. PRINCIPLES OF ABRASIVE WEAR. Wear. 1974;28:69-88.
[179] Chamberlain LM, Godek ML, Gonzalez-Juarrero M, Grainger DW. Phenotypic non-equivalence of murine (monocyte-) macrophage cells in biomaterial and inflammatory models. Journal of Biomedical Materials Research Part A. 2009;88A:858-871.
[180] Mørland B, Kaplan G. Macrophage activation in vivo and in vitro. Experimental Cell Research. 1977;108:279-288.
[181] Wu ACK, Grøndahl L, Jack KS, Foo MX, Trau M, Hume DA, et al. Reduction of the in vitro pro-inflammatory response by macrophages to poly(3-hydroxybutyrate-co-3-hydroxyvalerate). Biomaterials. 2006;27:4715-4725.
[182] Saino E, Focarete ML, Gualandi C, Emanuele E, Cornaglia AI, Imbriani M, et al. Effect of electrospun fiber diameter and alignment on macrophage activation and secretion of proinflammatory cytokines and chemokines. Biomacromolecules. 2011;12:1900-1911.
[183] Page J, Heitz BA, Joubert JR, Keogh JP, Sparer T, Saavedra SS, et al. In vitro assessment of macrophage attachment and phenotype on polymerized phospholipid bilayers. Journal of Biomedical Materials Research Part A. 2011;97A:212-217.
[184] Chen S, Jones JA, Xu Y, Low H-Y, Anderson JM, Leong KW. Characterization of topographical effects on macrophage behavior in a foreign body response model. Biomaterials. 2010;31:3479-3491.
[185] Refai AK, Textor M, Brunette DM, Waterfield JD. Effect of titanium surface topography on macrophage activation and secretion of proinflammatory cytokines

and chemokines. Journal of Biomedical Materials Research Part A. 2004;70A:194-205.

[186] Zhou FH, Foster BK, Zhou XF, Cowin AJ, Xian CJ. TNF-alpha mediates p38 MAP kinase activation and negatively regulates bone formation at the injured growth plate in rats. Journal of Bone and Mineral Research. 2006;21:1075-1088.

[187] Takayanagi H. Osteoimmunology: Shared mechanisms and crosstalk between the immune and bone systems. Nature Reveiws Immunology. 2007;7:292-304.

[188] Waterfield JD, Ali TA, Nahid F, Kusano K, Brunette DM. The effect of surface topography on early NF kappa B signaling in macrophages. Journal of Biomedical Materials Research Part A. 2010;95A:837-847.

[189] Tan KS, Qian L, Rosado R, Flood PM, Cooper LF. The role of titanium surface topography on J774A.1 macrophage inflammatory cytokines and nitric oxide production. Biomaterials. 2006;27:5170-177.

[190] Suska F, Esposito M, Gretzer C, Kalltorp M, Tengvall P, Thomsen P. IL-1 alpha, IL-1 beta and TNF-alpha secretion during in vivo/ex vivo cellular interactions with titanium and copper. Biomaterials. 2003;24:461-468.

[191] Nakashima Y, Sun DH, Trindade MCD, Maloney WJ, Goodman SB, Schurman DJ, et al. Signaling pathways for tumor necrosis factor-alpha and interleukin-6 expression in human macrophages exposed to titanium-alloy particulate debris in vitro. Journal of Bone and Joint Surgery. 1999;81A:603-615.

[192] Roach SK, Lee SB, Schorey JS. Differential activation of the transcription factor cyclic AMP response element binding protein (CREB) in macrophages following infection with pathogenic and nonpathogenic mycobacteria and role for CREB in tumor necrosis factor alpha production. Infection and Immunity. 2005;73:514-522.

[193] Jovanovic DV, Di Battista JA, Martel-Pelletier J, Jolicoeur FC, He Y, Zhang M, et al. IL-17 stimulates the production and expression of proinflammatory cytokines, IL-beta and TNF-alpha, by human macrophages. The Journal of Immunology. 1998;160:3513-3521.

[194] Hibbs Jr JB, Taintor RR, Vavrin Z, Rachlin EM. Nitric oxide: A cytotoxic activated macrophage effector molecule. Biochemical and Biophysical Research Communications. 1988;157:87-94.

[195] Mosser DM, Zhang X. Activation of Murine Macrophages. Current protocols in immunology. edited by John E Coligan [et al]. 2008.

[196] Meng F, Lowell CA. Lipopolysaccharide (LPS)-induced macrophage activation and signal transduction in the absence of Src-family kinases Hck, Fgr, and Lyn. The Journal of Experimental Medicine. 1997;185:1661-1670.

[197] Mosser DM, Edwards JP. Exploring the full spectrum of macrophage activation. Nature reviews immunology. 2008;8:958-969.

[198] Jenkins SJ, Ruckerl D, Cook PC, Jones LH, Finkelman FD, van Rooijen N, et al. Local macrophage proliferation, rather than recruitment from the blood, is a signature of TH2 inflammation. Science. 2011;332:1284-1288.

[199] Matthews D, Ocelik V, De Hosson JTM. Tribological and mechanical properties of high power laser surface-treated metallic glasses. Materials Science and Engineering: A. 2007;471:155-164.

[200] Chen B, Pang S, Han P, Li Y, Yavari AR, Vaughan G, et al. Improvement in mechanical properties of a Zr-based bulk metallic glass by laser surface treatment. Journal of Alloys and Compounds. 2010;504:S45-47

[201] Choi YC, Hong SI. Enhancement of plasticity in Zr-base bulk metallic glass by soft metal plating. Scripta Materialia. 2009;61:481-484.

[202] Magagnosc DJ, Kumar G, Schroers J, Felfer P, Cairney JM, Gianola DS. Effect of ion irradiation on tensile ductility, strength and fictive temperature in metallic glass nanowires. Acta Materialia. 2014;74:165-182.

[203] Petrusenko Y, Bakai A, Neklyudov I, Bakai S, Borysenko V, Wang G, et al. Low- and high-frequency fatigue of bulk metallic glasses. Journal of Alloys and Compounds. 2011;509:S123-127.

[204] Liontas R, Gu XW, Fu E, Wang Y, Li N, Mara NA, et al. Effects of helium implantation on the tensile properties and microstructure of Ni73P27 metallic glass nanostructures. Nano letters. 2014;14:5176-183.

[205] Rautray TR, Narayanan R, Kim K-H. Ion implantation of titanium based biomaterials. Progress in Materials Science. 2011;56:1137-1177.

[206] Neuman W, Neuman M. The nature of the mineral phase of bone. Chemical Reviews. 1953;53:1-45.

[207] Liu X, Chu PK, Ding C. Surface modification of titanium, titanium alloys, and related materials for biomedical applications. Materials Science and Engineering: R. 2004;47:49-121.

[208] Menéndez E, Hynowska A, Fornell J, Suriñach S, Montserrat J, Temst K, et al. Influence of the irradiation temperature on the surface structure and physical/chemical properties of Ar ion-irradiated bulk metallic glasses. Journal of Alloys and Compounds. 2014;610:118-125.

[209] Seah MP, Dench WA. Quantitative electron spectroscopy of surfaces: A standard data base for electron inelastic mean free paths in solids. Surface and Interface Analysis. 1979;1:2-11.

[210] Luo WD, Yang B, Chen GL. Effect of Ar+ ion irradiation on the microstructure and properties of Zr-Cu-Fe-Al bulk metallic glass. Scripta Materialia. 2011;64:625-628.

[211] Xie S, George EP. Hardness and shear band evolution in bulk metallic glasses after plastic deformation and annealing. Acta Materialia. 2008;56:5202-5213.

[212] Roy S, Yue CY, Lam YC, Wang ZY, Hu H. Surface analysis, hydrophilic enhancement, ageing behavior and flow in plasma modified cyclic olefin copolymer (COC)-based microfluidic devices. Sensors and Actuators B: Chemical. 2010;150:537-549.

[213] Sakai N, Fujishima A, Watanabe T, Hashimoto K. Quantitative evaluation of the photoinduced hydrophilic conversion properties of TiO2 thin film surfaces by the reciprocal of contact angle. The Journal of Physical Chemistry B. 2003;107:1028-35.

[214] Wang YB, Li HF, Zheng YF, Wei SC, Li M. Correlation between corrosion performance and surface wettability in ZrTiCuNiBe bulk metallic glasses. Applied Physics Letters. 2010;96:251909.

[215] Boyan BD, Hummert TW, Dean DD, Schwartz Z. Role of material surfaces in regulating bone and cartilage cell response. Biomaterials. 1996;17:137-146.

[216] Nakanishi K, Sakiyama T, Imamura K. On the adsorption of proteins on solid surfaces, a common but very complicated phenomenon. Journal of Bioscience and Bioengineering. 2001;91:233-244.

[217] Keselowsky BG, Collard DM, García AJ. Surface chemistry modulates focal adhesion composition and signaling through changes in integrin binding. Biomaterials. 2004;25:5947-5954.

[218] Arima Y, Iwata H. Effect of wettability and surface functional groups on protein adsorption and cell adhesion using well-defined mixed self-assembled monolayers. Biomaterials. 2007;28:3074-3082.

[219] Ponsonnet L, Comte V, Othmane A, Lagneau C, Charbonnier M, Lissac M, et al. Effect of surface topography and chemistry on adhesion, orientation and growth of fibroblasts on nickel-titanium substrates. Materials Science and Engineering C. 2002;21:157-165.

[220] Anselme K, Bigerelle M. Topography effects of pure titanium substrates on human osteoblast long-term adhesion. Acta Biomaterialia. 2005;1:211-222.

[221] Lord MS, Foss M, Besenbacher F. Influence of nanoscale surface topography on protein adsorption and cellular response. Nano Today. 2010;5:66-78.

[222] Falconnet D, Csucs G, Michelle Grandin H, Textor M. Surface engineering approaches to micropattern surfaces for cell-based assays. Biomaterials. 2006;27:3044-3063.

[223] Schwartz Z, Martin JY, Dean DD, Simpson J, Cochran DL, Boyan BD. Effect of titanium surface roughness on chondrocyte proliferation, matrix production, and differentiation depends on the state of cell maturation. Journal of Biomedical Materials Research. 1996;30:145-155.

[224] Ghibaudo M, Saez A, Trichet L, Xayaphoummine A, Browaeys J, Silberzan P, et al. Traction forces and rigidity sensing regulate cell functions. Soft Matter. 2008;4:1836-1843.

[225] Pelham RJ, Wang Y-l. Cell locomotion and focal adhesions are regulated by substrate flexibility. Proceedings of the National Academy of Sciences. 1997;94:13661-13665.

[226] Elosegui-Artola A, Bazellières E, Allen MD, Andreu I, Oria R, Sunyer R, et al. Rigidity sensing and adaptation through regulation of integrin types. Nature Materials. 2014;13:631-637.

[227] Discher DE, Janmey P, Wang Y-l. Tissue cells feel and respond to the stiffness of their substrate. Science. 2005;310:1139-1143.

[228] Engler AJ, Sen S, Sweeney HL, Discher DE. Matrix elasticity directs stem cell lineage specification. Cell. 2006;126:677-689.

[229] Yeung T, Georges PC, Flanagan LA, Marg B, Ortiz M, Funaki M, et al. Effects of substrate stiffness on cell morphology, cytoskeletal structure, and adhesion. Cell Motility and the Cytoskeleton. 2005;60:24-34.

[230] Tan JL, Tien J, Pirone DM, Gray DS, Bhadriraju K, Chen CS. Cells lying on a bed of microneedles: an approach to isolate mechanical force. Proceedings of the National Academy of Sciences. 2003;100:1484-1489.

[231] Smith KE, Hyzy SL, Sunwoo M, Gall KA, Schwartz Z, Boyan BD. The dependence of MG63 osteoblast responses to (meth) acrylate-based networks on chemical structure and stiffness. Biomaterials. 2010;31:6131-6141.
[232] Hoffler C, Moore K, Kozloff K, Zysset P, Brown M, Goldstein S. Heterogeneity of bone lamellar-level elastic moduli. Bone. 2000;26:603-609.
[233] Zysset PK, Guo XE, Hoffler CE, Moore KE, Goldstein SA. Elastic modulus and hardness of cortical and trabecular bone lamellae measured by nanoindentation in the human femur. Journal of Biomechanics. 1999;32:1005-1012.
[234] Welsch G, Boyer R, Collings E. Materials properties handbook: titanium alloys: ASM international; 1993.
[235] Sieniawski J, Ziaja W, Kubiak K, Motyka M. Microstructure and mechanical properties of high strength two-phase titanium alloys. Titanium Alloys-Advances in Properties Control. 2013:69-80.
[236] Lampin M, Warocquier-Clérout R, Legris C, Degrange M, Sigot-Luizard M. Correlation between substratum roughness and wettability, cell adhesion, and cell migration. Journal of Biomedical Materials Research. 1997;36:99-108.
[237] Provenzano PP, Keely PJ. Mechanical signaling through the cytoskeleton regulates cell proliferation by coordinated focal adhesion and Rho GTPase signaling. Journal of Cell Science. 2011;124:1195-1205.
[238] Parsons JT, Horwitz AR, Schwartz MA. Cell adhesion: integrating cytoskeletal dynamics and cellular tension. Nature Reviews Molecular Cell Biology. 2010;11:633-643.
[239] Fletcher DA, Mullins RD. Cell mechanics and the cytoskeleton. Nature. 2010;463:485-492.
[240] Wang N, Butler JP, Ingber DE. Mechanotransduction across the cell surface and through the cytoskeleton. Science. 1993;260:1124-1127.
[241] Khatiwala CB, Peyton SR, Putnam AJ. Intrinsic mechanical properties of the extracellular matrix affect the behavior of pre-osteoblastic MC3T3-E1 cells. American Journal of Physiology-Cell Physiology. 2006;290:C1640-1650.
[242] Kong HJ, Polte TR, Alsberg E, Mooney DJ. FRET measurements of cell-traction forces and nano-scale clustering of adhesion ligands varied by substrate stiffness. Proceedings of the National Academy of Sciences of the United States of America. 2005;102:4300-4305.
[243] Nemir S, West JL. Synthetic materials in the study of cell response to substrate rigidity. Annals of Biomedical Engineering. 2010;38:2-20.
[244] http://www.nhlbi.nih.gov/health/health-topics/topics/atherosclerosis.
[245] http://www.fda.gov/MedicalDevices/ProductsandMedicalProcedures/DeviceApprovalsandClearances/default.htm.
[246] Marrey RV, Burgermeister R, Grishaber RB, Ritchie RO. Fatigue and life prediction for cobalt-chromium stents: A fracture mechanics analysis. Biomaterials. 2006;27:1988-2000.
[247] Koster R, Vieluf D, Kiehn M, Sommerauer M, Kahler J, Baldus S, et al. Nickel and molybdenum contact allergies in patients with coronary in-stent restenosis. The Lancet. 2000;356:1895-1897.

[248] Mitra A, Agrawal D. In stent restenosis: bane of the stent era. Journal of Clinical Pathology. 2006;59:232-239.
[249] Cutlip DE, Baim DS, Ho KK, Popma JJ, Lansky AJ, Cohen DJ, et al. Stent thrombosis in the modern era a pooled analysis of multicenter coronary stent clinical trials. Circulation. 2001;103:1967-1971.
[250] Joner M, Finn AV, Farb A, Mont EK, Kolodgie FD, Ladich E, et al. Pathology of drug-eluting stents in humans - Delayed healing and late thrombotic risk. Journal of the American College of Cardiology. 2006;48:193-202.
[251] Lüscher TF, Steffel J, Eberli FR, Joner M, Nakazawa G, Tanner FC, et al. Drug-eluting stent and coronary thrombosis biological mechanisms and clinical implications. Circulation. 2007;115:1051-1058.
[252] Johnson W, Samwer K. A universal criterion for plastic yielding of metallic glasses with a (T/T g) 2/3 temperature dependence. Physical Review Letters. 2005;95:195501.
[253] Wang J, Li R, Hua N, Zhang T. Co-based ternary bulk metallic glasses with ultrahigh strength and plasticity. Journal of Materials Research. 2011;26:2072-2079.
[254] Hasan M, Schroers J, Kumar G. Functionalization of metallic glasses through hierarchical patterning. Nano Letters. 2015; In press.
[255] Kastrati A, Mehilli J, Dirschinger J, Dotzer F, Schühlen H, Neumann F-J, et al. Intracoronary stenting and angiographic results strut thickness effect on restenosis outcome (ISAR-STEREO) trial. Circulation. 2001;103:2816-2821.
[256] Briguori C, Sarais C, Pagnotta P, Liistro F, Montorfano M, Chieffo A, et al. In-stent restenosis in small coronary arteriesimpact of strut thickness. Journal of the American College of Cardiology. 2002;40:403-409.
[257] Song GL, Atrens A. Understanding magnesium corrosion - A framework for improved alloy performance. Advanced Engineering Materials. 2003;5:837-858.
[258] Halford GR. Fatigue and durability of structural materials: ASM International; 2006.
[259] Roland T, Retraint D, Lu K, Lu J. Fatigue life improvement through surface nanostructuring of stainless steel by means of surface mechanical attrition treatment. Scripta Materialia. 2006;54:1949-1954.
[260] Agarwal N, Kahn H, Avishai A, Michal G, Ernst F, Heuer A. Enhanced fatigue resistance in 316L austenitic stainless steel due to low-temperature paraequilibrium carburization. Acta Materialia. 2007;55:5572-5580.
[261] Nicoud F, Vernhet-Kovacsik H, Pérez-Martin A, Dauzat M, Moreno R. Arterial Stenting: From Hemodynamics and Wall Mechanics to Restenosis-Experimental in vivo and Theoretical Approaches.
[262] Berry JL, Manoach E, Mekkaoui C, Rolland PH, Moore Jr JE, Rachev A. Hemodynamics and Wall Mechanics of a Compliance Matching Stent: In Vitro and In Vivo Analysis. Journal of Vascular and Interventional Radiology. 2002;13:97-105.
[263] Kastrati A, Dirschinger J, Boekstegers P, Elezi S, Schuhlen H, Pache J, et al. Influence of stent design on 1-year outcome after coronary stent placement: A

randomized comparison of five stent types in 1,147 unselected patients. Catheterization and Cardiovascular Interventions. 2000;50:290-297.

[264] Kleinstreuer C, Li Z, Basciano CA, Seelecke S, Farber MA. Computational mechanics of Nitinol stent grafts. Journal of Biomechanics. 2008;41:2370-2378.

[265] Oyane A, Kim HM, Furuya T, Kokubo T, Miyazaki T, Nakamura T. Preparation and assessment of revised simulated body fluids. Journal of Biomedical Materials Research Part A. 2003;65:188-195.

[266] Palit GC, Elayaperumal K. Passivity and pitting of corrosion-resistant pure metals Ta, Nb, Ti, Zr, Cr and Al in chloride solution. Corrosion Science. 1978;18:169-179.

[267] Haynes CA, Norde W. Globular proteins at solid/liquid interfaces. Colloids and Surfaces B: Biointerfaces. 1994;2:517-566.

[268] Ochsenbein A, Chai F, Winter S, Traisnel M, Breme J, Hildebrand HF. Osteoblast responses to different oxide coatings produced by the sol-gel process on titanium substrates. Acta Biomaterialia. 2008;4:1506-1517

[269] Tanous D, Bräsen JH, Choy K, Wu BJ, Kathir K, Lau A, et al. Probucol inhibits in-stent thrombosis and neointimal hyperplasia by promoting re-endothelialization. Atherosclerosis. 2006;189:342-349.

[270] Curcio A, Torella D, Indolfi C. Mechanisms of smooth muscle cell proliferation and endothelial regeneration after vascular injury and stenting: approach to therapy. Circulation journal: official journal of the Japanese Circulation Society. 2010;75:1287-1296.

[271] Bai HZ, Masuda J, Sawa Y, Nakano S, Shirakura R, Shimazaki Y, et al. Neointima formation after vascular stent implantation. Spatial and chronological distribution of smooth muscle cell proliferation and phenotypic modulation. Arteriosclerosis, Thrombosis, and Vascular Biology. 1994;14:1846-1853.

[272] Dejana E. Endothelial cell-cell junctions: Happy together. Nature Reveiws Molecular Cell Biology. 2004;5:261-270.

[273] Śmieszek A, Donesz-Sikorska A, Grzesiak J, Krzak J, Marycz K. Biological effects of sol–gel derived ZrO2 and SiO2/ZrO2 coatings on stainless steel surface—In vitro model using mesenchymal stem cells. Journal of Biomaterials Applications. 2014:0885328214545095.

[274] Masalski J, Gluszek J, Zabrzeski J, Nitsch K, Gluszek P. Improvement in corrosion resistance of the 316l stainless steel by means of Al2O3 coatings deposited by the sol-gel method. Thin Solid Films. 1999;349:186-190.

[275] Lee PJ, Ho CC, Hwang CS, Ding SJ. Improved physicochemical properties and biocompatibility of stainless steel implants by PVA/ZrO2-based composite coatings. Surface and Coatings Technology. 2014;258:374-380.

[276] Gurappa I. Development of appropriate thickness ceramic coatings on 316 L stainless steel for biomedical applications. Surface and Coatings Technology. 2002;161:70-78.

[277] Sprague EA, Luo J, Palmaz JC. Human aortic endothelial cell migration onto stent surfaces under static and flow conditions. Journal of Vascular and Interventional Radiology. 1997;8:83-92.

[278] Dewey CF, Bussolari SR, Gimbrone MA, Davies PF. The dynamic-response of vascular endothelial-cells to fluid shear-stress. Journal of Biomechanical Engineeing. 1981;103:177-185.
[279] Davies PF. Flow-mediated endothelial mechanotransduction. Physiological Reviews. 1995;75:519-560.
[280] Senthi S, Munro JT, Pitto RP. Infection in total hip replacement: Meta-analysis. International Orthopaedics. 2011;35:253-260.
[281] Norowski PA, Bumgardner JD. Biomaterial and antibiotic strategies for peri-implantitis: A review. Journal of Biomedical Materials Research Part B. 2009;88B:530-543.
[282] Borkow G, Gabbay J. Copper as a biocidal tool. Current Medicinal Chemistry. 2005;12:2163-2175.
[283] Davis JR. Copper and copper alloys: ASM international; 2001.
[284] Zhao LZ, Chu PK, Zhang YM, Wu ZF. Antibacterial coatings on titanium implants. Journal of Biomedical Materials Research Part B. 2009;91B:470-480.
[285] Otter JA, French GL. Bacterial contamination on touch surfaces in the public transport system and in public areas of a hospital in London. Letters in Applied Microbiology. 2009;49:803-805.
[286] Borkow G, Gabbay J. Copper, an ancient remedy returning to fight microbial, fungal and viral infections. Current Chemical Biology. 2009;3:272-278.
[287] Grass G, Rensing C, Solioz M. Metallic copper as an antimicrobial surface. Applied Environmental Microbiology. 2011;77:1541-1547.
[288] Santo CE, Lam EW, Elowsky CG, Quaranta D, Domaille DW, Chang CJ, et al. Bacterial Killing by Dry Metallic Copper Surfaces. Appllied Environmental Microbiology. 2011;77:794-802.
[289] Sitthisak S, Knutsson L, Webb JW, Jayaswal RK. Molecular characterization of the copper transport system in Staphylococcus aureus. Microbiology. 2007;153:4274-4283.
[290] Santo CE, Morais PV, Grass G. Isolation and characterization of bacteria resistant to metallic copper surfaces. Applied Environmental Microbiology. 2010;76:1341-1348.
[291] Zheng YF, Zhang BB, Wang BL, Wang YB, Li L, Yang QB, et al. Introduction of antibacterial function into biomedical TiNi shape memory alloy by the addition of element Ag. Acta Biomaterialia. 2011;7:2758-2767.
[292] An YH, Friedman RJ. Concise review of mechanisms of bacterial adhesion to biomaterial surfaces. Journal of Biomedical Materials Research. 1998:338-348.
[293] Absolom DR, Lamberti FV, Policova Z, Zingg W, van Oss CJ, Neumann A. Surface thermodynamics of bacterial adhesion. Applied and Environmental Microbiology. 1983;46:90-97.
[294] Gallardo-Moreno AM, Pacha-Olivenza MA, Saldaña L, Pérez-Giraldo C, Bruque JM, Vilaboa N, et al. In vitro biocompatibility and bacterial adhesion of physico-chemically modified Ti6Al4V surface by means of UV irradiation. Acta Biomaterialia. 2009;5:181-192.

[295] Feng Q, Wu J, Chen G, Cui F, Kim T, Kim J. A mechanistic study of the antibacterial effect of silver ions on Escherichia coli and Staphylococcus aureus. Journal of Biomedical Materials Research. 2001:662-668.

[296] Jung WK, Koo HC, Kim KW, Shin S, Kim SH, Park YH. Antibacterial activity and mechanism of action of the silver ion in Staphylococcus aureus and Escherichia coli. Applied and Environmental Microbiology. 2008;74:2171-2178.

[297] Kim JS, Kuk E, Yu KN, Kim J-H, Park SJ, Lee HJ, et al. Antimicrobial effects of silver nanoparticles. Nanomedicine: Nanotechnology, Biology and Medicine. 2007;3:95-101.

[298] Hetrick EM, Schoenfisch MH. Reducing implant-related infections: active release strategies. Chemical Society Reviews. 2006;35:780-789.

[299] Dowling D, Betts A, Pope C, McConnell M, Eloy R, Arnaud M. Anti-bacterial silver coatings exhibiting enhanced activity through the addition of platinum. Surface and coatings Technology. 2003;163:637-640.

[300] Panyala NR, Peña-Méndez EM, Havel J. Silver or silver nanoparticles: a hazardous threat to the environment and human health. Journal of Applied Biomedicine. 2008;6:117-129.

[301] Feng QL, Cui FZ, Kim TN, Kim JW. Ag-substituted hydroxyapatite coatings with both antimicrobial effects and biocompatibility. Journal of Materials Science Letters. 1999;18:559-561.

[302] Wang WH. Roles of minor additions in formation and properties of bulk metallic glasses. Progress in Materials Science. 2007;52:540-596.

VITA

Lu Huang was born in Shangrao, China, on July 16, 1985. She graduated with a Bachelor's degree from the Department of Materials Science and Engineering at Beihang University (Beijing, China) with a concentration of materials corrosion and mitigation in 2006. From 2006 to 2011, she was engaged in the graduate study at the Department of Materials Science and Engineering at Beihang University under the advisement of Dr. Tao Zhang, and received her first Doctor of Philosophy in Materials Science in 2012. In January 2012, she enrolled in the graduate school at the University of Tennessee and worked as graduate research/teaching assistant under the guidance of Dr. Wei He and Dr. Peter K. Liaw in the Department of Materials Science and Engineering. She completed her Doctor of Philosophy in 2015 at the University of Tennessee.